

Universitat Autònoma de Barcelona
Institut de Biotecnologia i de Biomedicina

Parc Científic de Barcelona
Computer Simulation and Modeling Laboratory
Institut de Química Teòrica i Computacional

**ESTUDI DE LA
REACTIVITAT DE CATALASES
MITJANÇANT DINÀMICA MOLECULAR *AB INITIO***

TESI DOCTORAL
Mercedes Alfonso Prieto

Barcelona, desembre de 2009

Memòria presentada per **MERCEDES ALFONSO PRIETO**
llicenciada en Química i Bioquímica
per tal d'optar al títol de Doctor per la Universitat Autònoma de Barcelona.
Programa de doctorat d' *Estructura i funció de proteïnes*.
Bienni 2004-2006

Aquesta tesi ha estat realitzada al Parc Científic de Barcelona,
sota la direcció de la **Dra. Carme Rovira i Virgili**,
Professora d'Investigació ICREA,
i comptant amb la tutoria del **Dr. Xavier Daura Ribera**,
Professor d'Investigació ICREA
de l'Institut de Biotecnologia i de Biomedicina
de la Universitat Autònoma de Barcelona.

Barcelona, desembre del 2009

l'interessada

vist-i-plau de la directora

ACKNOWLEDGEMENTS

Aquesta tesi no hauria estat possible sense el suport i la col·laboració de tota la gent que m'ha fet costat durant aquests cinc anys. Donat que seria impossible posar el nom de tothom a la portada, voldria aprofitar aquest espai per agrair-los tantes coses com han arribat a fer per mi.

MOLTES GRÀCIES / MUCHAS GRACIAS / THANKS A LOT / VIELEN DANK

- *A la Carme*, per tenir la idea esbojarrada d'agafar una bioquímica que gairebé no sabia el que era la dinàmica molecular per fer una tesi de Car-Parrinello. Pel seu suport i paciència durant aquests anys, per estar sempre disponible per resoldre qualsevol dubte o problema, per tot el que m'ha ensenyat, per donar-me ànims quan ho veia tot negre ... i per les “activitats” extralaborals.
- *Al Xevi i a l'Albert*, per estar sempre disposats a donar-me un cop de mà (malgrat haver-me hagut d'aguantar com a companya de taula) i pels cafès, dinars, sopars i congressos compartits.
- *A Pietro*, por poner siempre el dedo en la llaga cuando hay que mejorar un artículo y por los momentos de ocio y gastronómicos.
- *A l'Ignasi i al Xavi*, per ser sempre tan optimistes i “creure's” els nostres càlculs.
- *To Peter*, for being so supportive, for his explanations making experiments easy to understand for theoreticians and for his English corrections.
- *To Mike*, for all his support during my stay in his group and for offering me the opportunity to continue doing research.
- *To Jochen*, for all he has taught me, for his assistance and patience and for making my stay in Philly so nice.
- *To Axel*, for all his help, either with calculations or with German, and for the dinners with jazz music.

- *Al Toni Rodríguez-Fortea*, per la seva ajuda amb els spins i les metadinàmiques.
- *Al Toni Planas, al Xavi Fernández-Busquets i al Juanjo Valle*, per ensenyar-me que hi ha “vida” més enllà dels hemos. *To Morten and Thomas*, for his help with NAMD and other stuff and for introducing me in the field of protein membranes.
- *Al Xavier Daura*, per fer-me de tutor, ajudar-me amb els tràmits burocràtics de la tesi i interessar-se per la meva recerca.
- *Al Fermín i al Marc*, perquè “lo mismo valen para un roto que para un descosido”, diga-li parlar d’esports, fer les millors croquetes, organitzar excursions, o bé resoldre dubtes de Fortran o de Grace.
- *A Javi*, por ser mi gurú / asistente técnico personal de Mac y por todos los cafés y tertulias compartidas. *A l’Oriol*, per saber explicar qualsevol terme informàtic a una ignorant com jo i *al Marc W.*, per encebar-nos amb la xocolata suïssa.
- *A Fernando*, por las sesiones de tango y milongas y por estar siempre de buen humor.
- *A las nuevas incorporaciones (Javi I., Pablo, Victor, Roland)*, por aguantarme estos meses de escritura de tesis. *Y a los visitantes (Mireia, Luis, Pawel, ...)* que han pasado por aquí y que siempre me han enseñado algo nuevo.
- *A mis compañeros de cursos de doctorado*, por todos los viajes, clases y visitas compartidas. A las brujis Bárbara y Nere, a Silvia, a Paloma (y su voz prodigiosa), al computerero Marc, a Sebastián, al matxaca Gus, a Héctor, a Javi-Wifi, a Francisco (y sus líneas rectas), a Ornella y a Pablo (y su “no me gustan las tartas”).
- *To the CMM groupies*, for making me feel part of the group. To the Kindergarten guys, Ekta and Jérôme (and his music), to Matteo and Bob (for sharing their office), to Marco, Grace, Ming-HSun, Guillaume, Russell and Vanessa. Y a Diego y Amanda por “cuidarme” tan bien.
- *Al recolzament logístic*: a la Sílvia Mora, a l’Ana López, a la Marga Aguilera, a la Maite Jiménez, a l’Eva Vila i als tècnics informàtics del CeRQT, l’IQTC, el CESCA i el BSC.

- *A mi familia:* a mi madre por todas la fiambreras y por el esfuerzo de comprender qué es esto de hacer una tesis de química teórica; a mi hermana, por ser tan loca y cariñosa.
- *A las amigas de toda la vida:* a Clara, Marga y Núria por estar siempre ahí cuando os he necesitado y por ayudarme a desconectar del trabajo cuando todo se hacía cuesta arriba.
- *A la Vero:* pels consultoris predoctorals i pels berenars “Buenas Migas”.
- *Al Dani:* perquè els bons amics no es paguen amb diners.

COLLABORATIONS

This thesis has been done in collaboration with the following research groups, to whom I am greatly indebted:

- **Prof. Ignacio Fita & Dr Xavi Carpena**

Institut de Biologia Molecular (IBMB-CSIC) and Institut de Recerca Biomèdica (IRB),
Parc Científic de Barcelona (Barcelona, Spain).

- **Prof. Peter Loewen**

Department of Microbiology, University of Manitoba (Canada).

- **Dr Jochen Blumberger**

Department of Chemistry, University of Cambridge (United Kingdom).
& Department of Physics and Astronomy, University College London (United Kingdom).

- **Prof. Michael L. Klein**

Center for Molecular Modeling, University of Pennsylvania (United States).
& Institute for Computational and Molecular Science, Temple University (United States).

- **Dr Antonio Rodríguez-Fortea**

Universitat Rovira i Virgili (Tarragona, Spain)

Part of this thesis has been performed during a research stay abroad:

09/2006-11/2006

3 month training short visit at University of Pennsylvania (Philadelphia, USA),
Center for Molecular Modeling (Prof Michael L. Klein).

Project: Electron and proton transfer in the reaction intermediates of heme catalases.

Funded by a BE fellowship, awarded by the Generalitat de Catalunya.

FELLOWSHIPS

The present thesis has been supported by the following fellowships:

- *Beca del programa de pràctiques “Passa l’Estiu al Parc!”* (07/2004-09/2004).
Awarded by Parc Científic de Barcelona.
- *Beca predoctoral al grup de Simulació Quàntica de Processos Biològics* (10/2004-12/2005).
Awarded by Parc Científic de Barcelona.
Funded by a Distinció de la Generalitat de Catalunya per la promoció de la recerca universitària awarded to Dr Rovira.
- *Beca de formació de personal investigador (FI)* (2005-2009).
Awarded by the Generalitat de Catalunya.
This thesis has been performed with the support of the Comissionat per a Universitats i Recerca - Departament d’Innovació, Universitats i Empresa of the Generalitat de Catalunya and the European Social Fund.
- *Beca per estades de recerca fora de Catalunya (BE)* (09/2006-11/2006).
Awarded by the Generalitat de Catalunya.

SYMBOLS AND ACRONYMS

Å	Angstrom
A	Helmholtz free energy
aa	aminoacid / protein residue
AIMD	<i>ab initio</i> molecular dynamics
ANC	<i>Aspergillus niger</i> catalase
AOS	allene oxide synthase
APX	ascorbate peroxidase
B3LYP	exchange-correlation functional
BLC	<i>Bovine liver</i> catalase
BOMD	Born-Oppenheimer molecular dynamics
BP86	exchange-correlation functional
BpKatG	<i>Burkholderia pseudomallei</i> catalase-peroxidase
CcP	cytochrome c peroxidase
CP	Car-Parrinello method
Cpd I	Compound I
Cpd I*	Compound I*
Cpd II	Compound II
Cpd III	Compound III
CPMD	Car-Parrinello molecular dynamics
CPO	chloroperoxidase
CP QM/MM	Car-Parrinello quantum mechanics / molecular mechanics
CV	collective variable
D-RESP	dynamically generated restrained electrostatic potential derived charges
DFT	density functional theory
e / e^-	electron
EA	electron affinity

ESP	electrostatic potential derived charges
ET	electron transfer
eV	electronvolt
FPMD	first principles molecular dynamics
fs	femtosecond
G	Gibbs free energy
HAT	hydrogen atom transfer
Hb	hemoglobin
HEC	<i>Human erythrocyte</i> catalase
HOMO	highest occupied molecular orbital
HPC	<i>Helicobacter pylori</i> catalase
HPH	<i>Escherichia coli</i> hydroperoxidase II
HRP	<i>Horse radish</i> peroxidase
IP	ionization potential
K	Kelvin
KatG	catalase-peroxidase
LPO	lactoperoxidase
LR	linear response approximation
LUMO	lowest unoccupied molecular orbital
M	multiplicity
Mb	myoglobin
MLC	<i>Micrococcus luteus</i> catalase / <i>Micrococcus lysodeikticus</i> catalase
MM	molecular mechanics
NLCC	non-linear core corrections
nm	nanometer
ns	nanosecond
P450	cytochrome P450
PAA	peroxoacetic acid
PBE	exchange-correlation functional
PCET	proton coupled electron transfer

PGHS	prostaglandin H synthase
PMC	<i>Proteus mirabilis</i> catalase
ps	picosecond
PSII	photosystem II
PT	proton transfer
PVC	<i>Penicillium vitale</i> catalase
QM	quantum mechanics
QM/MM	quantum mechanics / molecular mechanics
RC	bacterial reaction center
rc	reaction coordinate
RESP	restrained electrostatic potential derived charges
ROS	reactive oxygen species
Ry	Rydberg
S	spin quantum number
SOMO	single occupied molecular orbital
TS	transition state
u.a.	atomic units
u.e.	electron units

CONTENTS

OUTLINE	1
CHAPTER I. INTRODUCTION	5
1. Oxidative stress	7
1.1. Reactive oxygen species (ROS)	7
1.2. Protection against oxidative stress	8
2. Catalases	9
2.1. Biological function	9
2.2. Categorization	10
3. Monofunctional catalases	12
3.1. Topology	12
3.2. Classification	19
3.3. Kinetic properties	20
4. Oxidized intermediates	23
4.1. Experimental preparation	24
4.2. Characterization of the electronic structure	24
4.3. Determination of the protonation state of the ferryl oxygen	28
5. Open questions	30
OBJECTIVES	33
CHAPTER II. COMPUTATIONAL METHODS	37
1. Car-Parrinello molecular dynamics (CPMD)	39
1.1. Density Functional Theory (DFT)	39
1.2. <i>Ab initio</i> molecular dynamics (AIMD)	39
1.3. Car-Parrinello molecular dynamics (CPMD)	40
1.4. Plane waves basis set	42
1.5. Pseudopotentials	43
2. Quantum Mechanics/Molecular Mechanics (QM/MM)	43
2.1. General overview	43
2.2. QM-MM boundary. Bonding QM-MM interactions	45
2.3. Non-bonding QM-MM interactions	45
3. Metadynamics	47
3.1. Direct metadynamics	47
3.2. Collective variables	50
3.3. Lagrangian metadynamics	51

4. Electron transfer (ET)	53
4.1. Redox properties	53
4.2. Marcus theory	54
4.3. Energy gap method	56
4.4. Energy gap from QM/MM	58

CHAPTER III. DENSITY FUNCTIONAL STUDY ON MODELS OF CATALASE REACTION INTERMEDIATES

63	
1. Introduction	65
2. Computational details	66
2.1. Models	66
2.2. Simulation details	69
3. Results and discussion	70
3.1. Optimized structures	70
3.2. Structural comparison with other heme proteins	75
3.3. Electronic configuration	77
3.4. Proposed valence bond model for the electronic structure of Cpd I	93
4. Summary and conclusions	94

CHAPTER IV. STRUCTURE AND ELECTRONIC CONFIGURATION OF COMPOUND I INTERMEDIATES OF *HELICOBACTER PYLORI* AND *PENICILLIUM VITALE* CATALASES

97	
1. Introduction	99
2. Results and discussion	105
2.1. QM/MM models	105
2.2. Assignment of the oxidized intermediates of HPC and PVC	120
2.3. Proposed scheme for the transformations of oxidized catalase	122
2.4. Electronic consequences of heme modifications in catalase oxidized intermediates	124
3. Summary and conclusions	127

CHAPTER V. ELECTRON TRANSFER AND FERRYL PROTONATION IN CATALASES

129	
1. Introduction	131
2. Mechanistic analysis of Cpd I* formation	135
2.1. Cpd I reduction	135
2.2. Oxidation of a protein residue	138
2.3. Cpd I* formation	140
3. Results and discussion	141
3.1. Free energy of ET to Cpd I ($\Delta G^{\text{Cpd I, ET}}$)	141
3.2. Free energy of PT ($\Delta G^{\text{Cpd I}^*, \text{PT}}$)	146
3.3. Redox-active protein residues	154
3.4. Factors determining Cpd I* formation	157

3.5. Candidates for the radical site in HPC Cpd I* and possible ET pathways	158
3.6. Free energy of ET from Tyr to Cpd I in HPC ($\Delta G^{\text{Tyr/CpdI, ET}}$)	162
3.7. Protonation state of the Tyr cation radical	164
3.8. Formation of protein radicals in catalases	166
4. Conclusions	168

CHAPTER VI. ELECTRONIC STATE OF THE MOLECULAR OXYGEN RELEASED BY CATALASE

CHAPTER VI. ELECTRONIC STATE OF THE MOLECULAR OXYGEN RELEASED BY CATALASE	169
1. Introduction	171
2. Spin state analysis	173
2.1. Reactants and products	173
2.2. Possible reaction schemes	176
2.3. Implications for the mechanism of the catalytic reaction	186
3. Gas phase calculations	187
3.1. Reactants (Cpd I + H ₂ O ₂)	188
3.2. Products (Por-Fe ^{III} + H ₂ O + O ₂)	192
4. Summary and conclusion	196

CHAPTER VII. THE MOLECULAR MECHANISM OF THE CATALASE REACTION. 199

1. Introduction	201
2. Results and discussion	203
2.1. Reactants (Cpd I : H ₂ O ₂ complex)	203
2.2. Metadynamics simulations and reaction free energy landscape	206
2.3. Spin state analysis	216
2.4. Mechanism of Cpd I reduction by H ₂ O ₂	217
2.5. Influence of the distal His in Cpd I reduction	220
2.6. Comparison of the computed mechanisms with experimental data	222
3. Summary and conclusions	225

CHAPTER VIII. SUMMARY AND CONCLUSIONS

PUBLICATIONS AND PRESENTATIONS IN CONGRESSES

APPENDIX A. Additional information for Chapter IV

1. Computational details of the classical molecular dynamics simulations	A3
2. Computational details of the CP QM/MM calculations	A4

APPENDIX B. Additional information for Chapter V

1. Computational details	B3
1.1. Classical molecular dynamics simulations of the ET to Cpd I	B3
1.2. QM/MM calculations of the ET to Cpd I	B5
1.3. Metadynamics simulations of the PT to Cpd I*	B8

Contents

1.4. Classical molecular dynamics simulations of the ET from Tyr to Cpd I in HPC	B10
1.7. QM/MM calculations of the ET from Tyr to Cpd I in HPC	B11
1.8. QM/MM optimizations of the tyrosyl cation radical	B13
2. Preliminary calculations on Cpd I reduction	B14
2.1. Gas phase vertical ionization energies of Cpd I and Cpd II	B14
2.2. QM/MM vertical ionization energies of Cpd I and Cpd II	B17
2.3. Protonation of the Fe=O group and the distal His	B20
3. Preliminary calculations on Tyr oxidation.....	B23
4. Convergence of the ionization energies of the heme	B29
5. Outer-sphere energies for the ET to Cpd I	B33
6. Comparison to cytochrome c	B34
7. Further analysis of the redox-active residues	B35
8. Convergence of the ionization energies of Tyr351	B35
9. Contributions to the ET from Tyr351 to Cpd I	B38

APPENDIX C. Additional information for Chapter VI

1. Computational details	C3
1.1. Gas phase model	C3
1.2. Starting structures	C4
1.3. Geometry optimizations	C4
2. Analysis of the reactive oxygen species possibly involved in the catalytic reaction	C5
3. Orbital analysis	C6
3.1. Heme orbitals	C6
3.2. Dioxygen orbitals	C10
4. Effect of the protonation state of the propionic side chain	C11
5. Influence of the exchange-correlation functional	C13

APPENDIX D. Additional information for Chapter VII

1. Computational details of the QM/MM simulations	D3
2. Reaction pathway using a single geometric variable	D4
3. Computational details of the metadynamics simulations	D7
4. System evolution during metadynamics trajectory	D8
5. Spin state analysis	D15
5.1. Distribution of unpaired electrons	D15
5.2. Spin state energies	D20
5.3. Structure and spin state of the products (Enz + H ₂ O + O ₂)	D24
6. Dependence of the barriers for hydrogen atom transfer on the donor-acceptor distance.....	D27
7. Influence of the exchange-correlation functional	D29

BIBLIOGRAPHY

OUTLINE

OUTLINE

Hydrogen peroxide is a reactive oxygen species that is involved in oxidative damage as well as in intracellular redox-sensitive signal transduction. Therefore, a fine balance of the H_2O_2 concentration is essential for maintaining signaling without damaging biomolecules. *Catalases* are the primary enzymes regulating these hydrogen peroxide levels and thus they have been implicated as an important factor in inflammation, mutagenesis, prevention of apoptosis and stimulation of a wide spectrum of tumors.

Heme catalases are enzymes that decompose hydrogen peroxide into water and oxygen ($2 \text{H}_2\text{O}_2 \rightarrow 2 \text{H}_2\text{O} + \text{O}_2$). They are present in almost all aerobic organisms and are one of the most efficient enzymes known, with 10^6 molecules of H_2O_2 degraded per second. Indeed, because of the exceptional rate enhancement of H_2O_2 dismutation compared to catalysts that are not proteins, catalase was a key factor in the early recognition that enzymes are proteins and have substrate specificity.

It has been shown that some catalases contain a modified heme (*heme d*) instead of the most abundant *heme b* (i.e. iron-protoporphyrin IX). Although the reaction cycle performed by the two types of catalases is the same, the effect of the heme modification on the structure and electronic configuration of the reaction intermediates, as well as on their redox and acid-base properties is not known.

The principal active species of the catalase reaction cycle is a high valent iron species ($\text{Por}^{*+}\text{-Fe}^{\text{IV}}=\text{O}$) named *Compound I (Cpd I)*. Cpd I reacts with a molecule of hydrogen peroxide releasing water and molecular oxygen. This reaction is also performed by other heme proteins, although at much slower pace. The origin of this disparity has long been sought, and even though the catalase reaction has been known since 1940s, its detailed molecular mechanism has yet to be clarified.

The present thesis is aimed at answering these questions, considering two catalases as a test case: *Helicobacter pylori* catalase (HPC, a heme b-containing catalase) and *Penicillium vitale* catalase (PVC, based on heme d). This investigation will be performed by means of molecular dynamics (classical and *ab initio*).

The thesis is organized as follows. *Chapter I* introduces the enzymes under study, heme catalases, and presents the general objectives of this work. The basics of the methodologies used are given in *Chapter II*. Chapters III-VII contain a brief introduction to the problem investigated, followed by a description and discussion of the simulations performed. First, the effect of the heme modification on catalase intermediates is investigated in *Chapter III* by using gas phase models. In *Chapter IV*, we analyze the structure of the intermediates formed by HPC and PVC and ascertain the protonation state of catalase *Compound II (Cpd II)*. The factors determining that HPC and PVC show different oxidized intermediates (i.e. *Compound I** and *Compound I*, respectively) are investigated in *Chapter V*. In *Chapter VI*, we assess the validity of the arguments commonly used to predict the spin state of the molecular oxygen released by catalase. The molecular mechanism of the catalase reaction is studied in *Chapter VII*. Finally, *Chapter VIII* lists the main conclusions of this work. Additional information on the simulations performed in Chapters IV-VII can be found in *Appendixes A-D*.

CHAPTER I

INTRODUCTION

1. OXIDATIVE STRESS

Life evolved in an anaerobic world, thus without any selective pressure to avoid reactivity with oxygen. However, after the appearance of photosynthetic organisms, environmental oxygen levels rose very slowly and microorganisms had to develop mechanisms to defend themselves against oxygen, and also against partially reduced oxygen species, that are generated as by-products of aerobic metabolism (Imlay, 2008). The paradox of aerobic life is that, although oxygen is essential for living, it is also very harmful (Halliwell & Gutteridge, 1984).

1.1. Reactive oxygen species (ROS)

Oxygen toxicity is primarily mediated by partially reduced oxygen species, that are more reactive than oxygen itself (Imlay, 2008). Such reactive oxygen species (ROS) include singlet oxygen ($^1\Sigma_g^+ O_2$), superoxide (O_2^-), hydrogen peroxide (H_2O_2), hydroxyl radical (OH^\bullet), hypohalous acids (HXO , where $X=Cl, Br, I$) or peroxyxynitrite ($ONOO^-$).

ROS are inevitable by-products of aerobic metabolism (Imlay, 2008). Oxygen crosses membranes so freely that its intracellular concentration is essentially equivalent to that outside the cell. This intracellular oxygen can abstract electrons from exposed redox moieties of electron-transfer enzymes, such as flavoenzymes, generating O_2^- and H_2O_2 . Besides, about 5 percent of the time, the respiratory chain reduces oxygen to superoxide (instead of water), probably due to a “leak” of single electrons at a particular site of the mitochondrial electron transport chain.

O_2^- and H_2O_2 are also produced by some enzymes as part of their normal catalytic cycle. NADPH oxidase, present in phagocytic cells, generates superoxide to kill microorganisms. Some oxidases (such as urate oxidase, acyl Coa oxidase, L-glucolactone oxidase and monoamineoxidase) produce hydrogen peroxide when oxygenating their corresponding substrates, and 5-lipoxygenase releases superoxide when oxidizing essential fatty acids.

ROS are regarded as “biological toxins”, because they damage biological molecules. Superoxide and hydrogen peroxide can react with proteins containing transition metals, inactivating them. H_2O_2 can also react with ferrous iron associated with DNA (i.e. Fenton reaction) (Fenton, 1894), generating hydroxyl radical, which oxidizes DNA:



Hydroxyl radical can also be generated by the Haber-Weiss reaction (Haber & Weiss, 1934), in the presence of iron, copper or an ionizing radiation:



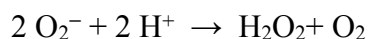
The hydroxyl radical is the most harmful ROS, because it can oxidize proteins, carbohydrates, lipids and nucleic acids.

Lately it has been suggested that H_2O_2 could play a role not only in oxidative stress, but also in intracellular redox-sensitive signal transduction. For instance, hydrogen peroxide has been implicated as a second messenger in the activation of transcriptional factor NF- κ B or in apoptosis (Yabuki, 1999; Islam, 1997; Sandstrom, 1993). Whether H_2O_2 acts as a toxin or as a cellular mediator will depend on their cellular concentration (Imlay, 2008). Therefore, a fine balance between H_2O_2 production and removal is necessary.

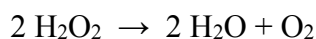
1.2. Protection against oxidative stress

Protection against oxidative stress includes two types of mechanisms: antioxidant defenses and repair systems (Imlay, 2008).

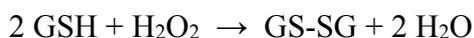
Antioxidant defenses remove ROS before they can damage biomolecules. Some are suicide compounds (such as vitamins C and E, uric acid, carotenoids or glutathione), because they are oxidized by ROS. Other are proteins, like ferritin, transferritin and ceruloplasmin, which store transition metals, thus avoiding the harmful Fenton and Haber-Weiss reactions. Besides, some enzymes, such as superoxide dismutase (SOD), catalase and glutathione peroxidase, catalyze the elimination of ROS. SOD catalyzes the disproportionation of superoxide, generating H_2O_2 :



The hydrogen peroxide molecule released by SOD must be rapidly removed, and this is accomplished either by catalase:



or by glutathione peroxidase (and other peroxidases):



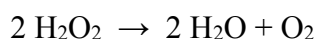
where GSH =reduced glutathione and GS-SG = oxidized glutathione.

By contrast the repair systems act when the damage has already occurred. Some of them are classified as direct, because they regenerate the damaged molecule; e.g. disulfide reductase or methionine sulfoxide reductase recover oxidized cysteines or methionines. Other repair systems are indirect, because they detect the damaged biomolecule and resynthesize the oxidized fragment or the complete biomolecule. Proteosome and phospholipases hydrolyze oxidized proteins or phospholipids, respectively, into their constituents. Likewise, there are endo- and exonucleases that preferentially cut oxidized DNA, such that DNA repair systems can resynthesize the oxidized fragment.

2. CATALASES

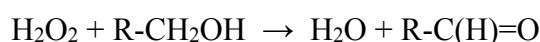
2.1. Biological function

As mentioned in the previous section, catalases are enzymes that dismutate hydrogen peroxide:



Therefore, they are very important for the removal of hydrogen peroxide and small peroxides before they can cause cellular damage (either directly or by generating hydroxyl radical). Hence, they are present in almost all aerobic organisms and even in some facultative anaerobes (Maté, 2001; Nicholls, 2001). In particular, in eukaryotic cells, catalase is located in the cytosol, the mitochondria and specially in peroxisomes and glyoxysomes. These organelles contain some oxidases (acyl-coA oxidase, urate oxidase, aminoacid oxidase) that produce H_2O_2 , which is in turn eliminated by the colocalized catalase.

Apart from this primary protective function, catalase can also play a role in signaling, as H_2O_2 can act as a second messenger (see section 1.1.). Catalase both regulates the levels of hydrogen peroxide and contributes to its compartmentalization. Besides, it is involved in the metabolization of methanol and ethanol (Zámocky, 2008):



Because of all its biological functions, catalase has been implicated in senile gray hairing (Wood, 2009), hemolysis of erythrocytes (Jacob, 1965; Kirkman & Gaetani 2006), diabetes mellitus (Ghot & Eaton, 2000), alcoholism (Medall, 2002), inflammation (Halliwell & Gutteridge, 1984), mutagenesis (Vuillame, 1987), prevention of apoptosis (Yabuki, 1999; Islam, 1997; Sandstrom,

1993) or stimulation of a wide spectrum of tumors (Miyamoto, 1996). For instance, a decreased catalase activity gives rise to increased H_2O_2 concentrations, that inactivate enzymes (e.g. tyrosinase in senile gray hairing or hemoglobin in erythrocytes) or even damage cells (e.g. pancreatic β cells in diabetes). By contrast, catalase overexpression in the brain increases the production of acetaldehyde, which is related to alcohol addiction. Altered levels of H_2O_2 also affect activation of the NF- κ B transcriptional factors, which are involved in the control of immune and inflammatory responses, cell proliferation and apoptosis.

2.2. Categorization

Catalases can be classified in three main groups (Zámocky & Koller 1999; Nicholls, 2001; Chelikani 2004; Zámocky 2008), depending on the quaternary structure, the subunit size and the prosthetic group: (i) the classical monofunctional enzymes, (ii) the bifunctional catalase-peroxidases, (iii) the non-heme catalases.

- *Monofunctional or typical catalases*

This is the largest and most studied group of catalases. They are called monofunctional because dismutation of hydrogen peroxide is their main activity, and any peroxidatic activity is minor and restricted to small substrates. They contain heme b or heme d as a prosthetic group and their quaternary structure is a tetramer. This group is the subject of the present thesis and thus will be explained in more detail in the next section (section 3).

- *Catalases-peroxidases or KatG*

This is the next largest group of catalases, so named because they exhibit a significant peroxidatic activity in addition to the catalase activity. Similar to small heme b-containing catalases, KatG contains heme b as a cofactor, but its quaternary structure is a dimer. Its active site is also different from monofunctional catalases (Figure 1), and resembles that of fungal and plant (class I) peroxidases (Chelikani, 2004). In addition, KatG exhibits a unique Trp-Tyr-Met covalent adduct (Figure 1), which has been shown to be essential for catalase, but not for peroxidase activity (Chelikani, 2004). The molecular mechanism of the catalase reaction in KatG is not yet known, but it is believed to be similar to that of monofunctional catalases, because both enzymes contain heme and the residues in the active site, albeit different, can play similar roles.

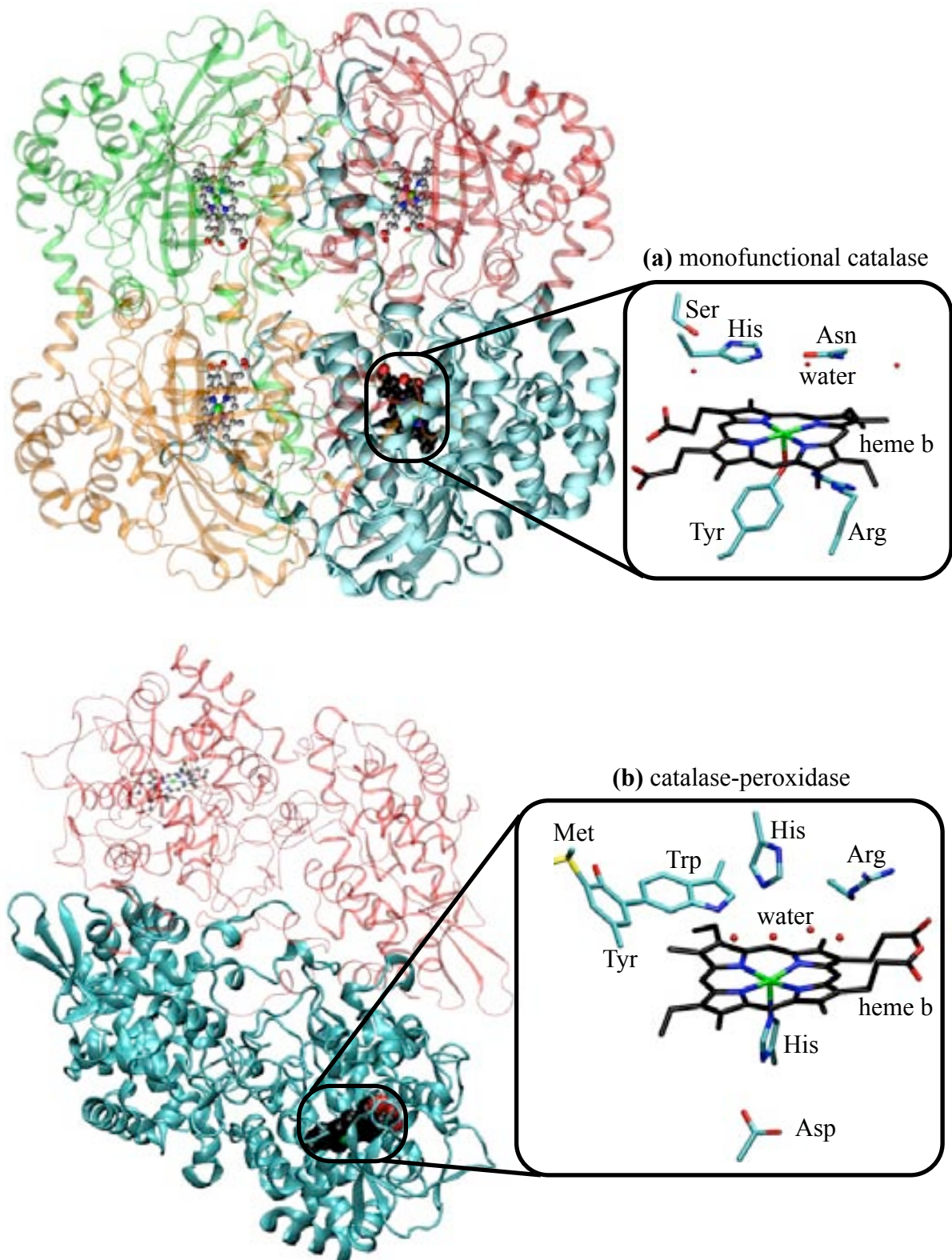
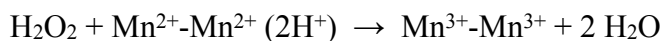


Figure 1. Comparison of the topology and the heme binding site of (a) a monofunctional catalase and (b) a catalase-peroxidase. The structures shown correspond to *Helicobacter pylori* catalase (HPC, PDB entry: 2IQF; Alfonso-Prieto, 2007) and *Burkholderia pseudomallei* catalase-peroxidase (BpKatG, PDB entry: 1MWV; Carpena, 2005). *Left*, the protein is displayed as cartoon picture, with each subunit in a different colour. *Right*, the heme binding pocket is shown in sticks.

- *Non-heme catalases*

Different from the two previous groups, the active site of these enzymes does not contain heme but a manganese cluster, and thus they are also called Mn-catalases (Zámocky and Koller, 1999; Nicholls, 2001; Zámocky, 2008). They are hexameric and each monomer bears a bridged binuclear Mn-cluster. Hence, the catalase reaction in Mn enzymes differs significantly from that in both monofunctional catalases (see section 3.3.) and catalase-peroxidases:



Their reaction rates are lower compared with heme catalases, which could explain why Mn-catalases have not become widespread in nature.

In addition, several heme containing-proteins have been observed to exhibit a low level of catalase activity (Nicholls, 2001). They include methemoglobin, metmyoglobin, most peroxidases and chloroperoxidase. This simply reflects the intrinsic ability of the isolated heme group to perform the catalase reaction, even in the absence of the protein.

3. MONOFUNCTIONAL CATALASES¹

3.1. Topology

- *Subunit structure*

As mentioned in the section 2.2., catalases are tetrameric proteins, formed by four identical subunits, each one containing a heme cofactor. Two different types of subunits can be distinguished in terms of size: small (~500 amino acids) subunits and large (~700 amino acids) subunits (Zámocky and Koller, 1999; Nicholls, 2001; Chelikani, 2004). As a consequence, two groups of catalases can be defined: small subunit and large subunit catalases, depending on the type of subunit that constitutes the enzyme.

¹ Monofunctional catalases are the subject of the present thesis, and thus hereafter the term catalases will stand for this type of catalases.

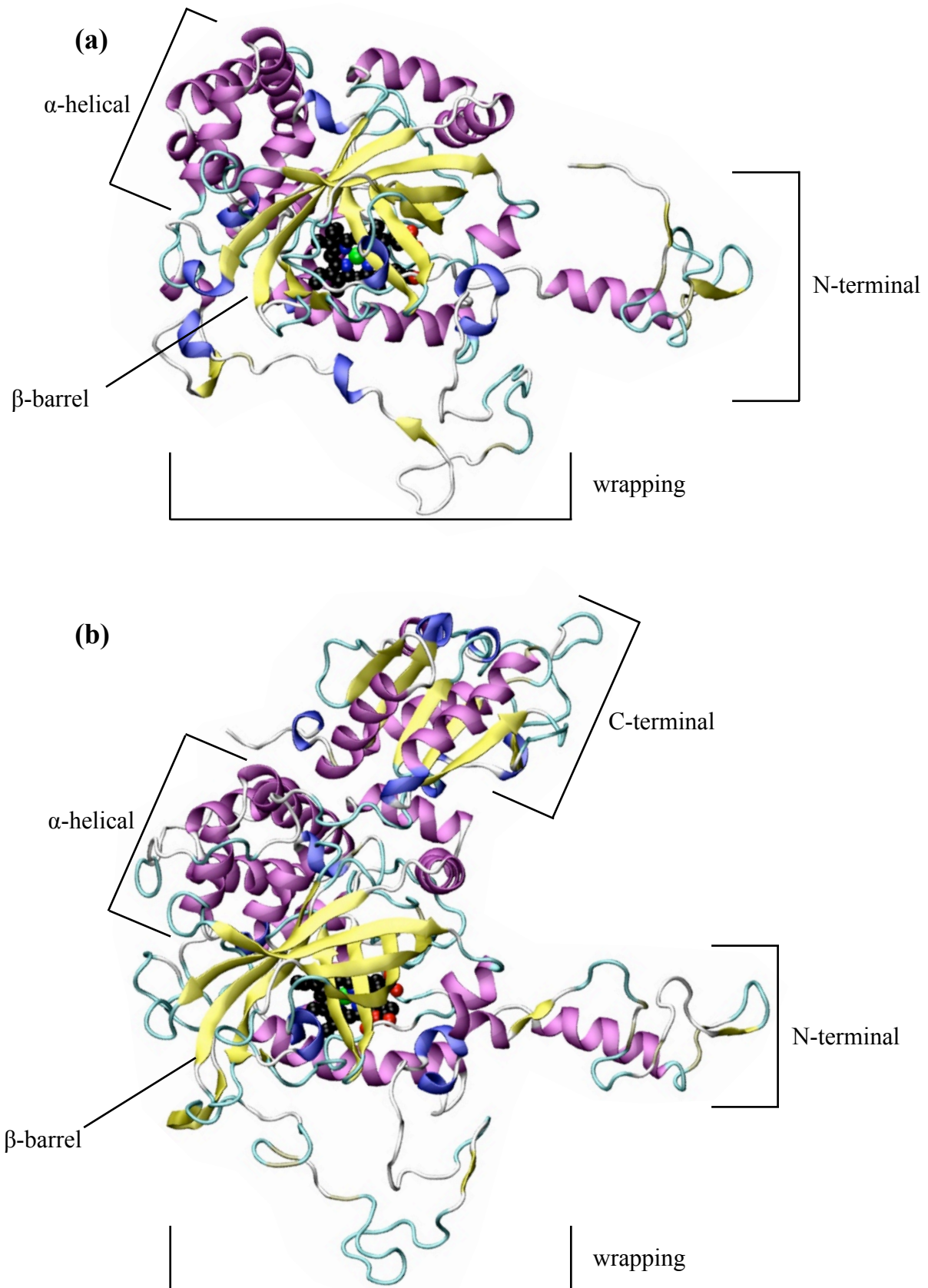


Figure 2. Comparison of the subunits of (a) a small subunit catalase (*Helicobacter pylori* catalase, HPC, PDB entry 2IUF) and (b) a large subunit catalase (*Penicillium vitale* catalase, PVC, PDB entry 2IQF) (Alfonso-Prieto, 2007). The protein is shown in cartoon representation, and the heme as spheres.

Despite the diversity of sequences and the different subunit size, all catalases share a common core (i.e. the *catalase fold*), which spans about 460 residues per subunit (Maté, 2001). This catalase fold is composed of four regions (Figure 2): (i) an amino terminal arm, (ii) an anti-parallel eight-stranded β -barrel domain, (iii) an extended region known as the “wrapping” domain, and (iv) an α -helical domain. The tertiary structure of small subunit catalases is formed by these four regions (Figure 2a), whereas in the large subunit enzymes there is an additional region, the C-terminal or flavodoxin-like domain (Figure 2b).

The *amino-terminal arm* is quite variable in length and contains the essential catalytic histidine. It is involved in extensive intersubunit interactions (shown in Figure 3), such that residues from this region contribute to define the heme pocket of a symmetry related subunit.

The second region, the *anti-parallel eight-stranded β -barrel domain*, is the central feature of the catalase fold. The first part of the β -barrel (β 1- β 4) contains most of the residues that define the heme distal side, whereas the second half contributes to the NADP(H) binding pocket. NADP(H) binding is exclusive of some small subunit catalases and it appears to protect the enzyme against inactivation by its own substrate, mainly in conditions of low H₂O₂ concentrations.

This globular β -barrel is connected to the α -helical domain by an extended region named the *wrapping loop*. This region contain the residues that define the heme proximal side, including the tyrosinate iron ligand, and it participates in extensive intersubunit interactions, specially with the amino-terminal domain from another subunit (see Figure 3).

The *α -helical domain* forms close associations with the α -helices of the β -barrel to stabilize the overall structure, and it contains the C-terminus of small subunit catalases. By contrast, in large subunit enzymes there is an additional segment between the α -helical domain and the C-terminus. This extra domain resembles flavodoxin, and thus it has been named *flavodoxin-like domain*. Such topology is usually associated to nucleotide binding; however, the binding of such cofactors has never been observed in large subunit catalases, and therefore, the function of this flavodoxin-like domain remains unknown.

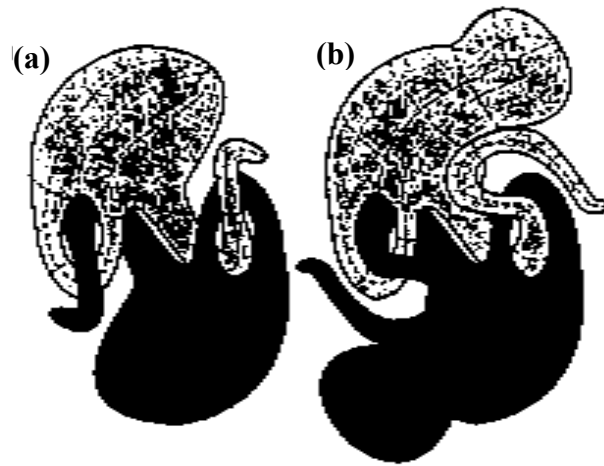


Figure 3. Illustration of the interweaving of two subunits in **(a)** small subunit and **(b)** large subunit catalases. Taken from reference (Nicholls, 2001).

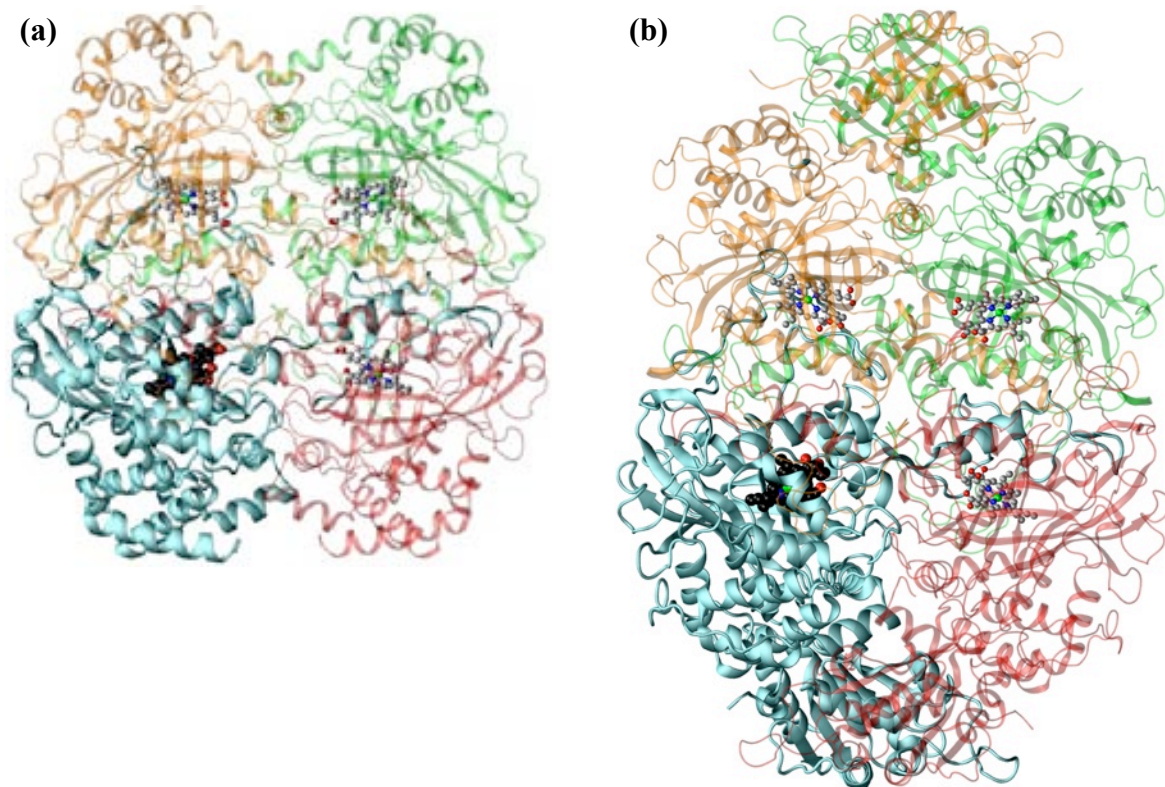


Figure 4. Comparison of the overall structures and sizes of **(a)** a small subunit catalase (*Helicobacter pylori* catalase, HPC, PDB entry 2IUJ) and **(b)** a large subunit catalase (*Penicillium vitale* catalase, PVC, PDB entry 2IQF) (Alfonso-Prieto, 2007). The protein is shown in cartoon representation, with the four subunits coloured blue, red, green and orange. The heme group in each subunit is shown as spheres.

- *Quaternary structure*

The quaternary structure of catalases (i.e. the organization of the four identical subunits into the tetramer) is also very well conserved among these enzymes (Nicholls, 2001). A unique feature of this molecular organization is the slipping of the amino-terminal arm of one subunit through the wrapping loop of a symmetry related subunit (Figure 3). This interweaving explains the unusual resistance to denaturation and proteolysis exhibited by catalases (Chelikani, 2004). The only difference between small and large subunit catalases is the overall dimensions of the tetramer (Nicholls, 2001), which are larger for large subunit catalases (see Figure 4), simply because each subunit is about 200 amino acids larger than in small subunit catalases.

- *Channels*

As can be seen in Figure 4, the heme group is deeply buried within the core of the catalase subunit, with the iron atom situated at about 20 Å from the nearest protein surface. Therefore, it is necessary to have access routes that will allow the H₂O₂ substrate to penetrate such a distance into the protein. Furthermore, the rapid turnover of catalases suggest that there must be separate inlet and outlet channels to allow the products to be released without interfering with the incoming substrate (Chelikani, 2004). Analysis of the catalase structures revealed two main channels, termed perpendicular and lateral, depending on their orientation with respect to the heme plane (Figure 5).

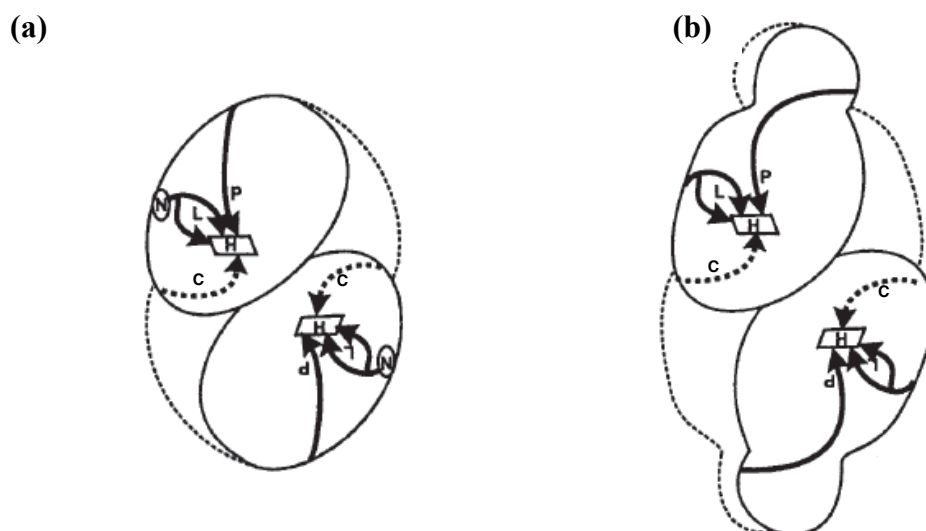


Figure 5. Putative channels in **(a)** a small subunit catalase and **(b)** a large subunit catalase. H = heme group, P = perpendicular or major channel, L = lateral or minor channel, C = channel connecting the proximal side of the heme with the central cavity of the tetramer and N = NADPH binding site. Taken from reference (Nicholls, 2001).

The *perpendicular channel* (P in Figure 5) has been considered the principal route by which hydrogen peroxide access the active site, and hence it has been also called the *major channel*. It is 30 Å (small subunit) or 50 Å (large subunit) long and is funnel-shaped, with a wide, hydrophilic part close to the surface and a narrow, hydrophobic part close to the heme, that selects H₂O₂ from water. By contrast, the *lateral channel*, also referred as the *minor channel* (L in Figure 5), has been proposed to be the pathway for product release or an alternative route for hydrogen peroxide access. Besides these two main channels, there is a third channel (C in Figure 5) which connects the proximal side of the heme with the central cavity of the tetramer, with an unknown (if any) role.

- *Heme binding pocket*

Catalases contain four heme groups, one in each subunit. Small subunit catalases contain an iron protoporphyrin IX group (heme b, Figure 6a), whereas most large subunit catalases bear an oxidized iron protoporphyrin IX group (heme d, Figure 6b) (Nicholls, 2001). This heme modification (Murshudov, 1996; Loewen, 1993) results in the saturation of the double bond across the β carbons of pyrrole III, together with the conversion of one of the propionates of the heme into a *cis*-hydroxy-γ-spirolactone (Figure 6b). Another difference is that heme d is flipped by 180° compared to heme b inside the active site, such that the relative disposition of the methyl and vinyl groups of pyrroles I and II is inverted.

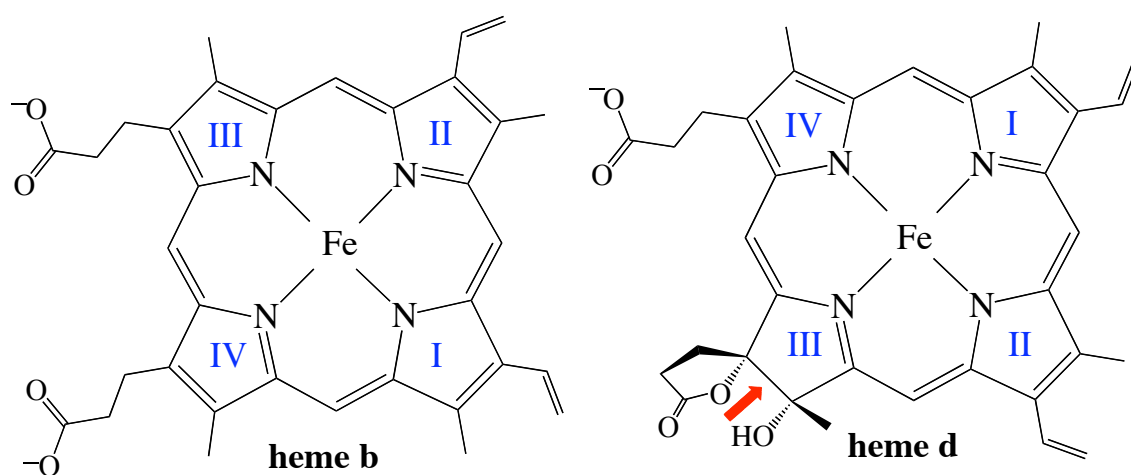


Figure 6. Molecular structure of heme b and heme d prosthetic groups. The double bond that becomes saturated in heme d is highlighted by an arrow. The numbering of the pyrroles is also indicated to show that, in the catalase binding pocket, heme d is flipped by 180° compared to heme b.

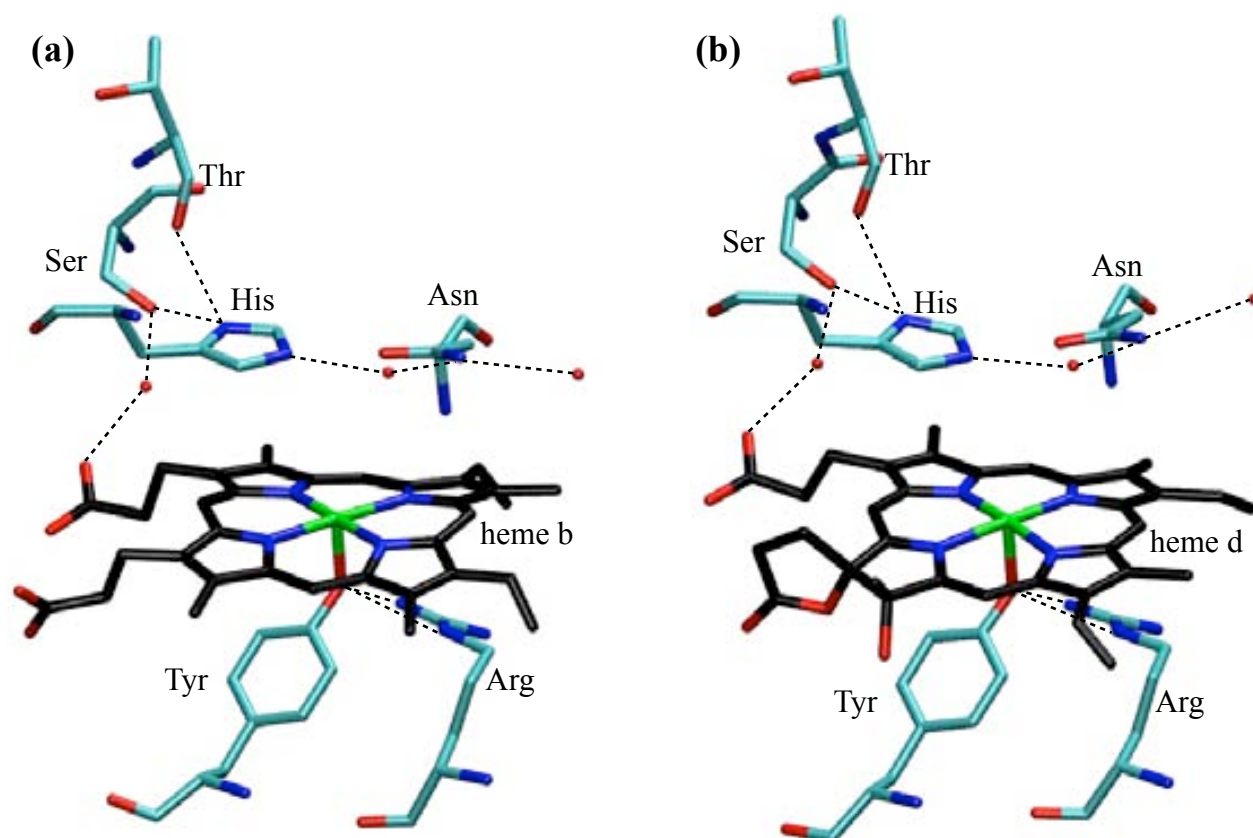


Figure 7. Heme binding pocket of **(a)** a small subunit catalase (*Helicobacter pylori* catalase, HPC, PDB entry 2IUJ) and a large subunit catalase **(b)** (*Penicillium vitale* catalase, PVC, PDB entry 2IQF) (Alfonso-Prieto, 2007).

Figure 7 shows the active site of catalase, which is the same for both heme b- and heme d-containing enzymes (Nicholls, 2001; Maté, 2001). In the proximal side (i.e. below the heme plane) there is an essential tyrosine, which is coordinated to the iron, and a conserved arginine residue, which is forming two hydrogen-bonds with the oxygen atom of Tyr. As a consequence, the essential tyrosine is deprotonated, and its negative charge is the reason why iron is in the oxidation state III (d^5 configuration).

The distal side (i.e. above the heme plane) contains an essential histidine, which acts as an acid-base catalyst during the catalase reaction. This His is situated almost parallel to the heme plane, above pyrrole III of heme b (i.e. His-III heme orientation) or pyrrole IV of heme d and inverted heme b (i.e. His-IV heme orientation). The N_{δ} atom of this essential His is hydrogen-bonded to a conserved Ser, and to the main chain carbonyl group of a Thr (Figure 7), thus favouring the δ tautomer of His (Nicholls, 2001). Besides, there is a conserved asparagine, which is not essential but enhances the reaction rate (Gao, 2008). The side chain carbonyl group of this Asn is

not involved in any interaction and, hence this Asn has been suggested to play a role in optimizing catalysis or in the exit of the products (Rovira, 2005 & 2006). Three conserved water molecules are also found: one hydrogen-bonded to the distal His and Asn, a second one connecting the distal Ser with one of the propionates of the heme, and a third one hydrogen-bonded to the distal Asn.

3.2. Classification

Phylogenetic analysis (Chelikani, 2004; Zámocky, 2008) showed that catalases are divided into three main clades (Table 1). Clade 1 contains eubacterial, algal and plant catalases of small subunit size and heme b as the prosthetic group. Clade 2 contains large subunit catalases from eubacteria and fungi, with an additional flavodoxin-like domain and mainly heme d as a cofactor. Clade 3 is the most abundant subfamily and is found in archaeobacteria, bacteria, fungi, protists, plants and animals. This clade contains small subunit catalases with heme b as a prosthetic group. Besides, some of these enzymes have been found to bind NADPH as a second “cofactor”, in order to protect the enzyme against inactivation at low H₂O₂ concentrations.

Table 1. Phylogenetic-based classification of catalases.

clade	subunit size	heme type	heme orientation	NADPH binding	representatives
clade 1	small	heme b	His-IV	–	<i>Pseudomonas syringae</i> catalase (CatF)
clade 2	large	heme d	His-IV	–	<i>Penicillium vitale</i> catalase (PVC) <i>E.coli</i> hydroperoxidase II (HPH)
		heme b	His-IV	–	<i>Aspergillus niger</i> catalase (ANC)
clade 3	small	heme b	His-III	+	<i>Micrococcus luteus</i> catalase (MLC) <i>Proteus mirabilis</i> catalase (PMC) <i>Bovine liver</i> catalase (BLC) <i>Human erythrocyte</i> catalase (HEC)
				–	<i>Helicobacter pylori</i> catalase (HPC)

3.3. Kinetic properties

- *Catalase activity*

The main activity of catalases is the dismutation of hydrogen peroxide into water and oxygen:



Reaction 1 (i.e. the *catalase* reaction) occurs in two steps (Schonbaum & Chance, 1976; Nicholls, 2001). In the first step (reaction 2), the Fe^{III}-porphyrin cofactor reacts with one molecule of H₂O₂, breaking the O-O bond. One of the peroxide oxygen atoms forms water and the second gets coordinated to the iron, yielding an intermediate named Compound I (Cpd I). In *Cpd I formation* two electrons are removed from the heme, one from the iron atom, which becomes Fe^{IV}, and the second from the porphyrin, which acquires cation radical character.



In the second step (reaction 3), Cpd I reacts with another molecule of H₂O₂. This reaction is known as the *catalatic* reaction, because only catalases are able to perform it with high efficiency. The H₂O₂ molecule transfers two protons to the axial oxo ligand, forming water, and two electrons to the heme. As a result, the two peroxide oxygen atoms become an oxygen molecule and the resting state of the enzyme is recovered.



In other words, in Cpd I formation (reaction 2), hydrogen peroxide acts as an oxidant, oxidizing catalase to Cpd I, whereas in the catalatic reaction (reaction 3) it acts as a reductant, recovering the resting state of catalase.

- *Kinetics of the catalase reaction*

Catalases are one of the most efficient enzymes known, with specific activities ranging from 20,700 to 273,800 units per milligram of protein and maximal turnover rates from 54,000 to 833,000 μmol H₂O₂ μmol heme⁻¹ s⁻¹ (Switala & Loewen, 2002)². This wide range of kinetic properties arises, at least in part, from subtle sequence and structural differences which influence substrate accessibility and product exhaust (catalases work at diffusion limit).

Small and large subunit catalases present different kinetic properties (Switala & Loewen, 2002). At high H₂O₂ concentrations, small subunit catalases exhibit lower velocities than predicted by the Michaelis-Menten equation because of inactivation by H₂O₂. By contrast, large subunit

² The values given should be regarded as apparent, because catalases do not exhibit Michaelis-Menten kinetics and do not become saturated with substrate.

enzymes are not inactivated as easily, and the observed velocities at high substrate concentrations are actually higher than predicted by the Michaelis-Menten equation (Switala & Loewen, 2002).

• *Peroxidase activity*

At low hydrogen peroxide concentrations and in the presence of some organic electron donors, catalase Cpd I may follow an alternative reductive pathway, resembling the catalytic cycle of peroxidases (Deiseroth & Dounce, 1970; Dunford, 1999; Veitch & Smith, 2001). In this *peroxidatic* pathway, Cpd I is one-electron reduced by an organic molecule (AH, reaction 4), yielding a new intermediate named Compound II (Cpd II). The transferred electron is accepted by the porphyrin, thus losing its radical character.



Cpd II can be reduced by another molecule of AH back to the resting state (reaction 5).

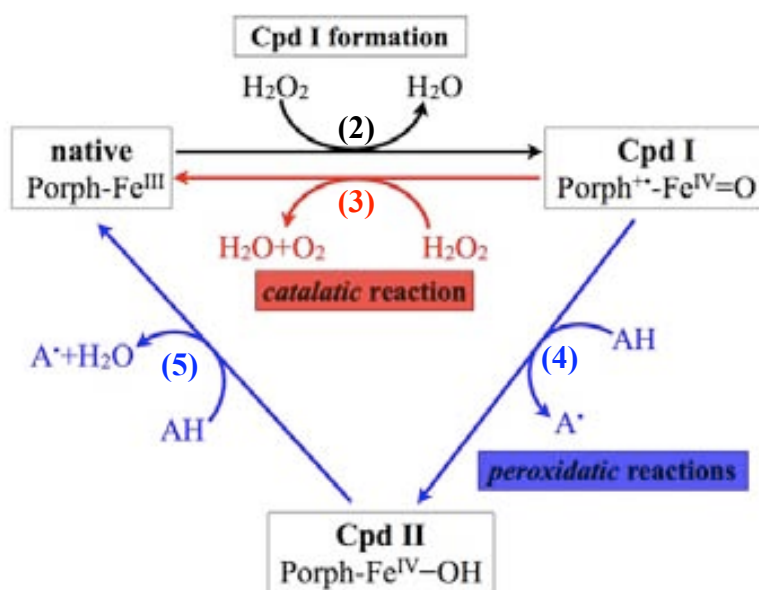


Figure 8. Main reactions performed by catalases.

Even though this peroxidatic pathway is not the main activity of catalases, it may become important in case H₂O₂ is not readily available and thus the catalytic reaction (reaction 3) slows down (deGroot, 2006; Kirkman & Gaetani, 2006). Using this two consecutive one-electron reductions, the enzyme is able to maintain the H₂O₂ consumption (by reaction 2), although without O₂ production, since reaction 3 is replaced by reactions 4 + 5 (see Figure 8).

Small subunit and large subunit catalases present different peroxidatic properties. Large subunit catalases exhibit much lower peroxidatic activities and appear not to form Cpd II at all (Kikuchi-Torii, 1992; Obinger, 1997; Chelikani, 2005). Whereas Cpd I of small subunit catalases, such as *Bovine Liver* catalase (BLC) or *Micrococcus luteus* catalase (MLC), is easily converted to Cpd II by treatment with ferrocyanide or ascorbate (i.e. AH), Cpd I of large subunit catalases, such as *E.coli* hydroperoxidase II (HPH), apparently is not reduced to Cpd II under the same conditions.

- *Formation of protein radicals*

When both H₂O₂ and AH reductants are absent, stalled Cpd I of some small subunit catalases is barely stable, and spontaneously evolves to another intermediate, named Compound I* (Cpd I*). A protein residue (aa, Tyr or Trp) transfers an electron to the heme, quenching the porphyrin cation radical and giving rise to an oxoferryl-protein radical intermediate (reaction 6) (Hillar, 1994; Ivancich, 1996).



Cpd I* formation (reaction 6) is very similar to Cpd II formation in the peroxidatic pathway (reaction 4). The only difference is the electron donor that reduces the porphyrin cation radical: an *exogenous* molecule (AH) in reaction 4, or an *endogenous* donor (a protein residue) in reaction 6.

Formation of protein radicals has been denoted in the literature as *radical migration* (from the porphyrin to the protein) (Hillar, 1994; Zámocky & Koller, 1999; Kirkman & Gaetani, 2006). It has also been detected in other heme proteins, such as cytochrome c peroxidase (CcP) (Sivaraja, 1999), catalase-peroxidases (KatG) (Ivancich, 2003; Jakopitsch, 2006; Singh, 2007; Colin, 2009), lactoperoxidase (LPO) (Fielding, 2008), cytochrome P450 (P450) (Spolitak, 2005, 2006 & 2008) and myoglobin (Mb) (Lardinois, 2004). In catalases, the propensity for forming protein radicals differ among small subunit and large subunit enzymes: Cpd I* formation has only been detected in some small subunit catalases, but not in large subunit enzymes (Nicholls, 2001).

- *Catalase inhibition*

At high H₂O₂ concentrations, inhibition of catalase is observed (Lardinois, 1995). Cpd I is one-electron reduced by superoxide (reaction 7), forming Cpd II, which in turn reacts with another molecule of hydrogen peroxide (reaction 8), yielding an inactive form of catalase, Compound III (Cpd III).





Cpd III may decay slowly to the resting state, losing superoxide, or it can lead to an irreversible inactivation of the enzyme (see Figure 9). As mentioned above, this inactivation by H_2O_2 occurs more easily for small subunit catalases than for large subunit enzymes.

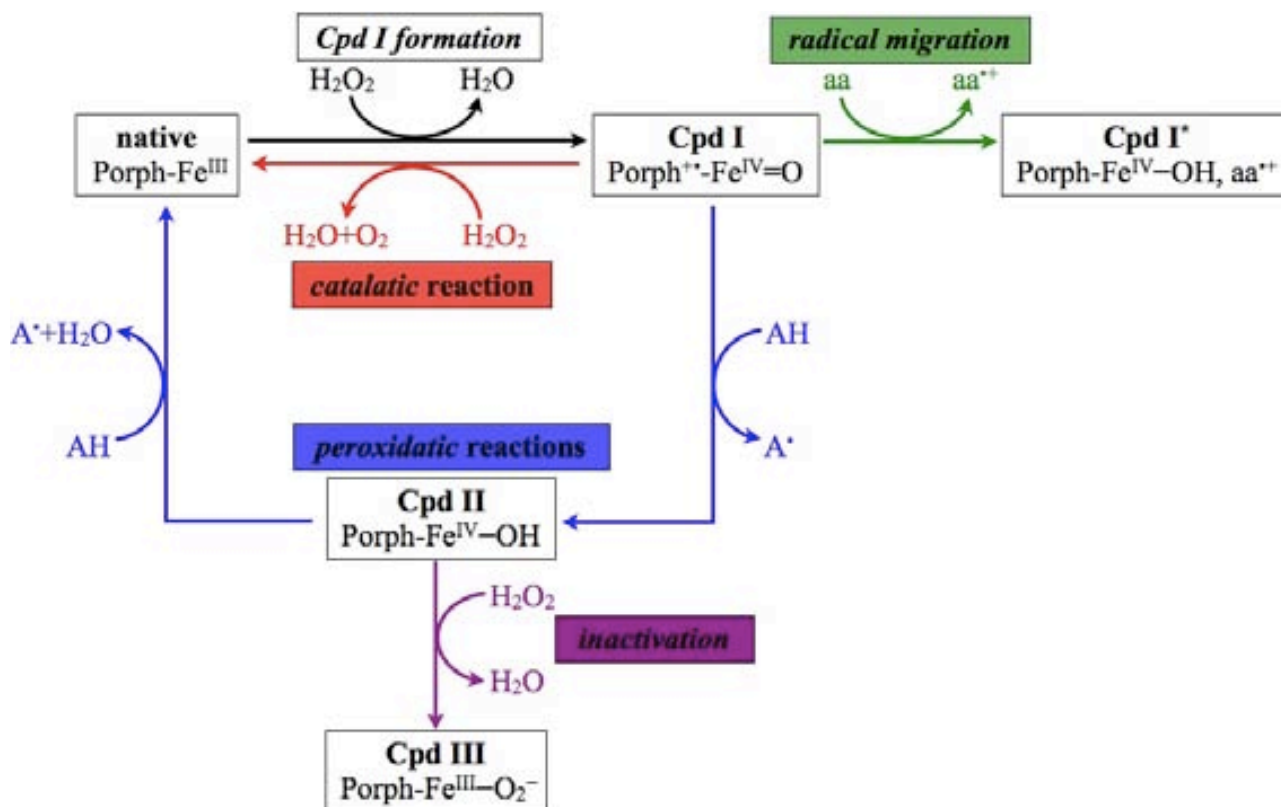


Figure 9. Side reactions of catalases. aa = Tyr, Trp.

4. OXIDIZED INTERMEDIATES

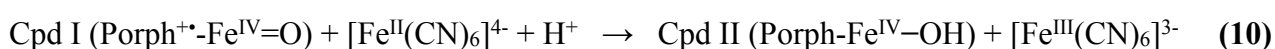
As mentioned previously, catalases form two main reaction intermediates: Cpd I, which is the primary active species, and Cpd II. Whereas in the catalase reaction (2 + 3) only Cpd I is observed, in the peroxidase reaction (2 + 4 + 5), both Cpd I and Cpd II are detected (Figure 8). Besides, under non-optimal conditions, another species is formed, Cpd I* (Figure 9). All these intermediates are one (Cpd II) or two (Cpd I and Cpd I*) oxidation equivalents above the resting state of the enzyme, and thus they will be hereafter called *oxidized intermediates*.

4.1. Experimental preparation

In order to characterize experimentally Cpd I and Cpd II, these intermediates are prepared in the laboratory by using pseudo-substrates (Nicholls, 2001; Maté, 2001). Cpd I is prepared by catalase treatment with an analog of the H₂O₂ substrate, peroxyacetic acid (PAA, reaction 9). PAA can oxidize catalase to Cpd I, but, in contrast to H₂O₂, it cannot reduce Cpd I back to the resting state (Jones & Middlemiss, 1972).



Further treatment of Cpd I with one-electron donors, such as ferrocyanide (reaction 10) or ascorbate (reaction 11), forms Cpd II (Kikuchi-Torii, 1982; Obinger, 1997; Nicholls, 2001):



Alternatively, in some small subunit catalases, Cpd I prepared with PAA is seen to spontaneously evolve to Cpd I*, in the absence of any added external reducing agent (Hillar, 1994 ; Zámocky & Koller, 1999; Nicholls, 2001; Kirkman & Gaetani 2006). This has been interpreted as the reduction of the porphyrin cation radical by an endogenous protein residue (reaction 6).

4.2. Characterization of the electronic structure

The electronic structure of these Compounds has been studied by UV-visible spectroscopy as well as Electron Paramagnetic Resonance (EPR).

- *UV-visible spectroscopy*

The typical UV-visible spectrum of a heme b-containing catalase is shown in Figure 10 (Nicholls, 2001). The native enzyme and the Cpd I and Cpd II intermediates can be easily distinguished by their different colours (brown, green and red, respectively), arising from the different oxidation state of the heme group in each species. Taking the native enzyme (Por-Fe^{III}) as the reference, Cpd I (Por^{+•}-Fe^{IV}=O) is two oxidation equivalents above the resting state, whereas Cpd II (Por-Fe^{IV}-OH) lacks just one oxidation equivalent.

The resting state catalase (Figure 10, brown line) exhibits a strong absorption maximum (Soret band) at 407-408 nm and smaller charge-transfer bands at 530 nm and 630 nm, i.e. it is

brown coloured (Nicholls, 2001; Maté, 2001). When converted to Cpd I (Figure 10, green line), the Soret band does not significantly shift, but its intensity decreases by $\sim 50\%$, and the charge-transfer bands are red-shifted to 600-700 nm, resulting in the characteristic green colour of Cpd I (Nicholls, 2001; Maté, 2001). By contrast, Cpd II (Figure 10, red line) is red coloured, due to the hypsochromic shift of the charge-transfer band, along with a red-shifted and less intense Soret band (Nicholls, 2001; Maté, 2001).

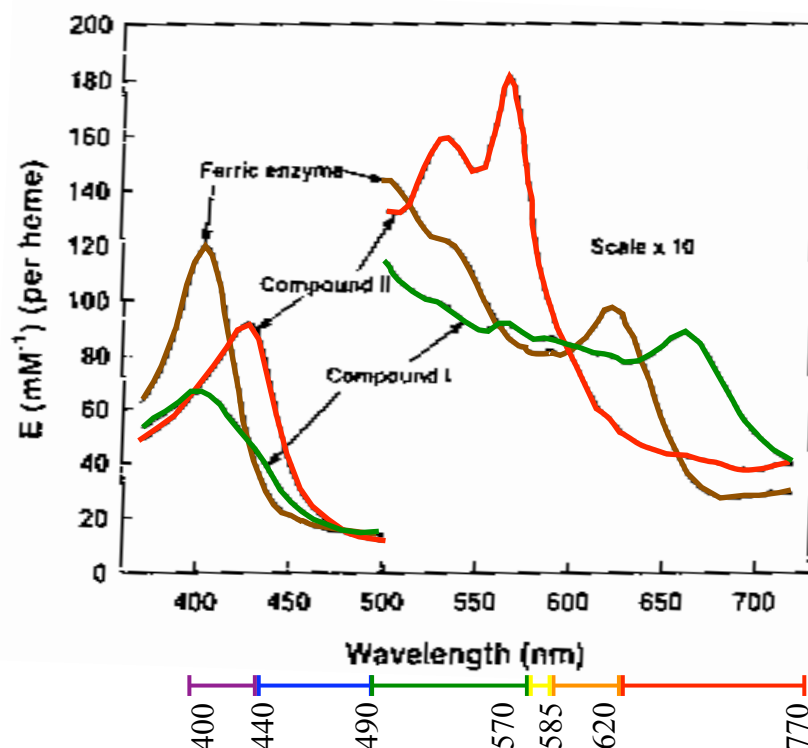


Figure 10. UV-visible spectra of *Bovine Liver* catalase (BLC). The following colouring was used: brown = native (ferric) enzyme, green = Cpd I, and red = Cpd II. Taken from reference (Nicholls, 2001).

In some small subunit catalases, it is observed that the typical spectrum of Cpd I is converted into a Cpd II-like spectrum in the absence of any added reducing agent (Murshudov, 2002; Alfonso-Prieto, 2007). This is assigned to the spontaneous evolution of stalled Cpd I to Cpd I* (see section 3.3.). Cpd I* is isoelectronic to Cpd II in the heme pocket (i.e. both contain Porph-Fe^{IV}-OH), and thus its spectral features are the same as Cpd II³. Hence, Cpd I* has been also denoted as Compound II* (Cpd II*) in the literature (Hillar, 1994; Zámocky & Koller, 1999; Kirkman & Gaetani, 2006). Nevertheless, we would rather use the notation Cpd I*, because the

³ The absorption bands for tyrosyl and tryptophanyl radicals (410 and 500-600 nm) are masked by the heme bands (Ivancich, 1997).

protein-heme complex is actually two oxidation equivalents above the resting state (Porph-Fe^{IV}-OH, aa⁺), as in Cpd I (Porph⁺-Fe^{IV}-OH, aa).

- *EPR spectroscopy*

The native enzyme and the Cpd I and Cpd II intermediates can also be studied by EPR, because they have unpaired electrons. EPR and ENDOR experiments on *Micrococcus luteus* catalase (MLC) (Benecky, 1993) or *Proteus mirabilis* catalase (PMC) (Ivancich, 1997) show that the native enzyme (Figure 11a, top) exhibits transitions at $g_y = 6.58$ and $g_x = 5.56$, characteristic of a high-spin ($S = 5/2$) ferric iron. When converted by PAA into Cpd I (Figure 11a, bottom), the ferric heme signal almost disappears and it is replaced by a weak signal at $g = 3.34$, together with the appearance of a sharp new signal at $g = 2$. This is interpreted as Cpd I having two unpaired electrons in the oxoferryl moiety ($^3[\text{Fe}^{\text{IV}}=\text{O}]$), in ferromagnetic interaction with another delocalized over the porphyrin ring ($^2[\text{Porph}^+]$), resulting in a total quartet spin state ($S = 3/2$) (Benecky, 1993). By contrast, when Cpd II is formed, the EPR becomes silent, because the ferryl ($^3[\text{Fe}^{\text{IV}}=\text{O}]$) signal is too weak and the porphyrin cation radical has been reduced ($^1[\text{Porph}]$).

Different from MLC and PMC, when BLC is treated with PAA at 0°C (Figure 11b), first the typical porphyrin-based radical is formed, followed by the appearance of a signal characteristic of a tyrosyl radical (Ivancich, 1996). This indicates an electron transfer from this protein residue to the porphyrin cation radical, resulting in a Cpd I* intermediate (see section 3.3.). Migration of the porphyrin radical into the protein has also been detected by EPR in other heme proteins such as CcP (Sivaraja, 1999), KatG (Ivancich, 2003; Jakopitsch, 2006; Singh, 2007; Colin, 2009), LPO (Fielding, 2008), P450 (Spolikat, 2005, 2006 & 2008) and Mb (Lardinois, 2004). Cpd I* is isoelectronic to Cpd II in the heme pocket (i.e. both contain Porph-Fe^{IV}-OH). Therefore, in UV-visible spectroscopy Cpd I* and Cpd II show the same spectral features (i.e. they are red-coloured), because the heme group (i.e. the main chromophore) has the same electronic configuration in both cases. Nevertheless, considering the complete protein-heme complex, Cpd I* actually lacks two electrons compared to the native enzyme, one from the heme (Porph-Fe^{IV}-OH) and the other from the protein (aa⁺), whereas Cpd II lacks just the electron from the heme (Porph-Fe^{IV}-OH). Because EPR can detect protein radicals, this technique can be used to distinguish between Cpd I* and Cpd II (i.e. to know the oxidation state of the complete protein-heme complex).

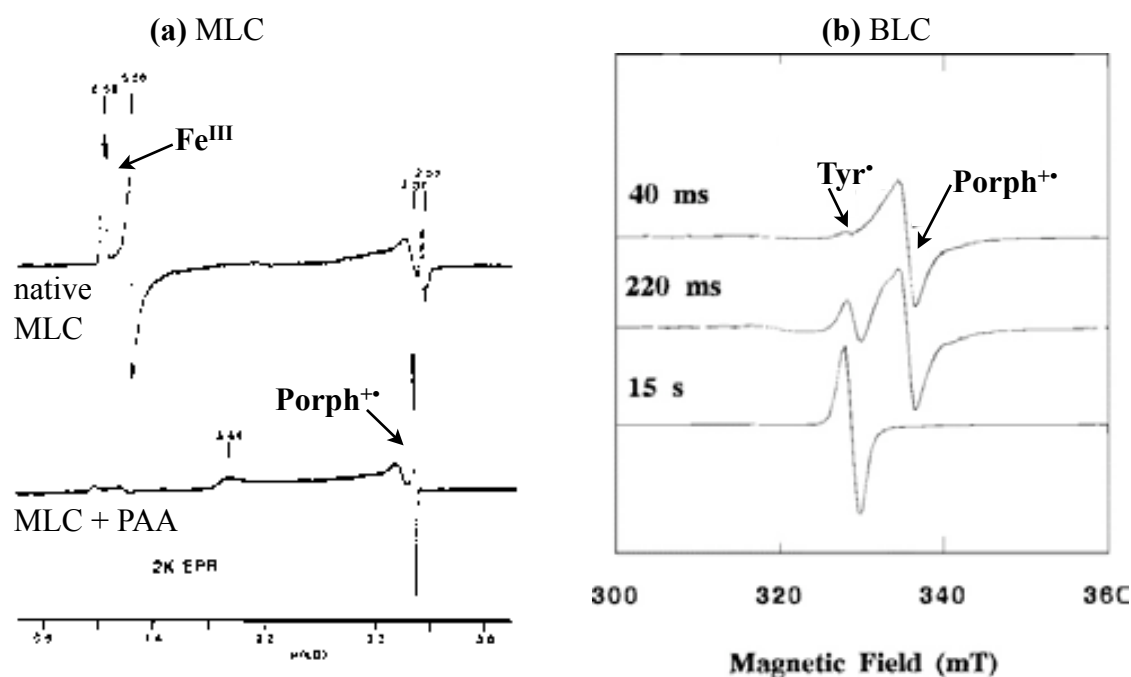


Figure 11. (a) Low-temperature absorption-derivative EPR of *Micrococcus luteus* catalase and its peroxyacetic acid oxidation product. (b) Reaction of BLC with PAA as monitored by the 4.2 K EPR spectra. The spectra were obtained on BLC samples for which the reaction was freeze-quenched at different times. Taken from references (Benecky, 1993) and (Ivancich, 1996), respectively.

- *Molecular orbitals*

We have seen that combination of UV-visible and EPR spectroscopies is necessary for an ambiguous identification of the electronic structure of catalase intermediates. This electronic structure can be rationalized in terms of the molecular orbitals shown in Figure 12.

All Cpd I, Cpd I* and Cpd II have two unpaired electrons located in the $\pi^*_{\text{Fe-O}}$ orbitals. Besides, Cpd I has an additional unpaired electron in a half-filled porphyrin orbital, whereas in Cpd II and Cpd I* both porphyrin orbitals are doubly occupied, because the porphyrin cation radical has been reduced by either an exogenous (AH) or an endogenous (aa) donor.

The spin density of the porphyrin cation radical in Cpd I has been often discussed in terms of originating from a half-filled porphyrin orbital with either A_{2u} or A_{1u} symmetry (Ghosh, 1994; Kuramochi, 1997; Hirao, 2006). There are two high-lying porphyrin orbitals (Figure 12), which are degenerated for a D_{4h} porphyrin (Liao & Scheiner, 2002). The a_{2u} orbital has contributions from the pyrrole nitrogens and the meso carbon atoms, whereas the a_{1u} orbital from the α and β pyrrole carbon atoms. Depending on which of the two orbitals is higher in energy (i.e the HOMO), the

electron removed from the porphyrin during Cpd I formation is abstracted from either the a_{2u} or the a_{1u} orbital, resulting in a porphyrin cation radical with either A_{2u} or A_{1u} symmetry, respectively.

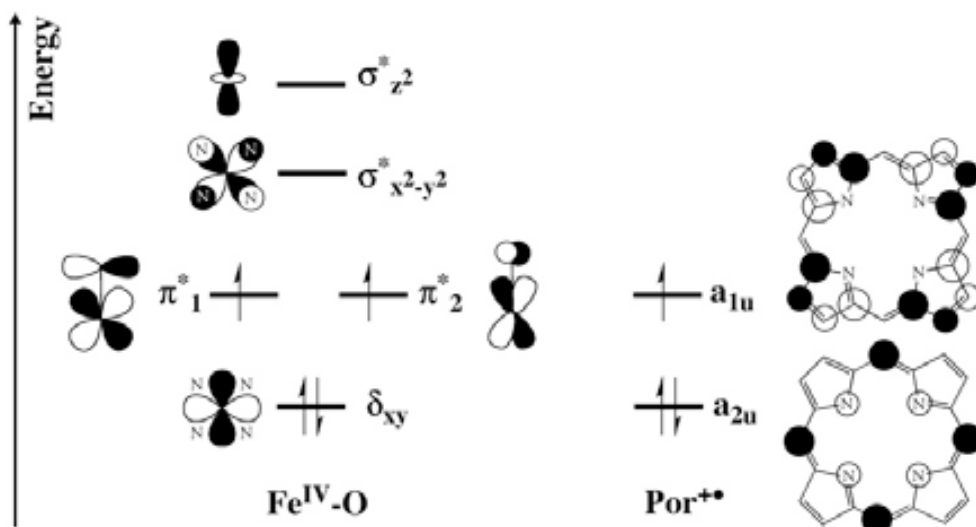


Figure 12. High-lying occupied and low-lying virtual orbitals of Cpd I for a Por- $\text{Fe}^{\text{IV}}=\text{O}$ system with C_{4v} symmetry, adapted from reference (de Visser, 2003). The π^*_1 and π^*_2 Fe-O orbitals result from the combination of the iron d_{xz} and d_{yz} orbitals with the p_x and p_y orbitals of the oxygen atom. The porphyrin high-lying orbitals should be named a_2 and a_1 (C_{4v} symmetry), but we keep the same nomenclature as for a totally symmetric D_{4h} porphyrin (a_{1u} and a_{2u}), as done in the literature.

4.3. Determination of the protonation state of the ferryl oxygen

The protonation state of the oxoferryl group can be discriminated by the Fe-O distance, measured by either X-Ray crystallography or Extended X-Ray Absorption Fine Structure (EXAFS) spectroscopy. A protonated oxoferryl group (i.e. Fe-OH) shows a longer distance (calculated at 1.77-1.81 Å, see Chapter III, Table 5) than a non-protonated oxoferryl group (i.e. Fe=O, calculated at 1.63-1.70 Å, see Chapter III, Table 5).

As can be seen in Table 2, Cpd I shows a short Fe-O distance (1.65-1.76 Å) and thus it is accepted that it contains an oxoferryl moiety ($\text{Fe}^{\text{IV}}=\text{O}$). On the contrary, the protonation state of Cpd II has been under discussion (Berglund, 2002; Nilsson, 2004; Rovira, 2005; Silaghi-Dumitrescu, 2004; Green, 2004; Hersleth, 2006; Green, 2006; Behan, 2006; Stone, 2006). Although this issue is not yet fully clarified, it is believed that Cpd II of some heme-containing proteins bears a hydroxoferryl moiety ($\text{Fe}^{\text{IV}}-\text{OH}$), instead of the traditional oxoferryl group, because of the long Fe-

O distances observed (1.82-1.93 Å). Cpd I*, being isoelectronic with Cpd II in the heme active site, is expected to bear a protonated oxoferryl group as well. Indeed, experimental data shows a long Fe-O bond length (1.80-1.87 Å, Table 2), consistent with a Fe^{IV}-OH group.

Table 2. Experimental Fe-O bond distances in the oxoferryl intermediates of heme proteins.

Compound I (Cpd I)		
protein	Fe-O length (Å)	reference
<i>Proteus mirabilis</i> catalase (PMC)	1.76	Andreoletti, 2003
<i>Penicillium vitale</i> catalase (PVC)	1.72	Alfonso-Prieto, 2007
Horse radish peroxidase (HRP)	1.65	Berglund, 2002
chloroperoxidase (CPO)	1.65	Stone, 2005
cytochrome P450 (P450)	1.65	Schlichting, 2000
Compound I* (Cpd I*)^a		
protein	Fe-O length (Å)	reference
<i>M. lysodeikticus</i> catalase (MLC)	1.87	Murshudov, 2002
<i>H. pylori</i> catalase (HPC)	1.80 - 1.85	Alfonso-Prieto, 2007
cytochrome c peroxidase (CcP)	1.67 1.87	Chance, 1986 Bonagura, 2003
<i>B. pseudomallei</i> KatG (BpKatG)	1.88	Ivancich, 2003
Compound II (Cpd II)		
protein	Fe-O length (Å)	reference
horseradish peroxidase (HRP)	1.64 1.70 1.93	Wasinger, 2003 Daiber, 2000 Berglund, 2002
myoglobin (Mb)	1.69 1.92	Chance, 1986 Hersleth 2002
chloroperoxidase (CPO)	1.82	Green, 2004
cytochrome P450 (P450)	1.82	Newcomb, 2008

Nevertheless, it should be noted that there is a discrepancy among the reported values for HRP and Mb Cpd II (Table 2). During crystal data collection, electrons generated by X-Ray irradiation can reduce Cpd I to Cpd II or Cpd II to $\text{Fe}^{\text{III}}\text{-OH}$ (Berglund, 2002; Hersleth, 2008), creating a mixture of oxidation states that complicates the determination of the Fe-O bond distance. UV-Vis spectroscopy has been used to monitor whether such *photoreduction* occurs, because the decrease in the oxidation state is accompanied by a color change (see section 4.2.). The pH at which the experiment is carried out can also influence the protonation state of the ferryl oxygen. For instance, Mössbauer experiments on PMC Cpd II (Horner, 2006 & 2007) have detected both a protonated (Fe-OH) and unprotonated (Fe=O) Cpd II species, whose ratio changes with pH.

5. OPEN QUESTIONS

Since Loew first used the term *catalase* in 1900, catalases have been the subject of many biochemical, spectroscopic and structural studies. Nevertheless, there are several questions that remain open in the particular case of monofunctional heme catalases (hereafter *catalases*):

- *Which are the effects of the heme modification on the reaction intermediates?*

Catalases may contain either heme b or heme d as a cofactor. Although heme d-containing catalases (such as *Penicillium vitale* catalase, PVC) operate via the same reaction cycle as heme b-containing enzymes (e.g. *Helicobacter pylori* catalase, HPC), it is not known whether the heme modification affects the structure and / or the electronic configuration of the principal intermediate (Compound I) and the ones formed under non-optimal conditions (Compound II and Compound I*).

- *Are catalase Compound II and Compound I* protonated?*

It is not yet fully clarified whether Compound II (Cpd II) is protonated in all heme proteins (i.e. it bears a hydroxoferryl moiety, $\text{Fe}^{\text{IV}}\text{-OH}$, instead of the canonical oxoferryl group, $\text{Fe}^{\text{IV}}\text{=O}$). Therefore, it would be interesting to probe whether Cpd II and Cpd I* are protonated in catalase and how protonation is influenced by the type of heme.

- *Which is the structure and electronic configuration of Compound I formed upon reaction with organic peroxides?*

Compound I (Cpd I) can be prepared in the laboratory by catalase treatment with peroxyacetic acid (PAA). However, interpretation of the heme oxidation state and the protonation state of the ferryl oxygen is often complicated by side reactions (typically proton and electron transfers) of this extremely reactive species. The combination of theoretical modeling with experimental studies may help to assign the actual structure and electronic configuration of the species formed.

- *Why do heme d-containing catalases not form Cpd II and I*?*

The different propensity for Cpd II formation of heme b- and heme d-containing catalases suggests that they may have different Cpd I / Cpd II redox potential. Nevertheless, other factors could play a role (protonation of the ferryl oxygen, abundance and distribution of electron-donating protein residues, ...). Understanding of this different behaviour may provide clues about the different reactivity of the two types of catalases.

- *Which is the molecular mechanism of the catalase reaction?*

Even though the catalase reaction has been known since 1940s and two experimental proposals have been put forward (Fita-Rossmann and Watanabe-Kato), the detailed mechanism of Cpd I reduction by H₂O₂ has yet to be elucidated. In particular, it is not known which is the role of the distal histidine in the reaction and how are the two electrons (*plus* two protons) of H₂O₂ transferred to Cpd I. A detailed mechanistic proposal should also explain why the catalase reaction is much slower in other heme proteins (e.g. myoglobin and peroxidases) than in catalases.

- *Which is the spin state of the molecular oxygen released during the catalase reaction?*

Using spin conservation arguments, some authors have suggested that the catalase reaction generates singlet oxygen. However it would not make biological sense to release large amounts of singlet oxygen out of the heme pocket, because it is a very powerful oxidant. Therefore, the validity of the arguments used to predict the spin state of the molecular oxygen released by catalase needs to be reassessed.

OBJECTIVES

OBJECTIVES

The present thesis is aimed at unraveling the mechanism of the catalase reaction and at understanding the effect of the heme modification on the properties of the catalase intermediates. *Helicobacter pylori* catalase (HPC) and *Penicillium vitale* catalase (PVC) have been used as examples of heme b- and heme d-containing catalases, respectively.

The following objectives have been pursued:

- Investigate the effect of the heme modification on the structure and electronic configuration of the catalase intermediates.
- Determine the protonation state of catalase Compound II and Compound I*.
- Assign the actual configuration of the species present in the crystal structures of oxidized HPC and PVC.
- Find out the origin of the different behaviour of HPC and PVC with respect to the formation of Compounds I* and II.
- Unravel the mechanism of the catalase reaction at a molecular level.
- Assess the validity of the arguments used to predict the spin state of the molecular oxygen released by catalase and ascertain whether it is produced as singlet or triplet O₂.

CHAPTER II

COMPUTATIONAL METHODS

1. CAR-PARRINELLO MOLECULAR DYNAMICS (CPMD)

The Car-Parrinello methodology (Car & Parrinello, 1985) is an approach to perform *ab initio* molecular dynamics (AIMD) based on Density Functional Theory (DFT).

1.1. Density functional theory (DFT)

DFT provides a framework to obtain the total energy of a polyatomic system given their atomic coordinates $\{\vec{R}_N\}$. According to *Hohenberg-Kohn theorems* (Hohenberg & Kohn, 1967), the ground state energy of a system of interacting electrons subject to an external potential $V(r)$ is a unique functional of the electron density, i.e. and it can be obtained by minimizing the energy functional with respect to the density,

$$E^{DFT} = \min_{\rho(\vec{r})} E[\rho(\vec{r})] \quad (1)$$

where the energy functional can also be expressed in terms of *single-electron Kohn-Sham (KS) orbitals* $\Psi_i(\vec{r})$ (Kohn & Sham, 1965):

$$E^{DFT} = \min_{\{\Psi_i\}} E^{KS}[\{\Psi_i(\vec{r})\}, \{\vec{R}_N\}] \quad (2)$$

1.2. *Ab initio* molecular dynamics (AIMD)

Assuming that the *Born–Oppenheimer approximation* holds, i.e. the electrons are moving in the field of fixed nuclei, *ab initio molecular dynamics (AIMD)* (Marx & Hutter, 2000) can be viewed as a series of DFT calculations at different instants of time, each one for a different set of atomic positions $\{\vec{R}_N\}$. These atomic positions are related by the Newton's equations of motion (e.o.m.),

$$M_N \ddot{\vec{R}}_N = -\frac{\partial E_{el}}{\partial \vec{R}_N} \quad (3)$$

which can be derived from the Lagrangian:

$$L = E_N^{kin} - E_{el} \quad (4)$$

where

$$E_N^{kin} = \sum_N \frac{1}{2} M_N \dot{\vec{R}}_N^2 \quad (5)$$

is the kinetic energy of the nuclei, M_N and $\{\vec{R}_N\}$ are nuclear masses and positions, respectively, and the electronic energy E_{el} is their potential energy, i.e. E^{DFT} , given by Equation 2.

The basic AIMD procedure (Figure 1) consists in repeating two main steps: i) for a given set of atomic coordinates $\{\vec{R}_N\}$, the total energy E^{DFT} is calculated by minimizing the density functional, ii) the Newton's equations of motion are solved to obtain the new nuclear coordinates.

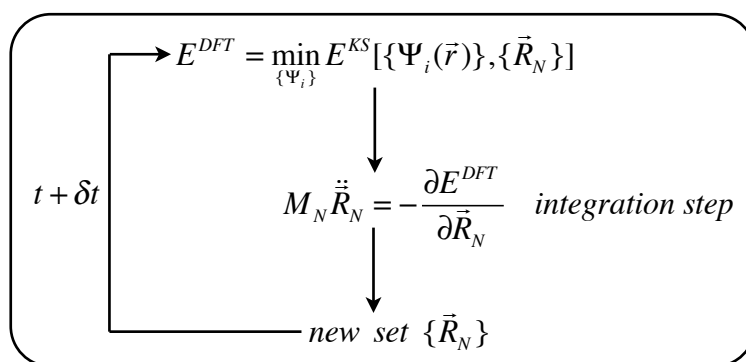


Figure 1. Schematic diagram of a *ab initio* molecular dynamics (AIMD). Adapted from (Rovira, 2005).

1.3. Car-Parrinello molecular dynamics (CPMD)

In contrast to this *Born-Oppenheimer molecular dynamics (BOMD)*, in the *Car-Parrinello method (CPMD)* (Car & Parrinello, 1985) both electrons and nuclei are evolved simultaneously, by including also the electrons as classical particles in an extended Lagrangian:

$$L = E_N^{kin} + E_{el}^{kin} - E^{KS} + \sum_{ij} \Lambda_{ij} \left[\int d\vec{r} \Psi_j^*(\vec{r}) \Psi_j(\vec{r}) - \delta_{ij} \right] \quad (6)$$

where $E_{el}^{kin} = \sum \mu \int d\vec{r} |\dot{\Psi}_i(\vec{r})|^2$ is a fictitious classical kinetic energy term associated with the electronic subsystem $\Psi_i(\vec{r})$, μ is a parameter that controls the timescale of the electronic motion, E^{KS} is the electronic potential energy calculated with DFT and Λ_{ij} are Lagrangian multipliers that

impose the orthonormality constraints between the orbitals. Therefore, the total energy of the CP Lagrangian, which is a constant of motion, is given by:

$$E_{tot}^{CP} = E_N^{kin} + E_{el}^{kin} + E^{KS} \quad (7)$$

and the equations of motions are:

$$\mu \ddot{\Psi}_i = \frac{\partial E^{KS}}{\partial \Psi_i^*} + \sum_j \Lambda_{ij} \Psi_j(\vec{r}) \quad (8a)$$

$$M_N \ddot{\vec{R}}_N = \frac{\partial E^{KS}}{\partial \vec{R}_N} \quad (8b)$$

The integrations of equations (8a) and (8b) provides the time evolution of not only the atomic positions $[\vec{R}_N(t)]$, but also the KS orbitals $[\Psi_i(\vec{r}, t)]$. In practice, because the orbitals are expanded in a basis set, what is obtained from the integration is the value of the expansion coefficients at each time instant.

Therefore, the basic CPMD procedure (Figure 2) is the same as for AIMD (Figure 1), except that (i) the electronic energy only needs to be calculated at the beginning of the simulation, because the electrons also evolve in time, following the nuclear motion, (ii) the equations of motion have to be integrated for both nuclei and electrons, and (iii) in each MD step we obtain a new set of orbital coefficients, besides the new nuclear positions.

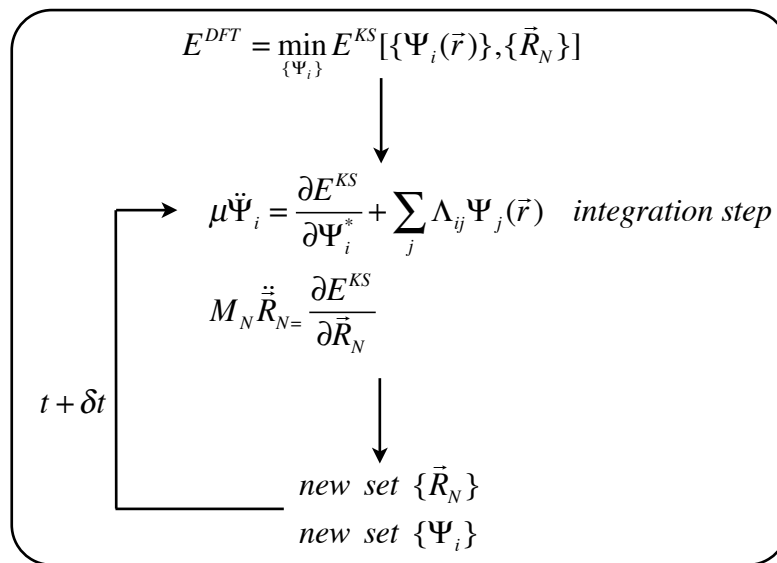


Figure 2. Schematic diagram of a Car-Parrinello molecular dynamics. Adapted from (Rovira, 2005).

The electronic energy obtained at a given instantaneous structure $\{\vec{R}_N\}$ generally differs slightly from the exact DFT energy. However, if the energy exchange between the electronic and nuclear subsystems is small, the trajectory generated will be identical to the one obtained in a BOMD simulation (Marx & Hutter, 2000, and references therein). This decoupling of the two subsystems can be achieved by a suitable choice of *the fictitious electronic mass* μ , such that the frequencies of the electrons are well separated from the nuclear frequencies. In that case, the electronic subsystem remains on the BO surface, oscillating around the ground state, and the forces on the atoms are practically the same as those in a BOMD (Marx & Hutter, 2000).

It can be demonstrated (Marx & Hutter, 2000 and references therein) that, provided that the electrons are initially in the ground state and μ is appropriately chosen, they will follow adiabatically the nuclear motion, remaining very close to the instantaneous ground state. Therefore, in a CP simulation, the electronic energy only needs to be calculated at the beginning of the simulation, and not at each step as in BOMD. By contrast, the simulation time step is shorter (0.1-0.2 fs) compared to BOMD (~1 fs), in order to describe properly the faster movement of the electrons.

1.4. Plane waves basis set

In a Car-Parrinello MD, it is computationally convenient to use *plane waves (PW)* as the basis set in which the KS orbitals are expanded (Marx & Hutter, 2000; Rovira, 2005). PWs can be expressed as:

$$\Psi_i(\vec{r}) = \frac{1}{\Omega^{1/2}} \sum_G^{G_{\max}} c_{ij} \exp(iG_j \vec{r}) \quad (9)$$

where Ω is the volume of the cell, G is the plane wave momentum, c_{ij} are the coefficients of the basis set expansion (which are updated at each MD step), and G_j are the reciprocal vectors (periodic boundary conditions are assumed). PW basis sets are denoted by an energy value E_{cut} , which is related to the maximum G value of the PW expansion (G_{\max}). The number of plane waves N_{PW} can be approximated as:

$$N_{\text{PW}} \approx \frac{\Omega}{6\pi^2} E_{\text{cut}}^{3/2} \quad (10)$$

Compared to the popular Gaussian functions, PWs are not centered at the atoms but extend throughout all the space, and thus they do not suffer from basis set superposition error (BSSE). However, PWs require the use of pseudopotentials to describe the effect of the core electrons (see section 1.5.).

1.5. Pseudopotentials

Plane waves are highly inefficient to describe the core electron wave functions. Indeed, they exhibit sharp spatial oscillations in closeness of the atomic nuclei, and a very large set of plane waves is required for an accurate chemical description. On the other hand, the core levels are well separated in energy from the valence electrons, and they do not play a role in the chemical bonding properties of the system. Thus, the core electron orbitals can be frozen in the KS equations and only the valence electrons are described explicitly. Their interactions with nuclei and core electrons are described by using effective potentials, the *pseudopotentials* (Marx & Hutter, 2000). The pseudopotential used throughout this thesis are of the norm-conserving type (Hamann, 1989) and have been generated using the recipe of Martins and Troullier (Troullier & Martins, 1991).

2. QUANTUM MECHANICS / MOLECULAR MECHANICS (QM/MM)

2.1. General overview

Quantum Mechanics / Molecular Mechanics (QM/MM) is a hybrid methodology which permits first-principles calculations within the reactive center of a system in a classical force field environment, thus combining the advantages of the two methods (Warshel & Levitt, 1976). Whereas classical force fields allow to treat big systems, first-principles methods are needed to study electronic reorganizations, such those that occur in certain protein-ligand interactions and chemical reactions.

In QM/MM molecular dynamics, the overall system is divided in two regions: the QM region, (i.e. the active site) is treated with AIMD, whereas the rest of the system (i.e. the protein and solvent) is described by classical MD (Figure 3). The total energy of the hybrid system can be thus written as:

$$E = E_{QM} + E_{MM} + E_{QM-MM} \quad (11)$$

where E_{QM} is the energy for the quantum subsystem, E_{MM} is the energy for the classical subsystem and E_{QM-MM} contains the interactions between the two regions.

In this thesis we have used the *QM/MM methodology developed by Laio, Vandevonede and Röthlisberger* (Laio, 2002a), which combines Car-Parrinello molecular dynamics with the classical molecular dynamics based on the GROMOS or AMBER force fields (hereafter CP QM/MM MD). E_{QM} is described by DFT and the potential created by the MM atoms, which polarizes the electronic density of the QM region, is included in the energy functional as an external potential. E_{MM} is computed using the AMBER parameters with the GROMOS force field equation. E_{QM-MM} is calculated as:

$$E_{QM-MM} = E_{QM-MM}^{bond} + E_{QM-MM}^{non-bond} \quad (12)$$

where E_{QM-MM}^{bond} and $E_{QM-MM}^{non-bond}$ are the bonding (section 2.2.) and non-bonding (section 2.3.) interactions between the QM and MM regions, respectively.

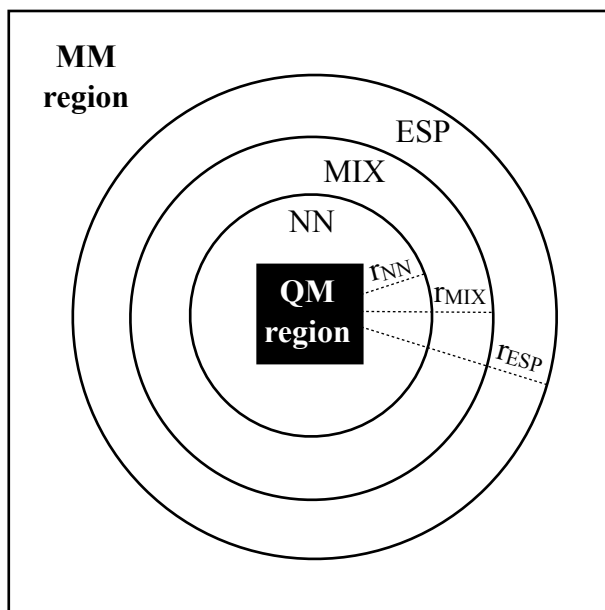


Figure 3. Schematic representation of the regions in a CPMD QM/MM calculation. QM= region described at a quantum mechanical level, and MM = region treated with classical mechanics. Within the MM region, four different layers are defined: (i) NN = MM atoms within $r < r_{NN}$, (ii) MIX = MM atoms within $r_{NN} < r < r_{MIX}$, (iii) ESP = MM atoms within $r_{MIX} < r < r_{ESP}$, and (iv) MM atoms outside r_{ESP} .

2.2. QM-MM boundary. Bonding QM-MM interactions.

The partitioning between the QM and MM regions have to be chosen such that it is as far as possible from the region of interest, e.g. from the atoms involved in the chemical reaction to be studied. In most cases this partitioning occurs at a chemical bond, and thus special care has to be taken to make sure that (i) the electronic structure of the QM subsystem is a good representation of an all QM calculation and (ii) the structure in the boundary region is preserved.

In this thesis two methods have been used to saturate the QM region: the link atom pseudopotential and the capping hydrogen. In the *link atom pseudopotential* approximation (von Lilienfeld, 2005), a scaled down pseudopotential with the required valence change is assigned to the boundary atom. E.g. when cutting through a single carbon-carbon bond, the link atom pseudopotential, named C_{ps} , contains one single valence electron ($ZV = 1$, hydrogenoid pseudopotential). Besides, it is required to constraint the distance between the link atom and the QM neighbour atom to the equilibrium distance, in order to preserve the electronic structure in the center of the QM subsystem. For instance, the C_{ps} pseudopotential is parametrized to reproduce the characteristics of a C-C bond (i.e. it is an empirical pseudopotential). An alternative approximation is the saturation of the dangling bond with a *capping hydrogen*, i.e. an additional dummy hydrogen atom. Spurious electrostatic interactions between the capping hydrogen and close-by classical atoms are excluded from the QM/MM Hamiltonian according to reference (Laio, 2004).

The bonding interactions at the QM-MM interface are accounted by the classical force field. Bonded, angular and dihedral terms involving MM and QM atoms are treated as in the classical MM Hamiltonian. These terms permit to keep stable the geometry at the interface.

2.3. Non-bonding QM-MM interactions

The remaining electrostatic and steric contributions between non-bonded atoms are taken into account as follows (Laio, 2002a):

$$E_{QM-MM}^{non-bond} = E_{QM-MM}^{electrostatic} + E_{QM-MM}^{vanderWaals} = \sum_{i \in MM} q_i \int \frac{\rho(r)}{|r - r_i|} dr + \sum_{\substack{i \in MM \\ j \in QM}} V_{vdW}(r_{ij}) \quad (13)$$

where r_i is the position of the MM atom i with charge q_i , $\rho(r)$ is the total (electronic plus ionic) density of the quantum system, and V_{vdW} is the van der Waals potential. The first term describes the

electrostatic interaction between the total density with the atomic partial charges of the classical system, whereas the second term describes the van der Waals interaction between atoms i and j .

- *Electron spill-out*

The above scheme for calculating the electrostatic interactions suffers from the so-called *electron spill-out problem*, i.e. an anomalous rearrangement of the electron density that tends to localize on the classical point charges of the MM atoms nearby the interface region. This problem is particularly pronounced when using a plane waves basis set, which is not atom-centered.

To solve this problem, in CP QM/MM MD the point charges of the classical system are replaced by a charge distribution (v_i) (Laio, 2002a), so that the $1/r$ behavior is maintained for large r , whereas for r values shorter than the covalent radius of atom i (r_{ci}) the Coulomb potential goes to a finite value:

$$E_{QM-MM}^{electrostatic} = \sum_{i \in MM} q_i \int \rho(r) v_i(|r - r_i|) dr = \sum_{i \in MM} q_i \int \rho(r) \frac{r_{ci}^4 - r^4}{r_{ci}^5 - r^5} dr \quad (14)$$

- *Multilayer approach*

Another problem is the very high computational cost of the explicit calculation of the electrostatic term in a PW-based approach. To speed up the calculation, CP QM/MM MD uses a *multilayer approach*. The MM subsystem is divided in four different regions (Figure 3), in which the QM-MM electrostatic interactions are calculated differently. For the atoms within the first region (NN region, $r < r_{NN}$), the QM-MM electrostatic interaction is calculated explicitly (equation 13). In the second region (MIX region, $r_{NN} < r < r_{ESP}$) equation 13 is only applied for those MM atoms whose charge $> 0.1 e$. For the MM atoms within the MIX region with charge $> 0.1 e$ or within the ESP region ($r > r_{ESP}$) a classical Coulomb (charge-charge) potential is used:

$$E_{QM-MM}^{electrostatic} \approx \sum_{\substack{i \in MM \\ j \in QM}} \frac{q_i Q_j^{RESP}}{|r_i - r_j|} \quad (15)$$

where Q_j^{RESP} are *dynamically generated RESP (D-RESP) charges*¹ (Laio, 2002b) assigned to the QM atoms. Outside the outer layer ($r > r_{\text{ESP}}$, see Figure 3) the QM electronic density is simply described as a multipole expansion (up to quadrupolar order).

3. METADYNAMICS

Metadynamics is novel molecular dynamics based technique aimed at enhancing the sampling of the phase space and at estimating the free energy landscape (Laio & Parrinello, 2002; Laio & Gervasio, 2008). The algorithm is based on a dimension reduction, defining a set of *collective variables* (s) which enclose the essential modes associated with the transitions in the analyzed process.

3.1. Direct metadynamics

Let us consider (Laio & Gervasio, 2008) a system of atomic coordinates x which is moving under an interatomic potential $V(x)$ (Figure 4a). In a standard molecular dynamics simulation the system is oscillating in one of the minima of the energy surface and the crossing to the other minima is rather unlikely, because the barrier is higher than the thermal energy ($1/2 k_b T$). In other words, the crossing is a *rare event* that cannot be observed within the typical simulation times. In order to accelerate the exploration of the phase space we can use metadynamics. This technique is based on defining a collective variable s which is an explicit function of a subset of coordinates x' [$s = f(x')$], e.g. a distance or a coordination number.

The metadynamics simulation starts in one of the minima of the energy surface. At the beginning of the simulation, the force acting on the system is given by the gradient of the potential V :

$$f_i^V = -\frac{\partial V}{\partial r_i} \quad (16)$$

¹ The D-RESP charges are calculated as follows. First the electrostatic potential created by the QM electronic density is calculated at the positions of MM atoms within the NN region (instead of the surface of a sphere as in the standard ESP formulation). Second a fitting is performed to find the (ESP) charges that better reproduce this potential. This fitting is carried out with a harmonic constraint such that the charges do not deviate from a reference value, which is taken as the Hirshfeld charges obtained from the QM electronic density. The resulting charges are called RESP charges. Note that the electrostatic potential due to the QM electronic density has to be computed anyway at every time step. Therefore R-RESP charges can be computed “on the fly” with no additional computational cost. Hence, they are called dynamically generated RESP (D-RESP) charges.

After a time interval t' , a small Gaussian-like repulsive potential term (V') is added, centered at the value of s at time t' (Figure 4b). This is repeated every time interval t' along the MD simulation, such that at time t the total potential is the sum of the interatomic potential V and the sum of the V' terms added up to that time, i.e. V_G :

$$V_T = V + V_G \quad \text{where} \quad V_G = \sum_{t'} w \exp\left(-\frac{[s(t) - s(t')]^2}{2(\delta s)^2}\right) \quad (17)$$

where w is the height of the Gaussian potential term, δs is its width and V_G is the *history-dependent potential* (i.e. the number of Gaussian terms added depends on the time passed). As a consequence, the force acting on the system is now the sum of two components, one coming from V and the other from V_G :

$$f_i^{V_T} = f_i^V + f_i^{V_G} = -\frac{\partial V}{\partial r_i} - \frac{\partial V_G}{\partial r_i} \quad (18)$$

When a Gaussian potential term is added to V_G , the total potential changes and hence the system needs to be equilibrated by using a thermostat. In addition, the resulting forces are also modified, and thus the metadynamics trajectory is not an equilibrium trajectory.

The added potentials V' progressively counterbalance the underlying free energy (Figure 4c), thus penalizing the regions of the phase space already explored. As a result, the system tends to escape from already visited points to another energy minimum, through the nearest and lowest-in-energy transition state. Hence, *metadynamics can accelerate the exploration of the phase space and the observation of rare events*. In other words, provided that the collective variables are properly chosen, the system will evolve by the same pathway that would have explored in a longer standard molecular dynamics.

Besides, *metadynamics can also be used for mapping the free energy surface (FES)* in the regions explored during the simulation as a function of s . The free energy surface can be estimated as the negative of the sum of the Gaussian potential terms (Laio & Parrinello, 2002):

$$G(s) = \lim_{t \rightarrow \infty} V_G(s, t) \approx \sum_{t'} w \exp\left[-\frac{[s(t) - s(t')]^2}{2(\delta s)^2}\right] \quad (19)$$

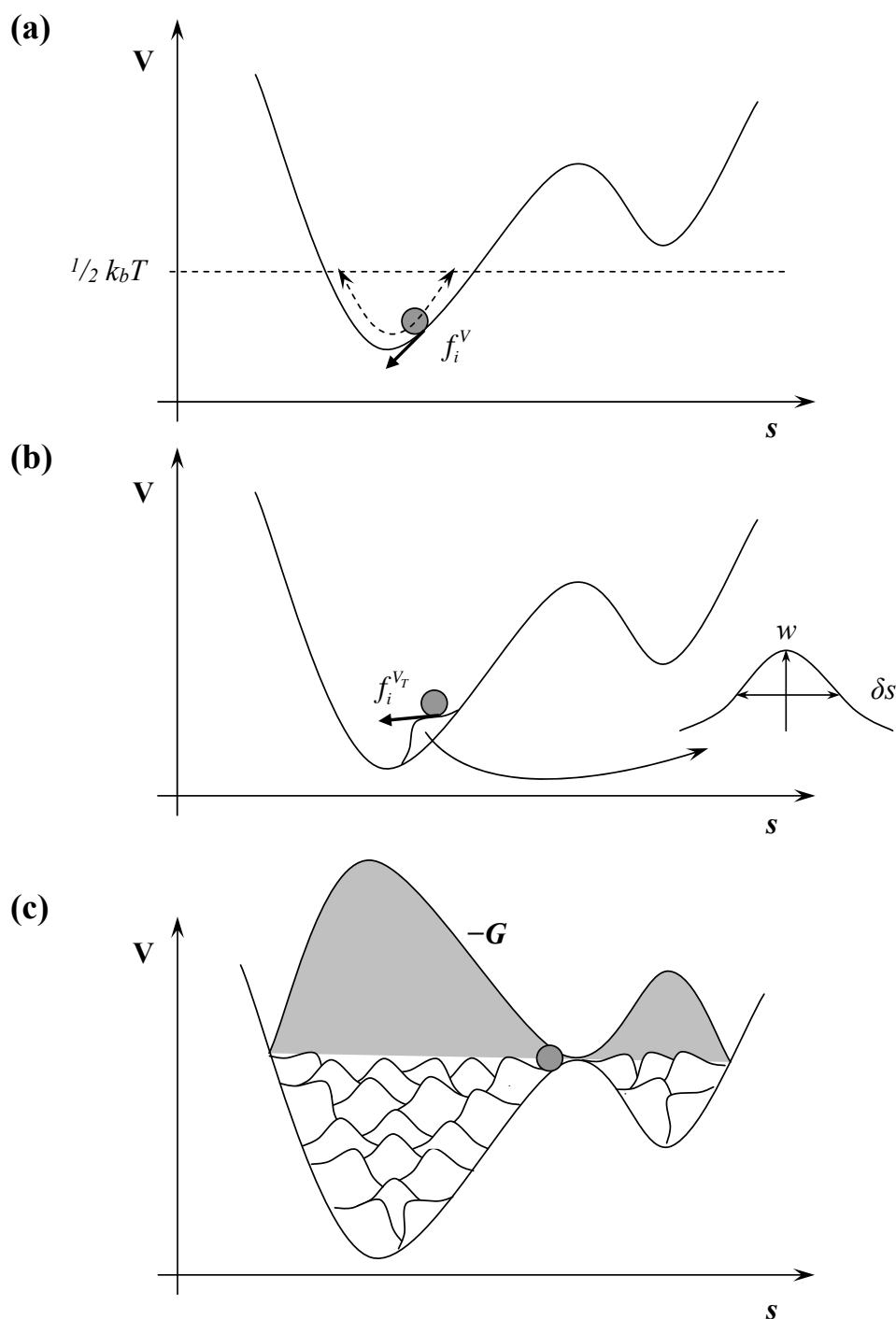


Figure 4. (a) Standard molecular dynamics simulation. The system evolves following the interatomic potential V , and thus the force acting on the system is f_i^V (equation 16).

(b) Metadynamics simulation (i.e. a Gaussian potential term with height w and width δs is added every certain time t' centered at the value of s at that moment). The system evolves following the modified potential $V^T = V + V^G$, and thus the force acting on the system is $f_i^{V_T}$ (equation 18).

(c) End of the metadynamics and reconstruction of the free energy surface (G , equation 19). Taken from reference (Biarnés, 2007).

The quality of the FES depends on the parameters defining the history-dependent potential (Laio, 2005). Large values of w and δs will allow a faster exploration of the collective variables space, although at expense of less accuracy.

3.2. Collective variables

The collective variables (CVs) to be used in a metadynamics simulation have to fulfill the following requirements (Iannuzzi, 2003; Ensing, 2005 & 2006; Laio & Gervasio, 2008):

- They are an explicit function of a subset of coordinates of the system.
- The mathematical function that define the CVs must be continuous and derivable.
- The reaction coordinate must be a combination of the chosen CVs.
- The CVs have to clearly differentiate between the initial and final states of the process.
- All the reaction modes with relaxation times similar to those of the CVs have to be included.

In this thesis, we have used as collective variables a combination of coordination numbers, which are defined using rational functions as in references (Iannuzzi, 2003) and (Boero, 2004). This definition has been successfully used in several previous studies of chemical and biochemical reactions using the metadynamics approach (Boero, 2004; Raiteri, 2006). In particular, in Chapter V we have used a difference between the coordination numbers of two different atoms, A and B, with respect to the same atom C, $\Delta N_{coord}(A, B; C)$, which is defined as:

$$\Delta N_{coord}(A, B; C) = N_{coord}(AC) - N_{coord}(BC) = \left[\frac{1 - (r_{AC} / d_{cut})^p}{1 - (r_{AC} / d_{cut})^{(p+q)}} \right] - \left[\frac{1 - (r_{BC} / d_{cut})^p}{1 - (r_{BC} / d_{cut})^{(p+q)}} \right] \quad (20)$$

where r_{AC} and r_{BC} are the interatomic distances, d_{cut} is a threshold distance for bonding, and p and q are exponents which determine the steepness of the decay of ΔN_{coord} with respect to r_{AC} and r_{BC} . Besides, in Chapter VII we have used the coordination number of a species A with a species B, $N_{coord}(A, B)$, which is given by:

$$N_{coord}(A, B) = \sum_{i=1}^{N_A} \frac{1}{N_A} \left[\sum_{j=1}^{N_B} \frac{1 - (r_{ij} / d_{AB})^p}{1 - (r_{ij} / d_{AB})^{(p+q)}} \right] \quad (21)$$

where N_A and N_B are the number of atoms of species A and B, respectively, r_{ij} are the interatomic distances, d_{AB} is the threshold distance for bonding and p and q are exponents which determine the steepness of the decay of N_{coord} with respect to r_{ij} .

3.3. Lagrangian metadynamics

In *direct metadynamics* (Laio & Gervasio, 2008), the collective variables are enforced to cross high barriers (\sim tenths of kcal mol⁻¹) in short times (a few ps) by adding a history-dependent potential V_G , which injects energy into the degrees of freedom associated of the collective variables. In some cases, this can lead to a non-homogeneous temperature distribution of the system, as well as to instabilities in the dynamics. In order to solve these problems, the extended lagrangian metadynamics method has been introduced. In particular, here we consider the *extended lagrangian metadynamics coupled to Car-Parrinello molecular dynamics* (Iannuzzi, 2003), in which the Car-Parrinello Lagrangian is extended by extra terms describing the fictitious dynamics of the collective variables.

In particular, the collective variables in the real system s are coupled to additional fictitious particles s' through a harmonic potential V_H :

$$V_H = \frac{1}{2}k [s' - s(x)]^2 \quad (22)$$

and these auxiliary collective variables s' are treated as additional degrees of freedom with a fictitious mass M and an associated fictitious kinetic energy $K_{s'}$ given by:

$$K_{s'} = \frac{1}{2}M v_{s'}^2 \quad (23)$$

In this way, the dynamics of these extra degrees of freedom can be explicitly controlled using thermostats and the trajectory of s' will be sufficiently soft as to maintain the stability of the algorithm (Ensing, 2005).

Because we are introducing an extra potential V_H , the total potential acting on the real system is modified:

$$V_T = V + V_H = V + \frac{1}{2}k [s' - s(x)]^2 \quad (24)$$

(where k is the spring constant of the harmonic potential), and also the resulting forces:

$$f_i^{V_T} = f_i^V + f_i^{V_H} = -\frac{\partial V}{\partial r_i} - \frac{\partial V_H}{\partial r_i} \quad (25)$$

Therefore, the dynamics of the real system in the real space (s) is driven by the sum of interatomic potential V and the harmonic potential V_H (Figure 5, right). The mass for this fictitious particle and the force constant of the coupling potential need to be tested to ensure that the coupled particle follows naturally the value of the associated collective variable in the real system.

The history-dependent potential V_G , instead of acting on the real system as in direct metadynamics, acts on the space of the auxiliary collective variable s' , i.e. the Gaussian potential terms V' are now centered on s' (Figure 5, left). Therefore, the dynamics in the space of the auxiliary CVs is driven by the forces coming from the harmonic potential V_H and the history-dependent potential V_G :

$$f_{s'}^{V_T} = f_{s'}^{V_H} + f_{s'}^{V_G} = -\frac{\partial V_H}{\partial s'_i} - \frac{\partial V_G}{\partial s'_i} \quad (26)$$

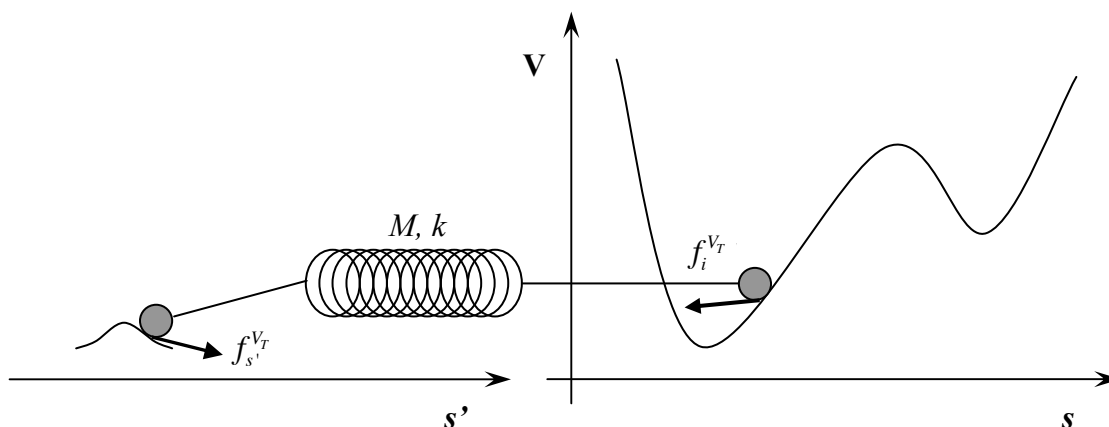


Figure 5. Metadynamics coupled to Car-Parrinello molecular dynamics. The dynamics of the real system in the s space is driven by the sum of interatomic potential V and the harmonic potential V_H , resulting in a force $f_i^{V_T}$ (equation 25). By contrast the dynamics of the fictitious particle in the s' space depends on the sum of the history-dependent potential V_G , and the harmonic potential V_H , resulting in a force $f_{s'}^{V_T}$ (equation 26). Taken from reference (Biarnés, 2007).

Similar to direct metadynamics (section 3.1.), the history-dependent potential V_G will penalize visiting the regions of the s' space already explored. Moreover, because s' is coupled to s through the harmonic potential, it will also accelerate the exploration of the s space. Therefore, the history-dependent potential V_G acting on the s' space will progressively counterbalance the interatomic potential V in the s space (Figure 6), such that the free energy surface (FES) can be reconstructed as

the negative of the sum of the Gaussian potential terms, as in direct metadynamics:

$$G(s) = \lim_{t \rightarrow \infty} V_G(s', t) \approx \sum_{t'} w \exp \left[\frac{[s'(t) - s'(t')]^2}{2(\delta s)^2} \right] \quad (27)$$

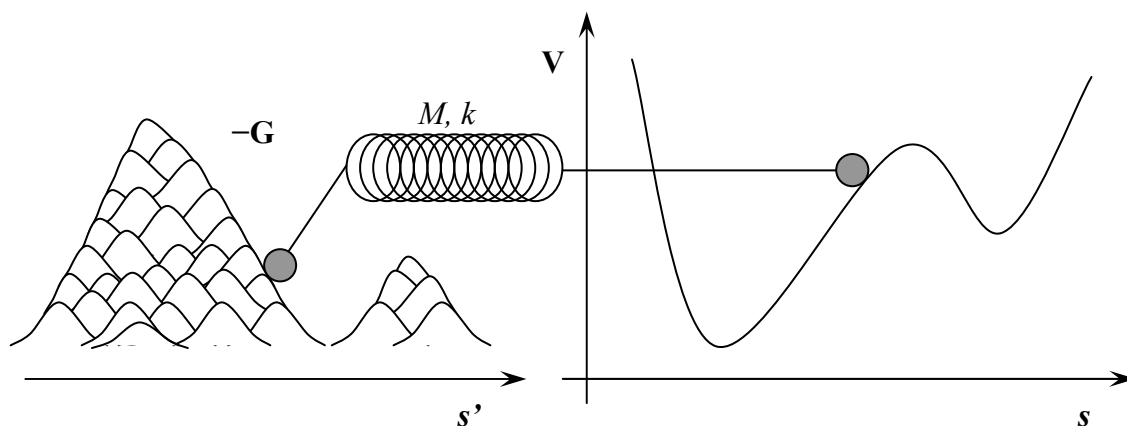


Figure 6. Completed simulation and reconstruction of the free energy profile (FES) for extended-Lagrangian metadynamics. Taken from reference (Biarnés, 2007).

4. ELECTRON TRANSFER CALCULATIONS

4.1. Redox properties

For a molecule that gets ionized (i.e. either reduced or oxidized), the following “redox” properties can be defined:

$$IP = E_O(R_R) - E_R(R_R), \quad EA = E_O(R_O) - E_R(R_O) \quad (28)$$

$$\lambda_R = E_R(R_O) - E_R(R_R), \quad \lambda_O = E_O(R_R) - E_O(R_O) \quad (29)$$

$$\lambda = (\lambda_R + \lambda_O) / 2 \quad (30)$$

$$\Delta E_{ox} = E_O(R_O) - E_R(R_R) = IP - \lambda_O \quad (31)$$

$$\Delta E_{red} = E_R(R_R) - E_O(R_O) = - (IP - \lambda_O) \quad (32)$$

where $E_M(R_N)$ is the potential energy in the reduced ($M=R$) or oxidized ($M=O$) state, at the minimum energy configurations of the reduced ($N=R$) or the oxidized ($N=O$) state. *The IP and the EA are the vertical ionization energies*, i.e. the ionization potential in the reduced state R and the electron affinity in the oxidized state O, respectively. *λ is the reorganization energy*, which measures the cost of adjusting the geometry of the molecule upon ionization. In particular, λ_R is the reorganization energy of the R state and λ_O is the reorganization energy of the O state. *ΔE_{ox} and ΔE_{red} are the adiabatic energies of oxidation and reduction*, respectively. These adiabatic ionization

energies differ from the vertical ionization energies in that they include the structural relaxation of the molecule upon ionization, and thus they are smaller than the IP and the EA, respectively.

Therefore, the calculation of these redox properties requires to optimize the geometry of the molecule under consideration in the oxidized and the reduced states (N=O, R), and then perform two single-point calculations at each minimum energy configuration, to obtain the potential energy in the oxidized and the reduced states (M=O, R)².

4.2. Marcus theory

Electron transfer (ET) reactions play a crucial role in several biological processes, such as cell respiration or photosynthesis. These biological electron transfers occur over donor-acceptor distances of about 4-24 Å (i.e. *long-range ET*) (Moser, 2006), and therefore the interaction between the redox-active orbitals of the donor and acceptor is assumed to be weak (i.e. *nonadiabatic ET*). Provided that neither breaking nor formation of chemical bonds occur (i.e. *outer-sphere ET*), the electron transfer is well described by semi-classical Marcus theory (Marcus & Sutin, 1985; Barbara, 1996), and its rate constant only depends on the reaction free energy or driving force (ΔG), the reorganization free energy (λ) and the quantum coupling between the donor and acceptor (H_{DA}):

$$k_{ET} = \frac{1}{\hbar} H_{DA}^2 (\pi / \lambda k_B T)^{1/2} \exp \left[-\frac{(\lambda + \Delta G)^2}{4 \lambda k_B T} \right] \quad (33)$$

In the Marcus picture (Marcus & Sutin, 1985), the donor (D) and acceptor (A) are described by two diabatic states in contact with a harmonic bath (solvent or protein), and rare thermal fluctuations of the bath bring the system to a configuration where the two diabatic states cross and electron transfer occurs. The main assumption of Marcus theory is that the free energy curves of the donor and acceptor are parabolic with respect to the reaction coordinate of electron transfer (Figure 7). Such reaction coordinate is taken to be the electron transfer energy or energy gap, $\Delta E = E_D - E_A$, and its fluctuations are assumed to follow a Gaussian distribution, thus resulting in harmonic

² In this thesis, such “static” calculations have been performed either in the gas phase (all QM) or in the presence of the protein environment (QM/MM). In both cases, E_M (M=O, R) is just the potential energy of the ionized molecule and its first-shell ligands (i.e. the total energy of the gas phase model or the QM part of the energy in the QM/MM model). Therefore, the calculated redox properties can be regarded to as “inner-sphere” (see below). The differences between the gas phase-derived and the QM/MM-derived redox properties are the possible steric constraints imposed by the environment on the geometry of the ionizable molecule, as well as the polarization of the electronic density of the QM region by the MM environment.

diabatic free energy curves. However, ΔE is very sensitive to the structural rearrangements of the system, and hence this approximation is only valid for systems which do not undergo significant changes in conformation or solvation upon ET i.e. within *the linear response (LR) regime*.

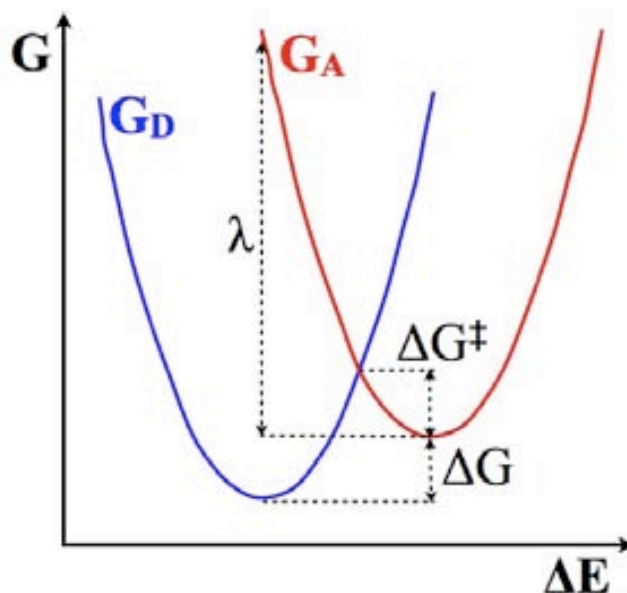


Figure 7. Diabatic free energy curves of the donor and acceptor. ΔE = electron transfer energy, ΔG = reaction free energy or driving force, λ = reorganization free energy, ΔG^\ddagger = activation free energy. Adapted from reference (Blumberger, 2008).

As can be seen in Figure 7, the difference between minima of the two parabolas give the *reaction free energy or driving force* (ΔG), the crossing point of the two curves is *the activation free energy* (ΔG^\ddagger) and their curvature determines *the reorganization free energy* (λ) (Barbara, 1996). This reorganization free energy is the free energy required for all structural adjustments (in the donor-acceptor pair and in the surrounding environment) which are needed in order to achieve the configuration required for the transfer of the electron. Therefore, λ includes a component from the vibration of the donor and acceptor (*intramolecular or inner-sphere reorganization energy*, λ^i) and from the polarization changes in the environment (*outer-sphere reorganization energy*, λ^o). λ equals $4\Delta G^\ddagger$ at zero driving force, because:

$$\Delta G^\ddagger = (\Delta G + \lambda)^2 / 4\lambda \quad (34)$$

4.3. Energy gap method

As explained in the previous section, the two central parameters in Marcus theory (Marcus & Sutin, 1985) are the reaction free energy or driving force (ΔG) and the reorganization free energy (λ). For pure ET reactions (i.e. that are not coupled to formation or breaking of bonds), the energy gap has been shown to be a good reaction coordinate, and thus ΔG and λ can be calculated by computing ΔE . In this energy gap method (Warshel, 1992; Blumberger, 2005; VandeVondele, 2007), first an ensemble of atomistic configurations is generated by running a molecular dynamics simulation. Then the energy gap is calculated for each configuration as the difference in total energy between the oxidized and the reduced states. Finally, ΔG and λ are obtained from the average and the variance of the energy gap along the simulation. Because these simulations are performed at constant volume, the free energy will be denoted hereafter as “A”.

- *Reduction half reaction*

Let us first consider the electron transfer between a ionizable group and an electrode, i.e. the (electrochemical) reduction of a single ionizable group:



where O and R denote the total system containing a ionizable group in the oxidized state or the reduced state, respectively. For this process, *the energy gap to be used as reaction coordinate (ΔE) is the vertical ionization energy*, which is calculated as:

$$\Delta E(R_N) = E_O(R_N) - E_R(R_N) \quad (35)$$

E_O and E_R are the ground state potential energy in the oxidized (O) and the reduced (R) states, respectively, and R_N indicates the nuclear configuration. In other words, in the potential energy surface of the R state (R_R) the energy gap is the ionization potential:

$$\Delta E(R_R) = E_O(R_R) - E_R(R_R) = \Delta E_R = IP \quad (35a)$$

while in the surface of the O state (R_O) it is the electron affinity:

$$\Delta E(R_O) = E_O(R_O) - E_R(R_O) = \Delta E_O = EA \quad (35b)$$

Therefore, two molecular dynamics simulations have to be run: one in the R state, to generate an ensemble of configuration where the IP will be calculated, and another in the O state, to obtain a distribution of EA values.

Then, the free energy diabatic curves of the O and R states (Figure 7) are calculated as:

$$A_M(\Delta E) = A_M - \frac{1}{\beta} \ln[p_M(\Delta E)] \quad (36)$$

where A is the free energy at constant volume, M refers to either the R or the O state, $\beta = 1/(k_b T)$ and $p_M(\Delta E)$ is the probability distribution of ΔE , $p_M(\Delta E) = \langle \delta(\Delta E - \Delta E(R^N)) \rangle_M$, with the brackets $\langle \dots \rangle_M$ denoting a canonical average in state M .

Once the free energy diabatic curves of the O and the R states are constructed (Figure 7), we can calculate ΔA and λ . Assuming the free energy of the electron equals zero, the reaction free energy turns out to be:

$$\Delta A = A_R - A_O = -\frac{1}{\beta} \ln \langle \exp(\beta \Delta E) \rangle_O = \frac{1}{\beta} \ln \langle \exp(-\beta \Delta E) \rangle_R \quad (37)$$

whereas the reorganization free energy, measuring the cost in free energy when distorting the ions from the equilibrium position of one diabatic state to the equilibrium position of the other state while remaining on the same diabatic curve (Figure 7), is given by:

$$\lambda_O = A_O(\Delta E_R^{\min}) - A_O(\Delta E_O^{\min}), \quad \lambda_R = A_R(\Delta E_O^{\min}) - A_R(\Delta E_R^{\min}) \quad (38)$$

where ΔE_R^{\min} and ΔE_O^{\min} are the position of the minima of the diabatic free energy curves of the R or O states, respectively, λ_O is the reorganization energy of the O state and λ_R is the reorganization energy of the R state.

In the LR regime (see section 4.2.), the equilibrium distributions of the energy gaps (IP and EA) are Gaussian and they have with identical widths, which coincide with the variance of the energy gap. As a result, the diabatic free energy curves of the R and O states are harmonic. When this LR approximation is applied, it turns out that:

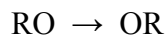
$$\Delta A^{LR} = -(\langle \Delta E_R \rangle + \langle \Delta E_O \rangle) / 2 \quad (39)$$

$$\lambda^{LR} = (\langle \Delta E_R \rangle - \langle \Delta E_O \rangle) / 2 \quad (40)$$

where $\langle \Delta E_R \rangle$ and $\langle \Delta E_O \rangle$ are the mean energy gaps in state R and O (i.e. $\langle EA \rangle$ and $\langle IP \rangle$), respectively.

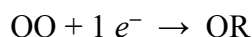
• *Redox reaction*

Let us now consider the electron transfer reaction between two ionizable groups:



In state RO, cofactor 1 is reduced and cofactor 2 is oxidized, whereas it is the opposite for state OR. For this process, *the energy gap to be used as a reaction coordinate (ΔE) is the electron transfer energy.*

In the nonadiabatic limit (i.e. the overlap between the donor and acceptor orbitals is essentially zero) the electron transfer can be decomposed into two separate processes, oxidation of the donor and reduction of the acceptor.



As a result, the electron transfer energy (ΔE) can be calculated as the difference in the ionization energies of the two cofactors:

$$\Delta E(R_N) = IE_1(R_N) - IE_2(R_N) = \Delta E_N \quad (41)$$

where:

$$IE_1(R_N) = E_{OO}(R_N) - E_{RO}(R_N) \quad (42a)$$

$$IE_2(R_N) = E_{OO}(R_N) - E_{OR}(R_N) \quad (42b)$$

and $N = RO, OR$ state. If the molecular dynamics is carried out in the RO state, IE_1 is the ionization potential of cofactor 1 and IE_2 is the electron affinity of cofactor 2, whereas, in state OR IE_1 and IE_2 are the electron affinity of cofactor 1 and the ionization potential of cofactor 2, respectively.

As for the reduction half reaction (equation 36-38), ΔE (here the electron transfer energy) can be used to construct the free energy diabatic curves of the RO and the OR states and to calculate ΔA and λ . Nevertheless, *in case the LR approximation holds*, it simply turns out that:

$$\Delta A^{LR} = (\langle \Delta E_{RO} \rangle + \langle \Delta E_{OR} \rangle) / 2 \quad (43)$$

$$\lambda^{LR} = (\langle \Delta E_{RO} \rangle - \langle \Delta E_{OR} \rangle) / 2 \quad (44)$$

where $\langle \Delta E_{RO} \rangle$ and $\langle \Delta E_{OR} \rangle$ are the mean electron transfer energies in state RO or OR, respectively.

4.4. Energy gap from QM/MM

The methodology used in this thesis to calculate the energy gap is *the QM/MM-based method recently developed by Blumberger* (Blumberger, 2008). It consists in (i) running a classical

molecular dynamics simulation of both oxidation states, (ii) generating an ensemble of configurations, and (iii) calculating the energy gap using QM/MM (in particular CP QM/MM).

In the QM/MM calculation, the cofactor where the ionization takes place is treated at the quantum level, whereas the chemically inert environment (the protein and the solvent) are treated by molecular mechanics. The oxidation or reduction reaction of the cofactor is enforced by increasing or decreasing, respectively, the total charge of the QM subsystem by 1 e , whereas for the rest of the system (MM region) the classical point charges, van der Waals and other force field terms remain unchanged.

- *Reduction half reaction*

For the (electrochemical) reduction of a single ionizable group ($O + 1 e^- \rightarrow R$) two classical molecular dynamics simulations have to be run: one in the O state and another in the R state. Then, an ensemble of configurations is extracted for each simulation, and at each ionic configuration the ionization energy is calculated by means of QM/MM.

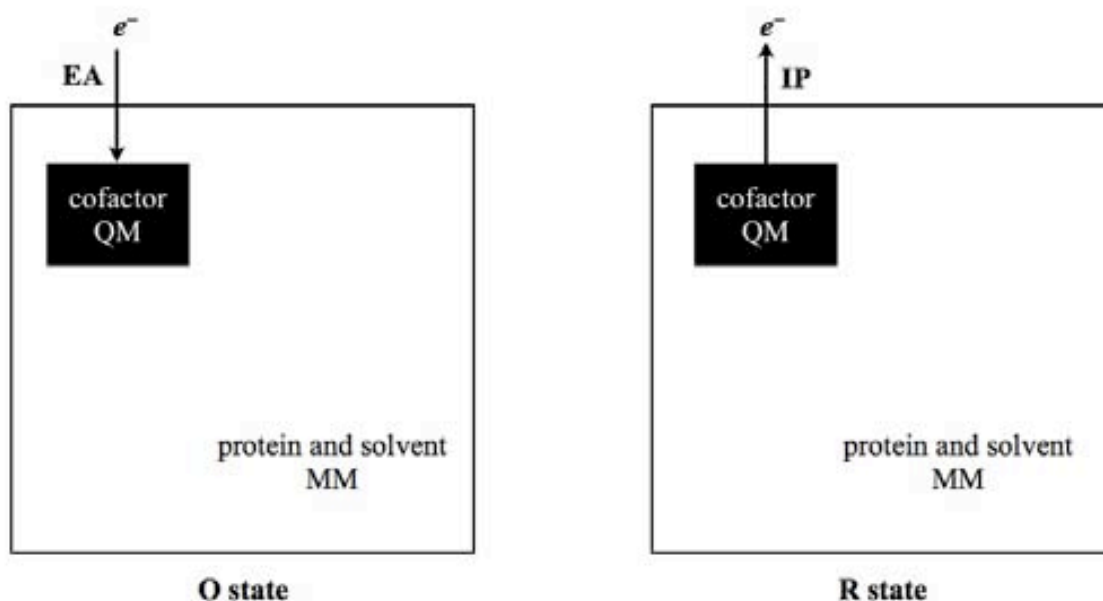


Figure 8. QM/MM scheme for the calculation of the (electrochemical) reduction of an ionizable group. R state = total system containing reduced cofactor and O state = total system containing oxidized cofactor. IP = ionization potential and EA = electron affinity, calculated using equations 35a and 35b.

In the QM/MM calculations, the cofactor that gets ionized is included in the QM region, whereas the protein and the solvent form the MM region (Figure 8). At each ionic configuration, two single-point QM/MM calculations are performed, with the cofactor either oxidized or reduced. The MM parameters are the same in both calculations and only the charge of the QM subsystem changes (N when the cofactor is considered to be oxidized and $N-1$ when it is taken as reduced). The difference between these two ground state energies is the ionization energy (equation 35), i.e. the EA (equation 35a) or the IP (equation 35b) depending on whether the snapshot belongs to the ensemble of the O state or to the ensemble of the R state, respectively.

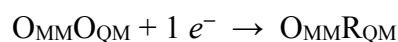
Once these two sets of ionization energies have been obtained (i.e. $\{EA_1, EA_2, \dots, EA_n\}$ and $\{IP_1, IP_2, \dots, IP_n\}$, where n = number of configurations), the average and variance of the two distributions is computed. In case the variance of the IP and the EA are (almost) equal, it indicates that the LR approximation is valid, and thus ΔA and λ can be calculated from the mean of the ionizations energies ($\langle EA \rangle$ and $\langle IP \rangle$, equations 39-40).

- *Redox reaction*

For the nonadiabatic electron transfer reaction between two ionizable groups ($RO \rightarrow OR$), two classical molecular dynamics simulations have to be run: one in the RO state and another in the OR state. Then, an ensemble of configurations is extracted for each simulation, and at each ionic configuration the electron transfer energy is calculated by means of QM/MM.

In the QM/MM calculations, since the donor-acceptor distance is large, it is expected that cofactor 2 is merely a spectator of the ionization of cofactor 1 and *vice versa*. Hence, only the cofactor that gets ionized is included in the QM region (either cofactor 1 or cofactor 2), and the cofactor that does not get ionized (cofactor 2 or cofactor 1, respectively) is described at the classical level, as the protein and solvent environment (Figure 9). Therefore, the non-ionized cofactor couples to the ionization of the other cofactor just through electrostatic interactions.

In other words, oxidation of the donor and reduction of the acceptor can be rewritten as:



and the corresponding ionization energies (equations 42a and 42b) are:

$$IE_1(R_N) = E(O_{QM}O_{MM})(R_N) - E(R_{QM}O_{MM})(R_N) \quad (42a')$$

$$IE_2(R_N) = E(O_{MM}O_{QM})(R_N) - E(O_{MM}R_{QM})(R_N) \quad (42b')$$

where the subscripts QM and MM indicate in which region each cofactor is (i.e. whether it is treated at the QM or the MM level).

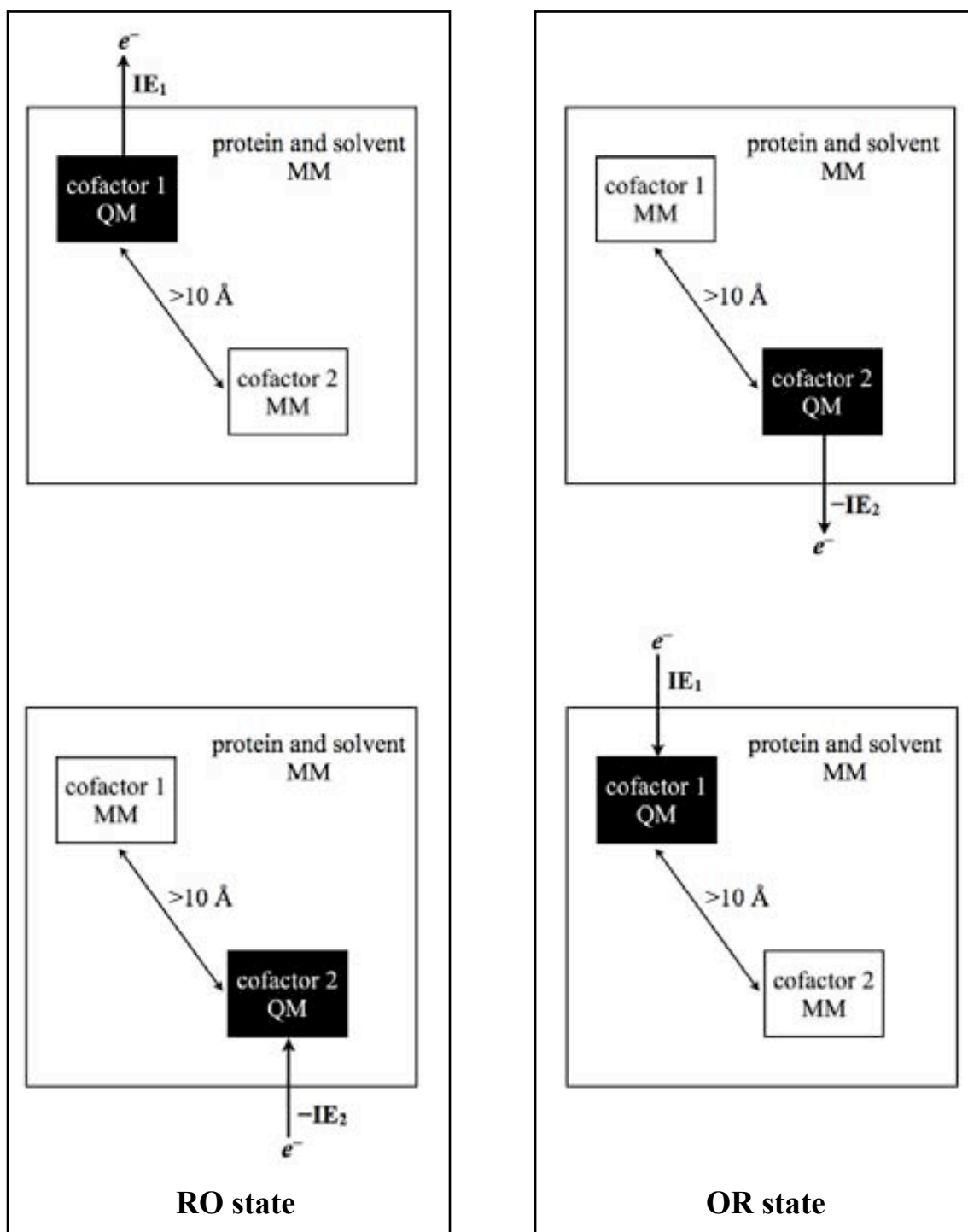


Figure 9. QM/MM scheme for the calculation of the electron transfer energy ($\Delta E = IE_1 - IE_2$) for large donor-acceptor distances. RO state = total system containing reduced cofactor 1 and oxidized cofactor 2 and OR state = total system containing oxidized cofactor 1 and reduced cofactor 2. IE_1 and IE_2 = ionization energies, calculated using equations 42a'-42b'.

In practice, four single-point QM/MM calculations have to be performed at the same ionic configuration of the RO state: two for calculating the ionization potential of cofactor 1 and another two for the electron affinity of cofactor 2 (Figure 9, left). Likewise, in the OR state two calculations are required to obtain the electron affinity of cofactor 1 and another two for the ionization potential of cofactor 2 (Figure 9, right). The difference of the ionization energies in each state (equation 41) gives the electron transfer energy, ΔE_{RO} and ΔE_{OR} , respectively .

As for the reduction half reaction, once these two sets of energy gaps have been obtained (i.e. $\{\Delta E_{RO,1}, \Delta E_{RO,2}, \dots, \Delta E_{RO,n}\}$ and $\{\Delta E_{OR,1}, \Delta E_{OR,2}, \dots, \Delta E_{OR,n}\}$, where n = number of configurations), the average and variance of the two distributions is computed. In case the variances of ΔE_{RO} and ΔE_{OR} are (almost) equal, it indicates that the LR approximation is valid, and thus ΔA and λ can be calculated from the mean of the electron transfer energies ($\langle \Delta E_{RO} \rangle$ and $\langle \Delta E_{OR} \rangle$, see equations 43-44).

- *Energy decomposition*

In QM/MM, the total potential energy of a given state is the sum of the potential energy of the QM and MM regions and the QM-MM interaction energy (Laio, 2002a):

$$E = E_{QM} + E_{MM} + E_{QM-MM} \quad (45)$$

Therefore, the vertical ionization energies can also be expressed as:

$$IE = IE_{QM} + IE_{MM} + IE_{QM-MM} \quad (46)$$

and thus the driving force and the reorganization energies can be decomposed into:

$$\Delta A = \Delta A_{QM} + \Delta A_{MM} + \Delta A_{QM-MM} = \Delta A^i + \Delta A^o \quad (47)$$

$$\lambda = \lambda_{QM} + \lambda_{MM} + \lambda_{QM-MM} = \lambda^i + \lambda^o \quad (48)$$

The contribution of the QM region (i.e. the ionizable cofactor and its first-shell ligands) is referred to as “inner-sphere”³, whereas the sum of the MM and QM-MM contributions (i.e. the remaining protein and solvent plus its electrostatic interaction with the redox-active center) is denoted as “outer-sphere”. Such decomposition is useful in order to probe the influence of the different parts of the system in the electron transfer, i.e. whether the environment reinforces or hinders the intrinsic propensity of the cofactor(s) for electron transfer.

³ This inner-sphere contribution is different from the inner-sphere contribution introduced in section 4.1., because here it includes thermal effects.

CHAPTER III

DENSITY FUNCTIONAL STUDY ON MODELS OF CATALASE REACTION INTERMEDIATES

1. INTRODUCTION

As explained in Chapter I (section 3.3.), the main activity of catalases is the dismutation of hydrogen peroxide ($2 \text{H}_2\text{O}_2 \rightarrow 2 \text{H}_2\text{O} + \text{O}_2$) (Nicholls, 2001; Maté, 2001; Chelikani, 2004). The first H_2O_2 molecule acts as a two-electron oxidant (reaction 1), generating Compound I (Cpd I), which is reduced back to the resting state by a second H_2O_2 molecule in a two electron-process (reaction 2).



Besides, at low H_2O_2 concentrations and in the presence of one-electron organic donors (AH), catalases have a peroxidase activity (Nicholls, 2001; Dunford, 1999). Here, Cpd I is one-electron reduced by AH to another intermediate, Compound II (Cpd II, see reaction 3), which in turn reacts with another molecule of AH to regenerate ferricatalase (reaction 4).



Therefore, catalases form two different reaction intermediates: Cpd I, the primary intermediate of the catalase reaction, and Cpd II, the secondary intermediate of the peroxidatic pathway. Crystallographic and spectroscopic studies (see Chapter I, section 4) have shown that Cpd I contains a $S = 3/2$ oxoferryl group in ferromagnetic interaction with a porphyrin cation radical (i.e. $\text{Por}^{\bullet+}\text{-Fe}^{\text{IV}}\text{=O}$) (Benecky, 1993). In contrast, in Cpd II the porphyrin cation radical has been reduced, and it is generally accepted that reduction is accompanied by protonation of the oxoferryl moiety (i.e. $\text{Por-Fe}^{\text{IV}}\text{-OH}$) (Rovira, 2003 & 2005).

Catalases may contain two different types of heme groups, either heme b or heme d (Nicholls, 2001). Heme b is a protoporphyrin IX, while heme d is a chlorin-like derivative (Murshudov, 1996; Obinger, 1997), where the double bond across the C_β atoms of pyrrole III is saturated and the propionate sidechain has been converted into a *cis*-hydroxy- γ -spirolactone (see Figure 1). The influence of the type of heme group in the properties of the aforementioned reaction intermediates is not known. However, the lack of Cpd II detection for heme d-containing catalases (Kikuchi-Torii, 1982; Obinger, 1997; Chelikani, 2005) suggests that these reaction intermediates may have different properties depending on the type of heme.

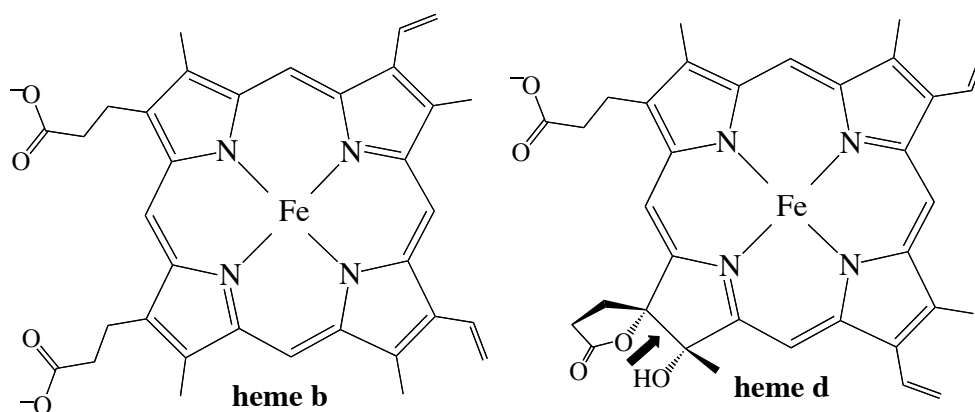


Figure 1. Heme cofactors present in catalases. The modification in heme d is highlighted with an arrow. Note that heme d is flipped by 180° compared to heme b.

Knowledge of the structure and electronic configuration of Cpd I and Cpd II is important for understanding the reactivity of catalases. In this chapter we perform DFT calculations on models of Cpd I and Cpd II to study the intrinsic properties of these reaction intermediates (i.e. without the influence of the different protein environment of each catalase). Different models are considered (see section 2) to separate the effects of the bare cofactor (model 1), the substituents (model 2), the axial ligation (model 3) and the distal residues (model 4). Both heme b and heme d models are investigated to assess the influence of the type of heme group on the structural and electronic properties of these intermediates.

2. COMPUTATIONAL DETAILS

2.1. Models

Figure 2 shows the Cpd I and Cpd II models investigated, considering both heme b and heme d cofactors. Model 1 corresponds to the bare cofactor without substituents, except for the *cis*-hydroxy- γ -spirolactone modification present in heme d (Figure 2a). The cofactor substituents are incorporated in model 2 (Figure 2b): the methyl and vinyl groups, and the propionate sidechains, which are modelled as protonated to mimic the positive charged environment (3 arginine residues) surrounding them inside the protein (Chapter I, section 3.2.). Models 3 and 4 incorporate the first-shell residues around the heme (Figures 2c and 2d).

Model 3 (Figure 2c) adds the proximal residues (see Chapter I, section 3.2.): the tyrosinate coordinated to the iron (modelled as a phenolate) and the arginine hydrogen bonded to the phenolate oxygen atom (methylguanidinium). Axial ligation has been demonstrated to influence the structure and electronic configuration of the catalytic intermediates of heme proteins (Rydberg, 2004). In particular, the proximal Arg hydrogen bonded to phenolate has been found to be important to tune the properties of catalase Cpd I (Green, 2001; de Visser, 2006) and Cpd II (Rovira, 2003).

Model 4 (Figure 2d) also includes the distal residues (see Chapter I, section 3.2.): the pocket water (hydrogen-bonded to the oxoferryl) and the essential histidine. This distal His is taken as protonated (i.e. methylimidazolium), assuming its pKa is similar to that reported in *Horse radish* peroxidase (HRP) Cpd I (5.0) (Jones & Dunford, 2006). For Cpd II model 4, two different isomers are considered (Figure 2e): an oxoferryl (Fe=O) Cpd II with a protonated distal His (Figure 2d), and a hydroxoferryl (Fe–OH) Cpd II with a neutral His (Figure 2e). Indeed, two different forms of Cpd II (oxoferryl and hydroxoferryl Cpd II) have been detected in *Proteus mirabilis* catalase (PMC) (Horner, 2006 & 2007). Moreover, the long Fe–O distances observed in the crystallographic structures of several heme proteins suggest that Cpd II bears a protonated oxoferryl group (i.e. Fe–OH).

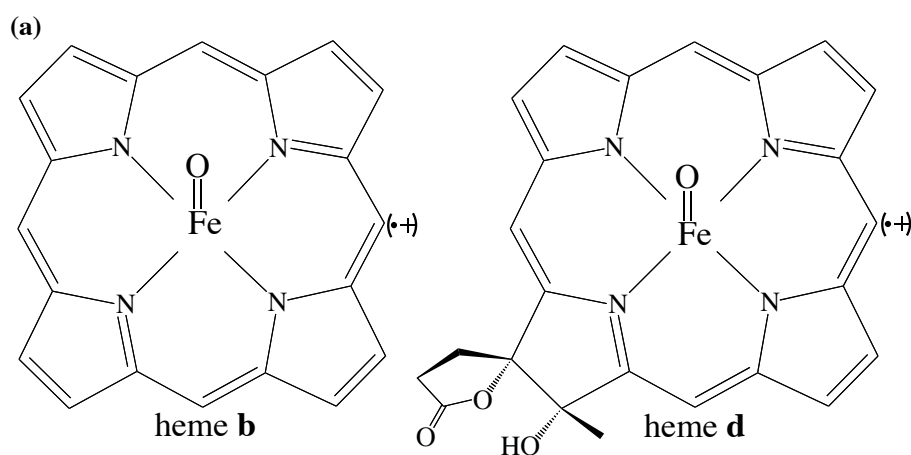


Figure 2. Gas phase models of the reaction intermediates of catalases. (a) Model 1. The porphyrin cation radical (•+) is present in Cpd I but not in Cpd II.

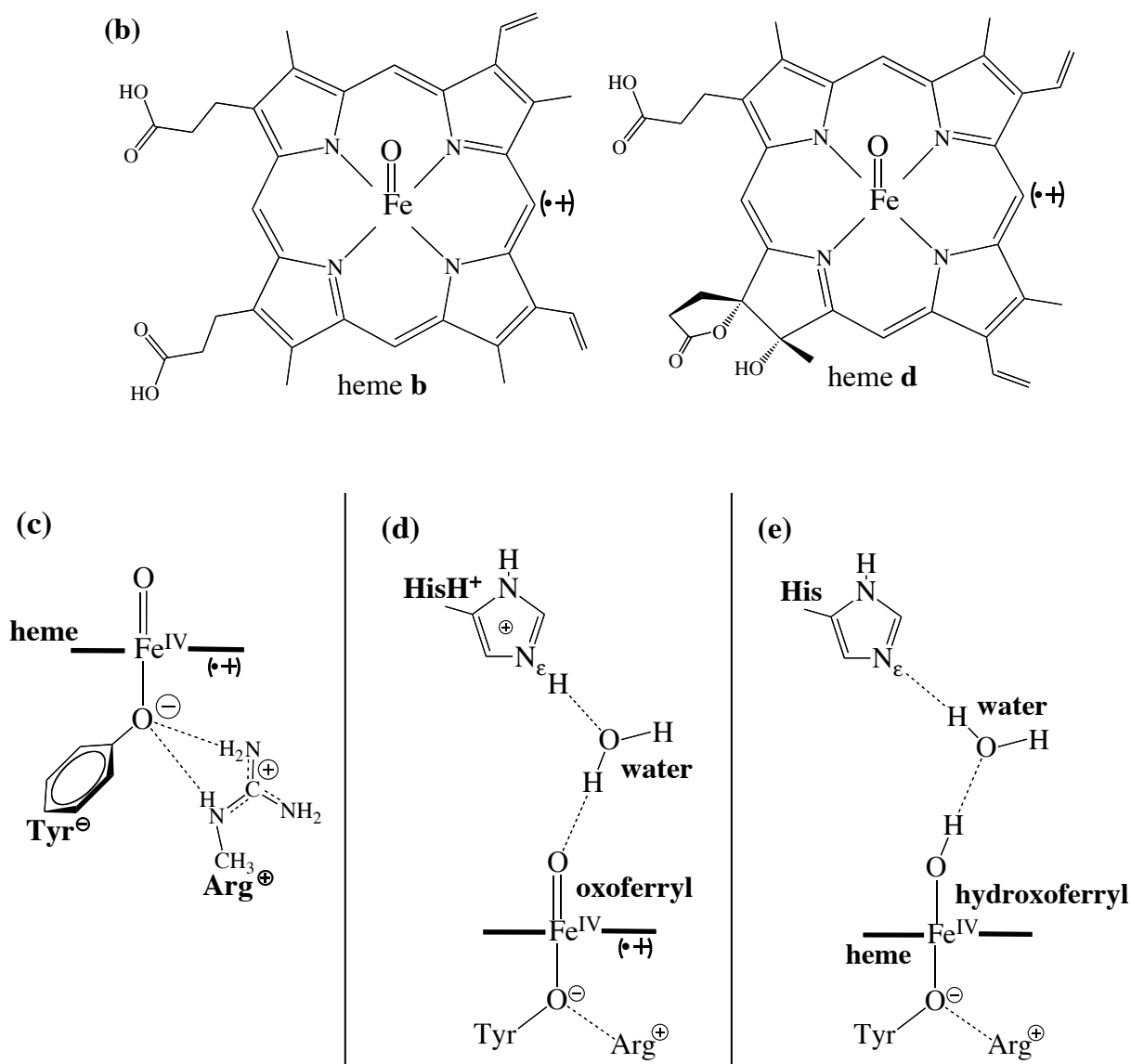


Figure 2 (cont.). Gas phase models of the reaction intermediates of catalases. **(b)** Model 2, **(c)** Model 3, **(d)** Model 4, oxoferryl, **(e)** Model 4, hydroxoferryl. The porphyrin cation radical ($\bullet+$) is present in Cpd I but not in Cpd II. The bold line in models 3 and 4 represents the heme group, either heme b or heme d.

The charge and the multiplicity of each of these models are shown in Table 1. The corresponding heme b and heme d models have the same charge and multiplicity. Cpd II results from one-electron reduction of Cpd I, and thus its charge decreases by +1 and it has one unpaired electron less compared to the same model in the Cpd I state.

Table 1. Charge and multiplicity of the gas phase models of catalase reaction intermediates, along with the box size used in the geometry optimizations (section 2.2.).

Model	Cpd I		Cpd II		heme b / heme d box size (Å ³)
	charge	multiplicity	charge	multiplicity	
1	+1	4	0	3	15×15×8 / 15×17×10
2	+1	4	0	3	21×20×9 / 20×19×10
3	+1	4	0	3	16×16×13 / 15×18×14
4	+2	4	+1	3	15×18.5×17 / 19×18.5×16.5

2.2. Simulation details

The calculations were performed using the generalized gradient-corrected approximation of the spin-dependent density functional theory (DFT-LSD) (Hohenberg, 1964, Kohn & Sham, 1965), following the prescription of Becke and Perdew (BP86) (Becke, 1986; Perdew, 1986). The Kohn-Sham orbitals were expanded in a plane waves (PW) basis set with a kinetic energy cutoff of 70 Ry. Ab initio pseudopotentials, generated within the Troullier-Martins scheme were used (Troullier & Martins, 1991). In the case of iron, the eight valence electrons pseudopotential supplemented with non-linear core corrections (NLCC) was used (Louie, 1982). The systems were enclosed in an orthorhombic isolated supercell of appropriate size (see Table 1) and the Poisson equation was solved using the Martyna and Tuckerman's method (Martyna & Tuckerman, 1999).

Geometry optimizations were carried out using the Car-Parrinello code (CPMD program) by means of molecular dynamics with annealing of the atomic velocities, until the norm of the nuclear gradient was lower than 5×10^{-4} a.u. / bohr. The terminal atoms of the aminoacids (Tyr and Arg in models **3** and **4**, and His in model **4**) were fixed to mimic the steric constraints imposed by the protein environment. In model **4**, it was needed to fix the C_β, C_γ, N_δ and C_δ atoms of the distal His in order to maintain the orientation of the imidazole ring parallel to the heme, as observed in all reported catalase structures. This computational setup will be used in all QM calculations throughout this thesis.

3. RESULTS AND DISCUSSION

3.1. Optimized structures

• Model 1

The main structural parameters describing the optimized structures of model **1** (Figure 2a) are listed in Table 1. Two different conformations are reported for Cpd I: distorted and planar. The optimized structure of heme b catalase Cpd I (Figure 3a) shows a significant distortion of the macrocycle, as previously reported in peroxidase Cpd I models (Deeth, 1999; Vangberg & Ghosh, 1999). Heme d catalase Cpd I is also distorted, although the deformation is less marked than for heme b (Figure 3c), in agreement with the experimental observation of β -substituted porphyrins displaying much less distorted cores (Scheidt, 2001). Since the X-Ray structures of catalases show a rather planar heme cofactor, a planar conformation was imposed by fixing the C_{α} -N- C_{α} - C_{meso} dihedrals (Figures 3b and 3d). The distorted conformation turns out to be more stable than the planar by only 2.2 / 1.9 kcal mol⁻¹ (heme b / heme d), reflecting the well-known softness of porphyrin deformations (Deeth, 1999; Vangberg & Ghosh 1999). Contrary to these Cpd I models, no ruffling was observed for Cpd II, in agreement with the suggestion that neutral porphyrins are less prone to ruffle (Vangberg & Ghosh 1999).

Heme b and heme d models exhibit very similar geometries. The *cis*-hydroxy- γ -spirolactone modification present in heme d does not induce any significant geometrical change, except for a slightly longer Fe- N_{Porph} distance for the modified pyrrole. The loss of the double bond between the C_{β} atoms of the modified pyrrole also results in a longer C_{β} - C_{β} bond length, due to the change from $C_{\text{sp}2}$ - $C_{\text{sp}2}$ to $C_{\text{sp}3}$ - $C_{\text{sp}3}$ bonding (highlighted with an arrow in Figure 1).

Table 1. Main structural parameters of gas phase model **1** (heme b / heme d, respectively).

parameter ^a	Cpd I, distorted	Cpd I, planar	Cpd II
Fe-O	1.68 / 1.68	1.68 / 1.67	1.68 / 1.68
Fe- N_{Porph}	1.96-1.96 / 1.98-2.01	1.99-2.00 / 1.99-2.03	2.00-2.00 / 1.99-2.03
Fe _{out-of-plane} ^b	0.06 / 0.08	0.07 / 0.09	0.06 / 0.08
\angle O-Fe-N	97.9-98.4 / 94.4-99.4	97.5-99.0 / 94.4-101.2	97.9-98.7 / 94.7-99.2

^a Distances are given in angstroms and angles in degrees.

^b Average Fe out-of-plane displacement: $Fe_{\text{out-of-plane}} = d_{\text{Fe-N}_{\text{Porph}}} \times \cos(\widehat{OFeN}_{\text{Porph}}) = d_{\text{Fe-N}_{\text{Porph}}} \times \sin(\widehat{FeN}_{\text{Porph}}N_{\text{Porph}})$

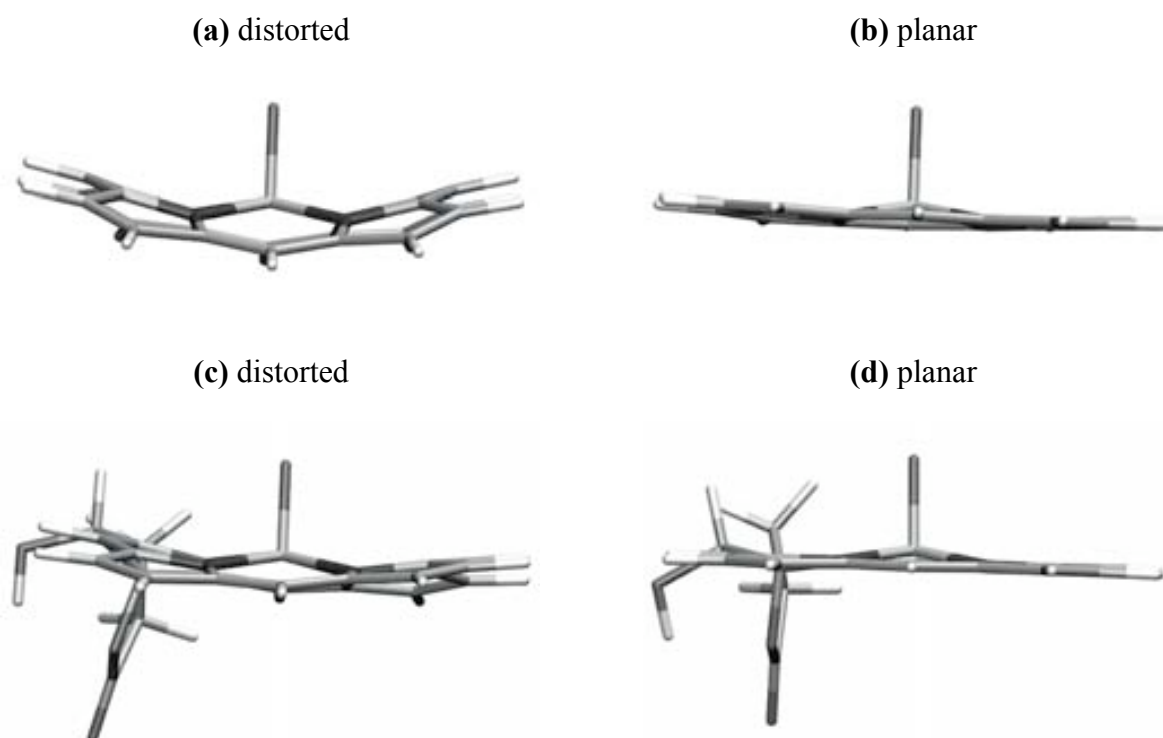


Figure 3. Comparison of the distorted and planar conformations of Cpd I in model 1. **(a)-(b)** heme b, **(c)-(d)** heme d. Heme d is shown with the *cis*-hydroxy- γ -spirolactone modification at the back.

All Cpd I models show almost identical Fe-O distances (1.67-1.68 Å, see Table 1) irrespective of the planarity of the macrocycle. The main structural change induced by the distortion is to shorten Fe-N_{Porph} distances (see Table 1). This is due to the reduction of the repulsion between the iron d orbitals and the nitrogen p orbitals upon bending of the macrocycle (Deeth, 1999; Vangberg & Ghosh 1999). The structure of Cpd II models is very similar to the planar Cpd I counterparts, despite the reduction of the porphyrin cation radical.

Overall, the Fe-O distance is almost identical (1.67-1.68 Å), regardless of the type of heme (heme b or heme d), the oxidation state (Cpd I or Cpd II) or the planarity of the porphyrin cation radical (distorted or planar Cpd I).

- *Model 2*

The incorporation of the macrocycle substituents in model 2 (Figure 2b) stabilizes a more planar structure of Cpd I, as already suggested (Deeth, 1999). Again, neither the different type of heme group nor the oxidation state modify significantly the structure of the intermediates (Table 2). In particular, the Fe-O distances (1.67-1.68 Å) are almost identical to model 1 (see Table 1).

Table 2. Main structural parameters of gas phase model 2 (heme b / heme d, respectively).

parameter ^a	Cpd I	Cpd II
Fe-O	1.68 / 1.68	1.67 / 1.68
Fe-N _{Porph}	1.99-2.01 / 1.98-2.01	2.00-2.01 / 1.98-2.00
Fe _{out-of-plane} ^b	0.05 / 0.08	0.08 / 0.06
∠O-Fe-N	96.1-100.6 / 93.0-99.6	96.0-99.9 / 95.4-98.9

^a Distances are given in angstroms and angles in degrees.

^b Average Fe out-of-plane displacement: $Fe_{out-of-plane} = d_{Fe-N_{Porph}} \times \cos(\widehat{OFeN_{Porph}}) = d_{Fe-N_{Porph}} \times \sin(\widehat{FeN_{Porph}N_{Porph}})$

• Model 3

Model 3 includes the tyrosinate coordinated to the iron and the proximal arginine (Figure 2c). As shown in Table 3, the Fe-O distance is very similar to the previous models and is independent of the type of heme or the oxidation state. This Fe-O distance (1.69 Å) as well as the Fe-O_{Tyr} bond length (2.08-2.09 Å) are in agreement with previous QM calculations on models with the same axial ligation (Green, 2001; Nilsson, 2004; Silaghi-Dumitrescu, 2004; Rovira, 2005).

Table 3. Main structural parameters of gas phase model 3 (heme b / heme d, respectively).

parameter ^a	Cpd I	Cpd II
axial ligation		
Fe-O	1.69 / 1.69	1.69 / 1.69
Fe-O _{Tyr}	2.09 / 2.08	2.10 / 2.09
O-O _{Tyr}	3.77 / 3.77	3.79 / 3.78
Fe-N _{Porph}	1.98-1.99 / 1.99-2.02	2.01-2.03 / 2.02-2.04
Fe _{out-of-plane} ^b	0.06 / 0.05	0.06 / 0.08
∠O-Fe-O _{Tyr}	176.8 / 178.2	177.9 / 179.1
∠Fe-O _{Tyr} -C	125.0 / 126.0	125.4 / 125.2
∠O-Fe-N	91.6-92.5 / 89.6-92.4	91.6-92.4 / 90.6-93.1
∠O _{Tyr} -Fe-N	85.0-91.4 / 86.3-90.6	86.3-90.3 / 86.2-90.1
proximal side		
O _{Tyr} -N _{Arg}	1.77-1.97 / 1.68-2.00	1.67-1.74 / 1.62-1.80

^a Distances are given in angstroms and angles in degrees.

^b Average Fe out-of-plane displacement: $Fe_{out-of-plane} = d_{Fe-N_{Porph}} \times \cos(\widehat{OFeN_{Porph}}) = d_{Fe-N_{Porph}} \times \sin(\widehat{FeN_{Porph}N_{Porph}})$

• Model 4

The distal residues are included in model 4 (Figures 2d and 2e). In Cpd I models, hydrogen-bonding to the distal residues lengthens the Fe-O distance from 1.69 Å (Table 3) to 1.70 Å (Table 4), as previously reported in peroxidase models (Bathelt, 2005; Behan, 2006).

Table 4. Main structural parameters of gas phase model 4 (heme b / heme d, respectively).

parameter ^a	Cpd I	oxoferryl Cpd II	hydroxoferryl Cpd II
axial ligation			
Fe-O	1.70 / 1.70	1.70 / 1.70	1.74 / 1.74
Fe-O _{Tyr}	2.09 / 2.04	2.08 / 2.05	2.04 / 2.02
O-O _{Tyr}	3.79 / 3.74	3.78 / 3.75	3.78 / 3.76
Fe-N _{Porph}	1.99-2.00 / 2.01-2.03	2.00-2.03 / 2.01-2.04	2.00-2.02 / 2.01-2.06
Fe _{out-of-plane} ^b	0.08 / 0.07	0.07 / 0.06	0.08 / 0.05
∠O-Fe-O _{Tyr}	176.8 / 177.5	176.9 / 177.8	178.9 / 178.8
∠Fe-O _{Tyr} -C	122.7 / 124.6	124.9 / 128.9	122.3 / 126.0
∠O-Fe-N	91.7-93.6 / 89.9-93.5	89.6-93.7 / 88.9-93.7	90.4-93.5 / 88.2-93.7
∠O _{Tyr} -Fe-N	85.1-90.7 / 84.1-92.5	84.5-91.1 / 85.8-91.7	86.6-90.1 / 86.9-92.5
proximal side			
O _{Tyr} -N _{Arg}	1.71-2.25 / 1.79-1.97	1.65-1.88 / 1.67-1.90	1.72-1.90 / 1.75-1.87
distal side			
O-H ₁ ^c	1.55 / 1.52	1.53 / 1.45	1.03 / 1.04
H ₁ -O _{Wat} ^c	1.04 / 1.05	1.05 / 1.07	1.62 / 1.57
O _{Wat} -H ₂ ^d	1.51 / 1.49	1.64 / 1.50	1.03 / 1.04
N _{ε,His} -H ₂ ^d	1.10 / 1.11	1.01 / 1.07	1.78 / 1.63
∠Fe-O-H ₁	131.7 / 138.1	125.8 / 128.8	113.5 / 118.0

^a Distances are given in angstroms and angles in degrees.

^b Average Fe out-of-plane displacement: $Fe_{out-of-plane} = d_{Fe-N_{Porph}} \times \cos(\widehat{OFeN_{Porph}}) = d_{Fe-N_{Porph}} \times \sin(\widehat{FeN_{Porph}N_{Porph}})$

^c H₁ is either on the water molecule (Cpd I and oxoferryl Cpd II) or on the FeO unit (hydroxoferryl Cpd II).

^d H₂ is either on the distal His (Cpd I and oxoferryl Cpd II) or on the water molecule (hydroxoferryl Cpd II).

In Cpd II models, the {oxoferryl Cpd II, HisH⁺} configuration (Figure 2d) turned out to be not stable, and spontaneously evolved to the {hydroxoferryl Cpd II, His} configuration (Figure 2e) during geometry optimization. In order to preclude this water-mediated proton transfer between the distal His and the ferryl oxygen (Figure 4), the N_ε-H distance was fixed. The hydroxoferryl form of Cpd II was found to be more stable than the oxoferryl form by 10.7 / 7.4 kcal mol⁻¹ (heme b / heme d). Therefore, our results suggest that Cpd II of catalases is most likely protonated.

The main structural change upon protonation of the oxoferryl unit is to increase the Fe-O distance (from 1.70 Å to 1.74 Å, see Table 4), as expected for a change from a double Fe=O bond to a single Fe-OH bond. This in agreement with the long Fe-O distances observed in the crystallographic structures of Cpd II for several hemeproteins (Chapter I, Table 2).

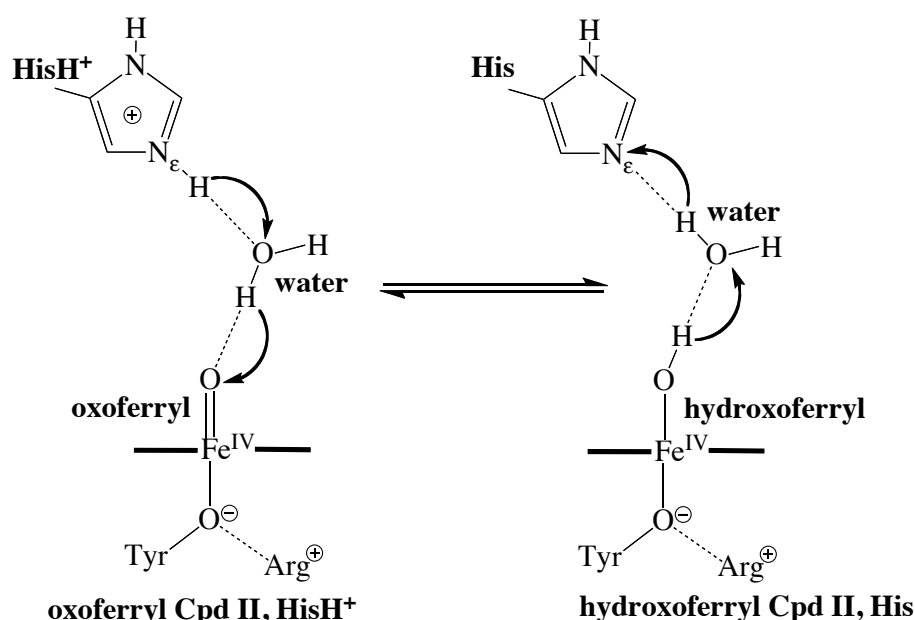


Figure 4. Interconversion between the oxoferryl and hydroxoferryl forms of Cpd II in model 4 (i.e. a water-mediated proton transfer).

In summary, *neither the planarity of the macrocycle nor the modification present in heme d modify significantly the structure of the reaction intermediates of catalases.* In particular, the iron-ligand distances are in agreement with previous calculations on heme b models with the same axial ligation (Green, 2001; Rydberg, 2004; de Visser, 2006). *The oxoferryl forms (Fe=O) of Cpd I and Cpd II show a similar Fe-O distance (1.67-1.70 Å), which is shorter than the hydroxoferryl form (Fe-OH) of Cpd II (1.74 Å).* Our results also suggest that *catalase Cpd II is most likely protonated*, because the proton transfer from the distal His to the oxoferryl Cpd II was found to be spontaneous.

3.2. Structural comparison with other hemeproteins

Table 5 shows the Fe-O distances calculated for the oxo- and hydroxoferryl forms of Cpd I and Cpd II for several hemeproteins. Regardless of the axial ligation, *all the oxoferryl forms show a short Fe-O distance (1.62-1.71 Å)*, which lengthens slightly with hydrogen bonding to the ferryl oxygen (1.66-1.72 Å). Our results (1.67-1.70 Å) are in line with these previous computational studies for heme-b containing proteins. Additionally, they demonstrate that *the modification present in heme d does not affect the Fe-O distance*.

By contrast, *the hydroxoferryl form of Cpd II exhibit a longer Fe-O distance (1.77-1.85 Å)*, consistent with the change from a double Fe=O to a single Fe–OH bond (see Table 5). Our results for both hemes (1.74 Å), albeit slightly shorter than previous studies, are in agreement with the lengthening of the Fe-O bond upon protonation. Most likely, the constraints on the position of the distal His imposed in our geometry optimizations do not allow the Fe-O bond to relax up to the expected ~ 1.8 Å equilibrium value (Table 5). In the QM/MM calculations of Chapter IV we will obtain an Fe-O distance of 1.78-1.80 Å, closer to the previously reported values (Table 5).

Recently, the protonation status of Cpd II has been debated in terms of the observed Fe-O distances (see Chapter I, section 4.3.). Distances ~ 1.8 Å are indicative of a hydroxoferryl Cpd II, whereas shorter bond lengths (~ 1.7 Å) correspond to an oxoferryl Cpd II. Because the Fe-O bond lengths observed for Cpd II crystal structures is 1.80-1.92 Å, the general consensus is that, in most hemeproteins, Cpd II bears a hydroxoferryl Fe–OH moiety (i.e. reduction of the porphyrin cation radical is accompanied by protonation of the ferryl oxygen) (Silaghi-Dumitrescu, 2004; Nilsson, 2004; Green, 2004; Rovira, 2005; Hersleth, 2006; Behan, 2006; Stone, 2006). In line with this hypothesis, our geometry optimizations of model 4 in the {oxoferryl Cpd II, HisH⁺} configuration yield a spontaneous proton transfer from the distal His to the ferryl oxygen¹, yielding a hydroxoferryl Cpd II (Figure 4). Therefore, *our results strongly suggest that catalase Cpd II contains a hydroxoferryl moiety*.

¹ A similar result was also obtained for a thiolate-ligated oxoferryl Cpd II model (Silaghi-Dumitrescu, 2004), but not for imidazole-ligated models (Silaghi-Dumitrescu, 2004; Bathelt, 2005), probably due the stronger push effect of thiolate or tyrosinate ligands compared to imidazole (Silaghi-Dumitrescu, 2004).

Table 5. Computed Fe-O distances for Cpd I and Cpd II (oxoferryl and hydroxoferryl forms). All the hemeproteins studied contain heme b and differ in the axial ligation, which is shown in parentheses. The exchange-correlation functional used in the calculations is also indicated.

catalase (Tyr⁻...Arg⁺)		
model	Fe-O distance (Å)	references
Cpd I, Fe=O	B3LYP: 1.62-1.66	Nilsson, 2004; Sicking; 2007; Green, 2001; de Visser, 2006
Cpd II, Fe=O	B3LYP: 1.63-1.66 VBP: 1.65 BP86: 1.67-1.68, 1.70 ^a	B3LYP: Nilsson, 2004 VBP: Horner, 2006 BP86: Rovira, 2005
Cpd II, Fe-OH	BP86: 1.77 B3LYP: 1.78-1.80 VBP: 1.79, PW91: 1.79	BP86: Rovira, 2005 B3LYP: Nilsson, 2004; Green 2006; Behan, 2006 VBP: Horner 2006 & 2007 PW91: Ghosh, 2006
peroxidase (His...Asp⁻) / myoglobin (His)		
model	Fe-O distance (Å)	references
Cpd I, Fe=O	B3LYP: 1.63-1.67, 1.66-1.70 ^a VBP: 1.64 BP86: 1.63-1.67	B3LYP: Nilsson, 2004; Green, 2000; Bathelt, 2005; Derat, 2005 VBP: Deeth, 1999 BP86: Silaghi-Dumitrescu, 2004 & 2005
Cpd II, Fe=O	von Barth-Hedin: 1.62 B3LYP: 1.63-1.68, 1.67-1.71 ^a BP86: 1.65-1.69, 1.69 ^a PW91: 1.66-1.67 VWN: 1.68	von Barth-Hedin: Ghosh 1994 B3LYP: Nilsson, 2004; Green 2006; Behan, 2006; Derat, 2006b BP86: Silaghi-Dumitrescu 2004 & 2005; Rovira, 2005; Hersleth, 2006; Ghosh 1994 PW91: Harris & Loew, 1995 VWN: Kuramochi, 1997
Cpd II, Fe-OH	B3LYP: 1.76-1.81, 1.79-1.89 ^a , BP86: 1.78-1.80	B3LYP: Nilsson, 2004; Green 2006; Behan, 2006; Derat, 2006b BP86: Silaghi-Dumitrescu 2004 & 2005; Hersleth, 2006
P450 (Cys⁻) / CPO (Cys⁻)		
model	Fe-O distance (Å)	references
Cpd I, Fe=O	B3LYP: 1.63-1.66, 1.66-1.69 ^a , BP86: 1.66, 1.72 ^a	B3LYP: Hersleth, 2006; Green, 1999; Stone, 2006; Schöneboom, 2002; Ogliaro, 2000 & 2001 BP86: Silaghi-Dumitrescu, 2004 & 2005
Cpd II, Fe=O	B3LYP: 1.66-1.67, BP86: 1.71	B3LYP: Hersleth, 2006; Stone, 2006; Behan, 2006; , Stone, 2006a,b; Lai, 2009 BP86: Silaghi-Dumitrescu, 2004 & 2005
Cpd II, Fe-OH	B3LYP: 1.80-1.83, 1.88-1.93 ^a PW91: 1.83, BP86: 1.85	B3LYP: Hersleth, 2006; Stone, 2006; Behan, 2006; Stone, 2006a,b; Lai, 2009 PW91: Ghosh, 2006 BP86: Silaghi-Dumitrescu 2004 & 2005

^a The oxoferryl group is hydrogen-bonded to the distal residues.

3.3. Electronic configuration

The location of the unpaired electrons in the gas phase catalase models was investigated by analyzing their spin density distributions. As explained in Chapter I (section 4.2.), Cpd I models of hemeproteins are expected to show unpaired spin density in the Fe=O moiety and over the porphyrin ring, whereas Cpd II models should have it only on the Fe=O moiety, due to the reduction of the porphyrin cation radical.

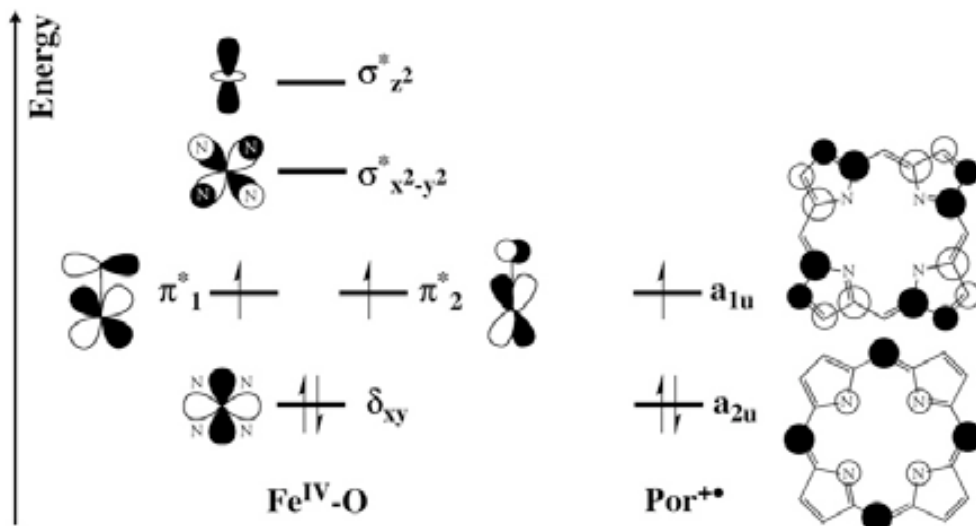


Figure 5. High-lying occupied and low-lying virtual orbitals of Cpd I for a Por-Fe^{IV}=O system with C_{4v} symmetry. Adapted from (de Visser, 2003). The π^*_1 and π^*_2 Fe-O orbitals result from the combination of the iron d_{xz} and d_{yz} orbitals with the p_x and p_y orbitals of the oxygen atom. The porphyrin high-lying orbitals should be named a_2 and a_1 for a C_{4v} symmetry, but we keep the same nomenclature as for a perfectly symmetric D_{4h} porphyrin (a_{1u} and a_{2u}), as done in the literature.

The spin density distribution of Cpd I models results from two singly occupied Fe-O π^* orbitals and one half-filled porphyrin orbital (Figure 5). For an oxoferryl porphyrin (Por-Fe^{IV}=O) with perfect C_{4v} symmetry, the a_{1u} and a_{2u} porphyrin orbitals are very close in energy (Ghosh, 1994; Liao & Scheiner, 2002), and thus small perturbations can easily alter their relative ordering (de Visser, 2003 & 2006). Depending on which of the two orbitals turns out to be higher in energy, the electron removed from the porphyrin during Cpd I formation can be abstracted from either the a_{1u} or the a_{2u} orbital, and thus the symmetry of the resulting porphyrin cation radical can be either A_{1u} or A_{2u}, respectively (Chapter I, section 4.1.). Upon reduction from Cpd I to Cpd II, the added electron usually fills the hole on the porphyrin, and thus in Cpd II models only the π^*_{FeO} orbitals bear unpaired electrons.

• *Model 1*

The spin density distributions for model **1** are depicted in Figure 6. Cpd I models show unpaired spin density on the FeO unit and delocalized over the porphyrin ring, in agreement with EPR experiments (Benecky, 2003). Let us first focus on the planar conformation of Cpd I (Figures 6a and 6b). For heme b planar Cpd I (Figure 6a) the spin density on the porphyrin is delocalized over the C_α and C_β atoms of the pyrroles (i.e. the porphyrin cation radical shows an A_{1u} symmetry). This is in line with previous UHF investigations (Strich & Veillard 1981 & 1983) on a Porp-Fe^{IV}=O system with perfect C_{4v} symmetry, which also found an A_{1u} porphyrin cation radical (see Figure 7). Besides, the positive (blue) spin density on the pyrrolic nitrogens and the meso carbons (i.e. A_{2u} symmetry) indicates some mixing between the a_{1u} and a_{2u} porphyrin orbitals. The two high-lying porphyrin orbitals are close in energy, and because in model **1** the porphyrin is not symmetric, they are allowed to mix.

The same spin density distribution (A_{1u}) is observed for heme d planar Cpd I (Figure 6b), consistent with the experimental observation that chlorins (i.e. porphyrins with one less double bond, as heme d) form cation radicals with A_{1u} symmetry (Hanson, 1981; Ozawa, 1994; Kitagawa, 1994). As depicted in Figure 7, the loss of the double bond across the C_β atoms of pyrrole III is expected to increase the energy of the a_{1u} orbital compared to porphyrins, because the a_{1u} orbital has contributions from the pyrrole β carbon atoms. Therefore, albeit higher in energy, the a_{1u} orbital is the HOMO of heme d planar Cpd I, as it is for C_{4v} Por-Fe^{IV}=O and heme b planar Cpd I. As a consequence, in the three cases the electron removed from the porphyrin during Cpd I formation is abstracted from the a_{1u} orbital, and thus the porphyrin cation radical displays A_{1u} symmetry.

Unlike the planar conformation, in heme b distorted Cpd I (Figure 6c) the spin density on the porphyrin is delocalized over the pyrrole nitrogens and the meso carbons (i.e. A_{2u} symmetry). The destabilization of the a_{2u} orbital with respect to a_{1u} can be rationalized in terms of the interaction between the a_{2u} porphyrin orbital and the δ_{xy} iron orbital (Figure 7) (Vangberg & Ghosh, 1999). This interaction is only possible for the distorted conformations of heme b Cpd I, but not for the planar, because only when the porphyrin is deformed the two orbitals have the appropriate symmetry to mix (Vangberg & Ghosh, 1999). This orbital mixing allows the transfer of electron density from the doubly occupied δ_{xy} iron orbital to the half-filled a_{2u} porphyrin orbital. As a consequence, in the distorted heme b Cpd I the number of unpaired electrons on the porphyrin is

less than 1 (0.29 e), whereas on the FeO unit there are more than 2 (2.71 e), as observed for a peroxidase Cpd I model (Deeth, 1999).

By contrast, both the planar (Figure 6b) and the distorted (Figure 6d) conformations of heme d Cpd I show a A_{1u} porphyrin cation radical. As explained above, the loss of the double bond across the C_β atoms of pyrrole III destabilizes the a_{1u} orbital relative to a_{2u} , because the a_{1u} orbital has contributions from the β pyrrole carbon atoms, whereas the a_{2u} orbital does not (Figure 7). Therefore, the electron removed from the porphyrin during Cpd I formation in heme d is abstracted from the a_{1u} orbital. Since the half-filled porphyrin orbital in heme d Cpd I is the a_{1u} orbital (and the a_{2u} orbital is doubly occupied), the interaction between the a_{2u} porphyrin orbital and the δ_{xy} iron orbital (observed for heme b distorted Cpd I) is not favoured. Nevertheless, again some mixing between the a_{1u} and a_{2u} porphyrin orbitals can be inferred in view of the positive (blue) spin density on the pyrrolic nitrogens and the meso carbons (Figure 6d).

Regarding the Cpd II models (Figures 6e and 6f), the unpaired spin density is only delocalized on the FeO unit, as expected upon reduction of the porphyrin cation radical. The electronic configuration of Cpd II is thus $(\delta_{xy})^2 (\pi^*_1)^1 (\pi^*_2)^1 (a_{1u})^2 (a_{2u})^2$, i.e. an oxoferryl neutral porphyrin ($\{\text{Por-Fe}^{\text{IV}}=\text{O}\}$).

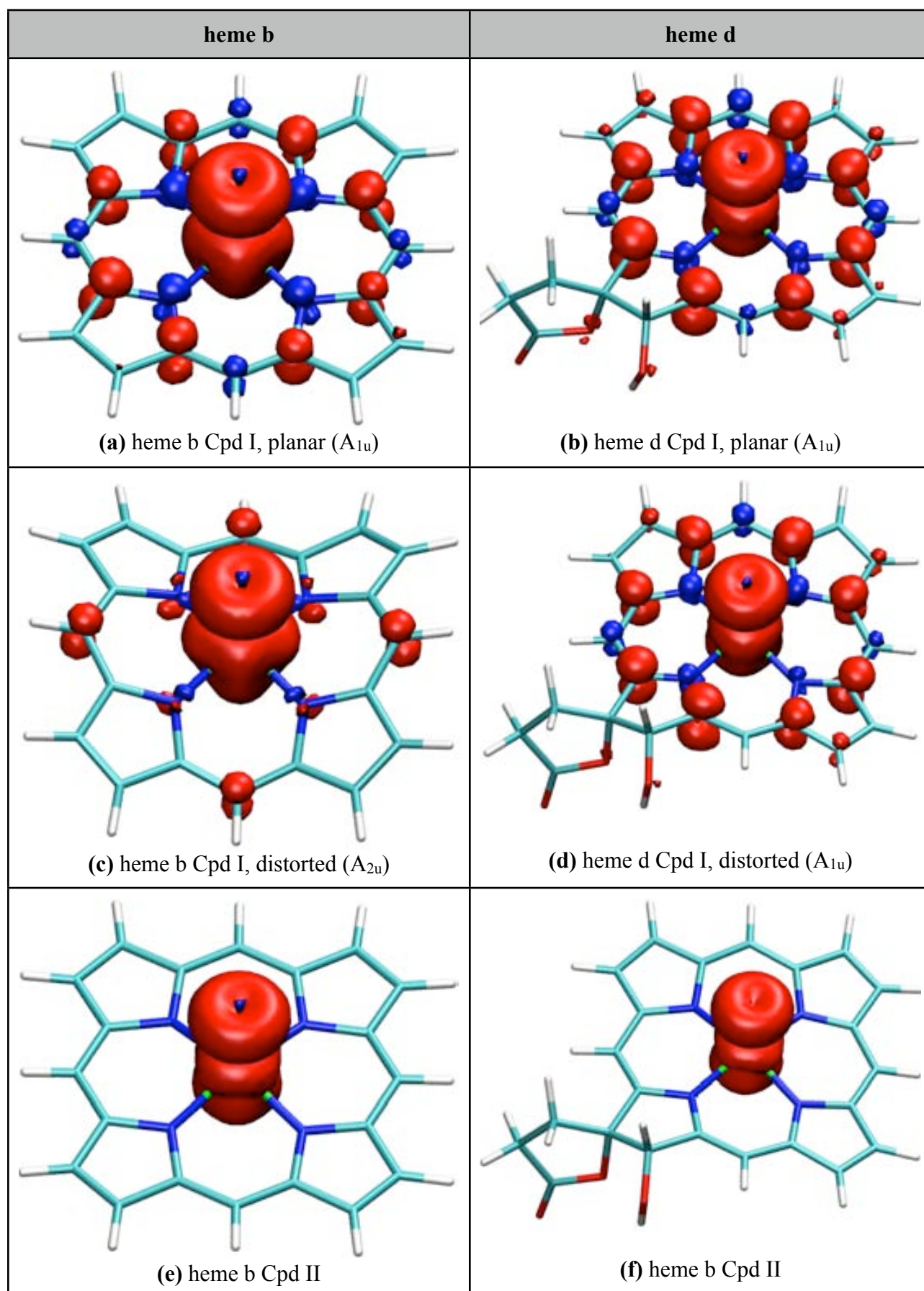


Figure 6. Spin density distributions of gas phase model 1. Spin isodensity surfaces are plotted at $0.004 e \text{ \AA}^{-3}$. The symmetry of the porphyrin radical in Cpd I models is indicated in parentheses.

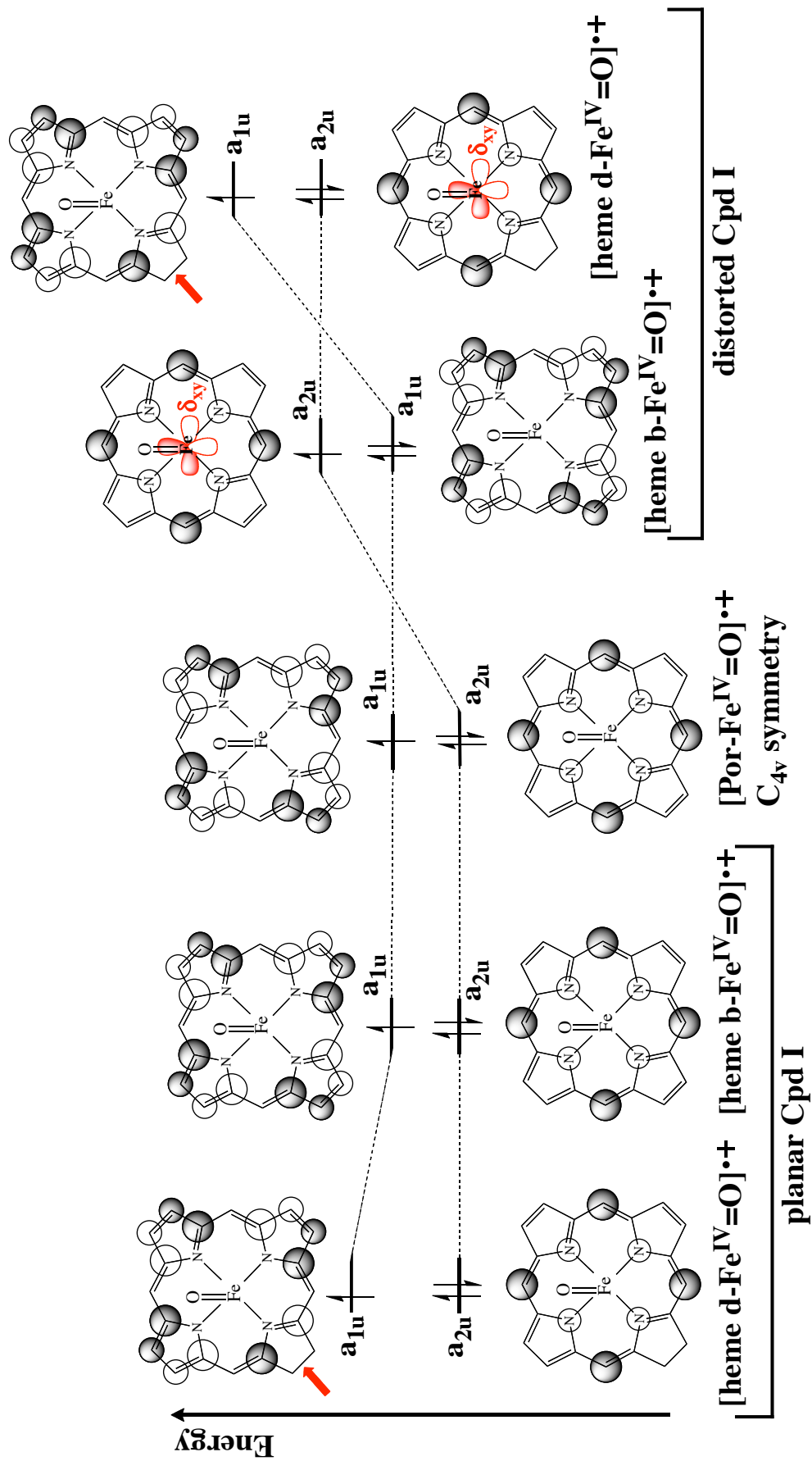


Figure 7. Changes on the relative energy of the a_{1u} and a_{2u} porphyrin orbitals of the oxoferryl porphyrin species as a result of the heme modification and distortion of the macrocycle.

A valence bond (VB) scheme can be used to rationalize these results. The electronic configuration of Cpd I in model 1 can be described using three different VB states (Figure 8). The two first VB structures correspond to a ferryl iron coupled to a porphyrin cation radical (i.e. {Por^{•+}-Fe^{IV}=O}), with either A_{1u} or A_{2u} symmetry, whereas the latter contains a perferryl iron (i.e. {Por-Fe^V=O}).

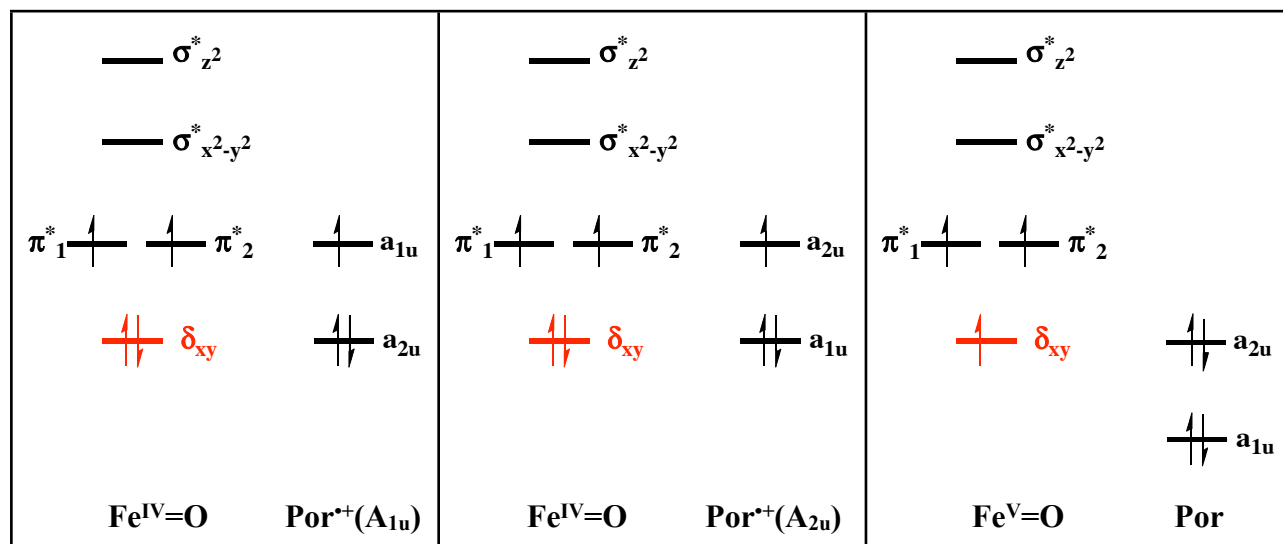


Figure 8. Possible valence bond (VB) states contributing to the electronic structure of Cpd I in model 1.

The planar conformation of heme b Cpd I (Figure 6a) and both conformations of heme d Cpd I (Figures 6b and 6d) have a larger contribution of the A_{1u} porphyrin radical state (i.e. {Por^{•+}(A_{1u})-Fe^{IV}=O}). By contrast, the distorted conformation of heme b Cpd I (Figure 6c) is best described as a combination of the A_{2u} porphyrin radical state (i.e. {Por^{•+}(A_{2u})-Fe^{IV}=O}) and the perferryl iron state (i.e. {Por-Fe^V=O}). This different electronic configuration explains the geometrical changes observed upon distortion (section 3.1.). The partial Fe^V character of the iron atom in the distorted conformation results in a smaller ionic radius and thus shorter Fe-N_{Porph} distances compared to the planar conformation (Table 1) (Vangberg & Ghosh, 1999). On the contrary, the Fe-O distance remains the same (Table 1), because the δ_{xy} orbital is non-bonding with respect to the Fe-O bond (see Figure 5).

- *Model 2*

Figure 9 shows the spin density distributions for model 2. Cpd I shows an A_{1u} porphyrin cation radical for both hemes (Figures 9a and 9b), similar to planar Cpd I in model 1. Indeed, in model 2 the optimized structures of both heme b and heme d Cpd I are rather planar. This planarity of the macrocycle allows conjugation of the porphyrin system with the vinyl substituents, and this will partially compensate the loss of aromaticity of the porphyrin upon radical formation. In line with this argument, the delocalization of the radical over the vinyl substituents (see Figure 9a,b) is probably due to the transfer of electron density from these β -substituents into the porphyrin. Because the a_{1u} orbital has contributions from the pyrrolic β carbon atoms, this electron donation favours the formation of an A_{1u} porphyrin cation radical (Figure 10). At the same time, the planarity of the porphyrin does not favour the formation of an A_{2u} porphyrin cation radical, because for a planar porphyrin the $\delta(\text{Fe}) - a_{2u}(\text{Por})$ orbital interaction is not symmetry-allowed. Notwithstanding, again the positive (blue) spin density on the pyrrole nitrogens and the meso carbons indicates some mixing between the a_{1u} and a_{2u} orbitals, and suggests that the energy gap between the two high-lying porphyrin orbitals is small.

The spin density distributions displayed by Cpd II models (Figure 9c and 9d) are identical to model 1 (Figures 6e and 6f). The unpaired spin density is localized only in the FeO unit, as expected upon reduction of the porphyrin cation radical.

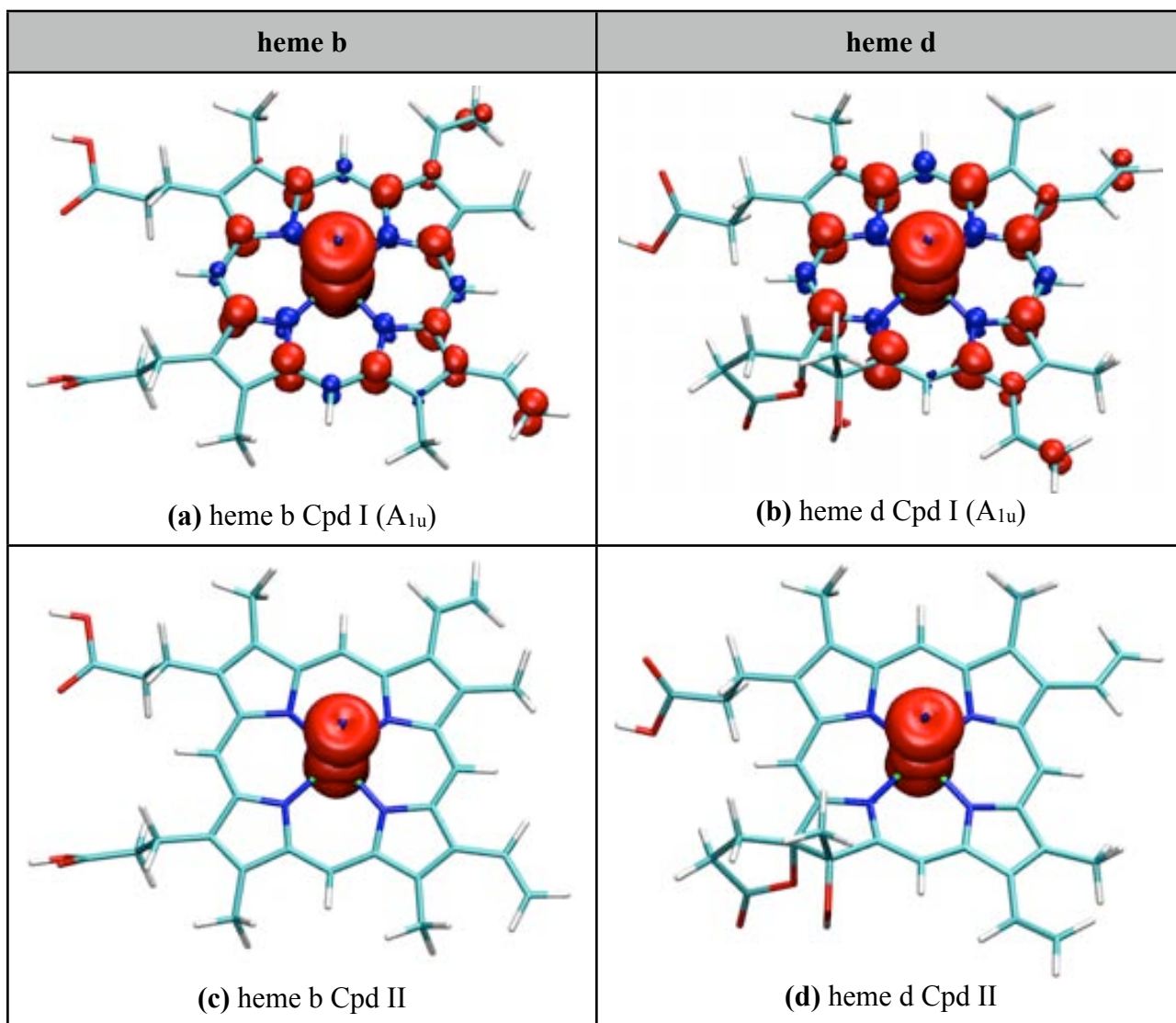


Figure 9. Spin density distributions of gas phase model 2. Spin isodensity surfaces are plotted at $0.004 e \text{ \AA}^{-3}$. The symmetry of the porphyrin cation radical in Cpd I models is indicated in parentheses.

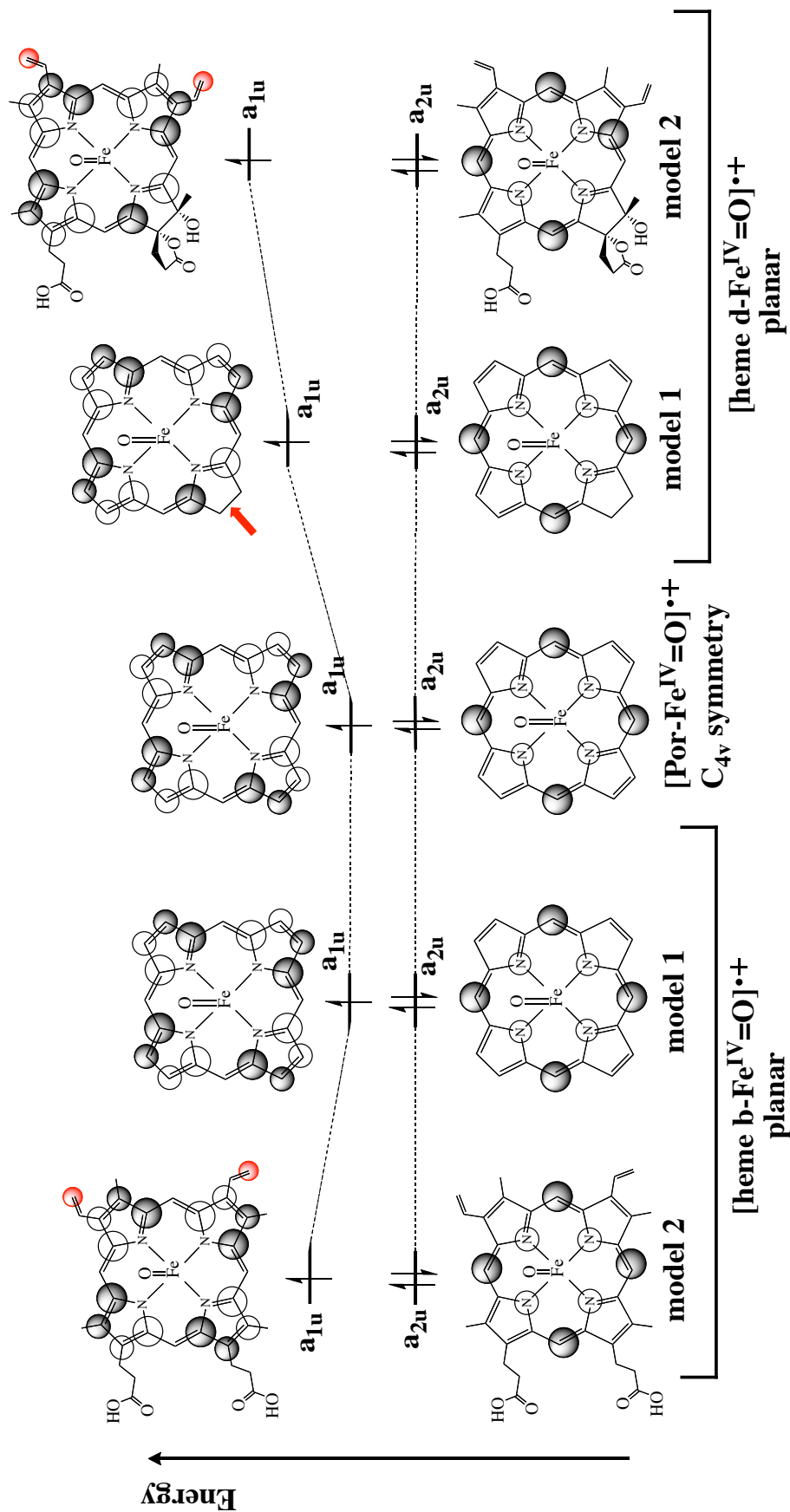


Figure 10. Changes on the relative energy of the a_{1u} and a_{2u} porphyrin orbitals of the oxoferryl porphyrin species as a result of the conjugation with the vinyl substituents.

• Model 3

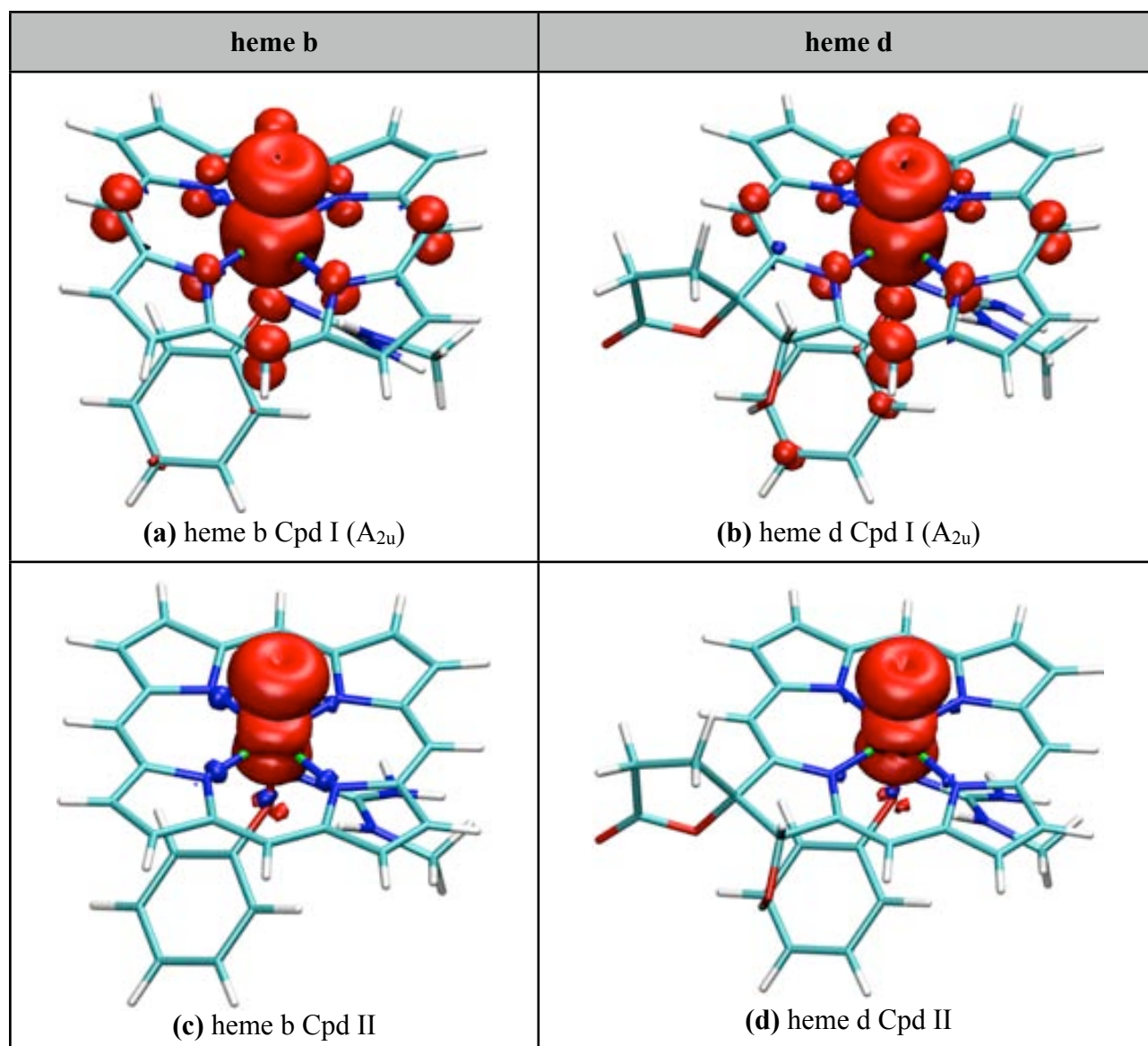


Figure 11. Spin density distributions of gas phase model **3**. Spin isodensity surfaces are plotted at $0.004 e \text{ \AA}^{-3}$. The symmetry of the porphyrin cation radical in Cpd I models is indicated in parentheses.

Figure 11 shows the spin density distributions for model **3**. Similar to model **1**, Cpd I is quite distorted for both heme b and heme d cofactors (see Figures 11a and 11b). Hence, heme b Cpd I shows a porphyrin cation radical with A_{2u} symmetry (Figure 11a), as the distorted conformation in model **1** (Figure 6c). Heme d Cpd I also exhibits an A_{2u} symmetry, what might seem unexpected in view of the A_{1u} porphyrin cation radical displayed by the model **1** counterpart. However, here we need to take into account the additional influence of the axial ligand. Owing to the interaction between the π system of the proximal phenolate (π_{Tyr}) and the a_{2u} orbital (Green, 2001; de Visser, 2006), the electron removed from the porphyrin during Cpd I formation is actually abstracted from

a mixed $\{a_{2u} - \pi_{\text{Tyr}}\}$ orbital (Figure 12). This is reflected in the delocalization of the radical onto the proximal Tyr (Figures 11a and 11b), in agreement with previous experimental (Chuang & Van Wart 1992) and computational studies (Rydberg, 2004; Green, 2001; de Visser, 2006).

Figure 12 depicts the relative energy of the high-lying porphyrin orbitals in distorted Cpd I, i.e. model **1** and model **3**. In heme b Cpd I, interaction of the a_{2u} orbital with the δ_{xy} iron orbital (occurring in both model **1** and model **3**) and mixing of the a_{2u} orbital with the HOMO of the Tyr (only in model **3**) result in the formation of an A_{2u} porphyrin cation radical. In heme d Cpd I, the loss of one double bond compared to heme b favours the formation of an A_{1u} porphyrin cation radical. In model **1**, the interaction of the a_{2u} orbital with the δ_{xy} iron orbital is not sufficient to overcome this intrinsic propensity for an A_{1u} state. In model **3**, the combined effect of the $a_{2u}-\delta_{xy}$ and $a_{2u}-\pi_{\text{Tyr}}$ interactions can eventually overcome this tendency to form an A_{1u} porphyrin cation radical, giving rise to an A_{2u} state.

Again, this can be rationalized using a valence bond (VB) description (Figure 13). As already proposed by de Visser (de Visser, 2006), two VB structures contribute to the electronic configuration of Cpd I in model **3** (Figure 13, top): an A_{2u} porphyrin cation radical state $\{\text{Por}^{\bullet+} (A_{2u})-\text{Fe}^{\text{IV}}=\text{O}, \text{Tyr}^-\}$ and a tyrosyl radical state $\{\text{Por}-\text{Fe}^{\text{IV}}=\text{O}, \text{Tyr}^{\bullet}\}$. The weight of each contribution depends on the energy gap between the a_{2u} porphyrin orbital and the HOMO of the Tyr. Delocalization onto the proximal Tyr is known to be decreased by hydrogen bonding to the proximal Arg (Green, 2001), and the protein electrostatics can also tune the energy difference between the A_{2u} porphyrin cation radical and tyrosyl radical states (de Visser, 2006). Besides, due to the distortion of the macrocycle, a perferryl iron state $\{\text{Por}-\text{Fe}^{\text{V}}=\text{O}, \text{Tyr}^-\}$ (Figure 13, bottom) could also participate in the electronic configuration of Cpd I, as in model **1**.

The spin density distribution of Cpd II models (Figures 10c and 10d) is very similar to the previous models and is consistent with an oxoferryl neutral porphyrin ($\{\text{Por}-\text{Fe}^{\text{IV}}=\text{O}\}$).

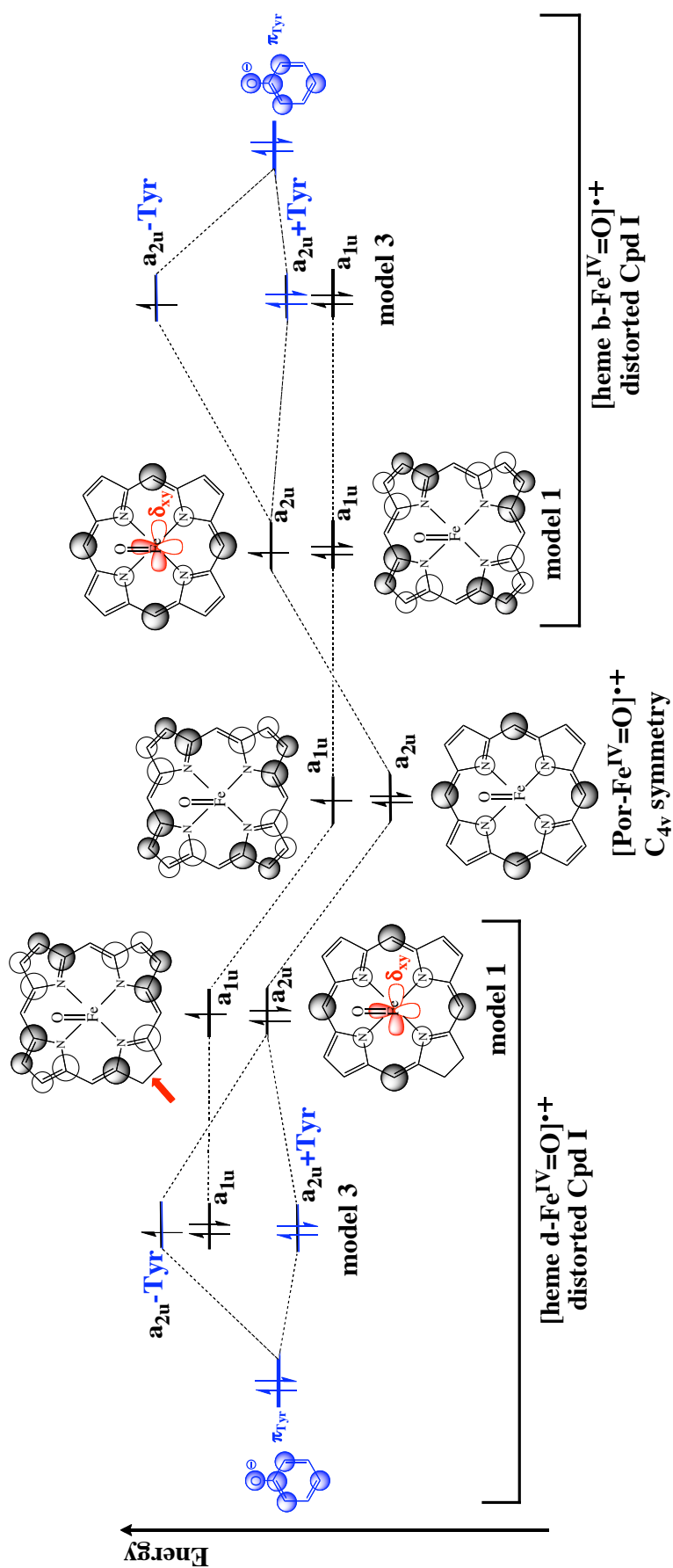


Figure 12. Changes on the relative energy of the a_{1u} and a_{2u} orbitals of the oxoferryl porphyrin species as a result of the axial ligation (shown in blue) in distorted Cpd I.

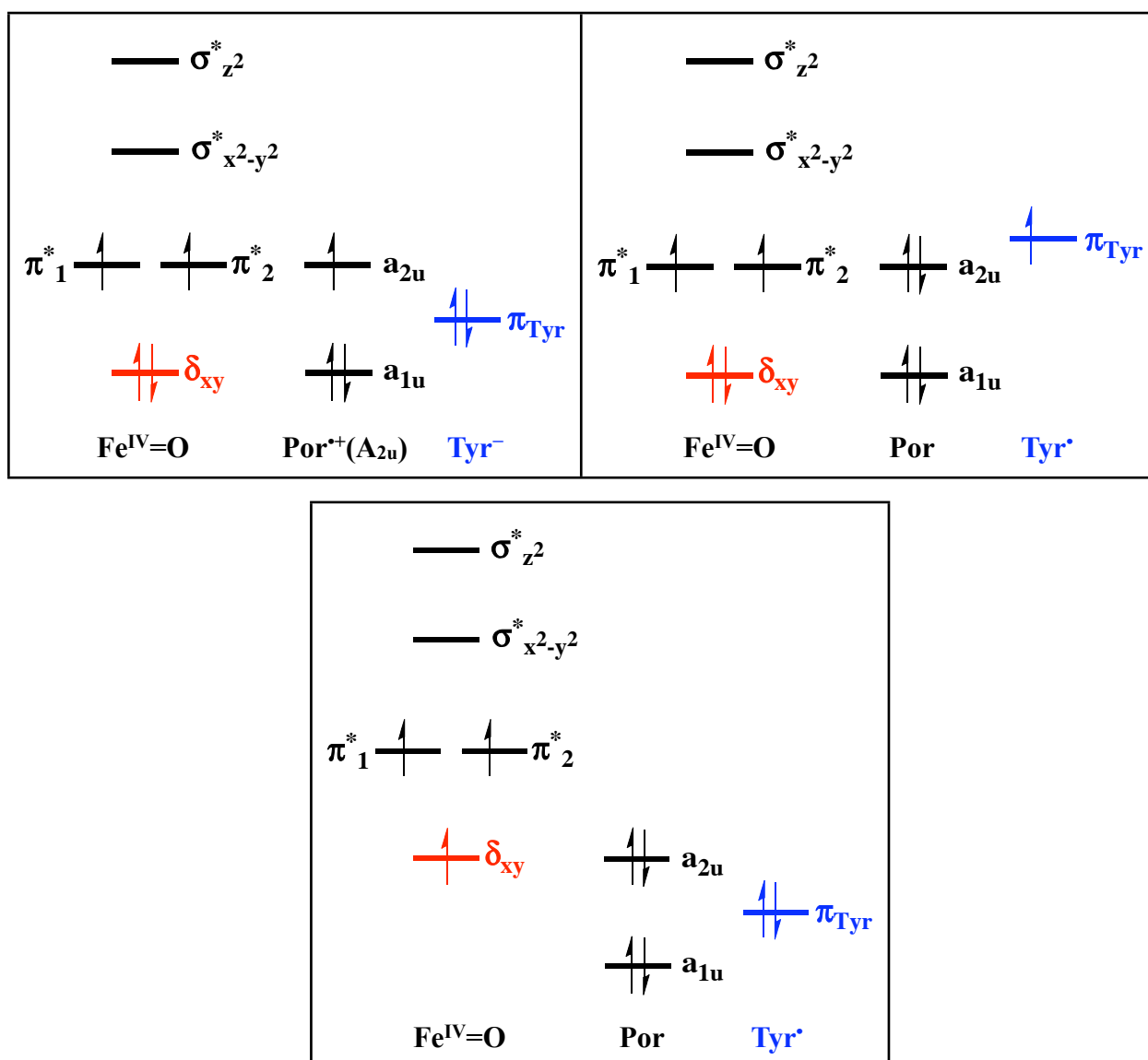


Figure 13. Possible valence bond (VB) states contributing to the electronic structure of Cpd I in model 3.

• *Model 4*

Figure 14 shows the spin density distributions for model 4. Similar to model 3, heme b Cpd I shows an A_{2u} porphyrin cation radical with some delocalization over the proximal phenolate (Figure 14a). However, in heme d Cpd I (Figure 14b) the symmetry of the unpaired spin density is the same as model 2 (A_{1u}), probably due to the loss of the macrocycle distortion (see below).

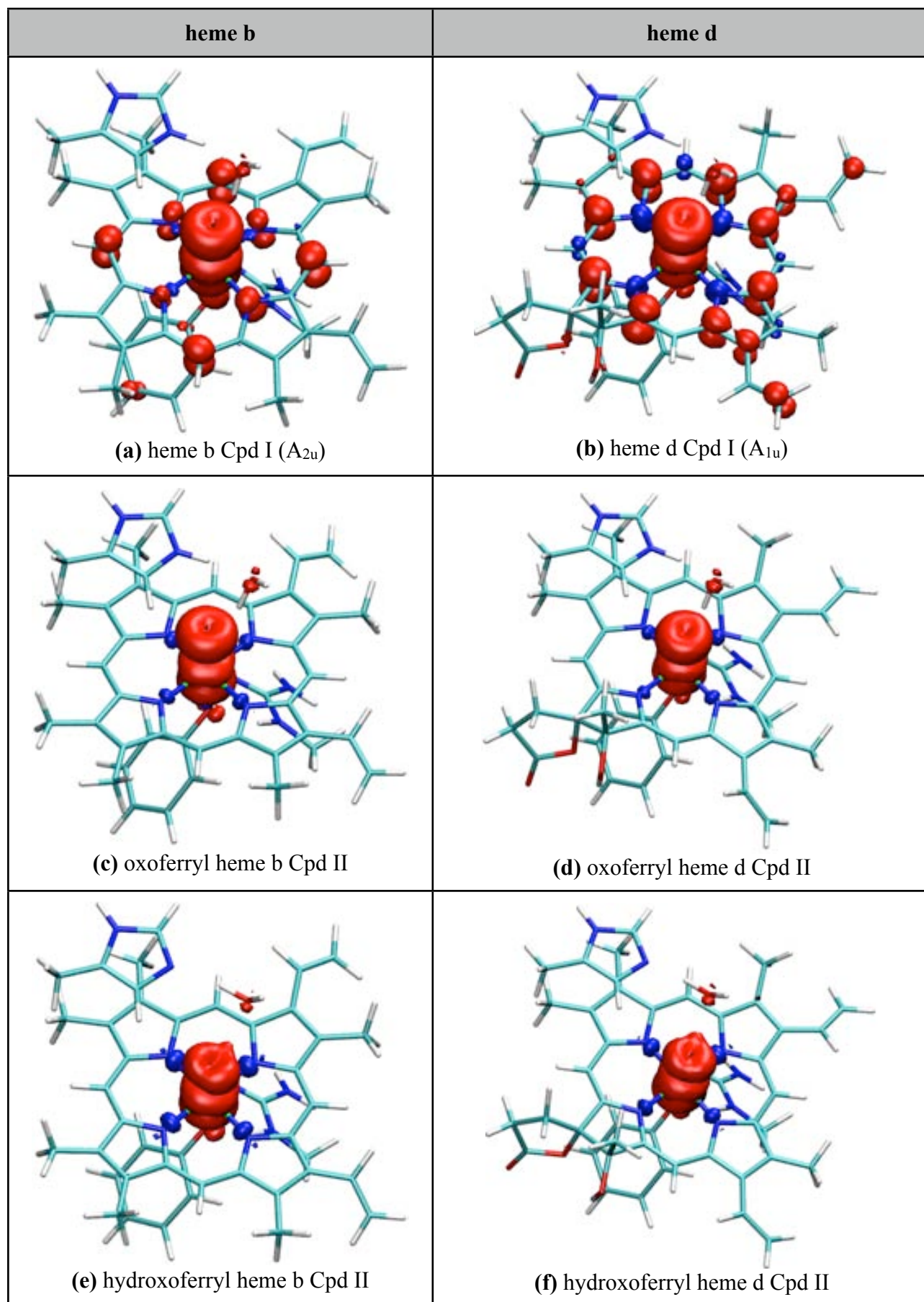


Figure 14. Spin density distributions of gas phase model 4. Spin Spin isodensity surfaces are plotted at $0.004 e \text{ \AA}^{-3}$. The symmetry of the Por^{*+} in Cpd I models is indicated in parentheses.

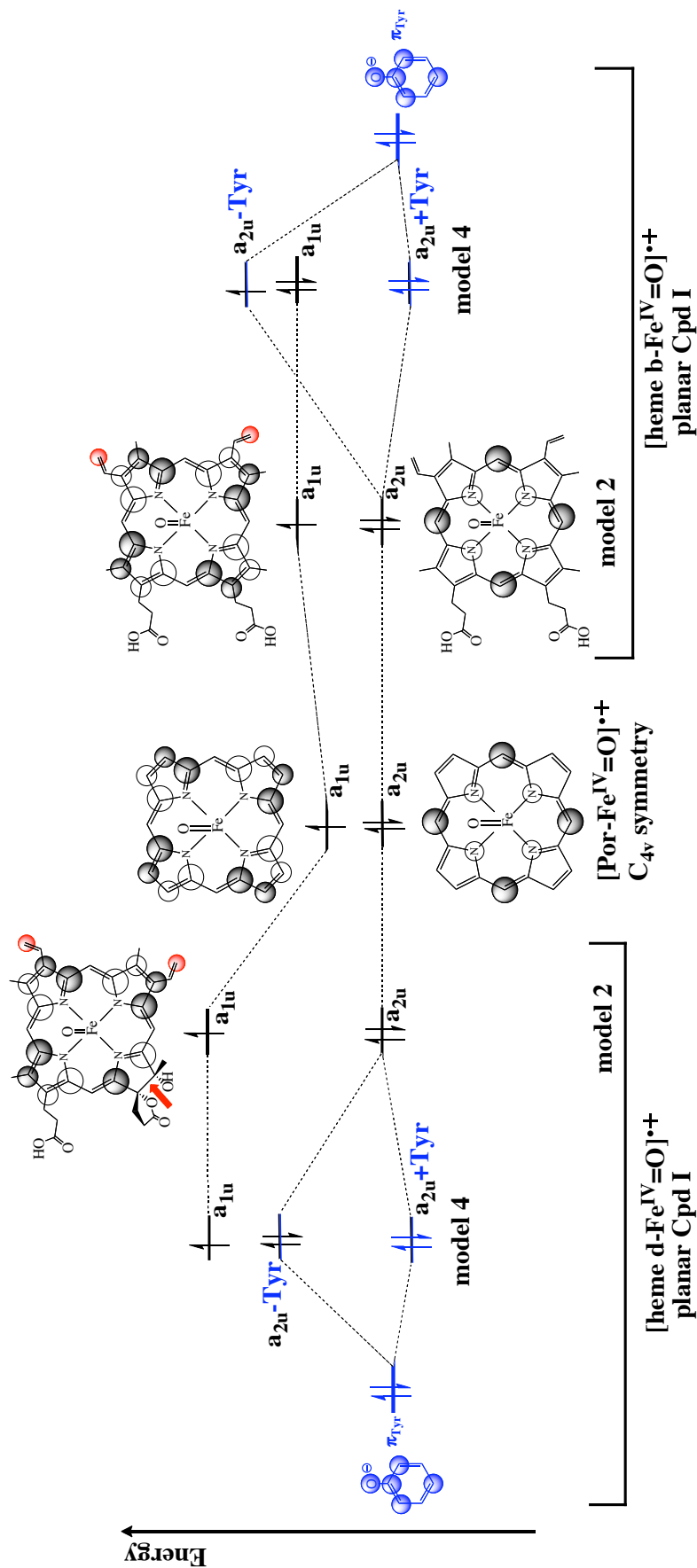


Figure 15. Changes on the relative energy of the a_{1u} and a_{2u} orbitals of the oxoferryl porphyrin species as a result of the axial ligation (shown in blue) in planar Cpd I.

Figure 15 depicts the relative energy of the high-lying porphyrin orbitals in planar Cpd I, i.e. model 2 and model 4. In both models, planarity of the macrocycle allows conjugation with the vinyl groups and electron donation from these β -substituents into the a_{1u} orbital, thus favouring an A_{1u} state. In heme b Cpd I, this effect is overcome by the mixing of the a_{2u} orbital with the HOMO of the Tyr, resulting in the formation of an A_{2u} porphyrin cation radical. By contrast, in heme d Cpd I, formation of an A_{1u} state is favoured by both the planarity of the macrocycle and the loss of the double bond across the β carbon atoms of pyrrole III. Therefore, the $a_{2u}-\pi_{\text{Tyr}}$ interaction is not sufficient to change the A_{1u} state into A_{2u} .

Overall, the spin density distributions of Cpd I models are in agreement with EPR experiments on synthetic compounds (Hanson, 1981). Porphyrin radicals (i.e. similar to heme b) were found to have an A_{2u} ground state, whereas chlorin radicals (i.e. similar to heme d) displayed an A_{1u} cation radical (Ozawa, 1992b; Jayaraj, 1995).

The unpaired spin density of Cpd II models (Figures 14c and 14d) is again fully localized on the FeO moiety, as expected. This spin density distribution does not change with protonation of the oxo group, i.e. oxoferryl (Figures 14c and 14d) versus hydroxoferryl Cpd II (Figures 14e and 14f).

• *Electronic structure of catalase Cpd I and Cpd II models*

The electronic structure of Cpd I in catalase is found to depend on the model and the type of heme. These changes in the symmetry of the spin density distribution (Table 6) can be rationalized in terms of the mixing between the a_{1u} and a_{2u} porphyrin orbitals, the δ_{xy} iron orbital and the HOMO of the proximal Tyr.

Table 6. Symmetry of the porphyrin cation radical in the different Cpd I models considered (Fig. 2).

Cpd I model	heme b	heme d
model 1 ^a	A_{2u}	A_{1u}
model 2	A_{1u}	A_{1u}
model 3	A_{2u}	A_{2u}
model 4	A_{2u}	A_{1u}

^a Distorted conformation (i.e. the most stable conformation of Cpd I in model 1).

As can be seen in Table 6, *heme b Cpd I preferentially forms an A_{2u} porphyrin cation radical, whereas an A_{1u} state is more likely for heme d Cpd I*, in agreement with experimental studies (Ozawa, 1992b; Jayaraj, 1995). Nevertheless, the results on the different models demonstrate that *the energy gap between the A_{1u} and A_{2u} $Por^{\bullet+}$ states is small and external perturbations (e.g. the protein environment) can easily change the symmetry of the porphyrin cation radical*. Furthermore, when the porphyrin is not symmetric, the a_{1u} and a_{2u} orbitals are allowed to mix, resulting in a porphyrin cation radical with contributions of both A_{1u} and A_{2u} states.

Besides, the a_{2u} porphyrin orbital can mix with other orbitals. On one hand, distortion of the macrocycle allows the interaction between the half-filled a_{2u} porphyrin orbital and the doubly occupied δ_{xy} iron orbital. Therefore, *upon distortion, the radical character of the porphyrin decreases at the expense of the iron electron density (i.e. the oxidation state of the iron increases)*. On the other hand, the a_{2u} porphyrin orbital can also mix with the HOMO of the proximal Tyr. As a result, *the proximal ligand has a partial tyrosyl radical character*, in line with previous studies (Chuang & Van Wart 1992; Green, 2001; de Visser, 2006).

In summary, as described for peroxidases (de Visser, 2003), *catalase Cpd I behaves as a chameleon species in response to small perturbations*.

3.4. Proposed valence bond model for the electronic structure of Cpd I

To explain the electronic structure of catalase Cpd I, we propose a valence (VB) model, extending the one suggested by de Visser and coworkers (de Visser, 2003 & 2006). According to the results of section 3.3. (Figures 8 and 13), four different VB states are of interest:

$$\begin{aligned} |a\rangle & \{Por^{\bullet+}(A_{2u})-Fe^{IV}=O, Tyr^{-}\} && (A_{2u} \text{ porphyrin cation radical}) \\ |b\rangle & \{Por^{\bullet+}(A_{1u})-Fe^{IV}=O, Tyr^{-}\} && (A_{1u} \text{ porphyrin cation radical}) \\ |c\rangle & \{Por-Fe^{IV}=O, Tyr^{\bullet}\} && (\text{tyrosyl radical}) \\ |d\rangle & \{Por-Fe^V=O, Tyr^{-}\} && (\text{perferryl iron}) \end{aligned}$$

and their combination gives rise to the actual electronic configuration Cpd I, i.e.

$$\Psi_{\text{Cpd I}} = c_a |a\rangle + c_b |b\rangle + c_c |c\rangle + c_d |d\rangle$$

The contribution of each state (c_a , c_b , c_c and c_d) depends on the energy gap among states, their orbital overlap and the difference in electrostatic energy (de Visser, 2003 & 2006).

The canonical Cpd I contains a ferryl iron (i.e. Fe^{IV}) coupled to a porphyrin cation radical ($\text{Por}^{\bullet+}$). For an ideal symmetric D_{4h} porphyrin, the two high-lying porphyrin orbitals (a_{1u} and a_{2u}) are practically degenerated (Liao & Scheiner, 2002), and thus either an A_{1u} or A_{2u} state can be formed (Figure 5). However, in reality Cpd I is not symmetric and both orbitals are allowed to mix. As a consequence, *the symmetry of the porphyrin cation radical reflects a mixture of the $|a\rangle$ and $|b\rangle$ VB states* (Figures 6a and 6b, and Figures 9a and 9b). For heme b Cpd I, $\Psi_{\text{Cpd I}}$ has more weight of the $|a\rangle$ state (Figure 6c and 14a), whereas heme d Cpd I has a larger contribution of the $|b\rangle$ state (Figures 6d and 14b).

The final shape of the unpaired spin density distribution also depends on the interaction of the a_{2u} porphyrin orbital with other orbitals (de Visser, 2003). On one hand, the a_{2u} porphyrin orbital can mix with the π system of the tyrosinate ligand (Figures 12 and 13). Because the proximal Tyr is a good electron donor (de Visser, 2006), it can transfer electron density into the porphyrin and thus *the proximal ligand acquires a partial tyrosil radical character* (Figures 11a and 11b and Figure 14a). The weight to the $|c\rangle$ state depends on the hydrogen bonding to the proximal Arg (Green, 2001; de Visser, 2006), the protein dielectric constant or electric fields (de Visser, 2006), because these factors tune the energy difference between the $|a\rangle$ and $|c\rangle$ states. On the other hand, *distorsion of the macrocycle increases the weight of the $|d\rangle$ VB state* (Figure 6c), by allowing the overlap between the porphyrin a_{2u} and the iron δ_{xy} orbital (Figure 7).

4. SUMMARY AND CONCLUSIONS

Catalases may contain two different types of heme groups: heme b and heme d (Figure 1) (Nicholls, 2001). Even though both heme b and heme d catalases form Cpd I and Cpd II as reaction intermediates, the influence of the type of heme on the structural and electronic properties of these intermediates is not known.

In this chapter we have been performed DFT calculations on gas phase models of heme b and heme d Cpd I and Cpd II with the objective of characterizing (i) the structure and electronic configuration of such intermediates and (ii) the impact of the different type of heme. The absence of the protein environment allows to study their intrinsic properties, independently of the different catalase protein sequences. Furthermore, by using different models (Figure 2) we have been able to

separate the effects of the bare cofactor (model 1), the substituents (model 2), the axial ligation (model 3) and the distal residues (model 4). The results obtained will be used in the forthcoming chapters of this thesis to interpret more complex systems.

Regardless of the model used, we found that *the structure of the reaction intermediates of catalases is not affected by the type of heme group*. In particular, *the Fe-O distance of the oxoferryl Cpd I and Cpd II models is 1.67-1.70 Å*, in agreement with previous computational (Table 5) and experimental studies (Chapter I, Table 2). The largest change is observed for hydroxoferryl Cpd II. *Protonation of the ferryl oxygen lengthens the Fe-O distance (1.74 Å)*, as expected for a change from a double (Fe=O) to a single (Fe–OH) bond (Table 5).

On the contrary, the electronic structure of catalase Cpd I is found to depend on the model and the type of heme. To explain these electronic properties, a valence (VB) scheme is proposed. Extending the previous scheme suggested by (de Visser, 2006), four VB structures are considered to account for the possible different symmetries of the porphyrin cation radical (A_{1u} or A_{2u}) or the delocalization of the radical into other sites (the proximal Tyr or the iron atom). In agreement with EPR experiments (Hanson, 1981), *heme b-containing Cpd I preferentially forms an A_{2u} porphyrin cation radical, whereas an A_{1u} state is more likely for heme d-containing Cpd I. The A_{2u} porphyrin cation radical is easily delocalized onto the proximal tyrosinate ligand*, as suggested by previous computational studies (Green, 2001; de Visser, 2006). Besides, *distorsion of the macrocycle decreases the radical character of the porphyrin and increases the oxidation state of the iron*. Therefore, as found in peroxidases (de Visser 2003), *catalase Cpd I behaves as a chameleon species in response to small perturbations*.

In summary, the conclusions of this chapter are the following:

- The structure of catalase Cpd I and Cpd II is similar to other hemeproteins.
- The modification present in heme d does not alter the structure of the reaction intermediates of catalase.
- The oxoferryl forms of Cpd I and Cpd II exhibit a short Fe=O bond (1.67-1.70 Å), whereas the hydroxoferryl form of Cpd II shows a longer Fe–OH bond (1.74 Å).
- Catalase Cpd II is likely to be protonated (i.e. Fe–OH)

- The electronic configuration of Cpd I can be easily changed by several factors, such as porphyrin distortion or the axial ligand, thus reflecting the chameleonic behaviour of this species.
- Heme b Cpd I forms preferentially an A_{2u} porphyrin cation radical, whereas an A_{1u} cation radical is more likely for heme d Cpd I.

STRUCTURE AND ELECTRONIC CONFIGURATION OF COMPOUND I INTERMEDIATES OF *HELICOBACTER PYLORI* AND *PENICILLIUM VITALE* CATALASES

M. Alfonso-Prieto, A. Borovik, X. Carpena,
G. Murshudov, W. Melik-Adamyanyan, I. Fita, C. Rovira, and P. C. Loewen.

The structures and electronic configuration of Compound I intermediates
of *Helicobacter pylori* and *Penicillium vitale* catalases
determined by X-ray crystallography and QM/MM Density Functional Theory calculations.

J. Am. Chem. Soc. **2007**, 129 (14), pp 4193–4205

1. INTRODUCTION

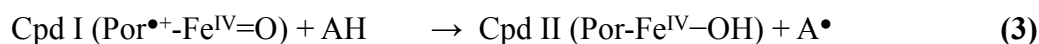
As explained in Chapter I, the primary intermediate of the *catalase* reaction is Compound I (Cpd I), a very strong oxidant that results from the reaction of the native enzyme with hydrogen peroxide (Nicholls, 2001). Alternatively, pseudo-substrates such as peroxyacetic acid ($\text{CH}_3\text{-COOOH}$, PAA) are used in the lab to prepare Cpd I for its characterization (Maté, 2001):



In some heme b-containing catalases, this stalled Cpd I is found to be barely stable and is prone to be reduced by a residue in the protein (aa = Tyr or Trp), forming Compound I* (CpdI*; see Chapter I, section 3.3.):



Additionally, in the presence of one-electron organic donors (AH), Cpd I may also be reduced to Compound II (Cpd II), i.e. the *peroxidatic* pathway (see Chapter I, section 3.3.):



Moreover, in crystallographic studies X-Ray irradiation may also photoreduce Cpd I, creating a mixture of different oxidation states (Chapter I, section 4.3.).



Therefore, one of the problems in the experimental characterization of Cpd I is to assign the electronic configuration of the species resulting from treatment with PAA (hereafter, *oxidized* catalase). A combination of techniques is often necessary to identify the actual intermediate formed (Cpd I, Cpd I* or Cpd II, see Figure 1).

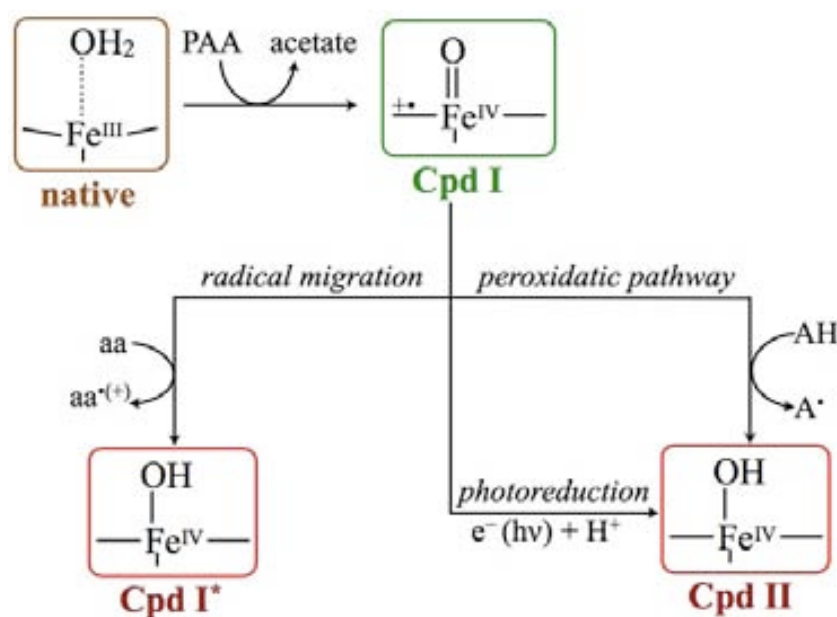


Figure 1. Possible intermediates formed upon treatment of catalase with peroxyacetic acid (PAA).

UV-visible and EPR spectroscopies as well as X-Ray diffraction have been used to investigate the oxidized intermediates of some catalases (Chapter I, section 4). ENDOR experiments have been recorded for PAA-treated *Micrococcus luteus* catalase (MLC) (Benecky, 1993) and *Proteus mirabilis* catalase (PMC) (Ivancich, 1997). They show the typical signature of a *canonical* Cpd I, a $S = 3/2$ oxoferryl unit in a ferromagnetic interaction with a $S = 1/2$ porphyrin π -cation radical (i.e. $\text{Por}^{\bullet+}\text{-Fe}^{\text{IV}}=\text{O}$). Differently, *Bovine liver* catalase (BLC) is found to form first the typical porphyrin cation radical, followed by one electron transfer from a protein residue, giving rise to an oxoferryl-tyrosyl radical intermediate (Ivancich, 1996). This species has been often denoted as Cpd II*, because it is isoelectronic to Cpd II in the heme and thus has similar spectral features (Chapter I, section 4.2.). Nevertheless, use of the Cpd II* notation is misleading, because it only reflects the oxidation state of the heme (the main chromophore in the UV-visible studies), whereas the overall protein-heme complex has lost two electrons (i.e. one from the heme and another from a protein residue). It would be preferable to use a terminology that accurately reflects the oxidation state of the complete protein-heme complex. Therefore, we will use the notation Cpd I*, indicating that the oxoferryl-protein radical intermediate has lost two electrons with respect to the resting state, as in the classic Cpd I. In both Cpd I and Cpd I* the iron is oxidized (i.e. Fe^{IV}), and only the second oxidation site is different, either the porphyrin (in Cpd I) or a protein residue (in Cpd I*). Moreover, this notation also recalls that Cpd I* is formed from Cpd I, by electron transfer from a protein residue to the porphyrin cation radical (Figure 1). On the contrary, in Cpd II only the iron is oxidized, since the second radical site has been reduced by an external donor, either a peroxidatic substrate or an electron generated by the X-Ray photons (Figure 1).

The first reported X-Ray structure for an oxidized catalase corresponds to oxidized PMC (Andreoletti, 2003), which is expected to contain Cpd I (i.e. $\text{Por}^{\bullet+}\text{-Fe}^{\text{IV}}=\text{O}$), taking into account the ENDOR experiments mentioned above (Ivancich, 1997). However, the observed Fe-O distance (1.76 Å, see Table 1) is intermediate between a Fe=O double bond (1.63-1.70 Å, according to DFT calculations, see Chapter III, Table 5) and a Fe-OH single bond (1.77-1.81 Å, see Chapter III, Table 5). Hence, it is not possible to discriminate whether the ferryl oxygen is protonated or not. Moreover, the low resolution of the structure (2.5 Å) and the use of restraints in the Fe-O distance during the refinement preclude a high confidence in the Fe-O bond length.

The second X-Ray structure corresponds to oxidized MLC at 2.0 Å resolution (Murshudov, 2002). It exhibits a Fe-O bond length of 1.87 Å (Table 1), indicative of a hydroxoferryl group, and,

due to the observed colour change from green to red (Chapter I, section 4.2.), it was assigned to bear a Cpd II (Murshudov, 2002). Nevertheless, the conversion of Cpd I to the presumed Cpd II occurred spontaneously in the absence of added reducing agent and before exposure to X-Rays, excluding a peroxidatic or a radiation-induced reduction (see Figure 1). Therefore, the observed reduction of the porphyrin cation radical is only consistent with an electron transfer from a protein residue, i.e. Cpd I* and not Cpd II is present in the sample (Figure 1).

Table 1. Reported crystal structures of the oxidized intermediates of catalases.

protein [PDB accession no.]	heme	resolution (Å)	Fe-O length (Å)	reference
PMC [1MQF]	heme b	2.5	1.76	Andreoletti, 2003
MLC [1GWF]	heme b	2.0	1.87	Murshudov, 2002
HPC [2IQF]	heme b	1.8	1.80 / 1.85 ^a	Alfonso-Prieto, 2007
PVC [2IUF]	heme d	1.7	1.72 / 1.72 ^a	Alfonso-Prieto, 2007

^a Values corresponding to the two independent protein subunits. Abbreviations used: PMC, *Proteus mirabilis* catalase; MLC, *Micrococcus lysodeikticus* catalase; HPC, *Helicobacter pylori* catalase; PVC, *Penicillium vitale* catalase.

Recently, high-resolution structures of PAA-treated *Helicobacter pylori* catalase (HPC) and *Penicillium vitale* catalase (PVC) and their UV-visible spectra have been obtained by the groups of P. Loewen (University of Manitoba) and I. Fita (IBMB-CSIC) (Alfonso-Prieto, 2007). HPC is a small subunit catalase containing heme b, whereas PVC is a large subunit catalase containing heme d (see Chapter I, section 3.1.). Both catalases share the same core structure (Figure 2), but PVC has an additional C-terminal domain with a flavodoxin-like structure. Besides, in PVC the heme group has been modified, such that the double bond across the C_β atoms of pyrrole III is saturated and the propionate sidechain has been converted into a *cis*-hydroxy- γ -spirolactone (Figure 2b). In collaboration with these experimental groups, we have performed DFT QM/MM calculations on the crystallographic structures of oxidized HPC and PVC with the objectives of (i) helping to assign the protonation state of the active site and (ii) elucidating the electronic changes caused by the heme modification (Figure 2b).

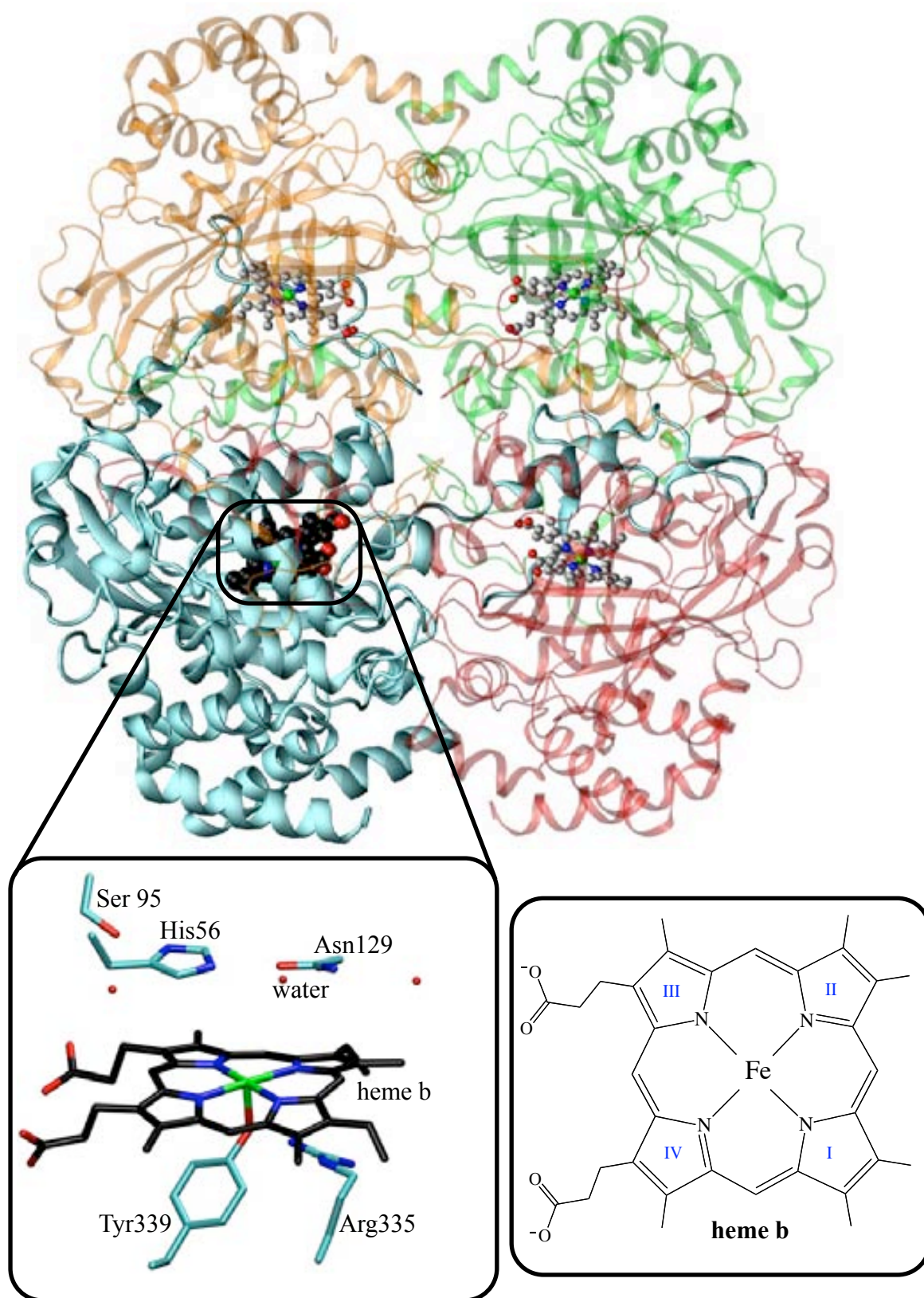


Figure 2. (a) Structure of *Helicobacter pylori* catalase (HPC). *Top*: cartoon picture of the protein, with the four subunits colored in blue, red, yellow and green, respectively. *Bottom*: heme binding pocket of one of the subunits (blue) and molecular structure of the heme b prosthetic group.

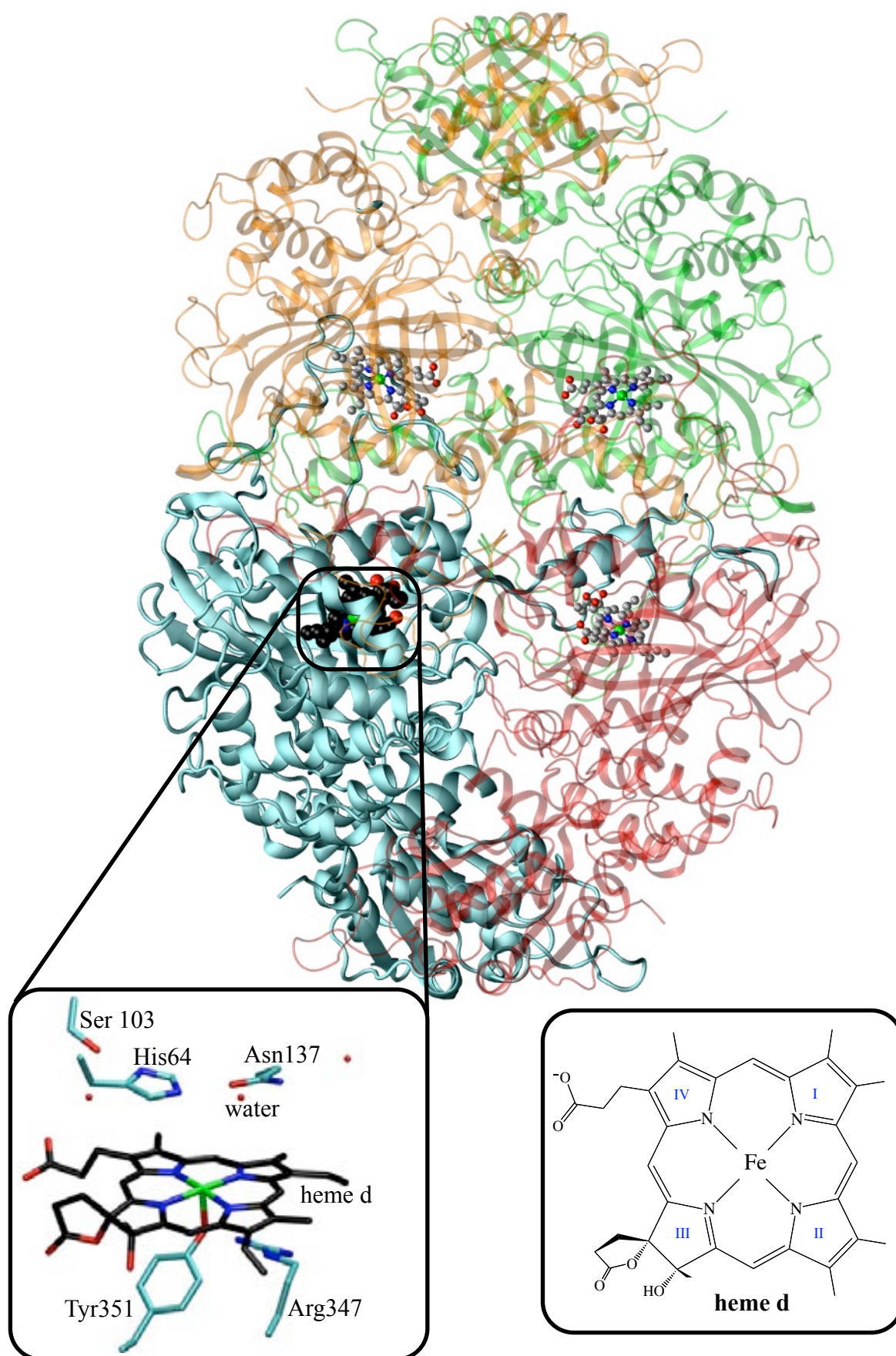


Figure 2. (b) Same representation for *P. vitale* catalase (PVC) and molecular structure of the heme d prosthetic group.

Oxidized PVC shows a short Fe-O bond length (1.72 Å, see Table 1) and is green coloured (Figure 3a), indicative of a canonical Cpd I (i.e. $\text{Por}^{\bullet+}\text{-Fe}^{\text{IV}}=\text{O}$). On the contrary, oxidized HPC exhibits a long Fe-O distance (1.80 / 1.85 Å, see Table 1) and is red-coloured (Figure 3b). This suggests that the ferryl oxygen has become protonated and that the porphyrin cation radical has been reduced by a protein residue, because the red colour is observed in the absence of added one-electron donor and before exposure to X-Rays, as for MLC. For comparison, treatment of BLC with PAA produces a spectrum (Figure 3c) consistent with Cpd I, and only with subsequent addition of a one-electron donor (ferrocyanide) does a typical Cpd II spectrum appear (Nicholls, 2001).

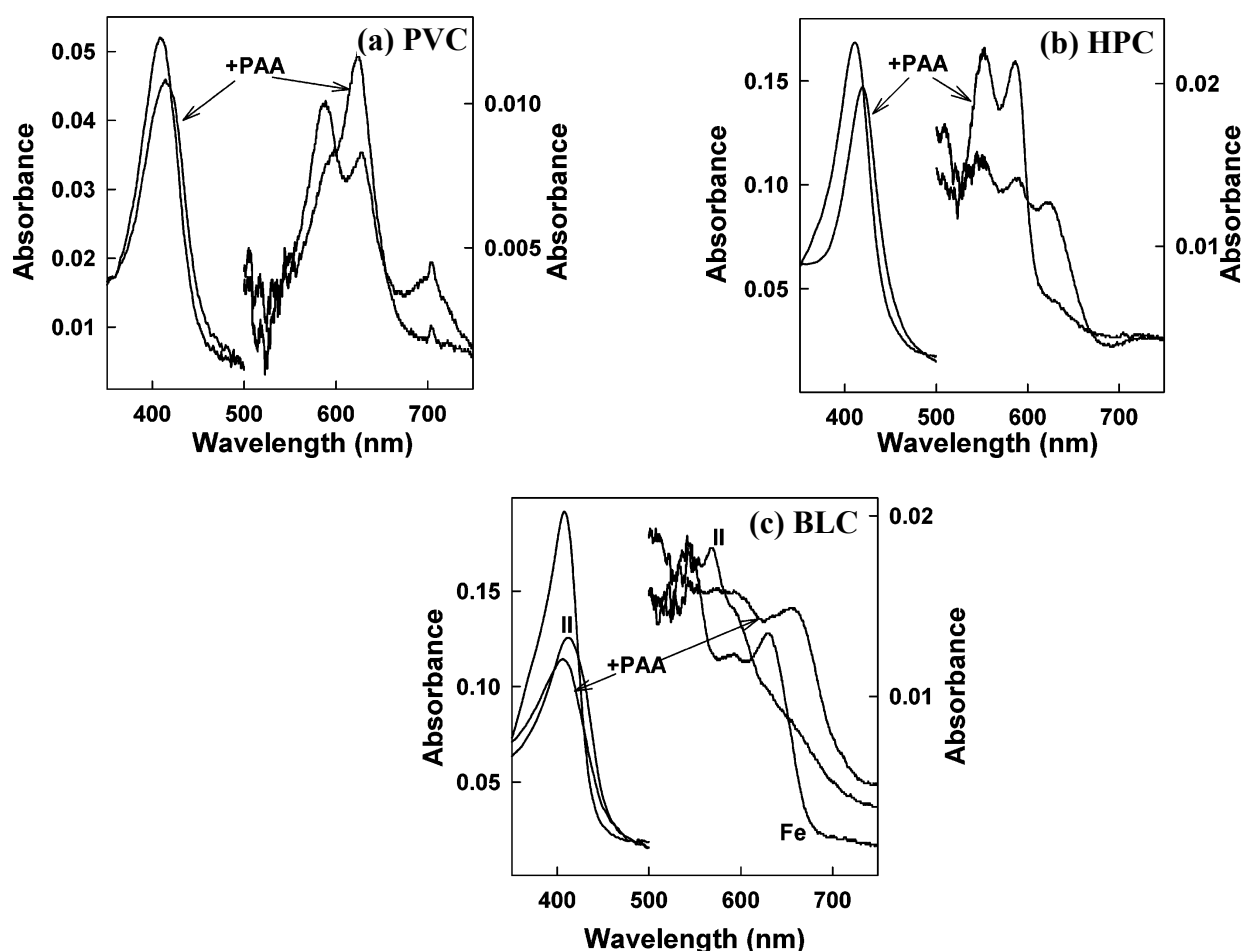


Figure 3. Changes in the UV-visible spectra of (a) PVC, (b) HPC and (c) BLC caused by mixing with peroxyacetic acid. Spectra were determined before and after the addition of PAA. For BLC, ferrocyanide was added after PAA addition to generate Cpd II (see Chapter I, section 4.2.). The left axes correspond to the absorbance at 350-500 nm and the right axes at 501-750 nm. Taken from reference (Alfonso-Prieto, 2007).

Interestingly, these two catalases show different propensity to be reduced. As explained in Chapter I (section 3.3.), Cpd I of heme d-containing catalases, such as *E.coli* hydroperoxidase II (HPH), apparently are not reduced to Cpd II by ferrocyanide or ascorbate treatment, whereas Cpd I of heme b-containing catalases, such as BLC, are converted easily to Cpd II under the same conditions (Obinger, 1997; Chelikani, 2005). Therefore, if the presence of Cpd I* (i.e. one-electron reduction of Cpd I) is the major explanation of longer Fe-O bond lengths, heme d-containing catalases may be found with predominantly short Fe-O bond lengths, as it seems to be the case for PVC. For heme b-containing catalases the outcome may vary depending upon differences in the ease of Cpd I* production and the experimental conditions, e.g. pH.

2. RESULTS AND DISCUSSION

2.1. QM/MM models

Figure 4 shows the six possible configurations of the oxidized intermediates of HPC and PVC considered in the QM/MM calculations (see Appendix A, section 2). First, we examined the canonical configuration of Cpd I (i.e. $\text{Por}^{\bullet+}\text{-Fe}^{\text{IV}}=\text{O}$, **Ia**), as described in previous studies (Green, 2001; Rydberg, 2004; de Visser, 2006). Then, taking into account the crystal structures of oxidized HPC and PVC were solved at a slightly acidic pH (5.6 and 5.2, respectively), a proton was added to the active site. Two different protonated forms were considered. Configuration **Ib** bears a proton on the distal histidine $\{\text{Por}^{\bullet+}\text{-Fe}^{\text{IV}}=\text{O}, \text{His-H}^+\}$, as the pKa of this residue is estimated to be 5.0 in *Horse radish* peroxidase (HRP) (Jones & Dunford, 2006). Alternatively, **Ic** explores the possibility of a proton transfer from the distal His to the ferryl oxygen, yielding a hydroxoferryl Cpd I (i.e. $\{\text{Por}^{\bullet+}\text{-Fe}^{\text{IV}}\text{-OH}^+\}$) (Rovira, 2005). Afterwards, one-electron reduced forms of Cpd I were considered. They are useful models of both Cpd II (i.e. $\{\text{Por-Fe}^{\text{IV}}\text{-OH}\}$) and Cpd I* (i.e. $\{\text{Por-Fe}^{\text{IV}}\text{-OH}, \text{aa}^{\bullet+}\}$), because both species are isoelectronic in the heme active site region, as mentioned in section 1. A larger QM region for Cpd I*, covering all protein residues (aa = Tyr or Trp) close to the heme where the radical can migrate, is beyond our computational capabilities. Similarly to Cpd I, three different protonation states were considered for Cpd II / Cpd I* model (Figure 4): non-protonated (**IIa**, $\text{Por-Fe}^{\text{IV}}=\text{O}$), and bearing a proton either on the distal His (**IIb**, $\{\text{Por-Fe}^{\text{IV}}=\text{O}, \text{His-H}^+\}$) or on the ferryl oxygen (**IIc**, $\text{Por-Fe}^{\text{IV}}\text{-OH}$).

Ia	Ib	Ic
His $\begin{array}{c} \text{O} \\ \\ \text{Fe}^{\text{IV}} \end{array}$	HisH ⁺ $\begin{array}{c} \text{O} \\ \\ \text{Fe}^{\text{IV}} \end{array}$	His $\begin{array}{c} \text{OH}^+ \\ \\ \text{Fe}^{\text{IV}} \end{array}$
charge=+1; M=4	charge=+2; M=4	charge=+2; M=4
IIa	IIb	IIc
His $\begin{array}{c} \text{O} \\ \\ \text{Fe}^{\text{IV}} \end{array}$	HisH ⁺ $\begin{array}{c} \text{O} \\ \\ \text{Fe}^{\text{IV}} \end{array}$	His $\begin{array}{c} \text{OH} \\ \\ \text{Fe}^{\text{IV}} \end{array}$
charge= 0; M=3	charge=+1; M=3	charge=+1; M=3

Figure 4. Oxidized intermediates considered in the QM/MM calculations.

• Oxidized HPC

Optimized structures. The main structural parameters of the six isomers considered (see Figure 4), in comparison with the crystal structure data for PAA-treated HPC, are listed in Table 2. The **IIb** configuration turns out to be not stable and spontaneously evolves to a **IIc**-like configuration, i.e. the proton on the distal His is transferred to the ferryl oxygen through the pocket water, yielding a hydroxoferryl Cpd II as in **IIc** (see Chapter III, Figure 4). To avoid such water-mediated proton transfer, the $N_{\epsilon, \text{His}}\text{-H}$ distance was constrained during the geometry optimization. The optimized structures of all the possible oxidized intermediates of HPC are shown in Figure 5a.

Table 2. Main structural parameters^a defining the active site structure of the oxidized intermediates (defined in Figure 4) of HPC. **(a)** Cpd I intermediates

parameter ^b	X-Ray ^c	Ia	Ib	Ic
iron coordination				
Fe-O	1.80/1.85	1.68	1.71	1.78
Fe-O _{Tyr}	1.95/1.92	2.14	2.05	1.99
O-O _{Tyr}	3.72/3.76	3.82	3.75	3.77
Fe-N _{Porph}	2.03/2.06 ^d	2.01-2.02	2.00-2.02	2.00-2.01
Fe _{out-of-plane}	0.036/0.033	0.214	0.108	0.054
∠O-Fe-O _{Tyr}	167.3/169.5	177.0	173.83	174.26
∠Fe-O _{Tyr} -C	128.7/126.7	127.5	122.08	124.00
O-H	–	–	–	0.99
∠Fe-O-H	–	–	125.55 ^f	109.39
distal side				
O···O _{wat}	2.98/2.91	2.79	2.54	3.31
N _{ε,His} ···O _{wat}	2.71/2.74	2.89	2.63 (1.56) ^g	2.90
N _{Asn} ···O _{wat}	3.23/3.08	3.83	4.11	3.89
Fe-O _{wat}	4.13/4.13	4.06	3.76	4.63
N _{ε,His} ···O	3.33/3.45	3.42	3.75 (3.16) ^h	3.41 (2.44) ⁱ
O···H _{wat}	–	1.85	1.49	2.60
N _{ε,His} ···H _{wat}	–	1.88	3.32	1.89
NH _{Asn} ···O _w	–	2.81	3.10	2.89
proximal side				
O _{Tyr} -N _{Arg⁺}	2.81/2.68 ^e	2.77-2.81	2.77-2.92	2.84-2.97
O _{Tyr} -HN _{Arg⁺}	–	1.79-1.88	1.76-2.02	1.84-2.07

^a Distances are given in angstroms and angles in degrees. ^b Atom names are shown in Figure 5b.

^c PDB code: 2IQF. Values corresponding to the two independent protein subunits.

^d An average of the four Fe-N distances is given for each subunit.

^e An average of the two N-O distances is given for each subunit.

^f Fe=O···⁺H-His angle.

^g The distance between the O_{wat} and the proton on the His is given in parentheses.

^h The distance between the oxoferryl oxygen and the proton on the His is given in parentheses.

ⁱ The distance between the proton on the hydroxoferryl oxygen and nitrogen of the His is given in parentheses.

Table 2 (cont.). Main structural parameters^a defining the active site structure of the oxidized intermediates (defined in Figure 4) of HPC. **(b)** Cpd II / Cpd I* intermediates.

parameter ^b	X-Ray ^c	IIa	IIb	IIc
iron coordination				
Fe-O	1.80/1.85	1.69	1.72	1.79
Fe-O _{Tyr}	1.95/1.92	2.07	2.05	2.00
O-O _{Tyr}	3.72/3.76	3.76	3.76	3.78
Fe-N _{Porph}	2.03/2.06 ^d	2.01-2.02	2.01-2.02	2.00-2.02
Fe _{out-of-plane}	0.036/0.033	0.120	0.101	0.058
∠O-Fe-O _{Tyr}	167.3/169.5	174.74	173.20	174.74
∠Fe-O _{Tyr} -C	128.7/126.7	124.19	123.02	124.59
O-H	–	–	–	0.99
∠Fe-O-H	–	–	–	10.783
distal side				
O···O _{wat}	2.98/2.91	3.36	2.48	3.34
N _{ε,His} ···O _{wat}	2.71/2.74	2.86	2.56 (1.49) ^g	2.89
N _{Asn} ···O _{wat}	3.23/3.08	2.92	4.10	3.84
Fe-O _{wat}	4.13/4.13	4.40	3.70	4.68
N _{ε,His} ···O	3.33/3.45	3.60	3.61 (3.04) ^h	3.53 (2.59) ⁱ
O···H _{wat}	–	2.58	1.37	2.60
N _{ε,His} ···H _{wat}	–	1.85	2.90	1.88
NH _{Asn} ···O _w	–	1.88	3.09	2.85
proximal side				
O _{Tyr} -N _{Arg⁺}	2.81/2.68 ^e	2.71-2.75	2.76-2.82	2.82-2.93
O _{Tyr} -HN _{Arg⁺}	–	1.72-1.82	1.77-1.90	1.82-2.02

^a Distances are given in angstroms and angles in degrees. ^b Atom names are shown in Figure 5b.

^c PDB code: 2IQF. Values corresponding to the two independent protein subunits.

^d An average of the four Fe-N distances is given for each subunit.

^e An average of the two N-O distances is given for each subunit.

^f Fe=O···⁺H-His angle.

^g The distance between the O_{wat} and the proton on the His is given in parentheses.

^h The distance between the oxoferryl oxygen and the proton on the His is given in parentheses.

ⁱ The distance between the proton on the hydroxoferryl oxygen and nitrogen of the His is given in parentheses.

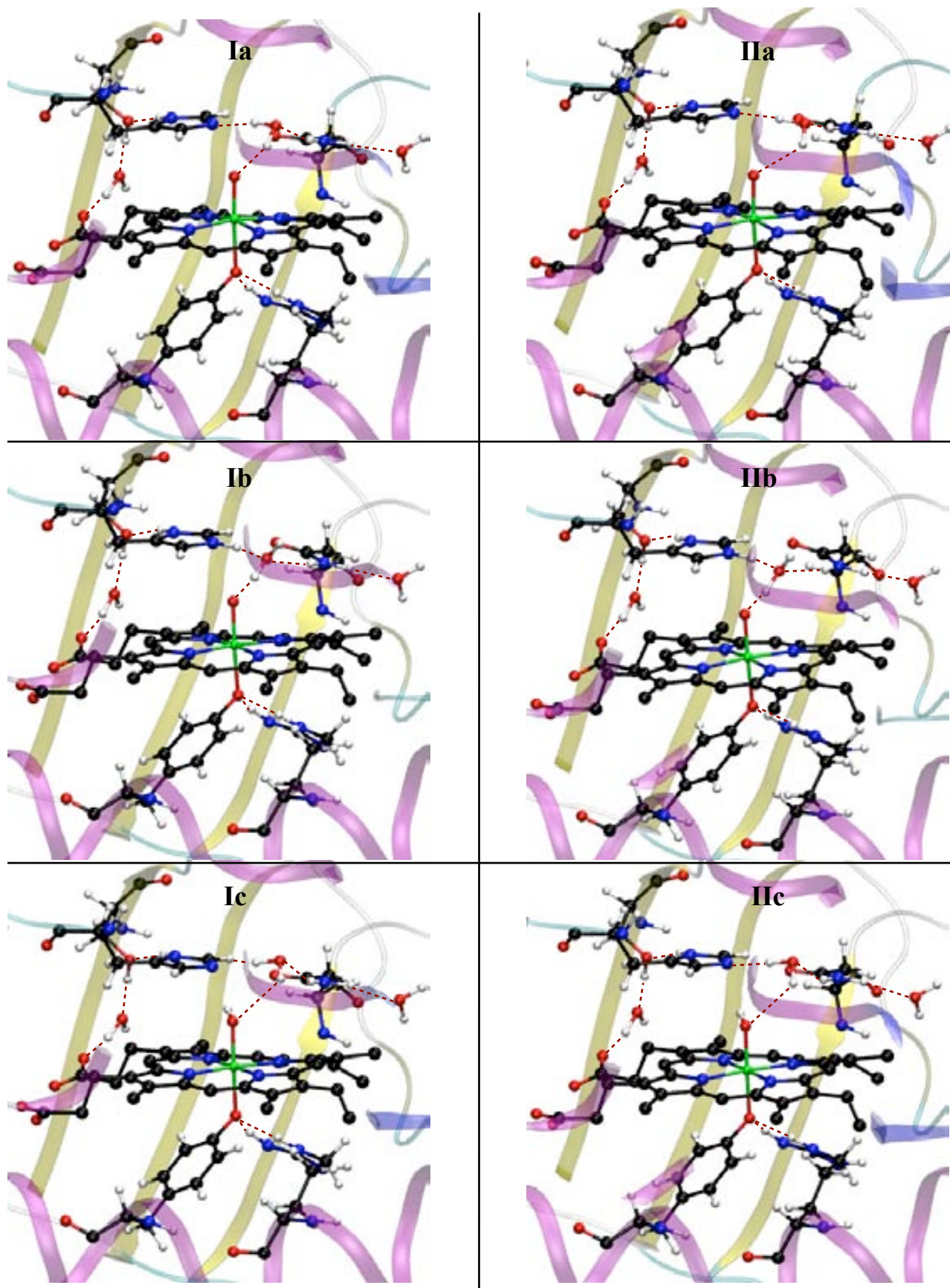


Figure 5. (a) Optimized structures of the six possible configurations considered for oxidized HPC (see Figure 4).

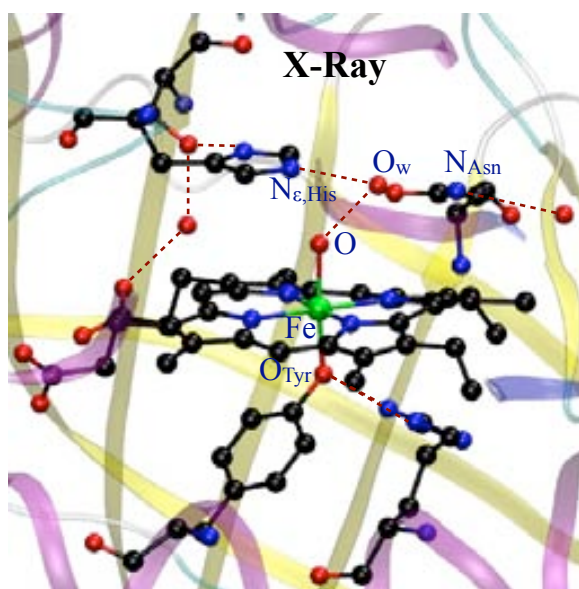


Figure 5. (b) X-Ray structure of PAA-treated HPC (PDB entry: 2IQF).

All the isomers show similar overall structures (Figure 5a), except for the variation of the iron-axial ligand bond distances (Table 2). The oxoferryl Cpd I configuration (**Ia**) displays the shorter Fe-O distance (1.68 Å) and the longer Fe-O_{Tyr} distance (2.14 Å). These values are in agreement with previous calculations on heme models having similar axial ligation (Green, 2001; Silaghi-Dumitrescu, 2004; Rovira, 2005; Hersleth, 2006). Almost identical iron-axial ligand bond distances are observed for the oxoferryl Cpd II (**Ia**) (1.69 and 2.07 Å, respectively, see Table 2), despite the one-electron reduction of the porphyrin cation radical. In both isomers a single water is hydrogen bonded to His56, Asn129, and the oxoferryl oxygen, as it is found in the experimental structure. Most likely, the network of hydrogen-bond interactions connecting the histidine N_δ with one heme propionate (through Ser95, see Figure 5) makes the His-N_ε atom a very good proton acceptor. As a consequence, the hydrogen-bond distance between His56 and the pocket water is shorter than the distance between the water and the Asn129 residue. Protonation of the distal histidine (**Ib** and **Ib**) only lengthens slightly the Fe=O bond (from 1.68-1.69 to 1.71-1.72 Å, see Table 2), as previously reported for other heme proteins (Nilsson, 2004; Silaghi-Dumitrescu, 2005; Green, 2006). The largest change occurs when the oxoferryl moiety is protonated (**Ic** and **Ic**). The Fe-O distance increases to 1.78-1.79 Å, respectively (Table 2), reflecting the change from a double to a single Fe-O bond. At the same time, the Fe-O_{Tyr} distance decreases from 2.14-2.07 to 1.99-2.00 Å (Table 2). Protonation is expected to reinforce this bond because most of the electron density of the Fe atom in the oxoferryl species **Ia** and **Ia** is used in the double bond with the distal oxygen (i.e. the orbital composed of the σ orbitals of O and O_{Tyr} and Fe { dz^2 } is more polarized toward the

O atom), reducing the density available for the single Fe-O_{Tyr} bond. Similar changes have previously been observed in calculations of Cpd II models (Rovira, 2005), and reflect the *push-pull* effect also observed in HRP (Derat, 2006b), Mb (Nilsson, 2004), CPO (Green, 2006; Behan, 2006a) or P450 (Behan, 2006b).

In comparison with the crystal structure of oxidized HPC (Figure 5b), the oxoferryl species **Ia** and **IIa** show a Fe-O distance shorter than the experimental distances (by 0.12-0.11 or 0.17-0.16 Å, depending on the protein subunit), and a longer Fe-O_{Tyr} distance (by 0.19-0.12 or 0.22-0.15 Å, see Table 2). Although protonation of the distal histidine (**Ib** and **IIb**) lengthens slightly the Fe=O bond, the distance is still much shorter (by 0.09-0.08 or 0.14-0.13 Å) than that observed in the crystal structure (Table 2), suggesting that the oxoferryl structure is not present in the crystal. On the contrary, in the hydroxoferryl isomers (**Ic** and **IIc**) the Fe-O distance is clearly longer than in the oxoferryls (1.78-1.79 Å, Table 2), and thus it is close to that observed in the crystal (1.80 / 1.85 Å). At the same time, the Fe-O_{Tyr} distance decreases to 1.99-2.00 Å (Table 2), in better agreement with the experimental values (1.95 / 1.92 Å). From the point of view of structure, both **Ic** and **IIc** are good candidates to be the species present in PAA-treated HPC. In other words, *the crystal structure of oxidized HPC is compatible with a hydroxoferryl form.*

Spin density distributions. The localization of the unpaired electrons of the six configurations considered (Figure 4) was investigated by analyzing their spin density distributions, shown in Figure 6. The spin densities of the Cpd I species (**Ia**, **Ib** and **Ic**) are very similar, being concentrated on Fe-O and showing a large delocalization on the porphyrin ring, consistent with a porphyrin radical character (see Chapter I, section 4.2.). There is also a small fraction of spin density on the atom that is covalently attached to the proximal ligand (the tyrosinate oxygen atom), as previously reported for gas phase models (Green, 2001; Rydberg, 2004; de Visser, 2006). The spatial symmetry of the spin density on the porphyrin reflects a mixture of A_{1u} (density on α and β pyrrole carbon atoms) and A_{2u} (density on the pyrrole nitrogen and meso carbon atoms). The spin density on a perfect D_{4h} Fe-porphyrin-O system has been often discussed in terms of originating from a half-filled orbital of either A_{1u} or A_{2u} symmetry (see Chapter I, section 4.2.). Nevertheless, in reality Cpd I is not symmetric, and both orbitals are allowed to mix. It is worth mentioning that a similar situation has been reported for Cpd I of horseradish peroxidase (HRP) using QM/MM calculations (Derat, 2005), suggesting that the spatial symmetry of the unpaired electrons in Cpd I is not

strongly affected by the different axial ligands, a tyrosinate in catalase or histidine in peroxidase. The weight of each contribution (A_{1u} or A_{2u}) to the spatial symmetry of the spin density on the porphyrin ring depends on the isomer (Figure 6). The spin density distribution of the **Ia** isomer shows mainly an A_{2u} character. Protonation (either **Ib** or **Ic**) results in a change on the symmetry, being more weighted on A_{1u} than A_{2u} . As expected, the spin density distributions of the Cpd II species (**IIa**, **IIb** and **IIc**) show that the porphyrin radical disappears and the spin density is fully localized on the Fe-O moiety, with a small contribution from the tyrosinate oxygen atom (Figure 6).

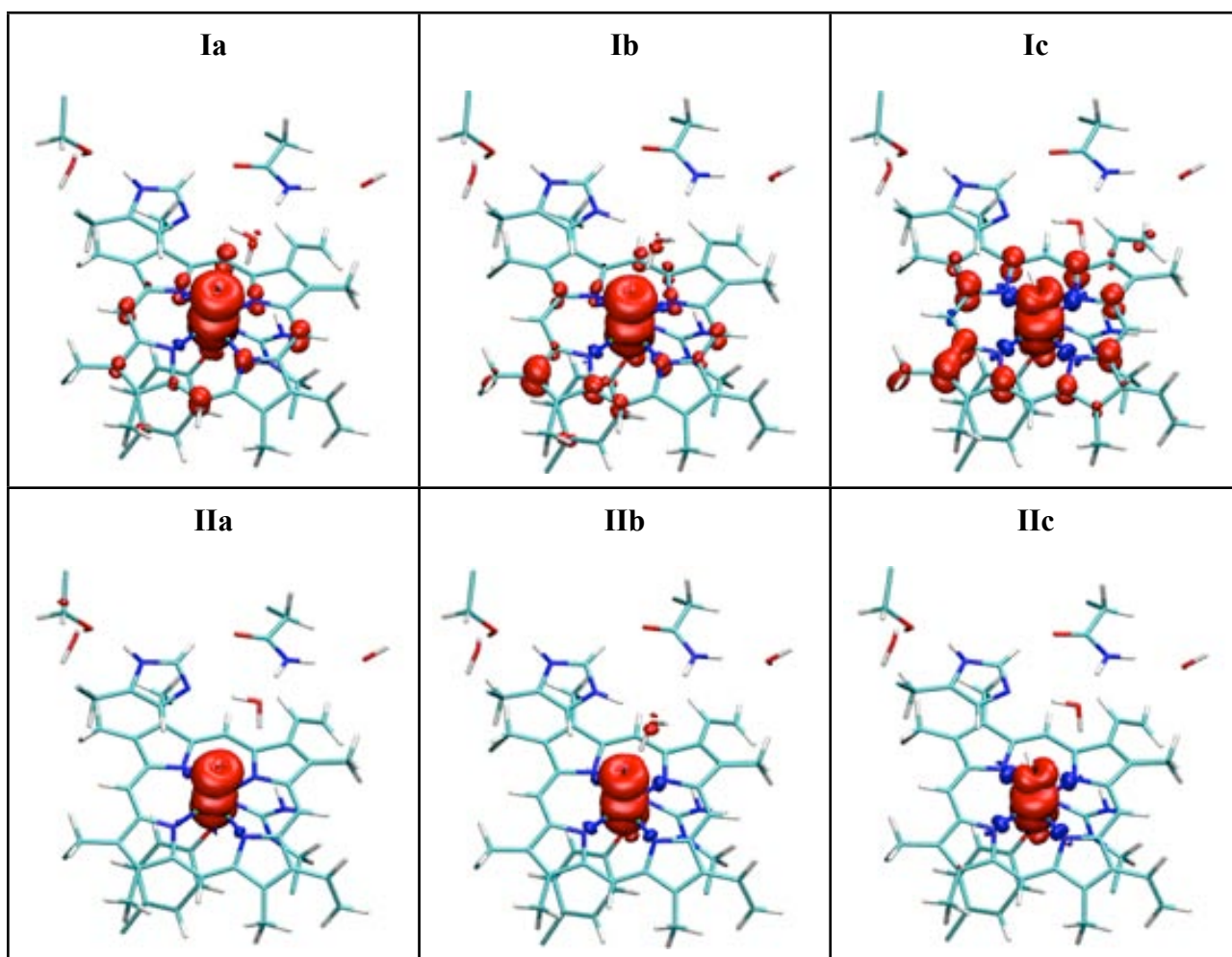


Figure 6. Spin density distributions of the six possible oxidized intermediates for HPC (see Figure 4). Only the QM atoms are displayed. Spin isodensity surfaces are plotted at $0.004 e \text{ \AA}^{-3}$.

• Oxidized PVC

Optimized structures. The main structural parameters of the six possible configurations considered, in comparison with the crystal structure data for oxidized PVC, are listed in Table 3. Differently from HPC, the **IIb** configuration turns out to be stable and no water-mediated proton transfer between the protonated distal His and the oxoferryl was observed. The optimized structures of all the possible oxidized intermediates of PVC, in comparison with the X-Ray structure, are shown in Figure 7.

In general, the active site structures calculated for the PVC isomers (Figure 7a) are similar to their HPC counterparts (Figure 5a). The oxoferryl forms show shorter Fe-O bond lengths (1.69-1.71 Å) than the hydroxoferryl forms (1.80 Å, see Table 3), regardless of the oxidation state of the porphyrin (i.e. Cpd I or Cpd II). The small differences between the reaction intermediates of the two catalases are a result of the spirolactone modification and the extra hydroxyl group on ring III of heme d in PVC. These modifications result in the C_{2D}-C_{3D} bond length in heme d being 0.21 Å longer than in heme b (1.56 compared to 1.35 Å), due to the change from a C_{sp}²-C_{sp}² to a C_{sp}³-C_{sp}³ bonding (see Figure 2). A second difference lies in the orientation of the hydroxyl ligand in the hydroxoferryl forms (**Ic** and **IIc**). For HPC is projected towards the pyrrole ring III and the distal His (see Figure 5), whereas in PVC it is projected in opposite direction away from the distal His (see Figure 7).

When comparing to the crystal (Figure 7b), the structures of all the oxoferryl forms are in good agreement with the experimental data. The Fe-O distances (**Ia** = 1.69 Å, **Ib** = 1.70 Å, **IIa** = 1.69 Å, and **IIb** = 1.71 Å, see Table 3) are in good agreement with the crystal structure, where the Fe-O bond length is 1.72 Å. The experimental Fe-O_{Tyr} distance of 2.00/2.04 Å is only slightly shorter than the calculated distances (**Ia** = 2.07 Å, **Ib** = 2.08 Å, **IIa** = 2.07 Å, and **IIb** = 2.05 Å, see Table 3). The water molecule in the heme pocket is again coordinated between the active site residues His64 and Asn137, as in the experimental structure. On the contrary, the Fe-O distances of the hydroxoferryl forms **Ic** and **I*** (1.80 Å, see Table 3) deviate by more than 0.05 Å from the experimental value (1.72 Å). Therefore, *the crystal structure of oxidized PVC is compatible with an oxoferryl form.*

Table 3. Main structural parameters^a defining the active site structure of the oxidized intermediates (defined in Figure 4) of PVC. **(a)** Cpd I intermediates

parameter ^b	X-Ray ^c	Ia	Ib	Ic
iron coordination				
Fe-O	1.72/1.72	1.69	1.70	1.80
Fe-O _{Tyr}	2.00/2.04	2.07	2.08	1.92
O-O _{Tyr}	3.72/3.76	3.36	3.76	3.74
Fe-N _{Porph}	2.03/2.02 ^d	2.01-2.06	2.01-2.06	2.00-2.05
Fe _{out-of-plane}	0.091/0.113	0.091	0.110	0.052
∠O-Fe-O _{Tyr}	175.6/175.6	175.0	179.2	178.0
∠Fe-O _{Tyr} -C	126.0/128.0	127.2	126.5	127.6
O-H	–	–	–	0.99
∠Fe-O-H	–	–	124.0 ^f	103.6
distal side				
O···O _{wat}	3.27/3.30	2.87	2.58	2.94
N _{ε,His} ···O _{wat}	2.71/2.74	2.95	2.68 (1.65) ^g	2.92
N _{Asn} ···O _{wat}	3.25/3.20	5.03	4.69	5.06
Fe-O _{wat}	4.29/4.32	4.30	3.93	4.52
N _{ε,His} ···O	3.37/3.43	4.26	3.99 (3.40) ^h	4.38 (5.07) ⁱ
O···H _{wat}	–	1.88	1,54	1.96
N _{ε,His} ···H _{wat}	–	1.97	3.21	1.95
NH _{Asn} ···O _w	–	4.03	3.71	4.05
proximal side				
O _{Tyr} -N _{Arg⁺}	2.82/2.83 ^e	2.90-2.91	2.92-2.97	2.96-3.04
O _{Tyr} -HN _{Arg⁺}	–	1.93-1.96	1.95-2.03	1.98-2.10

^a Distances are given in angstroms and angles in degrees. ^b Atom names are shown in Figure 7b.

^c PDB code: 2IQF. Values corresponding to the two independent protein subunits.

^d An average of the four Fe-N distances is given for each subunit.

^e An average of the two N-O distances is given for each subunit.

^f Fe=O···⁺H-His angle.

^g The distance between the O_{wat} and the proton on the His is given in parentheses.

^h The distance between the oxoferryl oxygen and the proton on the His is given in parentheses.

ⁱ The distance between the proton on the hydroxoferryl oxygen and nitrogen of the His is given in parentheses.

Table 3 (cont.). Main structural parameters^a defining the active site structure of the oxidized intermediates (defined in Figure 4) of PVC. **(b)** Cpd II / Cpd I* intermediates

parameter ^b	X-Ray ^c	IIa	IIb	IIc
iron coordination				
Fe-O	1.72/1.72	1.69	1.71	1.80
Fe-O _{Tyr}	2.00/2.04	2.07	2.05	1.99
O-O _{Tyr}	3.72/3.76	3.77	3.75	3.79
Fe-N _{Porph}	2.03/2.02 ^d	2.02-2.05	2.01-2.06	2.01-2.04
Fe _{out-of-plane}	0.091/0.113	0.100	0.101	0.043
∠O-Fe-O _{Tyr}	175.6/175.6	178.7	177.5	177.5
∠Fe-O _{Tyr} -C	126.0/128.0	122.7	124.0	125.6
O-H	–	–	–	0.99
∠Fe-O-H	–	–	–	1.042
distal side				
O···O _{wat}	3.27/3.30	2.93	2.55	2.96
N _{ε,His} ···O _{wat}	2.71/2.74	2.88	2.66 (1.61) ^g	2.80
N _{Asn} ···O _{wat}	3.25/3.20	4.82	3.47	4.70
Fe-O _{wat}	4.29/4.32	4.29	3.85	4.47
N _{ε,His} ···O	3.37/3.43	4.30	3.98	4.35 (5.04) ⁱ
O···H _{wat}	–	1.93	1.49	1.98
N _{ε,His} ···H _{wat}	–	1.88	3.17	1.81
NH _{Asn} ···O _w	–	3.83	3.47	3.68
proximal side				
O _{Tyr} -N _{Arg⁺}	2.82/2.83 ^e	2.79-2.85	2.86-2.87	2.96-2.94
O _{Tyr} -HN _{Arg⁺}	–	1.80-1.91	1.89-1.91	1.98-1.99

^a Distances are given in angstroms and angles in degrees. ^b Atom names are shown in Figure 7b.

^c PDB code: 2IQF. Values corresponding to the two independent protein subunits.

^d An average of the four Fe-N distances is given for each subunit.

^e An average of the two N-O distances is given for each subunit.

^f Fe=O···⁺H-His angle.

^g The distance between the O_{wat} and the proton on the His is given in parentheses.

^h The distance between the oxoferryl oxygen and the proton on the His is given in parentheses.

ⁱ The distance between the proton on the hydroxoferryl oxygen and nitrogen of the His is given in parentheses.

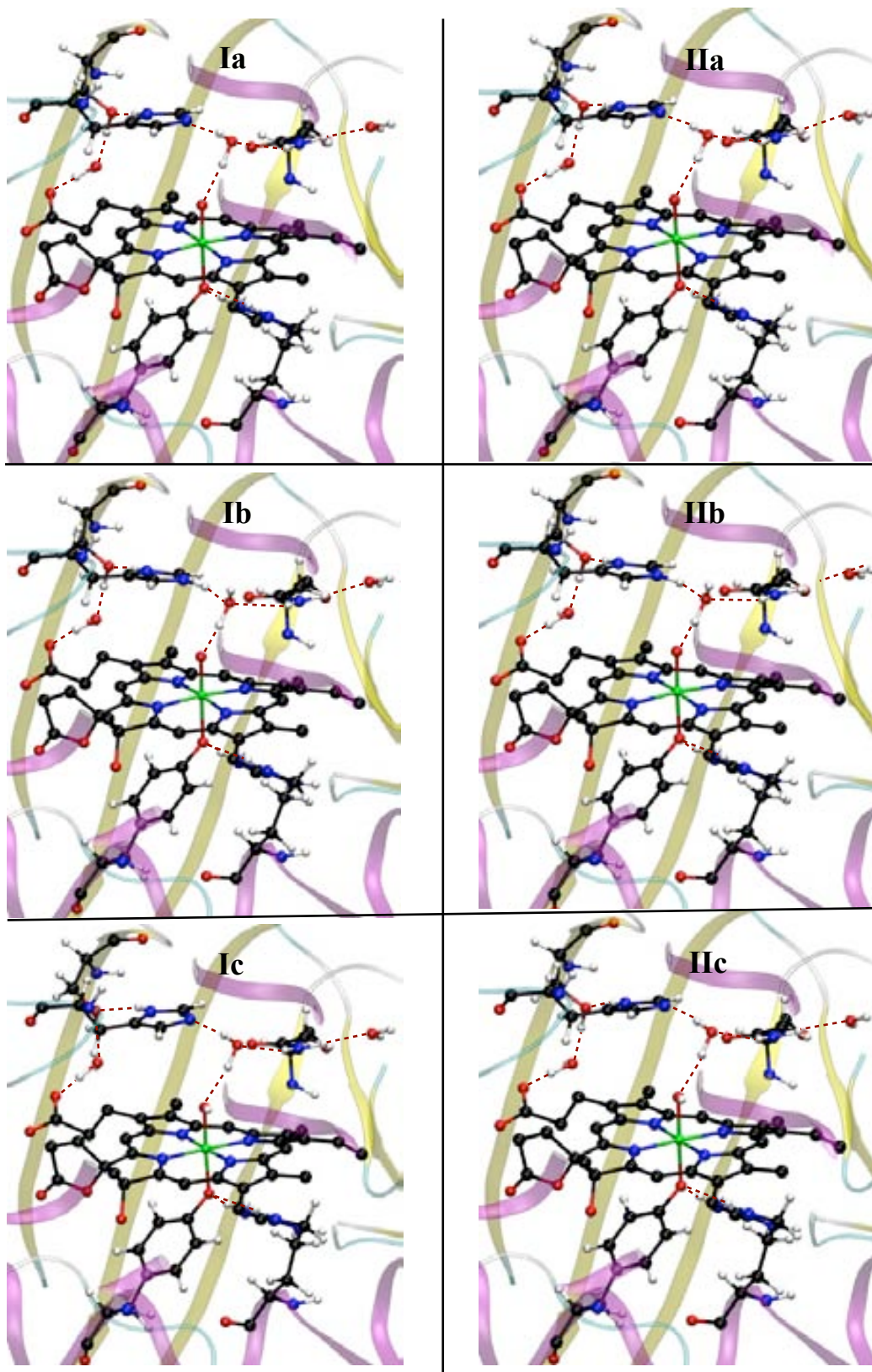


Figure 7. (a) Optimized structures of the six possible configurations considered for oxidized PVC (see Figure 4).

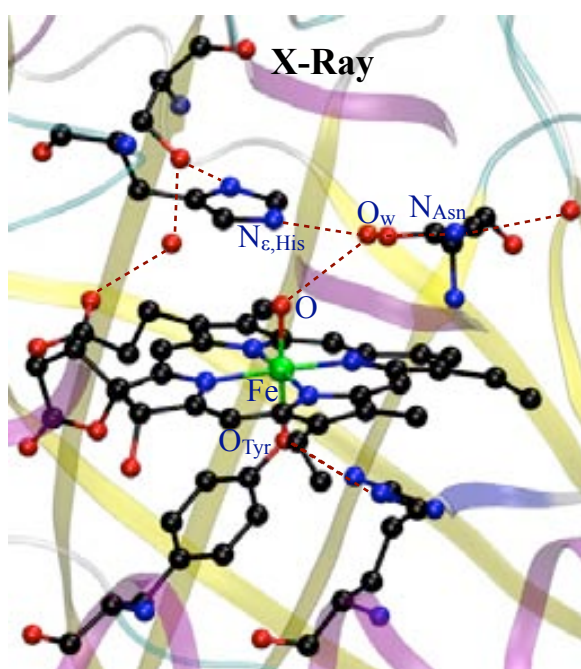


Figure 7. (b) X-Ray structure of PAA-treated PVC.

Spin density distributions. The localization of the unpaired electrons of the six configurations considered (Figure 4) was investigated by analyzing their spin density distributions, shown in Figure 8. The spin density in the primary species **Ia** of PVC is concentrated on the Fe=O, as in HPC (Figure 6), but the third unpaired spin shows a different distribution. It is not only delocalized over the porphyrin but also onto the distal histidine, and to a lesser extent onto the negatively charged oxygen atom and phenolate ring of the proximal ligand. Moreover, the spatial symmetry of the spin density on the porphyrin reflects a mixture of A_{1u} (density on α and β pyrrole carbon atoms) and A_{2u} (density on the pyrrole nitrogen and meso carbon atoms) states, but, unlike HPC, it is more weighted to A_{1u} . This symmetry change is in agreement with previous studies suggesting that chlorins may have ring cation radicals with A_{1u} symmetry (Hanson, 1981; Ozawa, 1994; Kitagawa, 1994; Ghosh, 1997). As explained in Chapter III, the loss of one double bond between the β carbon atoms of one the pyrroles destabilizes mainly the a_{1u} orbital, which has contributions from these atoms, relative to the a_{2u} orbital. Therefore, *the spatial symmetry of the unpaired electrons in Cpd I depends on the type of heme group (heme b in HPC or heme d in PVC).*

The spin density distribution of the hydroxoferryl Cpd I form (**Ic**) exhibits similar features to those of **Ia**, whereas protonation of the distal His (**Ib**) results in the disappearance of the spin density on the distal His. Besides, the symmetry of the spin density of the porphyrin changes, with the main contribution to the spin density being from the porphyrin a_{2u} orbital, and the spin density on the proximal tyrosinate increases. The spin density distributions of the Cpd II species (**IIa**, **IIb** and **IIc**) (Figure 8) show that the porphyrin radical has been reduced, and the spin density is fully localized on the Fe-O moiety, with a small contribution from the tyrosinate oxygen atom.

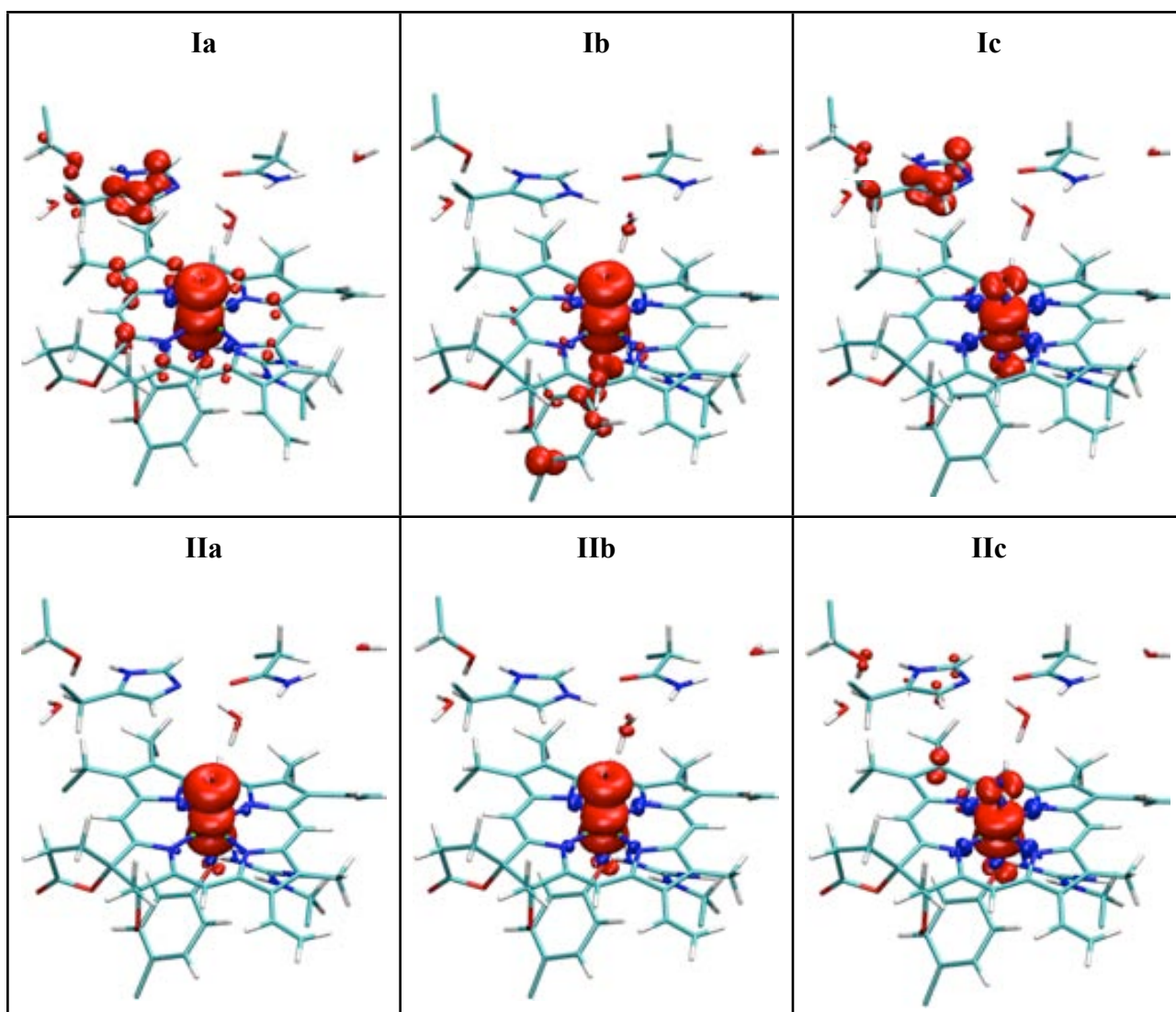


Figure 8. Spin density distributions of the six possible reaction intermediates for PVC (see Figure 4). Only the QM atoms are displayed. Spin isodensity surfaces are plotted at $0.004 e \text{ \AA}^{-3}$.

- *Temperature effects*

To analyze whether the spin density is affected by small structural fluctuations in the active site, short (\approx 1ps) CP QM/MM molecular dynamics simulations at room temperature were performed, starting from the optimized structures. For HPC-**Ia**, the shape of the spin density (Figure 9, *top*) does not change significantly during the dynamics, maintaining the A_{2u} -like symmetry of the unpaired spin on the porphyrin. Besides, in some snapshots a partial delocalization onto the proximal Tyr was observed, as previously reported (Green, 2001; Rydberg, 2004; de Visser, 2006).

On the contrary, the spin density of PVC-**Ia** “fluctuates” between the porphyrin and distal His with different weights during the dynamics (Figure 9, *bottom*). To probe the environmental effect responsible for the delocalization of the spin density onto the distal His, a large gas phase model, equivalent to the QM subsystem used for the QM/MM calculation was investigated. Upon geometry optimization, the distance between the distal His and the pyrrole of the porphyrin located just below (pyrrole III, see Figure 2b) increases by 0.2 Å with respect to the QM/MM optimized structure (3.88 Å), increasing its deviation with respect to the X-Ray structure (3.42-3.45 Å). This decrease in the overlap between the imidazole of His64 and the porphyrin pyrrole results in the disappearance of the spin density on the imidazole. Therefore, the π/π -cation stacking interaction between the imidazole and the pyrrole appears to be crucial for the fluctuation of the radical between the porphyrin and the distal His.

In addition, increases in the spin density on the proximal tyrosine are evident in some snapshots of the molecular dynamics. This delocalization of the spin density on the phenolate is to be modulated by the redox potentials of Tyr and the porphyrin cation radical, as well as their orbital overlap. The O-H $\cdots\pi$ interaction observed between the hydroxyl group of the heme d modification and the phenolate ring of the proximal tyrosinate may decrease the charge of the aromatic ring (Sulpizi & Carloni, 2000) and thus increase the oxidation potential of Tyr. However, no correlation was found between a longer *aromatic* hydrogen bond and a larger spin density on the tyrosinate.

In summary, our results indicate that *the oxoferryl Cpd I species of HPC has an A_{2u} -like porphyrin radical, whereas for PVC the radical “fluctuates” over the distal histidine, the porphyrin (with an A_{1u} symmetry) and, to a lesser extent, the proximal tyrosine.*

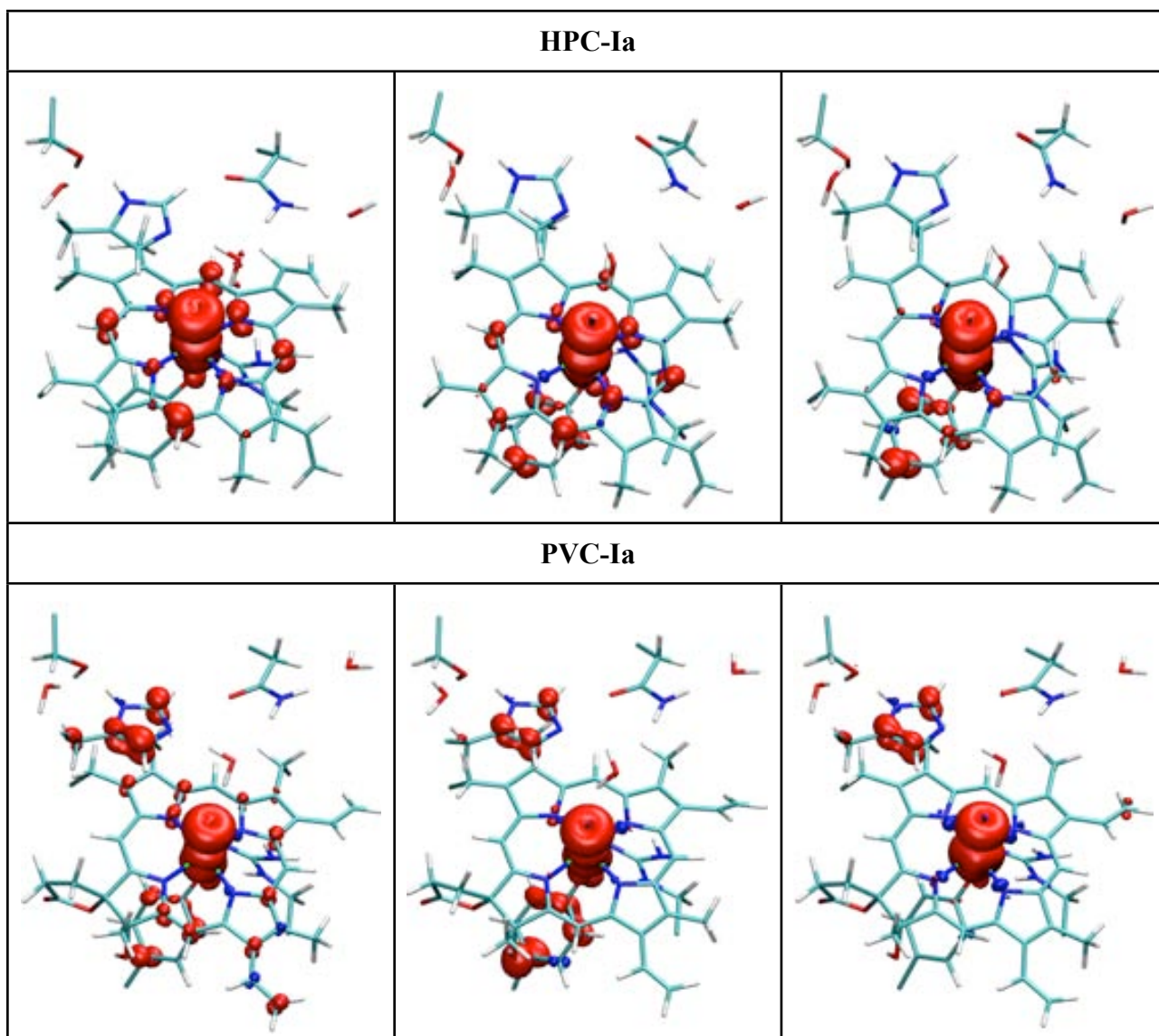


Figure 9. Fluctuations of the spin density distribution during the room temperature CP QM/MM molecular dynamics of the oxoferryl-porphyrin cation radical species, **Ia**. Only the QM atoms are displayed. Spin isodensity surfaces are plotted at $0.004 e \text{ \AA}^{-3}$.

2.2. Assignment of the oxidized intermediates of HPC and PVC

The calculated Fe-O distances for the **Ia** species (HPC-**Ia** = 1.68 Å, PVC-**Ia** = 1.69 Å) agree only with the oxidized PVC experimental bond length (1.72 Å). Upon protonation of the distal His, the calculated Fe-O bond lengths are increased by only 0.01-0.02 Å. Given the acidic crystallization conditions (pH 5.6 for HPC and pH 5.2 for PVC), and assuming that the pKa of the distal His is similar to that reported for HRP Cpd I (5.0) (Jones & Dunford, 2006), partial protonation of the distal His is likely. Therefore, species **Ib** is also a candidate for the crystal structure of oxidized PVC. Reduction of the porphyrin radical does not affect the calculated Fe-O distance of the

oxoferryl Cpd II isomers. Both the **IIa** species (HPC-**IIa** = 1.69 Å, PVC-**IIa** = 1.69 Å) and the **IIb** species (HPC-**IIb** = 1.72 Å, PVC-**IIb** = 1.71 Å) keep the short Fe-O distance. However, the green colour observed for oxidized PVC (Figure 3a) is indicative of the presence of a porphyrin radical, excluding both the **IIa** and the **IIb** species. Overall, *the short Fe-O distance observed in the crystal structure, along with its UV-vis spectrum (Figure 3a), is consistent with Ia and Ib being the predominant species for oxidized PVC.*

The calculated Fe-O distances for the **Ic** species (HPC-**Ic** = 1.78 Å, PVC-**Ic** = 1.80 Å) are only slightly shorter than the bond lengths in the crystal structure of oxidized HPC (1.80 / 1.85 Å). Nevertheless, accumulation of the **Ic** species is unlikely. The low pKa for the oxoferryl group associated with a positively charged porphyrin radical would cause a rapid water-mediated proton transfer from the oxoferryl to the distal histidine, yielding species **Ib**. Moreover, the Cpd II-like UV-visible spectrum of PAA-treated HPC (Figure 3b, i.e. red colour) excludes the presence of a porphyrin radical, thus discarding **Ic** as the species present in the crystal. For the **IIc** species, the calculated Fe-O bond lengths (HPC-**IIc** = 1.79 Å, PVC-**IIc** = 1.80 Å) are also very close to the experimental values, and their electronic configuration (i.e. Por-Fe^{IV}-OH) is indeed compatible with the spectroscopic data. As mentioned in section 2.1., the **IIc** species are useful as models of both Cpd II and Cpd I*, because they are isoelectronic in the heme active site region. However, Cpd II formation in the crystal structure of oxidized HPC can be discarded because (i) no exogenous reducing agent has been added and (ii) the color change from green to red occurs before X-Ray irradiation (see Figure 1). Moreover, a tyrosyl radical has been detected in HPC by EPR (Ivancich, personal communication), as in BLC (Ivancich, 1996), indicating that the porphyrin cation radical has been reduced by an endogenous protein (Tyr) residue. Therefore, only Cpd I* formation is compatible with all the experimental data. In summary, *the long Fe-O distance observed in the crystal structure, along with its UV-vis spectrum (Figure 3b), is consistent with IIc being the species present in oxidized HPC.*

These results support the hypothesis that quenching of the porphyrin radical and protein radical formation also involves protonation of the oxoferryl moiety. Formally this is a proton-coupled electron transfer mechanism, common in a wide variety of biological systems (Mayer, 2004; Reece, 2006; Markle, 2008; Reece & Nocera, 2009). Nevertheless, at this point we do not know why reduction of the porphyrin radical makes the Fe^{IV}=O bond to trap a proton and become

Fe^{IV}-OH. Moreover, the factors determining the different propensity of HPC and PVC to form Cpd I* remain to be investigated (see Chapter V).

A number of explanations are possible for the small discrepancy (0.01 to 0.05 Å) between the Fe-O bond lengths observed in crystal structures and those determined by QM/MM calculations. Experimentally, photoreduction of the Fe-O bond in Cpd I* to Fe^{III}-OH may have occurred during X-ray exposure. Indeed, the QM/MM optimized structure of the Fe^{III}-OH species for HPC yield a 1.81 Å Fe-O distance, similar to **IIc**. However, the red colour characteristic of Cpd I* or Cpd II did not change during data collection, excluding photoreduction. It could also be argued that the experimental distances are affected by a sizable error even for a resolution of 1.7 Å. However, the trends observed in Cpd I structures of heme-proteins (Chapter I, Table 2) clearly show that there are two cases: oxidized heme proteins with Fe-O about 1.70 Å and those with Fe-O about 1.80 Å. Therefore, we do not expect that the error of the experimental structures could be so large to mask these differences. Alternatively, small deviations in the calculated values can be attributed to two main causes. Because of the anharmonicity of the Fe-O vibrational mode, the values obtained from structure optimization (Tables 3 and 4) will shift to slightly longer distances if the dynamics of the Fe-O bond at room temperature are considered. In fact, the Fe-OH distance obtained from first principles MD simulations at room temperature was shown to be 0.02 Å longer than if determined by structure optimization at 0 K (Rovira, 2005). The second source of variability lies in the basis set size, the pseudopotential, and the exchange-correlation functional employed. Test calculations using different cutoff values and iron pseudopotentials (Appendix A, section 2) suggest variations in the computed Fe-O of ± 0.02 Å. Therefore, we do not expect that the error of the calculated distances could be so large to mask the ≈ 0.1 Å difference between Fe=O and Fe-OH.

2.3. Proposed scheme for the transformations of oxidized catalase

The possible catalase intermediates resulting from oxidation with PAA in the absence of exogenous electron donors are shown in Figure 10. Initially, PAA abstracts two electrons from the heme: one from the Fe^{III}, which is oxidized to Fe^{IV}, and the second from the porphyrin, which becomes a cation radical (i.e. the canonical Cpd I species). In other words, the oxoferryl species **Ia** (Porph⁺-Fe^{IV}=O) is formed first. Since the pKa of the distal His has been proposed to be 5.0 in peroxidases (Jones & Dundford, 2006) and the crystallization of oxidized HPC and PVC was carried out at acidic pH (5.6 and 5.2, respectively), partial protonation of the distal His is expected.

Thus, in the absence of electron transfer from the protein, either **Ia** or its His-protonated variant **Ib** will accumulate as the classic Cpd I. Proton transfer (PT) between the distal His and the oxoferryl (**Ic**, Porph^{•+}-Fe^{IV}-OH) is unlikely in light of the expected low pKa of the oxoferryl-porphyrin radical species. Moreover, the short Fe-O distance observed in the crystal structure of oxidized PVC (Table 3), along with its UV-vis spectrum (Figure 3a), is consistent with **Ia** and **Ib** being the predominant species present.

In case of electron transfer (ET) from a protein residue (aa = Tyr or Trp), the porphyrin radical is reduced and a protein radical (aa^{•(+)} = Tyr[•] or Trp^{•+}) is created, i.e. a Cpd I* species is formed. Upon migration of the radical, the active site is isoelectronic to the classic Cpd II, and therefore, it is reasonable to think that the initially formed oxoferryl species **IIa** (Porph-Fe^{IV}=O) traps a proton, forming the hydroxoferryl species **IIc** (Porph-Fe^{IV}-OH). Indeed, the long Fe-O distances observed in the crystal structures of oxidized HPC (Table 4) and MLC (Table 1), along with their spectral features (Figure 3b), are consistent with the presence of a **IIc** species. The active site histidine is a very likely proton donor to the oxoferryl, in light of the hydrogen-bonding network connecting them in the His-protonated variant **IIb** (i.e. HisH⁺⋯Wat⋯O=Fe, see Figures 5a and 7a).

Finally, for oxidized PMC, the low resolution of the structure and the use of restraints during the refinement resulted in an Fe-O distance intermediate between an oxoferryl (as in PVC) and a hydroxoferryl (as in HPC and MLC). However, the EPR spectrum clearly shows the signal of a porphyrin cation radical for the pH range 5-7. Because crystallization of PAA-treated PMC was carried out at pH 7.5, the distal histidine is most likely unprotonated and species **Ia** predominates.

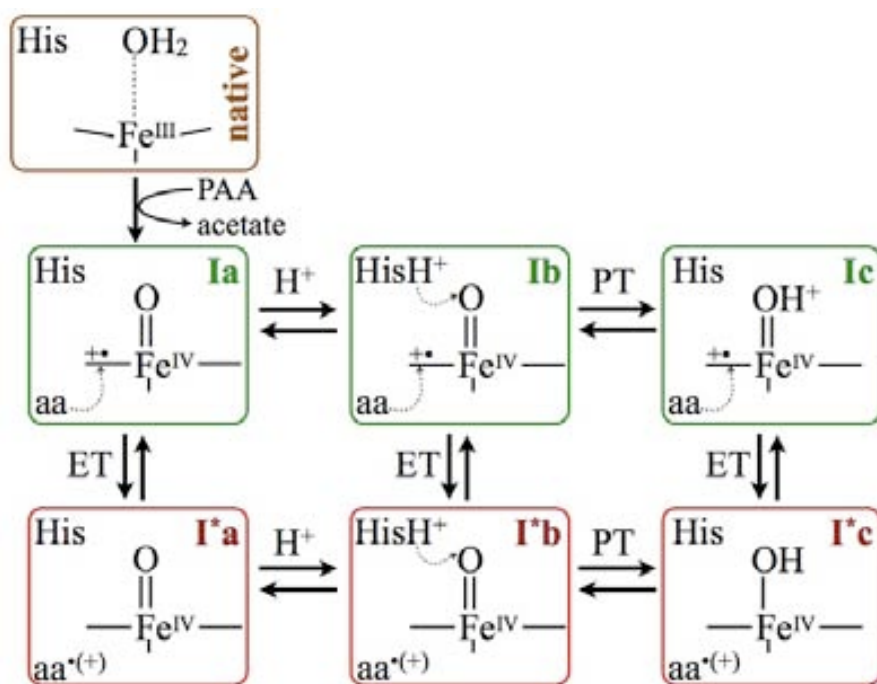


Figure 10. Possible transformations of catalase upon oxidation with PAA in the absence of exogenous electron donors. Note that the electronic configuration of **I*a**, **I*b** or **I*c** species in the heme active site region is isoelectronic with the **IIa**, **IIb** or **IIc** counterpart, respectively, and they only differ in the presence of a protein radical, located at ≥ 5 Å from the heme (Andreoletti, 2001). PAA = peroxyacetic acid; PT = proton transfer; ET = electron transfer; aa = Tyr or Trp.

2.4. Electronic consequences of heme modifications in catalase oxidized intermediates

Analysis of the spin-density distributions of the oxoferryl model **Ia** in HPC and PVC provides insight into the changes imposed by the presence of different heme types (Figure 2). In HPC, there is spin density on the porphyrin, corresponding to one unpaired electron localized on an A_{2u} -like porphyrin orbital (Figure 6). By contrast, the same unpaired electron in PVC is delocalized over the porphyrin (with an A_{1u} symmetry), the imidazole of the distal histidine and, to a lesser extent, the axial phenolate (Figure 8). Moreover, the spatial localization of the unpaired spin is modulated by thermal fluctuations (Figure 9).

This different localization of spin density between HPC-**Ia** and PVC-**Ia** can be rationalized in terms of the relative energies of the high-lying porphyrin orbitals (Chapter I, section 4.2.). The a_{1u} and a_{2u} porphyrin orbitals are nearly degenerated (Ghosh, 1994; Kuramochi, 1997; Scheiner, 2002) and their relative positions can be easily inverted (Figure 11). In heme b, the a_{2u} orbital is destabilized by interaction with the π system of the proximal Tyr (de Visser, 2006). As a

consequence, the a_{2u} porphyrin orbital becomes the donor of the electron removed from the porphyrin during Cpd I formation, as reflected in the A_{2u} symmetry of the spin density distribution on the porphyrin (Figure 11). In heme d, the formation of the *cis*-hydroxy- γ -spirolactone results in the loss of one double bond in pyrrole ring III. The decrease in the aromatic character of the macrocycle affects mainly the a_{1u} orbital, which has contributions from the pyrrole β carbon atoms (Figure 11). As a consequence, the energy of the a_{1u} orbital increases relative to the a_{2u} orbital, making the “ a_{1u} -like” porphyrin orbital the donor of the second electron during Compound I formation.

Furthermore, the unpaired spin on the porphyrin is observed to delocalize over the proximal Tyr and / or the distal His, and this delocalization is influenced by thermal fluctuations (Figure 9). Therefore, catalase Cpd I is a chameleon species whose electronic structure is highly sensitive to external perturbations, as already described for peroxidase Cpd I (de Visser, 2003). In heme b, the a_{2u} porphyrin orbital (which has contributions from the meso carbons and the porphyrin nitrogens) is able to mix with the HOMO of the proximal Tyr. As a result, the proximal ligand is partially oxidized, i.e. the electron is removed from a mixed ($a_{2u} - \pi_{\text{Tyr}}$) orbital (see Figure 11). This is similar to the partial radical character observed for the proximal thiolate ligand in P450 (Shaik, 2005; Bathelt, 2005; Harvey, 2006) and CPO (Stone, 2005).

Alternatively, in heme d, the a_{1u} orbital mixes with one π imidazole orbital. This mixing is possible because the imidazole of the distal histidine overlaps pyrrole ring IV, which carries substantial electron density in the a_{1u} orbital (Figure 11). As a result, the electron removed from the porphyrin of heme d in PVC is actually removed from a mixed orbital ($a_{1u} - \pi_{\text{His}}$), as reflected in the spin density distribution (Figure 9).

In summary, *in heme b-containing HPC the second electron removed during oxidation of the heme is abstracted mostly from the porphyrin* (Figure 21). Indeed, the EPR spectra of other heme b-containing catalases (PMC and MLC) shows a porphyrin cation radical (Lardinois, 1995; Benecky, 1993). Differently, *in heme d-containing PVC it is abstracted partially from the porphyrin and the histidine* (Figure 21). EPR characterization of Cpd I in a heme d-containing catalase, such as PVC or the closely related HP11, is needed to test this prediction.

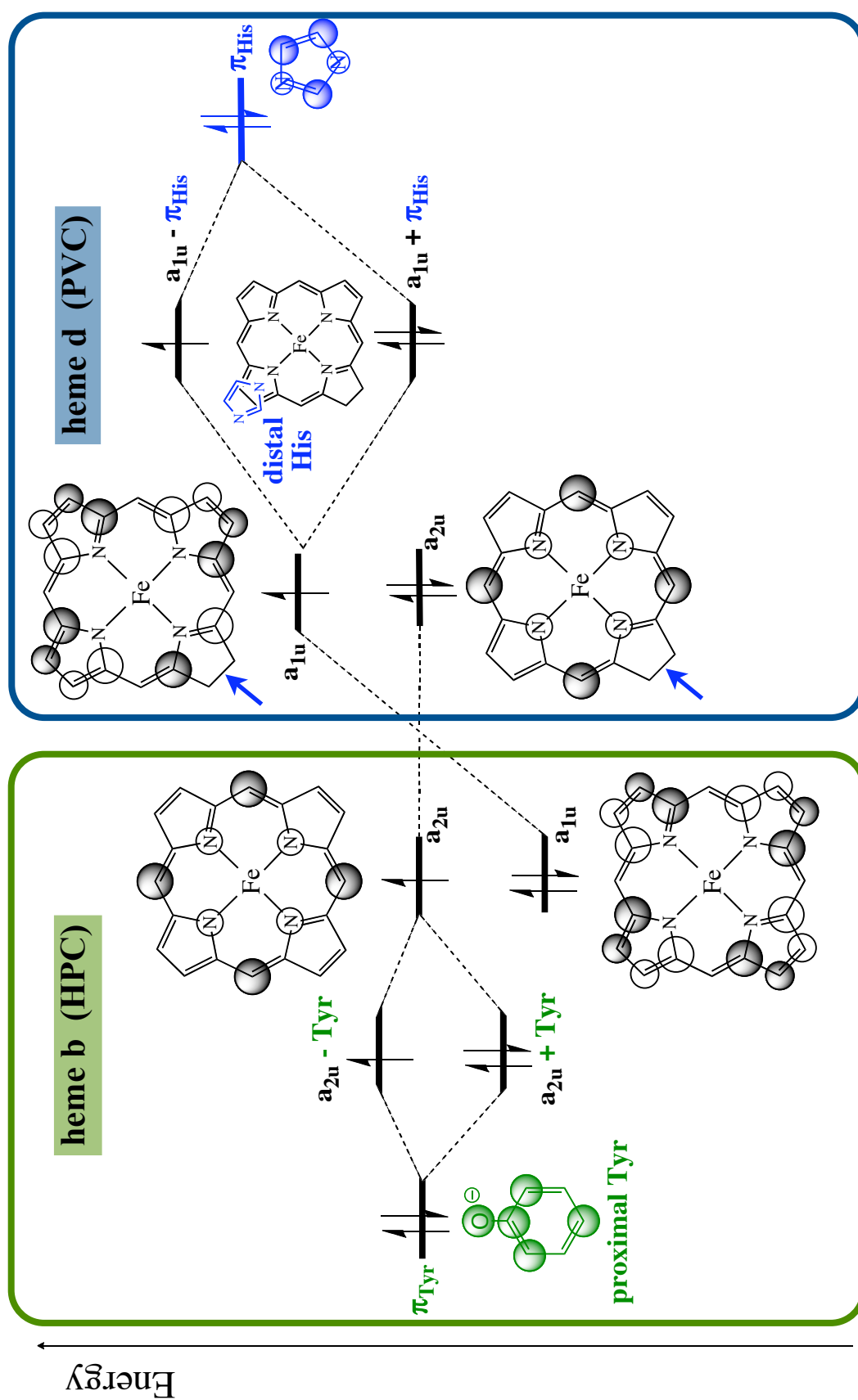


Figure 11. Changes on the relative energy of the a_{1u} and a_{2u} orbitals of the oxoferryl porphyrin species as a result of the heme modification (indicated by an arrow) and possible mixing with other orbitals (π_{Tyr} and π_{His}).

3. SUMMARY AND CONCLUSIONS

Oxidized heme intermediates (Cpd I, Cpd I* and Cpd II) are formed as part of the catalytic cycle of catalases, and also in peroxidases, catalases-peroxidases (KatGs) and cytochromes P450s. Therefore, knowledge of their structure and electronic configuration is essential to understand the reactions performed by these enzymes. Although the experimental characterization of these intermediates is complicated by radical migration and photoreduction (section 1), it appears to be a correlation between the radical location and the Fe-O distance (see Chapter I, Table 2). The presence of a porphyrin radical is associated with a short Fe-O distance, whereas reduction of the porphyrin radical is accompanied by a long Fe-O bond length, regardless of whether the donor is exogenous (Cpd II) or endogenous (Cpd I*). In other words, while Cpd I is better described as an oxoferryl, a hydroxoferryl group is most likely present in Cpd II and Cpd I*.

To probe the validity of this generalization in catalases, CP QM/MM calculations have been performed on the crystal structures of PAA-treated HPC and PVC. Comparison of the computational results with their X-ray structures and absorbance spectra leads to the conclusion that *oxidized PVC contains an oxoferryl $\text{Por}^{\bullet+}\text{-Fe}^{\text{IV}}=\text{O}$ species with partial protonation of the distal histidine, whereas oxidized HPC contains a hydroxoferryl $\text{Por-Fe}^{\text{IV}}\text{-OH}$ with the second oxidation site delocalized as a protein radical, $\text{aa}^{\bullet(+)}$* . Therefore, *the generalization that the presence of a porphyrin radical is associated with a short Fe-O bond, whereas migration of the porphyrin radical to the protein facilitates protonation of the Fe-O bond, is supported both experimentally and by CP QM/ MM calculations on oxidized HPC and PVC*. In order to explain these observations, we have proposed a simple scheme for the most likely transformations experienced by the primary Cpd I species.

Afterwards, we have analyzed the consequences of the heme modification in the electronic structure of the canonical Cpd I (**Ia**). *HPC-Ia shows the “standard” porphyrin radical, whereas in PVC-Ia the unpaired electron is shared between the porphyrin and the distal His*. This can be explained by a change in the relative energies of the porphyrin $\text{a}_{1\text{u}}$ and $\text{a}_{2\text{u}}$ orbitals, as a result of the *cis*-hydroxy- γ -spirolactone modification of the heme in PVC.

In summary, the conclusions of this chapter are the following:

- Peroxoacetic acid-treated HPC bears a protonated oxoferryl (Fe–OH) moiety.
- In contrast, an oxoferryl (Fe=O) unit is present in oxidized PVC.
- Combination of the computational and experimental data of these two catalases supports the prediction that reduction of the porphyrin radical is accompanied by the protonation of the ferryl oxygen.

- The canonical Cpd I in HPC contains a porphyrin-based radical.
- Differently, the radical is shared between the porphyrin and the distal histidine in PVC.
- The modification present in heme d explains the different electronic structure of Cpd I compared to heme b.

**ELECTRON TRANSFER
AND FERRYL PROTONATION
IN CATALASES**

1. INTRODUCTION

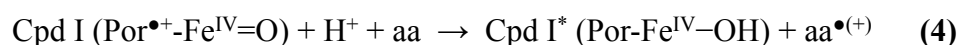
As introduced previously¹, the main activity of catalases is the reduction of Compound I (Cpd I) by hydrogen peroxide in a two-electron process, forming water and molecular oxygen and regenerating the resting state of the enzyme (i.e. the *catalatic* pathway):



However, at low H₂O₂ concentrations, reaction 1 slows down and hence Cpd I may undergo alternative reduction pathways (Figure 1). Using two consecutive one-electron reductions, ferricatalase is regenerated without O₂ production. Depending on the type of one-electron donor, two different mechanisms can be distinguished. In the presence of organic substrates, such as phenols or aromatic amines (AH), Cpd I follows the so-called *peroxidatic* pathway, forming Compound II (Cpd II). This mechanism is equivalent to the catalytic cycle of peroxidases (Chapter I, section 3.3.):



Alternatively, in the absence of *exogenous* reductants, a protein residue (aa, usually Tyr or Trp) may act as an *endogenous* donor:



This mechanism (electron transfer from aa to Cpd I) is often referred as “migration of the porphyrin radical into the protein”.

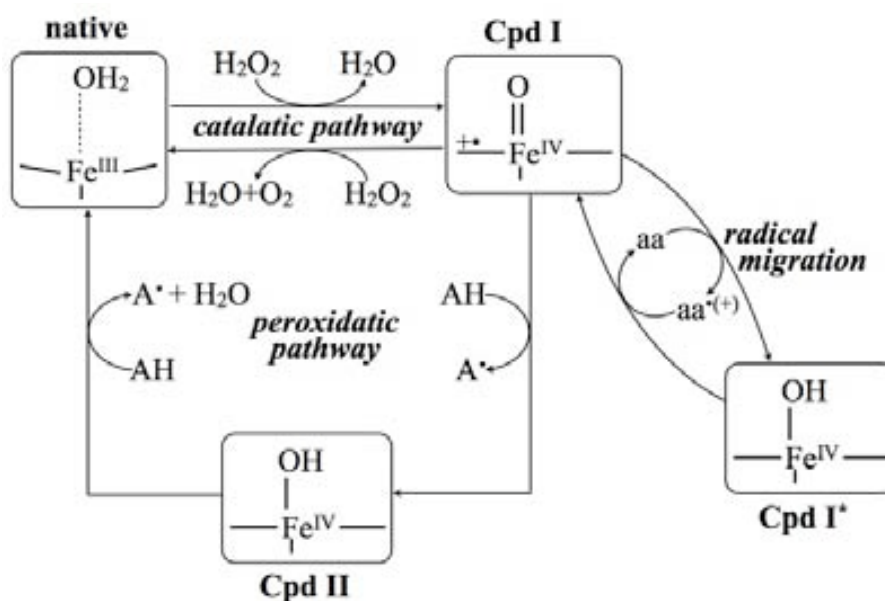


Figure 1. Possible transformations of Cpd I depending on the available reductant.

¹ Chapter I, section 3.3.

Migration of the radical has been observed not only in catalases (e.g. Bovine Liver catalase, BLC) (Ivancich, 1996), but also in other hemeproteins, such as myoglobin (Mb) (Lardinois, 2004), cytochrome c peroxidase (CcP) (Sivaraja, 1999), catalase-peroxidases (KatG) (Ivancich, 2003; Jakopitsch, 2006; Singh, 2007; Colin, 2009), lactoperoxidase (LPO) (Fielding, 2008), cytochrome P450 (P450) (Spolitak, 2005, 2006 & 2008), prostaglandin H synthase (PGHS) (Tsai & Kulmacz, 2009) or allene oxide synthase (AOS) (Wu, 2003). The resulting Compound I* (Cpd I*) species is isoelectronic to Cpd II in the active site and thus has similar spectral features (Chapter I, section 4.2.). Cpd II is known to be protonated (i.e. it bears a hydroxoferryl Fe–OH, instead of an oxoferryl Fe=O group) in several hemeproteins (Berglund, 2002; Nilsson, 2004; Silaghi-Dumitrescu, 2004; Green, 2004; Hersleth, 2006; Green, 2006; Behan, 2006; Stone, 2006), including catalases (Rovira, 2005; Alfonso-Prieto, 2007). Therefore, Cpd I*, being isoelectronic to Cpd II in the active site, is expected to be protonated as well. Indeed, formation of protein radicals (i.e. Cpd I*) in oxidized hemeproteins correlates with the observation of long Fe-O bond distances (~1.8-1.9 Å, see Chapter I, Table 2).

To confirm this generalization, in Chapter IV we performed QM/MM calculations on oxidized *Helicobacter pylori* catalase (HPC) and *Penicillium vitale* catalase (PVC). The long Fe-O distance observed for oxidized HPC, along with its Cpd II-like spectral features, were ascribed to the formation of Cpd I* (Por-Fe^{IV}-OH, aa^{•(+)}), demonstrating that electron transfer to the porphyrin, regardless of whether the electron is exogenous (reaction 2) or endogenous (reaction 4), facilitates protonation of the oxoferryl. On the contrary, oxidized PVC exhibits a short Fe-O distance and the green colour characteristic of a porphyrin cation radical, indicating that the canonical Cpd I (Por^{•+}-Fe^{IV}=O) was formed. Because Cpd I* is generated by electron transfer from a protein residue to Cpd I and protonation of the ferryl oxygen (reaction 4), the lack of Cpd I* formation in PVC could be due to (i) a different Cpd I reduction potential compared to HPC, (ii) different energetics of protonation of the oxoferryl group in Cpd II, or (iii) the characteristics of the endogenous donor. In the present chapter, the factors determining why HPC and PVC form distinct oxidized intermediates are investigated.

(i) Cpd I reduction potential

To date, reduction potentials of Cpd I in catalases are not known. This is due to the short lifetime of Cpd I and Cpd II intermediates and the difficulty in assigning the actual structure of the formed species (Ayala, 2007). Nevertheless, the different propensity for reduction to Cpd II of heme b- and heme d-containing catalases (Chapter I, section 4.2.) suggests that HPC and PVC may have different Cpd I reduction potentials. Because HPC is a small subunit catalase whereas PVC is a large subunit one (see Chapter IV, Figure 1), it could be argued that the different protein size is responsible for this difference. However, both *E. coli* hydroperoxidase II (HPH, a large subunit catalase) and a truncated form of HPH (resembling small subunit catalases) are apparently not reduced to Cpd II (Chelikani, 2005). Hence, the protein size (i.e. small or large subunit) does not appear to affect the reduction to Cpd II. Consistently, clade II of large subunit catalases includes both Cpd II-lacking HPH and PVC (heme d-containing catalases) and Cpd II-forming *Aspergillus niger* catalase (ANC, a heme b-containing catalase) (Lardinois, 1994). Therefore, the lack of Cpd II formation in PVC could be due to either the different protein sequence or the type of heme, but not to the size. It has been shown in CcP that single to triple point mutations can vary the redox potential within a range of 170 mV (DiCarlo, 2007). Because HPC and PVC only share 47% / 64% sequence identity / similarity², it is reasonable to think that the different protein sequence results in a different reduction potential. However, whereas wild-type truncated HPH (heme d-containing) does not apparently form Cpd II, a mutant (H392A) containing heme b does form this intermediate (Chelikani, 2005). This seems to play down the influence of the protein sequence, and points to the type of heme (heme b in HPC and heme d in PVC) as the main cause for the different redox properties. Nevertheless, the observed reduction potentials for d-type hemes fall within the normal range of those observed for b-type hemes in other proteins (Timkovich & Bondoc, 1990)³. Moreover, the ring oxidation potentials of synthetic chlorin models (a porphyrin with one less double bond, similar to heme d) are either lower or nearly identical to those of porphyrins, depending on the substituents (Hanson, 1981; Stolzenber, 1981; Ozawa, 1992a, 1992b & 1994; Jayaraj, 1995)⁴. Therefore, *whether HPC and PVC have different Cpd I reductions potentials and, in this case, whether the heme modification or the protein environment is responsible for this difference* (Murshudov, 1996), is not yet known.

² Excluding the variable N-terminal end and the C-terminal domain, following reference (Daz, 2009).

³ Fe^{III}/Fe^{II} reduction potentials, which are found to correlate with Cpd I/Cpd II reduction potentials.

⁴ Fe^{III}(ring/ring⁺) oxidation potential.

(ii) Protonation of the oxoferryl group

The overall process of Cpd I* formation (reaction 4) involves not only reduction of Cpd I but also protonation of the oxoferryl group. Therefore, it is also necessary to compare the energetics of oxoferryl protonation between HPC and PVC. In this regard, protonation of the oxoferryl group has been proposed to increase the peroxidatic activity in myoglobin (Mb) and haemoglobin (Hb) (Silaghi-Dumitrescu, 2007). Because the peroxidatic activity of HPD (a large subunit, heme d-containing catalase, as PVC) is much slower than that of BLC (a small subunit, heme b-containing catalase, as HPC) (Obinger, 1997), it can be argued that *HPC and PVC may have different energetics of oxoferryl protonation.*

(iii) Endogenous electron donors

In addition to the reduction potential of Cpd I and the oxoferryl protonation, Cpd I* formation may also be affected by the availability of endogenous electron donors. In peroxidases (English & Tsaprailis, 1995) and cytochrome P450 (P450) (Spolitak, 2006), it has been proposed that the decay from Cpd I to Cpd I* correlates with the number of endogenous oxidizable aminoacids and their distribution around the heme. For instance, in CcP and P450, mutation of the redox-active Trp and Tyr into less oxidizable residues (Phe) increases the lifetime of the porphyrin cation radical (Pfister, 2001; Spolitak 2008). *Horse radish peroxidase (HRP) or Proteus mirabilis catalase (PMC, a heme b-containing catalase) exhibit a stable porphyrin radical for the wild-type enzyme (Veitch, 2001; Ivancich, 1997), whereas a tyrosyl radical is observed upon a Phe172Tyr or Phe194Tyr mutation, respectively (Miller, 1995; Andreoletti, 2001). Therefore, a relation between radical migration and the number and distribution of redox-active protein residues around the heme may also hold for catalases.*

Theoretical modeling may overcome the experimental difficulties associated to the short lifetime of the redox couple and the actual structure of the species formed, because the oxidation state and the protonation state of the active site are explicitly given. In the present chapter, the factors determining the lack of Cpd I* formation in heme d-containing catalases compared to heme b are investigated using HPC and PVC as test cases. First, we apply the QM/MM-based methodology recently developed by Blumberger (Blumberger, 2008) to study the electron transfer (ET) to Cpd I. The free energies of ET of HPC and PVC are computed to determine whether these two catalases have different Cpd I reduction potentials. These energies are broken down into their protein and heme components to examine their contribution to the ET. Second, because Cpd II and

Cpd I* are expected to be protonated at neutral pH, the free energy of proton transfer to the oxoferryl group is also calculated for both catalases, using the metadynamics technique (Laio & Parrinello, 2002; Iannuzzi, 2003). Finally, we analyze the number and location of oxidizable aminoacids (i.e. possible endogenous donors) around the heme and we propose a possible candidate for the protein radical in HPC Cpd I* (Tyr351).

2. MECHANISTIC ANALYSIS OF Cpd I* FORMATION

Cpd I* formation (reaction 4) can be divided into two half-reactions: Cpd I reduction (reaction 4a) and oxidation of a protein residue (reaction 4b):



2.1. Cpd I reduction

In Cpd I reduction (reaction 4a), one electron and one proton are transferred to Cpd I. The electron donor is a redox-active protein residue (reaction 4b). The proton source is most likely the distal His, because (i) a partial protonation of the imidazole has been suggested on the basis of the estimated pKa of the distal His in HRP Cpd I (5.0) (Jones & Dunford, 2006) and the electron density found in the crystal structure of MLC Cpd II (Murshudov, 2002), (ii) the distal His is known to act as an acid-base catalyst during the *catalase* reaction (Fita & Rossmann, 1985). Therefore, it is reasonable to think that it may also transfer a proton to the oxoferryl during Cpd I* formation. Regardless of the electron and proton donors, three possible reaction schemes may be envisioned (Figure 2), depending on whether they are transferred stepwise or concertedly.

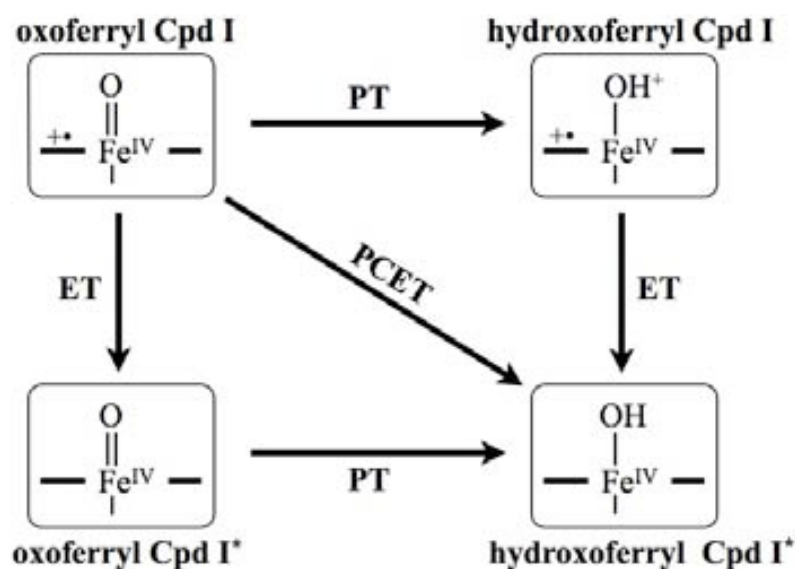
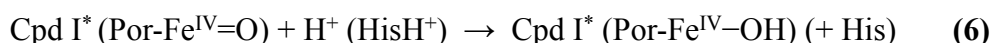


Figure 2. Possible reaction schemes to explain Cpd I reduction.

PT = proton transfer; ET = electron transfer; PCET = proton coupled electron transfer.

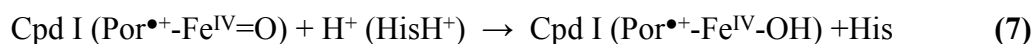
- *Electron transfer followed by proton transfer to the oxoferryl (ET + PT)*

Because Cpd I is a very strong oxidant (Nicholls, 2001), it may easily abstract an electron (reaction 5). Upon reduction of the porphyrin cation radical, the oxoferryl unit will rapidly trap a proton (reaction 6), because Cpd I* is isoelectronic to Cpd II, which is found to be basic in several heme proteins (Berglund, 2002; Nilsson, 2004; Rovira, 2005; Silaghi-Dumitrescu, 2004; Green, 2004; Hersleth, 2006; Green, 2006; Behan, 2006; Stone, 2006).



- *Proton transfer followed by electron transfer (PT + ET)*

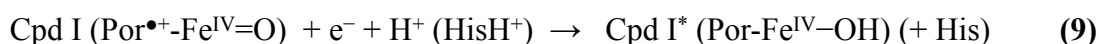
Alternatively, proton transfer may occur first (reaction 7), forming a hydroxoferryl Cpd I, which will then uptake an electron (reaction 8).



However, there is no experimental evidence of a porphyrin cation radical associated to a hydroxoferryl group. A protonated oxoferryl Cpd I is expected to have a low pKa due to the presence of the electron deficient porphyrin radical. As a consequence, the hydroxoferryl Cpd I would easily transfer back the proton to the distal His even before ET can take place. Hence, the PT + ET mechanism appears to be very unlikely.

- *Proton coupled electron transfer to Cpd I (PCET)*

Finally, the electron and the proton may transfer in a concerted way. This is in line with recent studies showing that high valent Fe=O species often participate in PCET mechanisms in heme enzymes (Derat, 2006; Shaik, 2008; Jeong, 2008; Wang, 2009).



In summary, only the ET+PT and PCET mechanisms (Figure 2) are compatible with the current knowledge on the chemistry of ferryl hemes. Therefore, the free energy of Cpd I reduction may be calculated as:

$$\Delta G^{\text{Cpd I reduction}} = \Delta G^{\text{Cpd I, PCET}} = \Delta G^{\text{Cpd I, ET}} + \Delta G^{\text{Cpd I}^*, \text{PT}} \quad (\text{eq. 1})$$

Computationally, it is more convenient to break down the overall free energy into the ET and the PT components.

$\Delta G^{\text{Cpd I, ET}}$ is the free energy change associated to the insertion of one electron into Cpd I (i.e. the “electrochemical reduction” of Cpd I), and it simply depends on $E^{\text{Cpd I}}$, the reduction potential of Cpd I:

$$\Delta G^{\text{Cpd I, ET}} = -nF E^{\text{Cpd I}} \quad (\text{eq. 2})$$

Because it is independent of the electron donor being a protein residue (in Cpd I* formation) or an exogenous substrate (in Cpd II formation) and Cpd I* and Cpd II are isoelectronic in the heme active site, $\Delta G^{\text{Cpd I, ET}}$ can be computed using Cpd II as a model of Cpd I*.

On the other hand, $\Delta G^{\text{Cpd I*, PT}}$ is the free energy change associated to protonation of the oxoferryl group of the heme, and it depends on the pKa of the oxoferryl Cpd I* (pKa^{FeO}). Assuming the distal His is the proton donor, proton transfer is driven by the pKa difference between His and the oxoferryl:

$$\Delta \text{pKa}^{\text{His/FeO}} = \text{pKa}^{\text{His}} - \text{pKa}^{\text{FeO}} \quad (\text{eq. 3})$$

and thus:

$$\Delta G^{\text{Cpd I*, PT}} = [2.3RT \Delta \text{pKa}^{\text{His/FeO}}] \quad (\text{eq. 4})$$

measuring the free energy change associated to the proton transfer from the distal His to the oxoferryl group of the heme. Similar to the ET, the PT can be studied using Cpd II as a model of Cpd I*. The pKa of the oxoferryl Cpd I* is expected to be the same as that of Cpd II, because both Compounds are isoelectronic in the heme active site

Therefore, the free energy associated to Cpd I reduction is:

$$\Delta G^{\text{Cpd I reduction}} = \Delta G^{\text{Cpd I, ET}} + \Delta G^{\text{Cpd I*, PT}} = [-nF E^{\text{Cpd I}}] + [2.3RT \Delta \text{pKa}^{\text{His/FeO}}] \quad (\text{eq. 5})$$

• Comparison HPC-PVC

In order to compare the propensity of Cpd I to be reduced in HPC (heme b) and PVC (heme d), we define the relative free energy of Cpd I reduction ($\Delta \Delta G^{\text{Cpd I reduction}}$) as:

$$\Delta \Delta G^{\text{Cpd I reduction}} = \Delta G^{\text{HPC, Cpd I reduction}} - \Delta G^{\text{PVC, Cpd I reduction}} \quad (\text{eq. 6})$$

Applying equation 4, $\Delta \Delta G^{\text{Cpd I reduction}}$ can be computed as:

$$\begin{aligned} \Delta \Delta G^{\text{Cpd I reduction}} &= [-nF (E^{\text{Cpd I, HPC}} - E^{\text{Cpd I, PVC}})] + [2.3RT (\Delta \text{pKa}^{\text{His/FeO, HPC}} - \Delta \text{pKa}^{\text{His/FeO, PVC}})] \\ \Delta \Delta G^{\text{Cpd I reduction}} &= (-nF \Delta E^{\text{Cpd I}}) + (2.3RT \Delta \Delta \text{pKa}^{\text{His/FeO}}) \quad (\text{eq. 7}) \end{aligned}$$

resulting in:

$$\Delta \Delta G^{\text{Cpd I reduction}} = \Delta \Delta G^{\text{Cpd I, ET}} + \Delta \Delta G^{\text{Cpd I*, PT}} \quad (\text{eq. 8})$$

Therefore, the lower propensity of heme d-containing catalases to form Cpd I* could be explained because (i) ET to heme d-containing Cpd I is thermodynamically less favourable (i.e. a lower reduction potential), (ii) PT to heme d-containing oxoferryl Cpd I* is less likely (i.e. a higher pKa of the oxoferryl or a smaller pKa difference between the distal His and the oxoferryl) or (iii) both ET and PT are less favourable.

2.2. Oxidation of a protein residue

Let us now analyze the second half-reaction in Cpd I* formation (oxidation of a protein residue, reaction 4b). Two types of protein radicals have been mostly detected in oxidized heme proteins: Tyr and Trp radicals (Sivaraja, 1989; Ivancich, 1996; Piontek, 1999a & 1999b; Chouchane, 2000; Ivancich, 2003; Wu, 2003; Lardinois & Ortiz de Montellano, 2004; Schönemann, 2004; Jakopitsch, 2006; Singh, 2007; Ranguelova, 2007; Pipirou, 2007; Fielding, 2008; Colin, 2009; Tsai & Kulmacz, 2009). The main difference between these two protein radicals is that, upon oxidation, the Tyr cation radical becomes deprotonated ($\text{Tyr} \rightarrow \text{Tyr}^\bullet + e^- + \text{H}^+$), whereas the $\text{Trp}^{\bullet+}$ does not ($\text{Trp} \rightarrow \text{Trp}^{\bullet+} + e^-$). Deprotonation of $\text{Tyr}^{\bullet+}$ prevents the back reduction of the radical, and thus all tyrosyl radicals observed experimentally are neutral (Svistunenko, 2005).

Let us assume that the radical formed in HPC Cpd I* is a Tyr radical (see section 3.5.), as has been detected in other catalases (BLC (Ivancich, 1996) and the F194Y PMC mutant (Andreoletti, 2001)). Then, three possible reaction schemes may be envisioned for the transfer of one electron and one proton (Figure 3), as in Cpd I reduction.

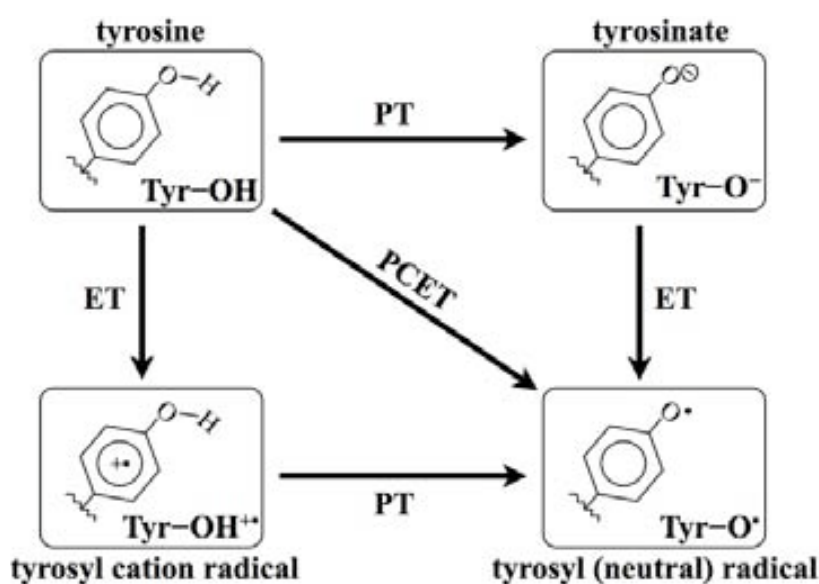
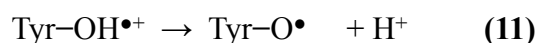
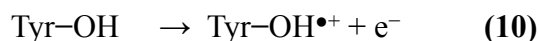


Figure 3. Possible reaction schemes to explain Tyr oxidation.

PT = proton transfer; ET = electron transfer; PCET = proton coupled electron transfer.

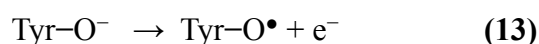
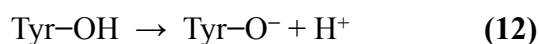
- *ET + PT*

The oxidation potential of Tyr is relatively high (1.38 V). Thus, in principle Cpd I is not a strong enough oxidant (0.88 V for HRP Cpd I) to abstract an electron from Tyr (reaction **10**). However, upon oxidation, the shift in the pKa of the phenolic proton (from ~9.9 to ~-2) results in the deprotonation of the Tyr cation radical (reaction **11**), thus compensating the endothermicity of the first step (Sjödín, 2005).



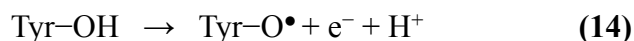
- *PT + ET*

Alternatively, in the presence of a suitable base, proton transfer may occur first (reaction **12**). Oxidation of the resulting phenolate (reaction **13**) is easier (0.68 V) than for neutral Tyr. However, most likely this mechanism will only operate at high pHs (Sjödín, 2005; Irebo, 2008), because the pKa of tyrosine is relatively high (~9.9):



- *PCET scheme*

Finally, the electron and the proton may transfer in a concerted way (reaction **14**), avoiding the building-up of a charged intermediate, though at the expense of a larger reorganization energy (Irebo, 2007 & 2008). In this case, the oxidation potential of Tyr is pH dependent, ranging from 0.97 V at pH=5 to 0.93 V at pH=7.



Of these three possible mechanisms, the stepwise ET + PT is the most likely, because ET from the Tyr residue to Cpd I is long-range (e.g. ~5 Å distance between the heme edge and Tyr in PMC F194Y (Andreoletti, 2001)). However, a PCET mechanism may also hold (Fecenko, 2006), specially in case Tyr is already hydrogen-bonded to the proton acceptor before oxidation (Sjödín, 2006; Irebo, 2008). Thus, the free energy of Tyr oxidation may be calculated as:

$$\Delta G^{\text{Tyr oxidation}} = \Delta G^{\text{Tyr, PCET}} = \Delta G^{\text{Tyr, ET}} + \Delta G^{\text{Tyr}^{\bullet+}, \text{PT}} \quad (\text{eq. 9})$$

Computationally, it is again more convenient to break down the overall free energy into the ET and the PT components.

$\Delta G^{\text{Tyr, ET}}$ depends on the oxidation potential of Tyr (E^{Tyr}):

$$\Delta G^{\text{Tyr, ET}} = [-nF E^{\text{Tyr}}] \quad (\text{eq. 10})$$

whereas $\Delta G^{\text{Tyr}(\bullet+), \text{PT}}$ depends on the pKa of the Tyr cation radical, $\text{pKa}^{\text{Tyr}(\bullet+)}$. Assuming that the proton acceptor is a histidine (see section 3.5.), the PT is driven by the pKa difference between Tyr⁺ and His:

$$\Delta \text{pKa}^{\text{Tyr}(\bullet+)/\text{His}} = \text{pKa}^{\text{Tyr}(\bullet+)} - \text{pKa}^{\text{His}} \quad (\text{eq. 11})$$

Therefore, similarly to equation 5 for Cpd I reduction:

$$\Delta G^{\text{Tyr oxidation}} = [-nF E^{\text{Tyr}}] + [2.3RT \Delta \text{pKa}^{\text{Tyr}(\bullet+)/\text{His}}] \quad (\text{eq. 12})$$

which is the free energy change associated to the abstraction of one electron from Tyr (i.e. the “electrochemical oxidation” of Tyr) *plus* proton transfer from the resulting tyrosyl cation radical to His.

- *ET from Cpd I to Tyr*

Since Tyr is actually oxidized by Cpd I:



ET from Tyr to Cpd I is driven by the redox potential difference:

$$\Delta E^{\text{Cpd I/Tyr}} = E^{\text{Cpd I}} - E^{\text{Tyr}} \quad (\text{eq. 13})$$

and equation 12 becomes:

$$\Delta G^{\text{Tyr oxidation}} = [-nF \Delta E^{\text{Cpd I/Tyr}}] + [2.3RT \Delta \text{pKa}^{\text{Tyr}(\bullet+)/\text{His}}] = \Delta G^{\text{Tyr/CpdI, ET}} + \Delta G^{\text{Tyr}(\bullet+), \text{PT}} \quad (\text{eq. 14})$$

2.3. Cpd I* formation

Summing up the two half-reactions (Cpd I reduction and Tyr oxidation), the overall reaction (Cpd I* formation) turns out to be:

$\text{Cpd I (Porph}^{\bullet+}\text{-Fe}^{\text{IV}}\text{=O)} + \text{His}_1\text{H}^+ + \text{Tyr} + \text{His}_2 \rightarrow \text{Cpd I}^* (\text{Porph-Fe}^{\text{IV}}\text{-OH)} + \text{His}_1 + \text{Tyr}^{\bullet} + \text{His}_2\text{H}^+$ (reaction 16), where His₁ is the distal His, that transfers a proton to the oxoferryl heme, and His₂ is the histidine close to the Tyr, that deprotonates the tyrosyl cation radical. Therefore, the free energy associated to the overall process is:

$$\Delta G^{\text{CpdI}^* \text{ formation}} = \Delta G^{\text{Tyr/CpdI, ET}} + \Delta \Delta G^{\text{Cpd I}^*, \text{PT}} + \Delta G^{\text{Tyr}(\bullet+), \text{PT}} \quad (\text{eq. 15})$$

3. RESULTS AND DISCUSSION

3.1. Free energy of ET to Cpd I ($\Delta G^{\text{Cpd I, ET}}$)

The free energy of ET to Cpd I for both catalases was calculated as explained in Appendix B (section 1.2.). For each catalase, 21 snapshots were extracted from the classical MD in the Cpd I (oxidized) state and another 21 from the trajectory in the Cpd II (reduced)⁵ state, and the vertical ionization energies were calculated by means of QM/MM. Table 1 shows the average vertical energy gaps obtained. Because the standard deviations of the EA and the IP turned out to be rather similar, the driving force (ΔA) and the reorganization energy (λ) were estimated applying the linear response approximation (Chapter I, equations 39-40).

Table 1. Average adiabatic energy of reduction ($\langle \Delta E \rangle$), average vertical energy gaps ($\langle \text{IP} \rangle$ and $\langle \text{EA} \rangle$), and reorganization free energy (λ) and driving force (ΔA) for the ET to Cpd I as obtained from the QM/MM calculations. $\Delta \Delta G^{\text{ET}}$ is the difference in the free energy of ET to Cpd I between the two catalases, $\Delta \Delta G^{\text{ET}} \approx \Delta \Delta A = [\Delta A^{\text{HPC}} - \Delta A^{\text{PVC}}]$. All the values are in eV and the errors correspond to standard deviations.

	HPC (<i>heme b</i>)	PVC (<i>heme d</i>)
$\langle \Delta E \rangle$	$-10.82^a \pm 14.45$	$-6.47^a \pm 17.97$
$\langle \text{IP} \rangle$	$7.22^b \pm 0.22$	$7.18^b \pm 0.25$
$\langle \text{EA} \rangle$	$5.48^b \pm 0.30$	$5.47^b \pm 0.30$
λ	$0.87^c \pm 0.26^d$	$0.86^c \pm 0.27^d$
ΔA	$-6.35^c \pm 0.26^e$	$-6.32^c \pm 0.27^e$
$\Delta \Delta G^{\text{ET}}$	-0.03 ± 0.38^f	

$$^a \langle \Delta E \rangle = \langle E_{\text{Cpd II}}(\text{R}_{\text{Cpd II}}) - E_{\text{Cpd I}}(\text{R}_{\text{Cpd I}}) \rangle$$

$$^b \langle \text{EA} \rangle = \langle (\Delta E_0)_{\text{Cpd I}} \rangle = \langle E_{\text{Cpd I}}(\text{R}_{\text{Cpd I}}) - E_{\text{Cpd II}}(\text{R}_{\text{Cpd I}}) \rangle, \quad \langle \text{IP} \rangle = \langle (\Delta E_0)_{\text{Cpd II}} \rangle = \langle E_{\text{Cpd I}}(\text{R}_{\text{Cpd II}}) - E_{\text{Cpd II}}(\text{R}_{\text{Cpd II}}) \rangle$$

$$^c \Delta A = [\langle \text{IP} \rangle + \langle \text{EA} \rangle] / 2, \quad \lambda = [\langle \text{IP} \rangle - \langle \text{EA} \rangle] / 2 \quad (\text{LR approximation})$$

$$^d \sigma_{\lambda} = \sqrt{(\sigma_{\text{IP}}^2 + \sigma_{\text{EA}}^2) / 2} \quad ^e \sigma_{\Delta A} = \sqrt{(\sigma_{\text{IP}}^2 + \sigma_{\text{EA}}^2) / 2} \quad ^f \sigma_{\Delta \Delta G^{\text{ET}}} = \sqrt{(\sigma_{\Delta A}^{\text{HPC}} + \sigma_{\Delta A}^{\text{PVC}})}$$

The most important result is that the relative free energy of ET to Cpd I ($\Delta \Delta G^{\text{ET}}$) is approximately zero, indicating that ET to PVC Cpd I is as difficult as for HPC. This is in agreement with the reduction potentials of d-type hemes falling within the normal range of b-type hemes in other proteins (Timkovich & Bondoc, 1990), even though the errors of the calculation are within the

⁵ Cpd II is used as a model of Cpd I* because both Compounds are isoelectronic in the heme active site.

same range of the small redox potential differences typical of biological cofactors (Blumberger, 2008). Moreover, gas phase and QM/MM calculations using Cpd I and Cpd II optimized structures gave the same tendency (see Appendix D, sections 2.1. and 2.2.).

The reorganization free energies are also very similar for HPC and PVC (around 0.9 eV). In catalases, the cofactor is deeply buried inside the protein and thus one expect a λ within the range observed for proteins with cofactors excluded from the solvent (0.25-0.9 eV) (Moser, 2006). Nevertheless, the obtained value is most likely an overestimation of the actual reorganization energy due to the non-polarizable force field (AMBER99, TIP3P water model) used in the calculation (Blumberger, 2008; Blumberger & Lamoreaux, 2008).

• ***Decomposition into heme and protein contributions***

The influence of the different parts of the system on the driving force and the reorganization energy was probed by decomposing the total values into the *inner-sphere* (i.e. heme and first-shell residues) and the *outer-sphere* (i.e. protein and solvent) contributions:

$$\Delta\Delta G^{\text{ET}} \approx \Delta\Delta A^{\text{ET}} = [\Delta\Delta A^{\text{i}} + \Delta\Delta A^{\text{o}}] \quad (\text{eq. 16})$$

where $\Delta\Delta A^{\text{i}} = \Delta\Delta A_{\text{QM}}$ and $\Delta\Delta A^{\text{o}} = (\Delta\Delta A_{\text{MM}} + \Delta\Delta A_{\text{QM-MM}})$ (see Chapter II, section 4.4.).

Contribution of the heme and the first-shell ligands. The inner-sphere energies are shown in Table 2. The intrinsic propensity for reduction of both hemes is found to be very similar, as indicated by the almost identical inner-sphere contributions to the driving force (i.e. $\Delta\Delta A^{\text{i}}$ only differ by ~88 meV). This is in line with the 10-320 meV change in the midpoint oxidation potentials of synthetic porphyrins (similar to heme b) compared to chlorins (similar to heme d) (Hanson, 1981; Stolzenber, 1981; Ozawa, 1992a, 1992b & 1994; Jayaraj, 1995). Consistently, the electron affinities ($\langle EA^{\text{i}} \rangle$) of both hemes are also very similar, as already observed for the gas phase and QM/MM optimized structures (Appendix B, sections 2.1. and 2.2.).

Table 2. Inner-sphere contribution (i.e. heme and first-shell residues) to the average adiabatic energy of reduction ($\langle \Delta E^i \rangle$) and the vertical energy gaps ($\langle IP^i \rangle$ and $\langle EA^i \rangle$), as well as the driving force (ΔA^i) and the reorganization free energy (λ^i) for the ET to Cpd I. All the values are in eV and the errors correspond to standard deviations.

inner-sphere	heme b	heme d
$\langle \Delta E^i \rangle$	$-8.00^a \pm 0.50$	$-8.32^a \pm 0.65$
$\langle IP^i \rangle$	$7.97^b \pm 0.11$	$8.22^b \pm 0.09$
$\langle EA^i \rangle$	$7.89^b \pm 0.12$	$7.82^b \pm 0.31$
λ^i	$0.04^c \pm 0.11^e$	$0.20^c \pm 0.23^e$
ΔA^i	$-7.93^c \pm 0.11^f$	$-8.02^c \pm 0.23^f$
$\Delta \Delta A^i$	$0.09^d \pm 0.26^g$	

$$^a \langle \Delta E^i \rangle = \langle E_{\text{Cpd II}}^{\text{QM}}(\text{R}_{\text{Cpd II}}) - E_{\text{Cpd I}}^{\text{QM}}(\text{R}_{\text{Cpd I}}) \rangle$$

$$^b \langle EA^i \rangle = \langle E_{\text{Cpd I}}^{\text{QM}}(\text{R}_{\text{Cpd I}}) - E_{\text{Cpd II}}^{\text{QM}}(\text{R}_{\text{Cpd I}}) \rangle, \langle IP^i \rangle = \langle E_{\text{Cpd I}}^{\text{QM}}(\text{R}_{\text{Cpd II}}) - E_{\text{Cpd II}}^{\text{QM}}(\text{R}_{\text{Cpd II}}) \rangle$$

$$^c \Delta A^i = [\langle IP^i \rangle + \langle EA^i \rangle] / 2, \lambda^i = [\langle IP^i \rangle - \langle EA^i \rangle] / 2$$

$$^d \Delta \Delta A^i = [\Delta A^{\text{HPC}(i)} - \Delta A^{\text{HPC}(i)}]$$

$$^e \sigma_{\lambda^i} = \sqrt{(\sigma_{IP^i}^2 + \sigma_{EA^i}^2) / 2} \quad ^f \sigma_{\Delta A^i} = \sqrt{(\sigma_{IP^i}^2 + \sigma_{EA^i}^2) / 2} \quad ^g \sigma_{\Delta \Delta A^i} = \sqrt{(\sigma_{\Delta A^{\text{HPC}(i)}}^2 + \sigma_{\Delta A^{\text{PVC}(i)}}^2)}$$

Surprisingly, the fluctuations of the EA^i in heme d were found to be much larger than those of the IP^i or the vertical ionization energies of heme b. This larger standard deviation is probably due to the *cis*-hydroxy- γ -spirolactone modification present in heme d (see Chapter IV, Figure 1). In the classical MD, the hydroxyl group of the modification displays two conformations (Figure 4): (a) hydrogen-bonded to the lactone and the π system of the proximal Tyr, and (b) hydrogen-bonded to Asp742. In the Cpd II state, only conformation (a) is possible. By contrast, in the Cpd I state, because the proximal Tyr has a partial radical character, the interaction of the OH group with the phenolate ring weakens, thus allowing the hydroxyl group to rotate and alternate between conformations (a) and (b). Hydrogen bonding to the negatively charged Asp in conformation (b) is expected to stabilize Cpd I and thus decrease the electron affinity of Cpd I. Likewise, hydrogen-bonding to heme d-like chlorins has been proposed to increase the oxidation potential of the macrocycle (Ivancich, 1998).

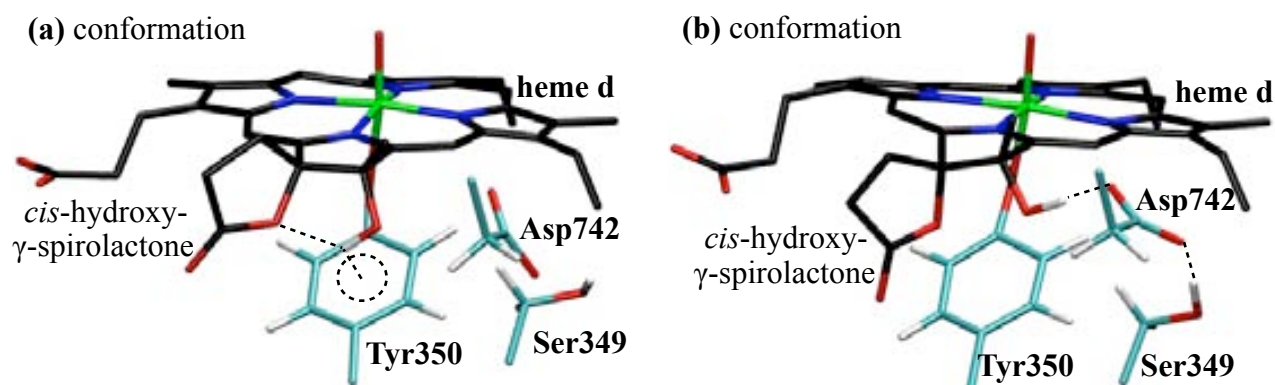


Figure 4. Possible conformations of the hydroxyl group of the *cis*-hydroxy- γ -spirolactone modification in heme d, observed during the classical MD simulations of PVC.

The inner-sphere reorganization free energy of heme b is similar to those calculated for model porphyrins, such as FeP(im)₂ (85 meV) (Sigfridsson, 2001) or ZnP (50-98 meV) (Amashukeli, 2004). On the contrary, heme d shows a larger λ^i (by 158 meV), with fluctuations that are twice broader. The inner-sphere reorganization free energy is known to correlate with the change in the iron-ligand bond lengths upon ET (Jensen & Ryde, 2001). However, the average variation in the Fe-O (0.03 / 0 Å, HPC and PVC, respectively), Fe-O_{Tyr} (0 / -0.02 Å) and Fe-N_{Por} (0.01-0.04 / 0.01-0.04 Å) distances is similar for both hemes. Only the change in the hydrogen-bonds between the proximal Tyr and Arg is slightly larger for heme d (0.13-0.18 Å, compared to 0.12-0.02 Å for heme b), what could explain the larger λ^i of heme d. Besides, the conformational change of the OH group of the heme d modification (Figure 4) further increases λ^i .

Contribution of the protein and solvent. The outer-sphere contribution (i.e. protein and solvent) to the ET is shown in Table 3 (see also Appendix B, section 5). The difference in the driving force ($\Delta\Delta A^o$), albeit small, has the opposite sign to $\Delta\Delta A^i$, indicating that the protein environment hinders Cpd I reduction (i.e. formation of Cpd I* or Cpd II) in PVC compared to HPC. There are two possible concerns to this result. First, it appears to contradict the lack of Cpd II formation in the truncated variant of HP11 (see section 1). However, it should be noted that the catalase core resulting from truncation, although having the same structure as small subunit catalases, still has a different sequence. Second, PVC (a large subunit catalase) is larger than HPC (a small subunit catalase) by ~800 protein residues, and thus the finite size errors of the calculation may not cancel when comparing the two catalases (Ayala, 2008).

As expected, the outer-sphere environment (λ^o) turns out to be the main responsible for the reorganization upon ET. Although for both catalases the cofactor is buried inside the protein core, λ^o is larger for HPC (0.84 eV) than for PVC (0.62 eV). This could be due to the main channel connecting the heme to the protein surface being shorter for HPC than for PVC (Switala & Loewen, 2002).

Table 3. Outer-sphere contribution (i.e. protein and solvent) to the average adiabatic energy of reduction ($\langle\Delta E^o\rangle$) and the vertical energy gaps ($\langle IP^o\rangle$ and $\langle EA^o\rangle$), as well as the driving force (ΔA^o) and the reorganization free energy (λ^o) for the ET to Cpd I. All the values are in eV and the errors correspond to standard deviations.

outer-sphere	heme b - HPC	heme d - PVC
$\langle\Delta E^o\rangle$	$-2.79^a \pm 14.66$	$-1.91^a \pm 18.22$
$\langle IP^o\rangle$	$-0.75^b \pm 0.19$	$-1.07^b \pm 0.27$
$\langle EA^o\rangle$	$-2.43^b \pm 0.22$	$-2.31^b \pm 0.35$
λ^o	$0.84^c \pm 0.29^e$	$0.62^c \pm 0.45^e$
ΔA^o	$1.59^c \pm 0.29^f$	$1.69^c \pm 0.45^f$
$\Delta\Delta A^o$	$-0.10^d \pm 0.53^g$	

$$^a \langle\Delta E^o\rangle = \langle\Delta E^{(QM-MM)}\rangle + \langle\Delta E^{MM}\rangle$$

$$^b \langle EA^o\rangle = \langle EA^{(QM-MM)}\rangle + \langle EA^{MM}\rangle, \langle IP^o\rangle = \langle IP^{(QM-MM)}\rangle + \langle IP^{MM}\rangle$$

$$^c \Delta A^o = \Delta A^{(QM-MM)} + \Delta A^{MM}, \langle\lambda^o\rangle = \langle\lambda^{(QM-MM)}\rangle + \langle\lambda^{MM}\rangle$$

$$^d \Delta\Delta A^o = [\Delta A^{HPC(o)} - \Delta A^{PVC(o)}]$$

$$^e \sigma_{\lambda^o} = \sqrt{(\sigma_{\lambda^{(QM-MM)}}^2 + \sigma_{\lambda^{MM}}^2)} \quad ^f \sigma_{\Delta A^o} = \sqrt{(\sigma_{\Delta A^{(QM-MM)}}^2 + \sigma_{\Delta A^{MM}}^2)} \quad ^g \sigma_{\Delta\Delta A^o} = \sqrt{(\sigma_{\Delta A^{HPC(o)}}^2 + \sigma_{\Delta A^{PVC(o)}}^2)}$$

In summary, calculation of the free energy of ET to Cpd I shows that *ET to PVC Cpd I is as easy as for HPC*. The impact on the reduction potential of the different heme or protein environment is very small, and they have opposite signs. *Heme d is a little easier to reduce than heme b, but the protein frame of PVC slightly hinders ET compared to the HPC*, resulting in almost identical reduction potentials. Albeit overestimated, *the reorganization free energy of both catalases (~0.9 eV) is in line with the cofactor being buried in the protein core*.

3.2. Free energy of PT ($\Delta G^{\text{Cpd I}^*, \text{PT}}$)

The free energy of the proton transfer from the distal His to the ferryl oxygen of Cpd II⁶ was computed by means of metadynamics simulations (see Appendix B, section 1.3.). Two collective variables (or reaction coordinates) were chosen (see Figure 5). The first collective variable [$\text{CV}_1 = N_{\text{coord}}(\text{O}_w\text{-H}_1) - N_{\text{coord}}(\text{O}\text{-H}_1)$] measures the degree of proton transfer from the pocket water to the oxoferryl, whereas the second [$\text{CV}_2 = N_{\text{coord}}(\text{O}_w\text{-H}_2) - N_{\text{coord}}(\text{N}_\epsilon\text{-H}_2)$] gives an idea of the deprotonation of the distal His.

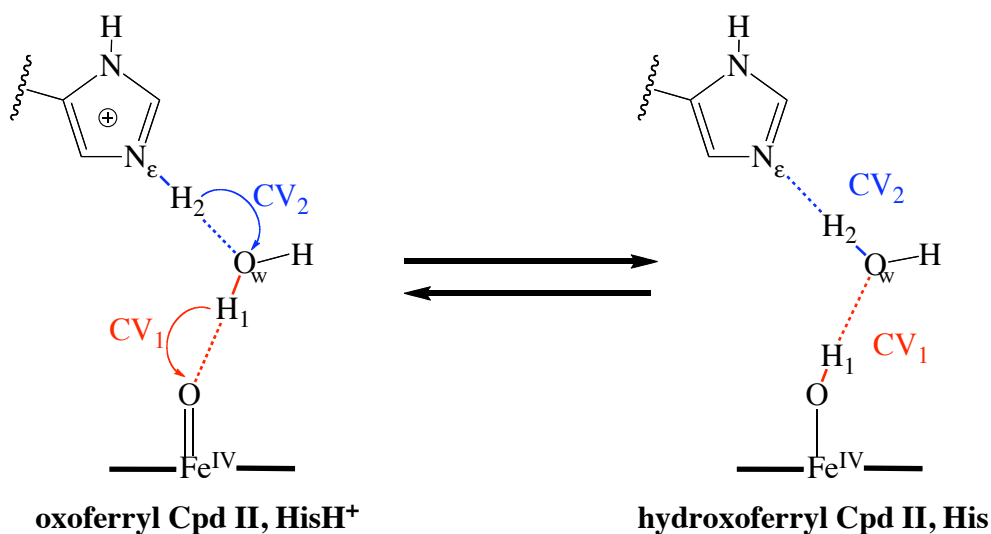


Figure 5. Collective variables used to model the water-mediated proton transfer from the protonated distal His to the oxoferryl.

• HPC

The free energy surface (FES) reconstructed from the metadynamics simulations of HPC Cpd II is displayed in Figure 6. It shows two minima (**R** and **R***), corresponding to the {oxoferryl Cpd II, HisH⁺} reactants, separated by a transition state (**TS**) from the {hydroxoferryl Cpd II, His} products, which are also represented by two different minima (**P*** and **P**). The overall barrier of PT turns out to be ~2 kcal/mol and the products are ~15 kcal/mol more stable than the reactants.

⁶ Cpd II is used as a model of Cpd I* because both Compounds are isoelectronic in the heme active site, and thus their basicity is expected to be very nearly identical.

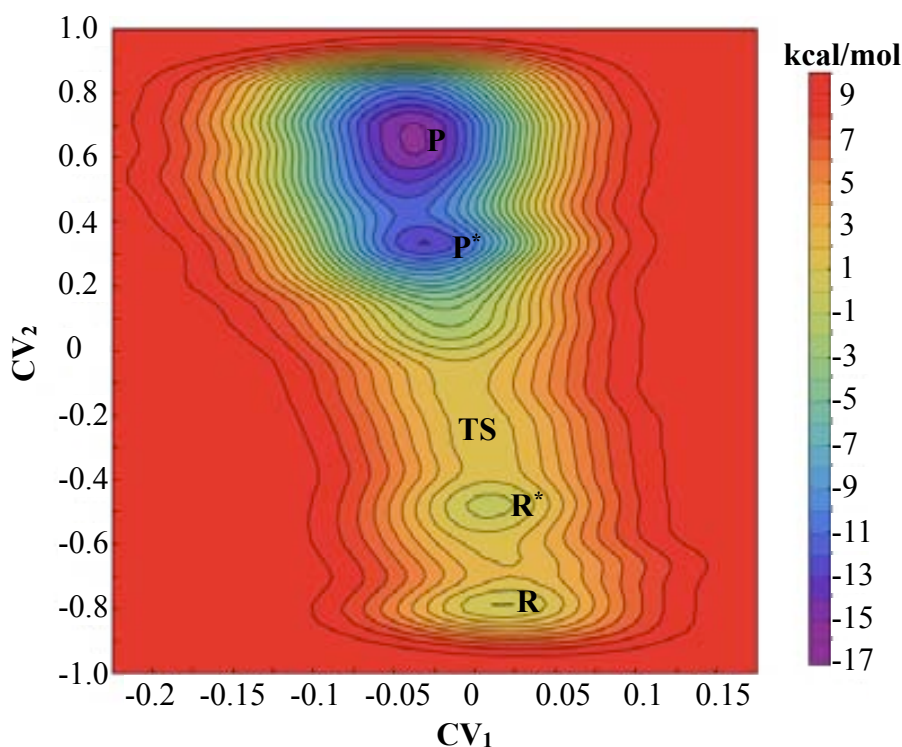


Figure 6. Free energy landscape reconstructed from the metadynamics simulation of HPC. Energies are given in kcal/mol and contours lines are plotted at 1 kcal/mol.

The atomic reorganization along the PT is shown in Figure 7. Starting from the equilibrium structure of the {oxoferryl Cpd II, HisH⁺} reactants (**R**), the active site hydrogen bonding network reorganizes at a 2 kcal/mol cost, yielding configuration **R***, which is degenerated with **R**. On going from **R** to **R***, the hydrogen-bonds of the water molecule with both the oxoferryl (O-H₁) and the distal His (O_w-H₂) shorten (by ~ 0.5 and ~ 0.3 Å, respectively, see Table 4). This increases the polarization of the covalent bonds that need to be broken during the PT (i.e. the O_w-H₁ and N_ε-H₂ bond distances lengthen by ~0.06 Å). As a consequence, the O_w-H₁ bond breaks in the **TS** (1.26 Å). While this H₁ proton is transferred from the pocket water to the oxoferryl group, H₂ hops from the distal HisH⁺ to the transient OH⁻ (Figure 7) and restores the water molecule, completing the reaction. In the {hydroxoferryl Cpd II, His} products, protonation of the oxoferryl unit lengthens the Fe-O distance (from ~1.7 to ~1.8 Å, see Table 4), as expected for the transition from a double (Fe=O) to a single (Fe-OH) bond. At the same time, the Fe-O_{Tyr} bond shortens (from ~2.08 to ~2.00 Å), due to the *push-pull* effect (Nilsson, 2004; Rovira, 2005; Derat, 2006b; Green, 2006; Behan, 2006a,b; Wang & de Visser, 2007). Initially, the pocket water maintains the hydrogen-bonding to the hydroxoferryl group and the distal His (**P***). However, the system easily relaxes to another configuration of the products (**P**), which is more stable by ~2 kcal/mol. The water molecule moves upwards, breaking the hydrogen-bond with the hydroxoferryl group. Hence, the

hydroxoferryl group rotates freely around the Fe-O bond, and the pocket water interacts with both distal residues, His and Asn.

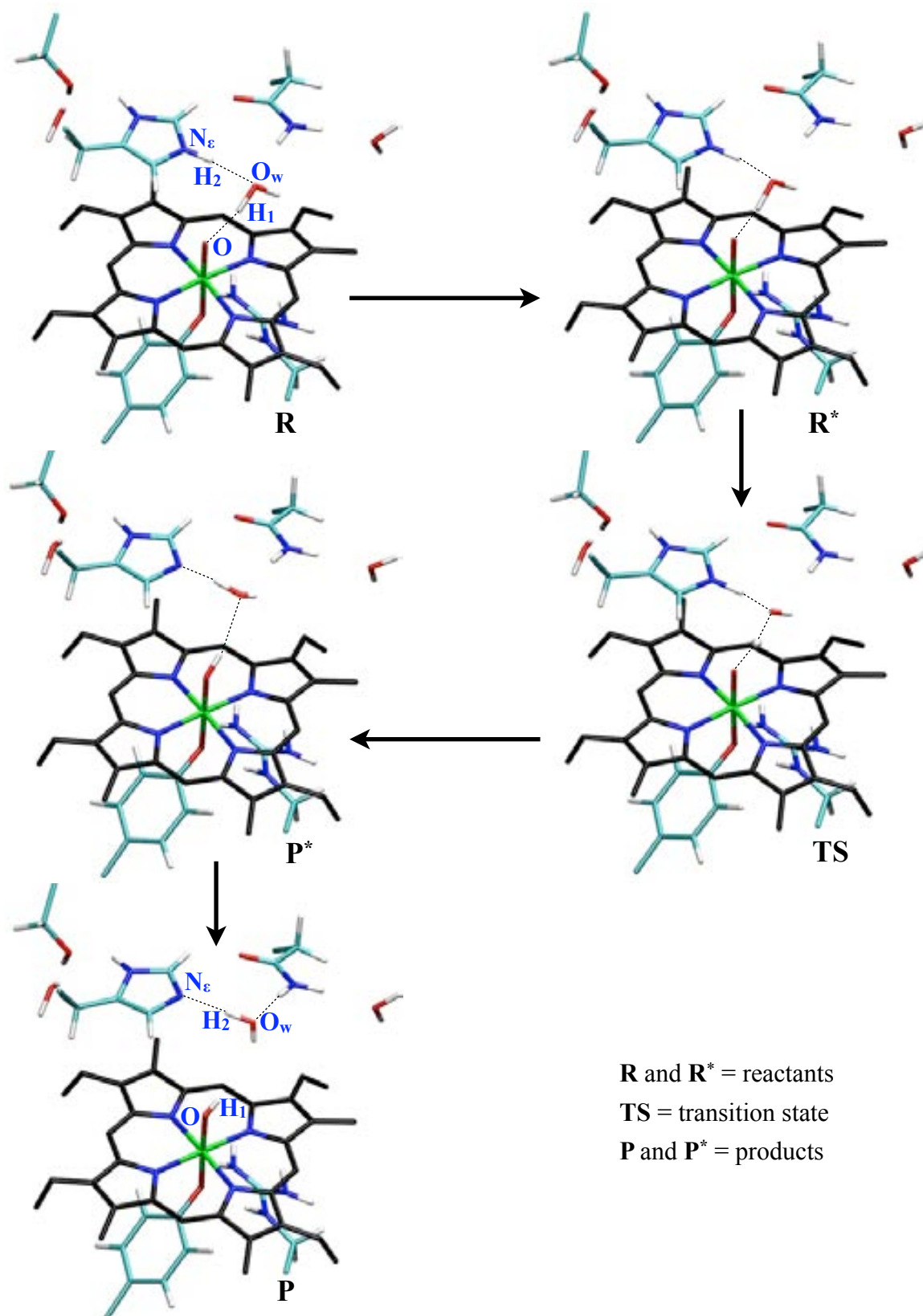


Figure 7. Atomic rearrangements along the PT pathway of HPC Cpd II. Average structures along the metadynamics simulation are shown. Only the QM atoms are displayed.

Table 4. Representative distances^a for the minima found along the PT pathway in HPC Cpd II. The values correspond to averages (with standard deviation) along the metadynamics simulation.

distance (Å)	R	R*	TS	P*	P
O-H₁	1.75 ± 0.17	1.46 ± 0.10	1.32 ± 0.20	1.00 ± 0.04	0.99 ± 0.04
O_w-H₁	1.03 ± 0.04	1.09 ± 0.06	1.26 ± 0.27	2.34 ± 0.74	3.26 ± 0.89
O_w-H₂	2.11 ± 0.17	1.65 ± 0.06	1.42 ± 0.08	1.08 ± 0.04	1.02 ± 0.03
N_ε-H₂	1.03 ± 0.04	1.09 ± 0.04	1.16 ± 0.06	1.50 ± 0.03	1.80 ± 0.12
Fe-O	1.71 ± 0.02	1.72 ± 0.02	1.73 ± 0.03	1.79 ± 0.05	1.82 ± 0.06
Fe-O_{Tyr}	2.08 ± 0.05	2.09 ± 0.09	2.05 ± 0.06	2.02 ± 0.07	2.01 ± 0.05
O_w-NH_{Asn}	3.12 ± 0.38	3.28 ± 0.38	3.32 ± 0.37	2.73 ± 0.46	2.24 ± 0.35
H_w-N_{Porph}	3.24 ± 0.29	2.91 ± 0.27	3.10 ± 0.70	3.50 ± 0.67	3.50 ± 0.46

^a For atom names see Figure 7.

Therefore, *the water-mediated PT from the distal His to the oxoferryl group in HPC Cpd II or Cpd I* is almost barrierless* (~2 kcal/mol, see Figure 6). This is in line with the spontaneous proton transfer observed during optimization of the {oxoferryl Cpd II, HisH⁺} configuration (see Chapter IV, section 2.1.). Our result also show that *protonation of the ferryl oxygen stabilizes significantly Cpd II or Cpd I** (by ~15 kcal/mol). This explains why protonation of the oxoferryl group in PMC Cpd II was found to be irreversible. Specifically, the oxoferryl Cpd II was protonated by lowering the pH to 5.3, but the resulting hydroxoferryl Cpd II was not converted back to the oxoferryl form by adjusting the sample pH back to 8.3 (Horner, 2006 & 2007).

• PVC

Figure 8 displays the FES reconstructed from the metadynamics simulations of PVC Cpd II. It shows two minima (**R** and **P**) separated by a transition state (**TS**). The overall barrier of the PT is ~3.5 kcal/mol and the hydroxoferryl Cpd II is ~4.5 kcal/mol more stable than the oxoferryl.

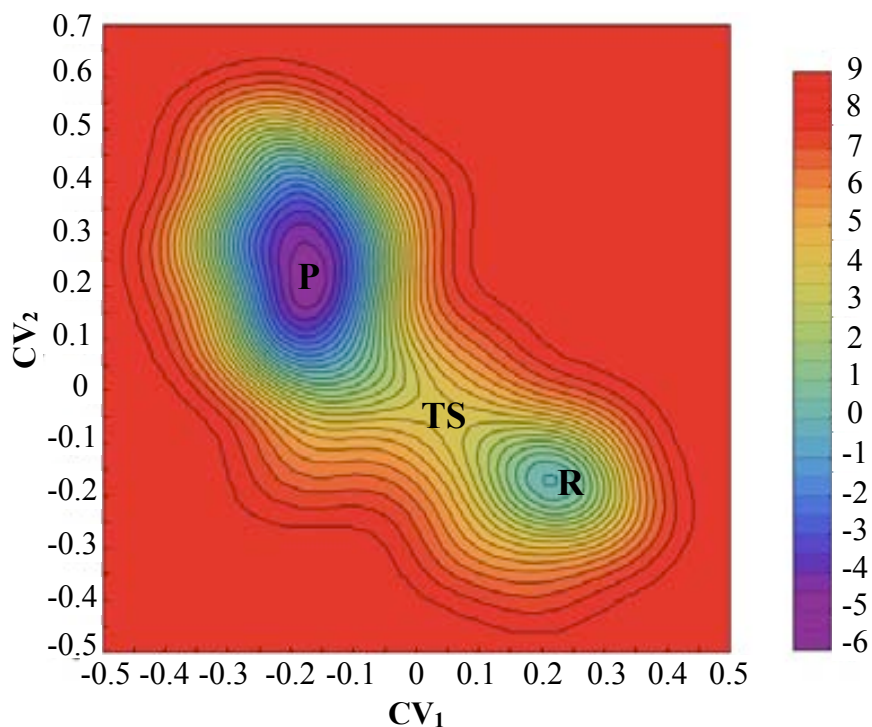


Figure 8. Free energy landscape reconstructed from the metadynamics simulation of PVC. Energies are given in kcal/mol and contours lines are plotted at 0.5 kcal/mol.

The atomic reorganization along the PT is shown in Figure 9. In the reactants (**R**, i.e. {oxoferryl Cpd II, HisH⁺}), the pocket water is hydrogen-bonded to the oxoferryl group and the protonated distal His, as in HPC. In the **TS**, the two covalent bonds O_w-H₁ and N_ε-H₂ break (Table 5), and thus the two protons H₁ and H₂ are transferred almost simultaneously. This is in contrast to HPC, where PT of H₂ from the pocket water to the oxoferryl precedes the PT of H₁ from the distal His to the water molecule. The resulting protonation of the oxoferryl is reflected in the change in the iron-axial ligand distances (Table 5), as explained above. In the {hydroxoferryl Cpd II, His} configuration (**P**), the pocket water remains hydrogen-bonded to the distal His and the hydroxoferryl (Figure 9).

Overall, *the water-mediated PT from the distal His to the oxoferryl group in PVC Cpd II or Cpd I* has a small barrier (~3.5 kcal/mol, see Figure 8). Besides, protonation of the ferryl oxygen stabilizes Cpd II or Cpd I* (by ~4.5 kcal/mol).*

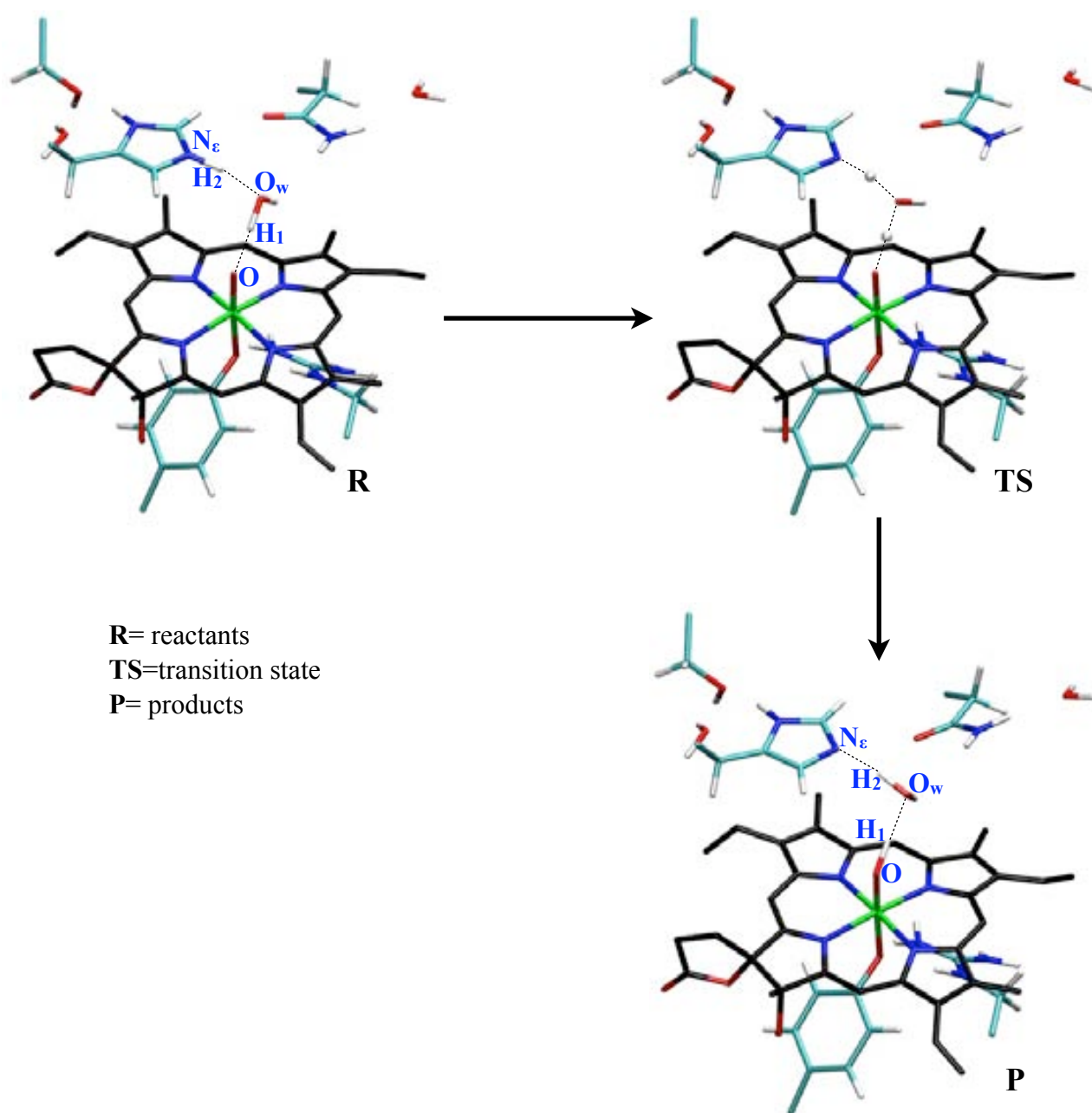


Figure 9. Atomic rearrangements along the PT pathway in PVC Cpd II. Average structures along the metadynamics simulation are shown. Only the QM atoms are displayed.

Table 5. Representative distances^a for the minima found along the PT pathway in PVC Cpd II. The values correspond to averages (with standard deviation) along the metadynamics simulation.

distance (Å)	R	TS	P
O-H₁	1.60 ± 0.09	1.25 ± 0.06	1.06 ± 0.04
O_w-H₁	1.03 ± 0.03	1.18 ± 0.03	1.74 ± 0.20
O_w-H₂	1.65 ± 0.15	1.30 ± 0.05	1.06 ± 0.04
N_e-H₂	1.11 ± 0.02	1.21 ± 0.04	1.67 ± 0.15
Fe-O	1.71 ± 0.03	1.71 ± 0.03	1.76 ± 0.03
Fe-O_{Tyr}	2.04 ± 0.06	1.98 ± 0.05	1.99 ± 0.07
O_w-NH_{Asn}	3.28 ± 0.29	3.94 ± 0.28	3.05 ± 0.37
H_w-N_{Porph}	3.01 ± 0.44	3.10 ± 0.24	2.92 ± 0.24

^a For atom names see Figure 9.

• Comparison HPC-PVC

Two main differences can be seen when comparing the PT free energy profiles of HPC and PVC Cpd II / Cpd I* (Figure 10). First, the energy barrier is lower for HPC (~ 2 kcal/mol) than for PVC (~ 3.5 kcal/mol). This is consistent with the spontaneous proton transfer found only for HPC during optimization of the {oxoferryl Cpd II, HisH⁺} configuration (see Chapter IV, section 2.1.). Second, the stabilization of Cpd II / Cpd I* by protonation is much larger for HPC (~ 15 kcal/mol) than for PVC (~ 4.5 kcal/mol). As a consequence, back PT from the hydroxoferryl to the distal His is more favourable in PVC (~ 4.5 + 3.5 = 8 kcal/mol, see Figure 10) compared to HPC (~ 15 + 2 = 17 kcal/mol).

The energy difference between the two isomers of Cpd II (hydroxoferryl and oxoferryl forms, i.e. ΔG) can be used to estimate the population distribution between them. Applying Boltzmann's law:

$$\frac{[N_{Fe-OH} / N_{Fe=O}]^{HPC}}{[N_{Fe-OH} / N_{Fe=O}]^{PVC}} = \frac{\exp[-\Delta G^{HPC} / RT]}{\exp[-\Delta G^{PVC} / RT]} = \frac{8.27 \times 10^{10}}{1.88 \times 10^3} = 4.39 \times 10^7 \quad (\text{eq.17})$$

Therefore, at equilibrium the population of the oxoferryl Cpd II / Cpd I* is negligible for HPC, whereas approximately 1-2 out of one thousand molecules is in the oxoferryl form for PVC. On this

basis, it is reasonable to assume that the population of the oxoferryl Cpd II / Cpd I* is larger for PVC than for HPC. Because the oxoferryl Cpd II / Cpd I* has a smaller IP than the hydroxoferryl in both catalases (see Appendix B, section 2.2.), we conclude that back oxidation to Cpd I is more likely for PVC than for HPC.

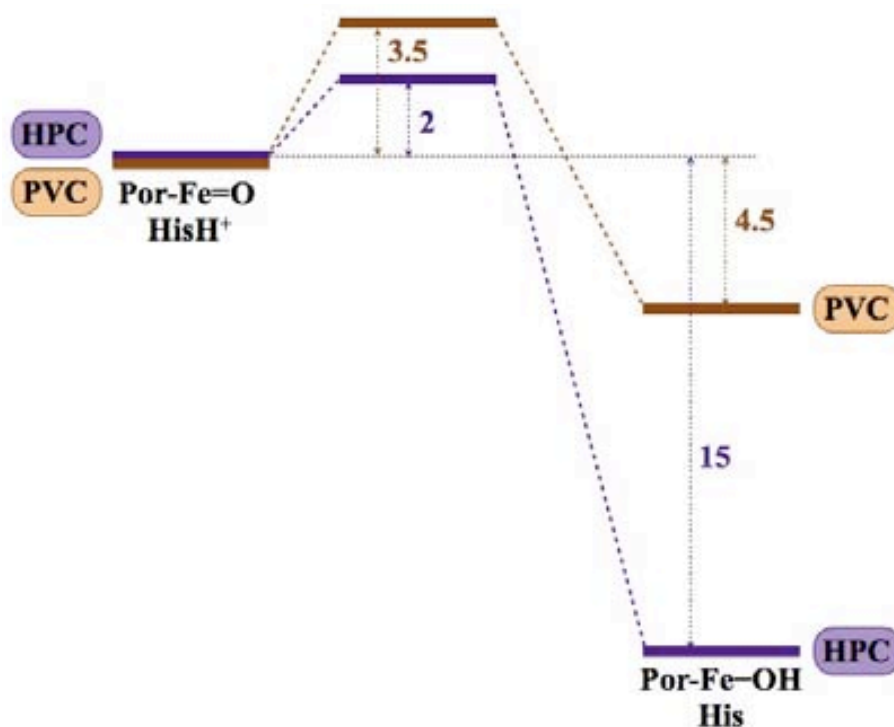


Figure 10. Comparison of the free energy profiles of PT from the distal HisH⁺ to Fe=O in HPC and PVC Cpd II / Cpd I*.

The different PT barriers obtained for HPC and PVC suggest that Cpd I reduction follows a different mechanism in the two catalases. Figure 11 contains our proposed mechanism for Cpd I* formation in HPC and PVC, that is consistent with our results and the available experimental data. As mentioned above, the fact that the PT is spontaneous for HPC indicates that ET and PT occur simultaneously (i.e. PCET). In contrast, it cannot be ruled out that the two transfers are stepwise (ET+PT) for PVC, because the spontaneous PT was not observed (Chapter IV, section 2.1.) and the PT barrier is somewhat higher. In case the two transfers are decoupled, there will be an additional effect that will favour oxidation back to Cpd I in PVC: the intermediate oxoferryl PVC Cpd I* (Por-Fe^{IV}=O) could donate an electron back to the protein residue, recovering the initial oxoferryl Cpd I (Por⁺-Fe^{IV}=O), even before PT could take place.

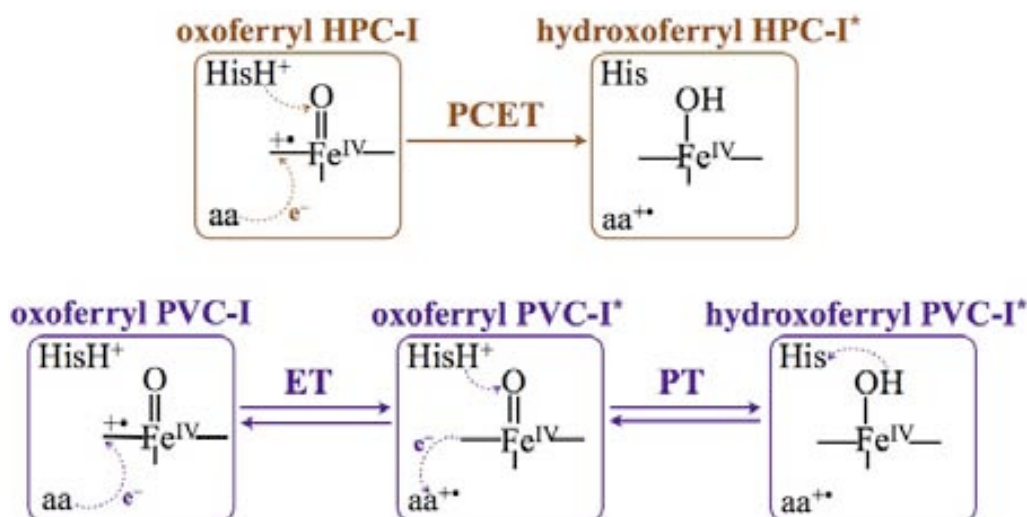


Figure 11. Proposed mechanism of Cpd I* formation in HPC and PVC.

In summary, *protonation of the oxoferryl stabilizes Cpd I* in two different ways: (i) it makes Cpd I* formation more exothermic than a simple ET, and (ii) it hinders the oxidation back to Cpd I.* Since PVC is less affected by these two factors than HPC, *the back conversion to Cpd I is more likely for PVC than for HPC.*

3.3. Redox-active protein residues

As mentioned in section 1, the decay of Cpd I to Cpd I* depends not only on the Cpd I reduction potential but also on the number and distribution of redox-active protein residues around the heme (English & Tsaprailis, 1995; Spolitak, 2006). Therefore, in this section we analyze possible differences between HPC and PVC with respect to this factor. Table 8 shows the number of electron-donating aminoacids in HPC and PVC at 7, 14 or 20 Å⁷ from the heme group⁸ and in the whole protein. It is noteworthy that HPC, whose porphyrin cation radical rapidly migrates into the protein, has twice the number of redox-active residues (13.0%) than PVC (5.8%), which does not form Cpd I*. Therefore, regardless of the Cpd I reduction potential of the two catalases, PVC is less likely to form Cpd I* due to the smaller number of oxidizable residues in the protein.

⁷ ET rates decrease exponentially with distance between the redox couple, and thus it has been proposed that the upper limit for efficient ET is 14 Å (Reece, 2006; Moser, 2006) or 20 Å (Gray, & Winkler, 2003).

⁸ The number of electron donating residues at a given distance from the heme group was measured considering a sphere of 7 Å, 14 Å, 20 Å or ∞ Å (whole protein) around the heme and counting the number of redox-active aminoacids within this sphere.

Table 6. Number of electron-donating aminoacids (Tyr, Trp, Cys, Met and His residues) at a given distance from the heme group for HPC / PVC. The analysis was performed on the crystal structures of oxidized HPC and PVC (PDB entries: 2IUJ and 2IQF) (Alfonso-Prieto, 2007).

distance ^a (Å)	# total protein residues	# redox-active residues ^b	% ^c
7	67 / 69	6 / 5	9.0 / 7.2
14	219 / 217	28 / 21	12.8 / 9.7
20	463 / 478	64 / 40	13.8 / 8.4
whole protein	1964 / 2759	256 / 160	13.0 / 5.8

^a Sphere of 7 Å, 14 Å, 20 Å or ∞ Å (whole protein) around the heme.

^b Number of Tyr + Trp + Cys + Met + His residues within this sphere for HPC / PVC. Oxidized methionines (16 for HPC and 20 for PVC) are excluded, as they cannot longer act as electron donors. For a detailed analysis, see Appendix B, section 7.

^c Number of redox-active residues ×100 / total number of protein residues.

Assuming all the redox-active aminoacids donate equally well, the increase in probability due to the larger number of possible electron donors ($N_{\text{electron donors}}$) can be estimated as an increase of entropy by $[-k_b T \ln(N_{\text{electron donors}})]$. Hence, ET from a protein residue to HPC Cpd I is more likely than for PVC by

$$\frac{k_b T \ln N_{\text{electron donors}}^{\text{HPC}}}{k_b T \ln N_{\text{electron donors}}^{\text{PVC}}} = \frac{\ln N_{\text{electron donors}}^{\text{HPC}}}{\ln N_{\text{electron donors}}^{\text{PVC}}} \quad (\text{eq. 18})$$

Considering the total number of redox-active aminoacids in the protein, this results in a probability increase of only 1.1 times. Therefore, the main factor contributing to Cpd I* formation in HPC is the stabilization of Cpd I* by PT to the oxoferryl group, and the larger number of electron donors has just a minor weight.

The majority of protein radicals detected in oxidized hemeproteins correspond to Tyr or Trp residues (section 2.2.), which are the aminoacids with the lowest oxidation potentials (Fecenko, 2006; Jovanovic, 1991). Therefore, it is reasonable to assume that Tyr and Trp are also the most likely radical sites in Cpd I* of catalases (i.e. the endogenous electron donors to Cpd I). Indeed, tyrosyl radicals have been reported in BLC (Ivancich, 1996, 1997 & 1999) and the F194Y mutant of PMC (Andreoletti, 2001). As can be seen in Table 7, the number of Tyr + Trp residues is much larger for HPC (7.3%) than for PVC (2.8%), consistent with Tyr residues being more abundant in HPC (100) than in PVC (44). Applying equation 18, reduction of HPC Cpd I by a Tyr or Trp residue is 1.5 times more probable than for PVC.

Table 7. Number of Tyr and Trp residues at a given distance from the heme group (HPC / PVC).

distance (Å)	Tyr	Trp	Tyr + Trp	% ^a
7	1 / 1 ^b	0 / 0	1 / 1	1.5 / 1.4
14	12 / 4	6 / 3	18 / 7	8.2 / 3.2
20	34 / 7	12 / 7	46 / 14	9.9 / 2.9
whole protein	100 / 44	44 / 32	144 / 76	7.3 / 2.8

^aNumber of Tyr+Trp $\times 100$ / total number of protein residues.

^bThe closest Tyr residue is the proximal ligand coordinated to the heme iron, which has been discarded to be the radical site by EPR experiments in BLC (Ivancich, 1997).

Since ET rates decrease exponentially with distance between the redox couple, it is reasonable to assume a threshold distance for efficient ET of 14 Å (Reece, 2006; Moser, 2006). Figure 12 focus on the Tyr and Trp residues within 14 Å of the heme. Again it can be observed that there are more electron donors in HPC (12 Tyr + 6 Trp) than in PVC (4 Tyr + 3 Trp, see Table 7). This reinforces the idea that, *although the Cpd I reduction potential of the two catalases is very similar, ET from the protein to Cpd I is more likely in HPC than in PVC due to the larger number of Tyr and Trp residues close to the heme.* Nevertheless, because the increase in probability is only 1.5-fold, *the contribution of the larger number of electron donors to favour Cpd I* formation in HPC is less important than the large stabilization of HPC Cpd I* by PT to the oxoferryl group.*

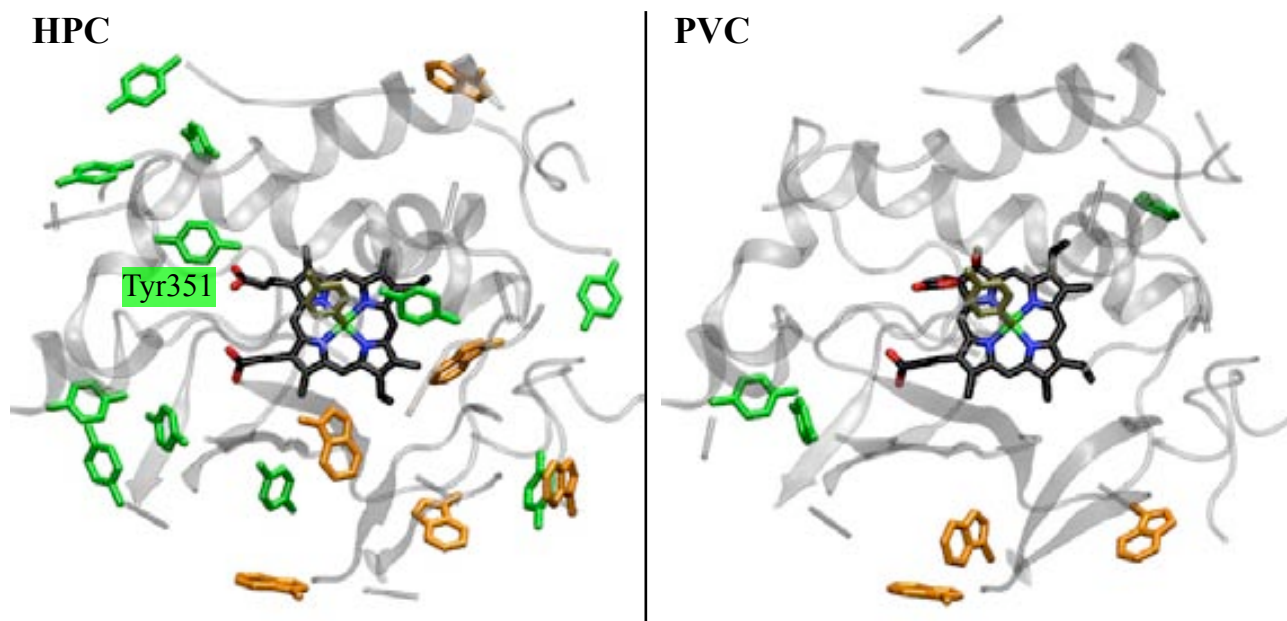


Figure 12. Distribution of Tyr and Trp residues within 14 Å of the heme group. The following colouring was used: grey = protein, black = heme cofactor, tan = proximal iron ligand, green = Tyr, orange = Trp. Tyr351 is the redox-active residue closest to the heme in HPC (section 3.5.).

3.4. Factors determining Cpd I* formation

Catalases are found to form distinct oxidized intermediates upon treatment with peroxyacetic acid (PAA)⁹. In HPC (a small subunit, heme b-containing catalase), a hydroxoferryl neutral porphyrin associated to a protein radical (Cpd I*) is generated. By contrast, PVC (a large subunit, heme d-containing catalase) forms the canonical Cpd I (i.e. an oxoferryl porphyrin cation radical) (Alfonso-Prieto, 2007). Understanding of this different behaviour may provide clues about the different reactivity of heme d-containing catalases compared to heme b.

Three factors can explain the lack of Cpd I* formation in PVC: (i) the Cpd I reduction potential, (ii) the energetics of protonation of the oxoferryl group and (iii) the nature of the endogenous donor. *The Cpd I reduction potential of the two catalases is very similar, and thus it does not appear to contribute significantly to the resistance of PVC to form Cpd I**. However, the number of endogenous electron donors (i.e. Tyr and Trp) close to the heme is larger in HPC than in PVC. Hence, *the probability of ET from a protein residue to HPC Cpd I increases owing to the larger number of electron donors compared to PVC*. This is agreement with wild-type PMC forming Cpd I (Ivancich, 1997), whereas the F194Y PMC mutant, that introduces a redox-active protein residue close to the heme, shows a tyrosyl radical (i.e. Cpd I*) (Andreoletti, 2001).

After ET, *protonation of the oxoferryl group stabilizes Cpd I* in both catalases, because it increases the exothermicity of Cpd I* formation and precludes oxidation back to Cpd I*. This explains why P450 forms a significant fraction of Cpd I at pH > 7, whereas at low pH only Cpd I* is observed (Spolitak, 2005 & 2006). At low pH, the oxoferryl becomes protonated, thus stabilizing Cpd I*. Comparing HPC and PVC, *the stabilization of Cpd I* by PT is smaller for PVC than for HPC, and thus it is easier that PVC reverts to Cpd I*.

In summary, *PVC and HPC form distinct oxidized intermediates primarily due to the different stabilization of Cpd I* by PT, but also due to the different number of endogenous electron donors*. The different propensity to form Cpd I* could explain why heme b-containing catalases, such as HPC or BLC, are easily reduced to Cpd II by ferrocyanide or ascorbate, whereas heme d-containing catalases, such as PVC or HP11, apparently do not form Cpd II (Obinger, 1997; Chelikani, 2005). Ferrocyanide and ascorbate are one-electron donors (AH) that convert Cpd I into

⁹ We recall that PAA is used to form Cpd I in the laboratory instead of H₂O₂, because it avoids that the enzyme returns to the resting state.

Cpd II (Chapter I, section 4.2.). It has been proposed in catalases (Nicholls, 2001) and P450 (Spolitak, 2008) that this reduction occurs through Cpd I*, i.e. first a protein residue reduces Cpd I to Cpd I*, and second the protein radical is reduced by AH:



Most likely, the narrowness of the channels leading to the catalase active site precludes the access of these substrates to the heme (i.e. Cpd I), whereas a protein radical (i.e. Cpd I*) is more easily accessible, provided that it is closer to the binding site of AH on the protein surface. Indeed, it has been shown in LPO that oxidation of AH may be carried out by two different oxidizing species, either the canonical Cpd I (Por^{•+}-Fe^{IV}=O) or Cpd I* (Porph-Fe^{IV}-OH, aa^{•+}), depending on the size of the substrate (Fielding, 2008). Therefore, we suggest that PVC and HP II (heme d catalases) do not react with ferrocyanide and ascorbate because they are not able to stabilize Cpd I* formation as largely as HPC and BLC (heme b catalases).

3.5. Candidates for the radical site in HPC Cpd I* and possible ET pathways

As mentioned in section 3.3., most protein radicals detected in oxidized hemeproteins correspond to Tyr or Trp. Hence, in the present analysis only Tyr and Trp residues will be considered as possible radical sites in HPC Cpd I*. Since the oxidizable protein residue should be at most at 14 Å of the edge of the heme group for the ET to occur at a reasonable rate (Moser, 2006; Reece, 2006), there are 18 possible candidates for the radical site in HPC Cpd I* (12 Tyr and 6 Trp, see Table 7 and Figure 12).

HPC Cpd I* has not been characterized by EPR spectroscopy yet. However, the type and location of the protein radical is known for other catalases. Tyrosyl radicals have been detected for BLC (Tyr369) (Ivancich, 1996, 1997 & 1999) and the F194Y PMC mutant (Tyr194) (Andreoletti, 2001). In the human erythrocyte catalase (HEC), Tyr370 was also proposed to form a tyrosyl radical, based upon sequence alignment and the similarity of the local structure environment compared to BLC (Putnam, 2000). On the same basis, we suggest that the protein radical in HPC is formed at Tyr351, which is the HPC residue equivalent to BLC Y389 and HEC Y370 (see Figure 13). The other possible candidate (the residue equivalent to Tyr194 in the Y194F mutant of PMC) is a phenylalanine (Phe196) in HPC. In this sense, HPC is similar to wild-type PMC, which has a Phe at position 194 and do not form Cpd I* (Ivancich, 1997). Therefore, ET from Phe196 to HPC Cpd I is unlikely.

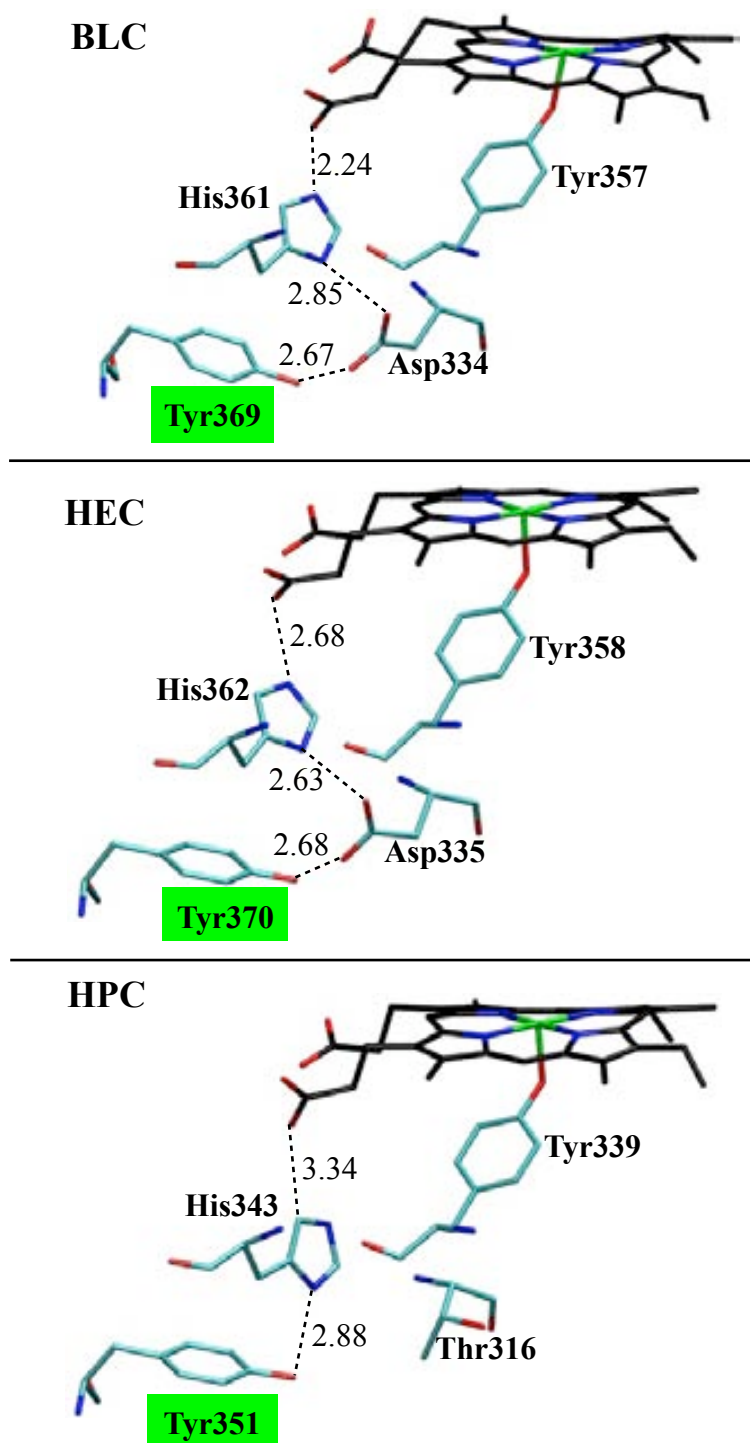


Figure 13. Tyrosine radical sites in BLC (Tyr369, detected by EPR) (Ivancich 1996, 1997 & 1999), HEC (Tyr370, proposed by structural analysis) (Putnam, 2000) and HPC (Tyr351, considered in this chapter) and structural comparison of their environment.

In the three heme b-containing catalases of Figure 13 (BLC, HEC and HPC), the tyrosine radical site (hereafter Tyr_x) is the redox-active residue closest to the heme group (excluding the proximal Tyr iron ligand), in line with ET rates decaying exponentially with the distance between

the redox couple. Inspection of the crystal structure reveals two possible ET pathways from Tyr351 to Cpd I in HPC (Figure 14). On one hand, radical migration may occur through the carbonyl group of the proximal Tyr (i.e. the *backbone* pathway), as suggested for HEC (Putnam, 2000) and the P450-putaredoxin complex (Guallar, 2008). Alternatively, the propionate sidechains of the heme group may act as electron conduits (i.e. the *propionate* pathway), as proposed for ascorbate peroxidase (APX) (Guallar, 2008; Wallrapp & Guallar, 2008).

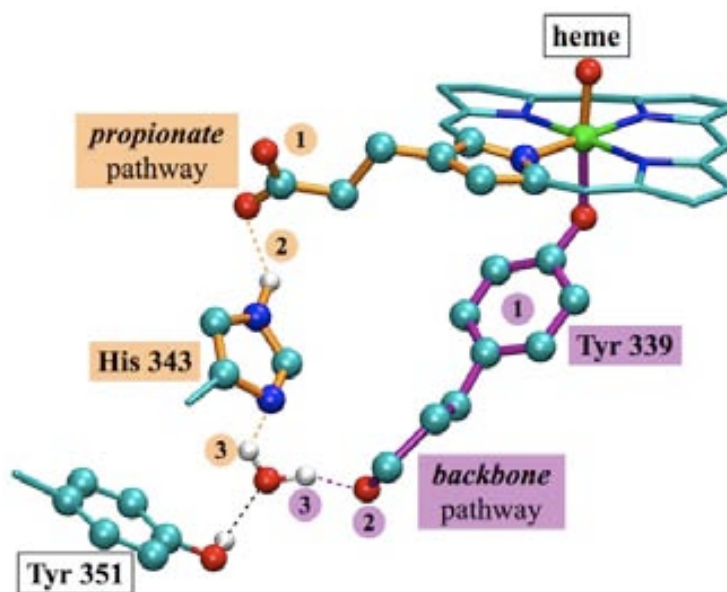


Figure 14. Snapshot of the classical MD of HPC showing the two possible ET pathways between Tyr351 and the heme group (i.e. Cpd I) in HPC. Water molecules may provide a link between the carbonyl group of the proximal Tyr and Tyr351 (the *backbone* pathway, shown in violet) or between His343 and Tyr351 (the *propionate* pathway, shown in orange).

In the backbone pathway (shown in violet in Figure 14), the proximal Tyr is the first electron donor to the porphyrin cation radical. ET from the phenolate ring to the porphyrin (step 1) is very easy, as inferred from the spin density distribution of HPC Cpd I (**Ia** in Chapter IV, Figure 8). The resulting phenoxyl radical may easily delocalize onto the peptide bond of the proximal Tyr (step 2), as has been observed in a Photosystem II (PSII) model (Pujols-Ayala, 2003). Then, the water molecule hydrogen-bonded to the proximal Tyr and Tyr351 (step 3) mediates reduction of the peptide bond radical by Tyr351.

In the propionate pathway (shown in orange in Figure 14), the spin density on the porphyrin may delocalize into the oxygen lone pairs of the propionates (step 1), as recently proposed for APX

(Guallar, 2008; Guallar & Wallrapp, 2008). It has been suggested (Putnam, 2000) that the hydrogen-bonded His and Asp in BLC and HEC, mediate the electron transfer from Tyr_X to the heme (see Figure 13). However, a Thr residue is found in place of this Asp in HPC, disrupting the hydrogen-bonding network. A direct electron transfer from Tyr351 to His343 might be feasible through lone pair- π or π - π interactions (DiLabio & Johnson, 2007). Nevertheless, in case a water molecule bridges these two residues (replacing Asp), the ET could occur at higher rates through the resulting hydrogen-bonding network (steps 2 and 3). Indeed, a water molecule was observed to bridge His343 and Tyr351 during the classical MD of HPC (see Figure 14).

Regardless of the pathway, ET would yield a tyrosyl cation radical, which either continues migrating onto other Tyr or Trp residues (i.e. it is a transient radical site) or becomes stabilized by deprotonation (Svistunenko, 2005; Hoganson, 2004; Faller, 2003). As mentioned in section 2.2., oxidation of a Tyr decreases the pK_a of its phenolic proton by ~12 pH units, but deprotonation also requires the presence of a proton acceptor in the vicinity (Narváez, 2004; Fecenko, 2006). In this regard, it is interesting that in all cases (Figure 13) Tyr_X has a nearby His that may act as a proton acceptor, similar to the His hydrogen-bonded to Tyr_Z in PSII (Tommos & Babcock, 2000). Although Tyr_X and His are not directly hydrogen bonded in catalases, as in PSII, a water molecule in HPC (Figure 14) or the Asp residue in BLC and HEC (Figure 13) may act as a proton shuttle between them. Therefore, the presence of the nearby His343 is another argument in favour of Tyr351 being the radical site.

In summary, based on (i) the experimental data on other catalases, (ii) the distance between the cofactor and the plausible radical site, (iii) the existence of a reasonable ET pathway and (iv) the presence of a nearby base (His 343), we propose that Tyr351 is a likely radical site in HPC Cpd I*. The nearby His343 may play a dual role: first, it could participate in the ET from Tyr351 to Cpd I (i.e. the propionate pathway), and second, it could stabilize the resulting tyrosyl cation radical by deprotonation. Therefore, we decided to investigate the energetics of ET from Tyr351 to Cpd I and the protonation state of the resulting tyrosyl cation radical.

3.6. Free energy of ET from Tyr to Cpd I in HPC ($\Delta G^{\text{Tyr/Cpd I, ET}}$)

To probe our proposal of Tyr351 being the protein radical site, we computed the driving force of the ET from Tyr351 to Cpd I (reaction **15**) (see details in Appendix B, sections 1.4. and 1.5.). 21 snapshots were extracted from the classical MD in the {Tyr, Cpd I} (RO) state and another 21 from the trajectory in the {Tyr^{•+}, Cpd II} (OR)¹⁰ state, and the vertical ET energies were calculated by means of QM/MM.

Table 8 shows the average vertical energies in the {Tyr, Cpd I} state and the {Tyr^{•+}, Cpd II} state. Two different values are given for the EA of Tyr^{•+}, corresponding to the two different conformations of the tyrosyl cation radical observed during the classical MD simulation. Initially, Tyr351 is hydrogen-bonded to His343 through a water molecule (*His*-conformation, see Figure 15). However, at ~17 ns Tyr^{•+} rotates around the C_β-C_γ bond, breaking the hydrogen bond with the water-His pair, and becomes hydrogen-bonded to Glu1516 (*Glu*-conformation, see Figure 15).

Table 8. Average vertical energy gaps ($\langle \text{IP} \rangle$ and $\langle \text{EA} \rangle$) and vertical ET energies ($\langle \Delta E \rangle$) for ET from Tyr351 to Cpd I.

{Tyr, Cpd I} state ^a		{Tyr ^{•+} , Cpd II} state ^b		
$\langle \text{IP} \rangle_{\text{Tyr}} \text{ (eV)}$	7.08 ± 0.31	$\langle \text{IP} \rangle_{\text{Cpd II}} \text{ (eV)}$	7.21 ± 0.35	
$\langle \text{EA} \rangle_{\text{Cpd I}} \text{ (eV)}$	5.48 ± 0.30	$\langle \text{EA} \rangle_{\text{Tyr}^{\bullet+}} \text{ (eV)}$	His-conf ^d	4.82 ± 0.23
			Glu-conf ^d	4.41 ± 0.40
$\langle \Delta E \rangle_{\text{Tyr, Cpd I}} \text{ (eV)}$	1.95 ± 0.43^c	$\langle \Delta E \rangle_{\text{Tyr}^{\bullet+}, \text{Cpd II}} \text{ (eV)}$	His-conf ^d	-2.39 ± 0.42^c
			Glu-conf ^d	-2.80 ± 0.53^c

$$^a \langle \text{IP} \rangle_{\text{Tyr}} = \langle E_{\text{Tyr}^{\bullet+}}(\text{R}_{\text{Tyr}}) - E_{\text{Tyr}}(\text{R}_{\text{Tyr}}) \rangle, \langle \text{EA}_{\text{Cpd I}} \rangle = \langle E_{\text{Cpd I}}(\text{R}_{\text{Cpd I}}) - E_{\text{Cpd II}}(\text{R}_{\text{Cpd I}}) \rangle$$

$$\langle \Delta E_{\text{Tyr, Cpd I}} \rangle = \langle \text{IP}_{\text{Tyr}} \rangle - \langle \text{EA}_{\text{Cpd I}} \rangle$$

$$^b \langle \text{IP} \rangle_{\text{Cpd II}} = \langle E_{\text{Cpd I}}(\text{R}_{\text{Cpd II}}) - E_{\text{Cpd II}}(\text{R}_{\text{Cpd I}}) \rangle, \langle \text{EA} \rangle_{\text{Tyr}^{\bullet+}} = \langle E_{\text{Tyr}^{\bullet+}}(\text{R}_{\text{Tyr}^{\bullet+}}) - E_{\text{Tyr}}(\text{R}_{\text{Tyr}^{\bullet+}}) \rangle$$

$$\langle \Delta E_{\text{Tyr}^{\bullet+}, \text{Cpd II}} \rangle = \langle \text{EA}_{\text{Tyr}^{\bullet+}} \rangle - \langle \text{IP}_{\text{Cpd II}} \rangle$$

$$^c \sigma_{\Delta E} = \sqrt{(\sigma_{\text{IP}}^2 + \sigma_{\text{EA}}^2)}$$

^d See Figure 15.

¹⁰ The electronic configuration of the heme active site in Cpd I^{*} is the same as in Cpd II.

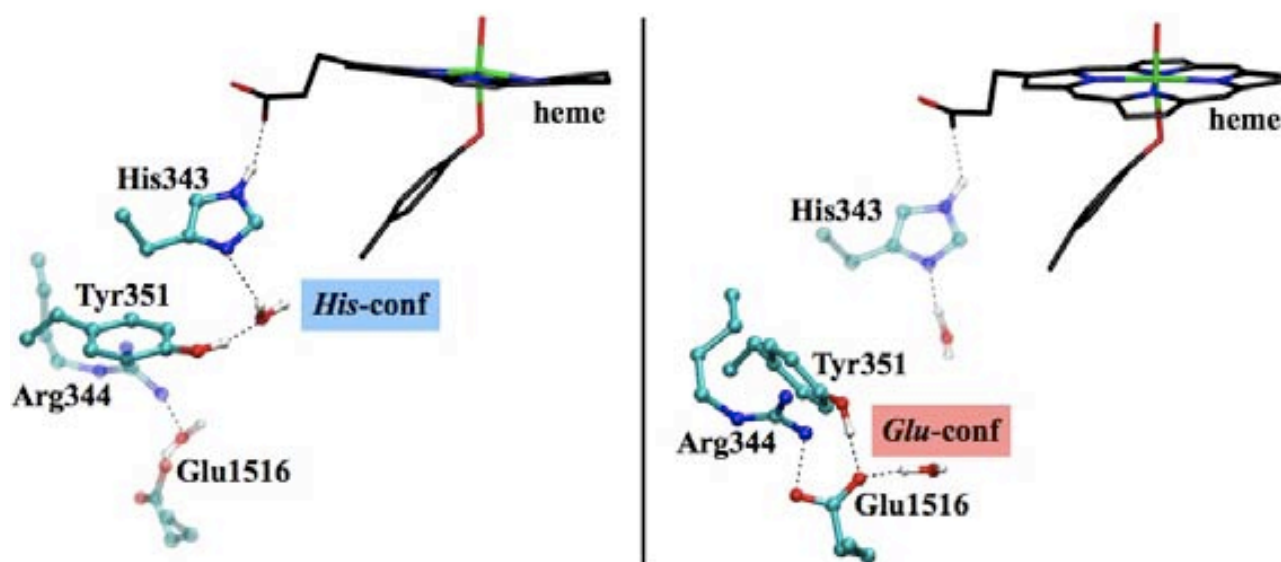


Figure 15. Representative structures of the two possible conformations of the tyrosyl cation radical (i.e. *His*- or *Glu*-conformation) observed during the classical MD in the $\{\text{Tyr}^{\bullet+}, \text{Cpd II}\}$ state.

The fluctuations of the ionization energies of the heme and Tyr are similar (~ 0.3 eV, see Table 8). Therefore, the linear response approximation can be applied (see Chapter I, equations 43-44) to calculate the driving force and reorganization free energy (Table 9). ΔA turns out to be only slightly negative, indicating that the ET from Tyr351 to Cpd I is only moderately exothermic, as proposed for the ET from Tyr_Z to P680⁺ in PSII (Blomberg, 1998). Nevertheless, the exothermicity of the overall reaction (i.e. Cpd I* formation) is expected to increase by the concomitant protonation of the oxoferryl group of the heme (section 3.2.). Besides, deprotonation of the resulting tyrosyl cation radical (section 2.2.) would make the overall reaction even more exergonic. Therefore, in case such PT occurs (see section 3.7.), it would favour Cpd I* formation.

Table 9. Average driving force ($\langle \Delta A \rangle$) and reorganization free energy (λ) for the ET from Tyr351 to Cpd I.

	His-conf^d	Glu-conf^d
ΔA (eV) ^a	-0.22 ± 0.43^c	-0.42 ± 0.49^c
λ (eV) ^b	2.17 ± 0.43^c	2.37 ± 0.49^c

$$^a \Delta A = (\langle \Delta E \rangle_{\text{Tyr}, \text{Cpd I}} + \langle \Delta E \rangle_{\text{Tyr}^{\bullet+}, \text{Cpd II}}) / 2$$

$$^b \lambda = (\langle \Delta E \rangle_{\text{Tyr}, \text{Cpd I}} - \langle \Delta E \rangle_{\text{Tyr}^{\bullet+}, \text{Cpd II}}) / 2$$

$$^c \sigma_{\Delta A} = \sigma_{\lambda} = \sqrt{(\sigma_{\Delta E(\text{Tyr}, \text{Cpd I})}^2 + \sigma_{\Delta E(\text{Tyr}^{\bullet+}, \text{Cpd II})}^2) / 2}$$

^d See Figure 15.

The reorganization energy (λ in Table 9) turns out to be unusually large, partially due to the fluctuations of the water molecules involved in the hydrogen-bonding network to Tyr351 (see Appendix B, section 8). It should also be taken into account that the non-polarizable force field used in the calculations is known to overestimate λ (Blumberger, 2008; Blumberger & Lamoreaux 2008), and that the different dimensions of the heme cofactor and Tyr could also affect the result (Blumberger, 2008; Ayala, 2008).

3.7. Protonation state of the Tyr cation radical

As mentioned previously, the resulting tyrosyl cation radical is expected to deprotonate upon ET. To know whether this is the case in HPC, we have investigated the protonation state of the tyrosyl cation radical by means of QM/MM geometry optimizations (details are given in Appendix B, section 1.6.).

• *Optimized structures*

Figure 16 shows the optimized structures of Tyr351 in its three possible states: reduced state, {oxidized state, His-conformation} and {oxidized state, Glu-conformation}. In the reduced state (Figure 16a), Tyr351 is hydrogen-bonded to His343 through a water molecule. In the {oxidized state, His-conformation} (Figure 16b) the tyrosyl cation radical is not stable and spontaneously transfers its proton (through the bridging water) to His343, resulting in a neutral tyrosyl radical and a protonated His (i.e. Tyr[•] and His⁺). This is consistent with the relative pKa's of Tyr^{•+} and histidine (ca. -2 and 6, respectively). In the {oxidized state, Glu-conformation} (Figure 16c) the tyrosyl cation radical also gets spontaneously deprotonated by the nearby Glu1516, yielding a neutral tyrosyl radical and a protonated glutamic acid (i.e. Tyr[•] and GluH). This is again in agreement with the relative pKa's of Tyr^{•+} and Glu (ca. -2 and 4, respectively). The same results were obtained using gas-phase models instead of QM/MM (Appendix B, section 3.1.)

Therefore, regardless of the proton acceptor, *PT from the tyrosyl radical cation to the hydrogen-bonded base is spontaneous*. In other words, formation of the tyrosyl radical is a PCET process (Hoganson, 2004; Chang, 2004). The resulting neutral tyrosyl radical is more stable by 22.8 kcal/mol (His-conformation) or 21.4 kcal/mol (Glu-conformation) compared to the tyrosyl cation radical (see Appendix B, section 10). As a consequence, *this PT will further increase the exothermicity of Cpd I* formation*.

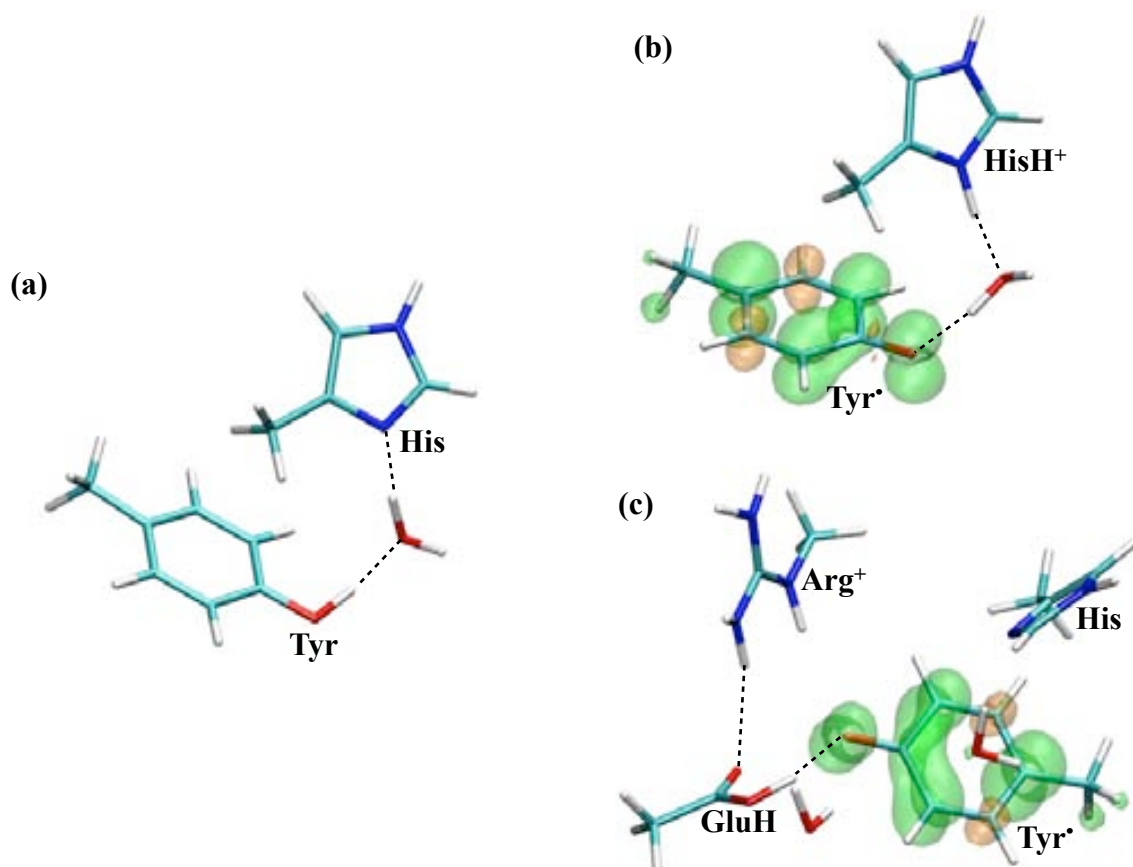


Figure 16. Optimized QM/MM structures of Tyr351. **(a)** reduced state, **(b)** oxidized state, His-conformation, **(c)** oxidized state, Glu-conformation. Only the QM atoms are displayed. Spin isodensity surfaces at $0.004 \text{ e } \text{\AA}^{-3}$ are also shown.

Nevertheless, it should be noted that deprotonation by Glu1516 requires a conformational change of the tyrosyl cation radical to approach the glutamate. At neutral pH, this is unlikely to happen because $\text{Tyr}^{\bullet+}$ will be rapidly deprotonated by His343. By contrast, at low pH, when His343 is already protonated and thus cannot act as a base, such a conformational change would help $\text{Tyr}^{\bullet+}$ to find an alternative proton acceptor (i.e. Glu1516). A similar situation has been proposed for the bacterial reaction center (RC): a histidine is the primary base at neutral pH, whereas a glutamate is a secondary proton acceptor acting only at low pH (Narváez, 2002).

• *Calculation of redox properties*

PT is also found to modify the redox properties of the tyrosyl radical. The redox energies were calculated as explained in Appendix B, section 1.6. and Table 10 shows the results obtained for the two possible redox couples, either tyrosine / tyrosyl neutral radical or tyrosine / tyrosyl cation radical.

Table 10. Redox energies of Tyr (B) / Tyr[•] (+HB)^a compared to Tyr (B) / Tyr^{•+} (B)^b. IPⁱ and EAⁱ are the ionization potential and the electron affinity, respectively, ΔEⁱ is the adiabatic energy of oxidation, and λⁱ is the reorganization energy. Only the inner-sphere contribution (i.e. the Tyr and the first-shell hydrogen-bonded residues) is considered. All the values are in eV.

model		IP ⁱ	EA ⁱ	ΔE ⁱ	λ ⁱ
His-conf	Tyr[•]	7.03 ^c	5.31 ^c	6.38 ^d	0.86 ^e
	Tyr^{•+}	7.03 ^f	6.89 ^f	7.32 ^g	0.07 ^h
Glu-conf	Tyr[•]	6.75 ^c	4.92 ^c	6.29 ^d	0.91 ^e
	Tyr^{•+}	6.75 ^f	5.93 ^f	7.16 ^g	0.41 ^h

^a QM/MM optimized structures without constraints. B = His or Glu

^b QM/MM optimized structures fixing the O_{Tyr}-H_{Tyr} distance. B = His or Glu.

^c IPⁱ_{Tyr(B)} = E^{QM}_{Tyr^{•+}(B)}(R_{Tyr(B)}) - E^{QM}_{Tyr(B)}(R_{Tyr(B)}), EAⁱ_{Tyr[•](+HB)} = E^{QM}_{Tyr[•](+HB)}(R_{Tyr[•]}) - E^{QM}_{Tyr(B)}(R_{Tyr[•](+HB)})

^d ΔEⁱ = E^{QM}_{Tyr[•](+HB)}(R_{Tyr[•](+HB)}) - E^{QM}_{Tyr(B)}(R_{Tyr(B)})

^e λⁱ = (IPⁱ_{Tyr(B)} - EAⁱ_{Tyr[•](+HB)}) / 2

^f IPⁱ_{Tyr(B)} = E^{QM}_{Tyr^{•+}(B)}(R_{Tyr(B)}) - E^{QM}_{Tyr(B)}(R_{Tyr(B)}), EAⁱ_{Tyr^{•+}(B)} = E^{QM}_{Tyr^{•+}(B)}(R_{Tyr^{•+}(B)}) - E^{QM}_{Tyr(B)}(R_{Tyr^{•+}(B)})

^g ΔEⁱ = E^{QM}_{Tyr^{•+}(B)}(R_{Tyr^{•+}(B)}) - E^{QM}_{Tyr(B)}(R_{Tyr(B)})

^h λⁱ = (IPⁱ_{Tyr(B)} - EAⁱ_{Tyr^{•+}(B)}) / 2

The EA of the neutral Tyr[•] is lower than for cationic Tyr^{•+} (Table 10). This reminds the increase in the IP of the hydroxoferryl Cpd II compared to the oxoferryl form. As a consequence, PT to His or Glu is expected to hinder reduction of the tyrosyl radical by the porphyrin or other protein residues, thus stabilizing the radical on Tyr351. The reorganization energy of the neutral Tyr[•] is larger than for cationic Tyr^{•+} (Table 10), as expected for PCET compared to a simple ET.

In summary, *the tyrosyl cation radical obtained after ET is spontaneously deprotonated by the hydrogen-bonded base, mainly His343. This increases the exothermicity of the overall reaction, thus favouring Cpd I* formation. Besides, this PT also stabilizes the radical on Tyr351, because it hinders reduction of the tyrosyl radical by the porphyrin or other protein residues.*

3.8. Formation of protein radicals in catalases

Protein radicals (i.e. Cpd I*) have been detected in several heme proteins. In globins (Mb and Hb), protein radicals are implicated in pathological oxidative reactions and protein-protein crosslinking (Lardinois, 2004, Svistunenko, 2005). By contrast, tyrosyl or tryptophanyl radicals in heme enzymes are either part of the enzymatic mechanism or observed under non-optimal catalytic conditions. In CcP (Sivaraja, 1999; Dunford 1999; Veitch & Smith, 2001), KatGs (Ivancich, 2003;

Jakopitsch, 2006; Singh, 2007; Colin, 2009), LPO (Fielding, 2008), lignin peroxidase (Bloding, 1999a & 1999b), PGHS (Tsai & Kulmacz, 2009) or AOS (Wu, 2003), formation of a protein radical is necessary for the electron transfer from the substrate to the heme. In contrast, protein radicals are detected in the peroxide shunt pathway of P450 only when the substrate is missing, i.e. under non-optimal catalytic conditions (Spolikat, 2005, 2006 & 2008).

Likewise, protein radicals in catalases are observed at low H₂O₂ concentrations and in the absence of exogenous reductants (Nicholls, 2001; Kirkman & Gaetani, 2007). Thus, with respect to the catalytic reaction, Cpd I* is considered to be an inactive form of the enzyme, because it regenerates ferricatalase without O₂ production. However, with respect to the peroxidatic cycle, protein radicals could play a role in the reduction of certain peroxidatic substrates (as in CcP and KatGs). For instance, ferrocyanide has been suggested to be reduced by catalase Cpd I* instead of Cpd I (see section 3.4.) (Nicholls, 2001). Therefore, unraveling the factors involved in protein radical formation in catalases could be useful to understand their peroxidatic activity, as well as the oxidative activity of other heme proteins.

To date, two tyrosyl radicals have been detected in catalases by EPR, Tyr369 in BLC (Ivancich, 1996, 1997 & 1999) and Tyr194 in the F194Y PMC mutant (Andreoletti, 2001). Besides, X-Ray and spectroscopic data suggest that MLC (Murshudov, 2002), HEC (Putnam, 2000) and HPC (Alfonso-Prieto, 2007) could also form a protein radical. In this chapter, *we propose Tyr351 as a likely candidate for the radical site in HPC based on (i) the experimental data on other catalases, (ii) the distance from the cofactor (iii) the existence of a reasonable ET pathway and (iv) the presence of a nearby base (His 343)*. In order to probe our proposal, the driving force of the ET from Tyr351 to Cpd I and the protonation state of the resulting tyrosyl cation radical have been investigated by means of QM/MM calculations.

Our results show that *ET from Tyr351 to Cpd I is only slightly exothermic*. Nevertheless, *the subsequent spontaneous PT to the hydrogen-bonded His343 increases the exothermicity, favouring Cpd I* formation*. Moreover, deprotonation stabilizes the radical at Tyr351 because *PT also hinders reduction of the tyrosyl radical either by the porphyrin or by other protein residues*. This is similar to the effect of the protonation of the oxoferryl heme in Cpd I reduction.

Overall, formation of protein radicals in catalases depends on two factors. On one hand, ET to Cpd I requires that the redox-active protein residue is close ($\leq 14 \text{ \AA}$) to the heme cofactor (Moser, 2006; Reece, 2006), and that there is a reasonable ET pathway. On the other hand, because the driving force of ET is small, stabilization of the radical by the nearby residues is necessary to increase the exothermicity of the overall reaction and prevent back ET. In case of tyrosyl radicals, this role is played by a (hydrogen-bonded) base that deprotonates the initially formed tyrosyl cation radical.

4. CONCLUSIONS

- HPC and PVC have similar Cpd I reduction potentials.
- Upon ET, the distal His transfers a proton to the oxoferryl group of the heme (PT).
- Protonation of the oxoferryl group increases the exothermicity of Cpd I* / Cpd II formation, making back oxidation to Cpd I more difficult.
- Cpd I* formation is favoured in HPC because (i) the number of electron-donating protein residues is larger than in PVC and (ii) Cpd I* is more stable.
- Tyr351 is a good candidate for the radical site in HPC.
- Although ET from Tyr351 to Cpd I is only slightly exothermic, the spontaneous deprotonation (PT) of the resulting tyrosyl cation radical by His343 increases the exothermicity of Cpd I* formation, making back reduction of the tyrosyl radical very difficult.

In summary, Cpd I* formation in catalases depends on three factors: (i) the presence of a redox-active protein residue at an adequate distance, along with a reasonable ET pathway from the cofactor, (ii) the easiness of protonation of the oxoferryl heme and (iii) the stabilization of the resulting protein radical. Independently of the type of cofactor (heme b or heme d), Cpd I is reduced provided that there is an electron-donating protein residue in the vicinity. However, the ET process is only slightly exothermic, and thus it can be easily reverted unless other factors contribute to stabilize Cpd I* formation. One of such factors is the protonation of the oxoferryl heme, because it increases the exothermicity of the overall reaction and hinders reoxidation of the heme. Moreover, in case the putative endogenous donor is a tyrosine residue, deprotonation of the tyrosyl cation radical further contributes to stabilize Cpd I* formation, because it increases the exothermicity of the process and it hampers back reduction of the protein radical by the heme.